MAGNETIC PROPERTIES OF SINGLE-LAYER AND TRILAYER STRUCTURED CoFeB BASED MAGNETIC THIN FILMS

A thesis submitted

by

Anabil Gayen

to

Indian Institute of Technology Guwahati

in

Partial fulfillment of the requirement for the award of the degree of
Doctor of Philosophy in Physics

Department of Physics
Indian Institute of Technology Guwahati
Guwahati 781 039, Assam, India
May 2018

MAGNETIC PROPERTIES OF SINGLE-LAYER AND TRILAYER STRUCTURED CoFeB BASED MAGNETIC THIN FILMS

A thesis submitted

by

Anabil Gayen

to

Indian Institute of Technology Guwahati

in

Partial fulfillment of the requirement for the award of the degree of
Doctor of Philosophy in Physics

Department of Physics
Indian Institute of Technology Guwahati
Guwahati 781 039, Assam, India
May 2018

STATEMENT

The work contained in the thesis entitled "***Magnetic properties of single-layer and trilayer structured CoFeB based magnetic thin films***" has been carried out by me under the supervision of Prof. Perumal Alagarsamy at the Department of Physics, Indian Institute of Technology Guwahati. This work has not been submitted elsewhere for the award of any degree.

May 2018

(Anabil Gayen)
Roll No: 126121015
Department of Physics
Indian Institute of Technology Guwahati
Guwahati – 781039
India.

CERTIFICATE

It is certified that the work contained in the thesis entitled "***Magnetic properties of single-layer and trilayer structured CoFeB based magnetic thin films***" submitted by Mr. Anabil Gayen (Roll No: 126121015), a Ph.D. student of the Department of Physics, Indian Institute of Technology Guwahati for the award of degree of Doctor of Philosophy has been carried out under the supervision of Prof. Perumal Alagarsamy. This work has not been submitted elsewhere for the award of any degree.

May 2018

(Dr. Perumal Alagarsamy)
Professor
Department of Physics
Indian Institute of Technology Guwahati
Guwahati – 781039
India.

Dedicated to

My beloved parents . . .

ACKNOWLEDGEMENTS

It is my privilege to express deep sense of gratitude to my thesis supervisor Prof. Perumal Alagarsamy for his resourceful guidance, constructive criticisms and careful supervision in guiding me throughout my research work. His knowledge, relevant ideas and energetic spirit have helped me to complete the thesis work successfully. I am grateful to my doctoral committee members (Prof. S. Ravi, Dr. D. Pamu and Prof. S. Senthilvelan) for reviewing my research work regularly and providing valuable guidelines and suggestions for the improvement of my research work. I am thankful to Prof. Subhradip Ghosh, HOD Department of Physics, Prof. S. Basu and Prof. P. Poulose, the former HODs, Department of Physics for their immense supports.

I am very much thankful to Dr. Subhankar Bedanta, NISER Bhubaneswar and Dr. J. Arout Chelvane, DMRL India for magnetic domain observation using Kerr microscope.

I am grateful to Indian Institute of Technology Guwahati, and Government of India, Ministry of Human Resource Development for the financial support.

I express my sincere thanks to Dr. Sidananda Sarma, scientific officer in department of physics, for guiding me to operate various high precision instruments in department of physics. Also, I thank Mr. Chandan Borgohain, Dr. Kula Kamal Senapati and Mr. Kesho Singh, scientific officers of CIF, who have patiently and enthusiastically extended their expertise in handling various instruments that I have used for my research work.

I am fortunate to have my senior, Dr. Akhilesh Kr. Singh and other lab seniors, Dr. Bhargab Deka, Mr. Bhagban Kisan, Dr. P.C. Shyni, Dr. Tribedi Bora, Dr. T. Santosh and Dr. Rahul Das, who helped me in various ways throughout my research work. My lab mates, Dr. Bipul Deka, Dr. R. Gopalrao, Arnab, Ravi, Rajkumar, Gobinda, Bibhuti, Pratap, Camelia, Aneeta, Dolly and Anirban will always be remembered for the wonderful time we shared together. Special thanks to Buddhadeb, Kamal, Joydip, Nawaz for the joyous discussions we had. I thank Rajkumar a lot for all his help and criticism towards me.

Heartfelt thanks to Bishuda and Rameshda for making me feel at home from the very first day at IITG. Literally they were my local guardians. Sudinda deserves a special mention for his charismatic presence and never ending support. Koushik is always there to lend his support. I really adore our brotherhood from the very first day I met you. Sayan, (Sayandeep) thanks for all your moral support and love. I cannot express my gratitude in words for my

best buddy, Bhargabda (Dhon). You'll be the best one for rest of my life. Certainly without your company I'll not be able to finish the job.

The group of charming peoples, Kallol, Ramiz, Ashis, Sourav, Abhijit, Rahul, Shibananda, Srikrishna, Noor, a special thanks to all of you for all those wonderful moments and making my IITG life memorable.

I owe a lot to my beloved parents. My parents and my Kaka (Monojit Gayen) have encouraged me lot to pursue my PhD career. Without their infinite motivation and support I'll not be able to finish my PhD. I sincerely thank my brothers (Anirban and Anway), sisters (Trina and Mampu) and all my family members for their moral support and constant encouragements. Loads of love to cute Gendu (Aryan) and Kyao (Ritoja). My dear Dadu and my Mother are responsible for whatever minimal success I have in my life, and they will remain the major motivation for me till the last day of my life. Rumi, most adorable friend and companion of my life, I owe you a world of thanks for the belief and faith you have shown towards me and for supporting me through all the ups and downs of my life. Thanks for being my shadow. Finally my sincere thanks are due to all those have been helped me in whatever manner and bring me to this position, some of whom I may have inadvertently forgotten to mention in this acknowledgement.

Anabil Gayen

PREFACE

Spintronics is the study of phenomena related to the spin of electrons and of devices that take advantage of the spin of the electron along with its charge. In contrast to conventional electronics, which is limited to transport and manipulation of electric charges in the form of electrons, spintronics makes use of both the spin and charge degree of freedom of the electron. This opens the door to novel effects and futuristic spintronics devices based on the manipulation and control of the spin degree of freedom by means of electric and magnetic fields. Spintronics phenomena occur when the concepts of magnetic engineering (spin), semiconductor engineering (electric charge) and light are overlapped. Interestingly, the time between discovering new spintronics-related materials or phenomena and the development and commercialization of devices using such materials or phenomena has been decreasing.

Among various magnetic materials surveyed for targeting magnetic tunnel junction and spin-valve junction as spintronics devices, CoFeB based thin film is found to be one of the promising materials suitable for various spintronics applications in modern magneto-electronic devices due to their tunable magnetic properties. A careful review of the literature on CoFeB based thin films suggests that the magnetic properties of the films are strongly dependent on film thickness. For example, ultra-thin CoFeB films with thickness less than 5 nm exhibit a strong perpendicular magnetic anisotropy due to interfacial effects. Hence, extensive studies have been carried out on CoFeB films to understand spin polarization, magnetic domain structure, ferromagnetic resonance and damping properties, corrosion properties, *etc*. With increasing film thickness above 5 nm and up to 70 nm, the strong perpendicular magnetic anisotropy observed in ultra-thin films transforms into in-plane magnetic anisotropy with magnetization oriented along the film plane direction. Thicker CoFeB based films are also grown on flexible substrates to investigate the influence of strain on the magnetic anisotropy of CoFeB films with applications in flexible electronics in mind. In addition, thick CoFeB based films with high in-plane magnetic anisotropy field as well as high saturation magnetization have been used as soft magnetic underlayers for obtaining high signal to noise ratio in perpendicular magnetic recording media. On further increasing film thickness, the effective magnetic anisotropy induced by the stress in the films overcomes the in-plane magnetic anisotropy and increases the degree of local disorder in the easy-axis of as-deposited films. Therefore, thicker CoFeB films become magnetically

hard and display transcritical loop characterized by two magnetization reversal processes. However, most of the earlier reported works have been majorly focused on either tuning the magnetic properties of CoFeB films at ultra-thin level from application point of view or studying the magnetic properties of the CoFeB films at random thicknesses and compositions using different fabrication processes. There are no systematic and detailed studies have been carried out to investigate the effects of composition, film thickness over a wide range of thicknesses and measurement temperature on the magnetic properties of CoFeB films prepared by a single fabrication technique.

Nevertheless, thicker CoFeB based films exhibiting high resistivity, high permeability, high saturation magnetization and appropriate anisotropy field were explored for the applications in magnetic flux amplifiers, magnetic recording heads, soft magnetic underlayers in perpendicular magnetic recording media, flexible electronics, *etc*. However, only a few reports are available in the literature related to tuning of magnetic properties of thick CoFeB films despite their vast applicability. In order to tune the magnetic properties of thick CoFeB films by controlling the development of effective magnetic anisotropy at larger thickness, the following methods are generally adopted: (i) fabricating multilayer structured thin films having ferromagnetic layers separated by non-magnetic (metallic and non-metallic) layer and (ii) executing controlled heat treatment of the amorphous precursor under different annealing environments. It may be noted that the fabrication of multilayer films with more number of layers (N) not only increases the number of interfaces, but also complicates interlayer coupling between the ferromagnetic layers. In addition, the magnetic coupling between ferromagnetic layers vary indiscriminately with spacer layer material and its thickness. Nevertheless, there are no systematic studies available on magnetic interactions between (i) ferromagnetic layers through different spacer layer materials as a function of spacer layer thickness, (ii) different ferromagnetic layer thicknesses with different domain structures. The latter one, especially as a function of temperature, is expected to introduce different types of magnetic interactions and temperature dependent interface roughness induced interlayer coupling.

This motivated us to plan this thesis work with the following aims: (i) to study the effect of composition and temperature on the magnetic properties of single-layer amorphous $Co_{80-y}Fe_yB_{20}$ (t nm) thin films over a wide range of thickness from 7 to 200 nm, (ii) to investigate the effect of spacer layer materials and its thickness and temperature on the magnetic interactions between two CoFeB262 layers having same domain structure [symmetric Substrate/CoFeB262 (20 nm)/[Cr,Ta (x nm)]/CoFeB262 (20 nm)] and different

domain structures [asymmetric, Substrate/CoFeB262 (100 nm)/[Cr,Ta (x nm)]/CoFeB262 (20 nm)], (iii) To understand the effect of top CoFeB262 layer thickness and temperature on the magnetic properties of thick CoFeB262 (100 nm) bottom layer through different spacer layer materials (Cr and Ta) in trilayer Substrate/CoFeB262 (100 nm)/[Cr,Ta (x nm)]/CoFeB262 (y nm) films with y = 2, 5, 10, 30 and 50 nm, and (iv) to explore the possibility of tuning the magnetic properties of thick CoFeB262 (100 nm) film using simple trilayer film structure.

The present thesis is organized as follows: **Chapter 1** presents a brief introduction to the content of the thesis along with a review of literature relevant to the thesis work. The motivation and aim of thesis works are also included in this chapter. **Chapter 2** summarizes the fundamental aspects of magnetism including basics of magnetism, intrinsic properties of magnetic materials, anisotropy, magnetic domains and walls, interlayer coupling in multilayer thin films and various models utilized in the analysis of the data for the presently investigated films. **Chapter 3** discusses the experimental techniques including the sample preparation methodologies used in the present studies. The basic principle and the theory behind the experiments, the experimental set up and the measurement / methodology leading to the determination of the physical properties are also briefly discussed. **Chapter 4** discusses thickness dependent structural and magnetic properties of amorphous $Co_{80-y}Fe_yB_{20}$ (t nm) thin films with two different compositions [$Co_{40}Fe_{40}B_{20}$ (CoFeB442) and $Co_{20}Fe_{60}B_{20}$ (CoFeB262)] at room temperature. The temperature dependent magnetic properties of CoFeB thin films in the temperature range between 30 and 700 K at different thicknesses are also examined in this chapter. The **fifth chapter** is meant for preparing trilayer Substrate/CoFeB262 (y nm)/[Cr,Ta (x nm)]/CoFeB262 (20 nm) films with y = 20 and 100, and x = 0 – 6 and studying the effect of spacer layer materials and its thickness, and temperature on the magnetic interactions between CoFeB262 layers having same domain structure (symmetric) and different domain structures (asymmetric). **Chapter 6** focuses on understanding the effect of top CoFeB262 layer thickness on the magnetic properties of thick CoFeB262 bottom layer through different spacer layer materials (Cr and Ta) in trilayer Substrate/CoFeB262 (100 nm)/[Cr,Ta (x nm)]/CoFeB262 (y nm) films with y = 2, 5, 10, 30 and 50 nm. The summary of conclusions drawn from this thesis work and a brief write-up about the future scope of research in these types of materials is presented in **Chapter 7**. References and list of publications, originated out of this thesis work and the publications from other collaborative research works, are listed at the end of the thesis.

CONTENTS

1.	**Prologue**	01
	1.1. Introduction	03
	1.2. Motivation behind the work	05
	1.3. Objective of the thesis work	08
2.	**Fundamental aspects and theoretical modeling**	11
	2.1. Introduction	13
	2.2. Origin of magnetism	13
	2.2.1. Diamagnetism	14
	2.2.2. Paramagnetism	14
	2.2.3. Ferromagnetism	16
	2.2.4. Antiferromagnetism	19
	2.3. Intrinsic properties of magnetic materials	20
	2.3.1. Exchange Interaction	20
	2.4. Anisotropy	23
	2.4.1. Magnetocrystalline anisotropy	25
	2.4.2. Shape anisotropy	26
	2.4.3. Induced anisotropy	28
	2.4.4. Magnetostrictive anisotropy	29
	2.4.5. Magnetic surface anisotropy	29
	2.5. Magnetic domains and domain walls	30
	2.6. Magnetic properties of amorphous and nanocrystalline materials	34
	2.7. Interlayer coupling in multilayer thin films	35
	2.7.1. Exchange coupling	35
	2.7.1.1. Direct exchange coupling	35
	2.7.1.2. Indirect exchange coupling	36
	2.7.2. Magnetostatic coupling	36
	2.7.2.1. Topological coupling	36
	2.7.2.2. Stray field coupling	37
	2.7.2.3. Domain wall stray field coupling	38

3.	**Experimental Methods**	41
	3.1. Introduction	43
	3.2. Techniques used for sample preparation	43
	3.2.1. Sputtering technique	43
	3.2.1.1. DC sputtering technique	44
	3.2.1.2. Magnetron sputtering technique	45
	3.2.2. Calibration of deposition rate	47
	3.3. Structural property characterization	49
	3.3.1. X-ray diffraction	49
	3.3.2. X-ray reflectivity	50
	3.3.3. Transmission electron microscopy	52
	3.4. Magnetic property characterization	53
	3.4.1. Vibrating sample magnetometer	55
	3.5. Magnetic domain structure analysis	56
	3.5.1. MOKE microscope	56
	3.5.2. Magnetic force microscope	59
4.	**Thickness dependent properties of single-layer CoFeB magnetic thin films**	63
	4.1. Introduction	65
	4.2. Experimental details	66
	4.3. Results and discussion	68
	4.3.1. Structural properties	68
	4.3.2. Magnetic properties	72
	4.3.2.1. Room temperature magnetic properties	72
	4.3.2.2. Temperature dependent magnetic properties	80
	4.4. Summary	85
5.	**Magnetic interactions in trilayer structured CoFeB films with different domain structures: Effect of spacer layer**	87
	5.1. Introduction	89
	5.2. Experimental details	91
	5.3. Results and discussion	92
	5.3.1. Structural properties	92

	5.3.2. Magnetic properties	93
	5.3.2.1. Room temperature magnetic properties	93
	5.3.2.2. Temperature dependent magnetic properties	104
	5.4. Summary	110
6.	**Tuning magnetic properties of thick CoFeB films by simple trilayer structure: Effect of top CoFeB layer thickness**	113
	6.1. Introduction	115
	6.2. Experimental details	117
	6.3. Results and discussion	119
	6.3.1. Structural properties	119
	6.3.2. Magnetic properties	119
	6.3.2.1. Room temperature magnetic properties	119
	6.3.2.2. Temperature dependent magnetic properties	127
	6.4. Summary	133
7.	**Summary and scope for future work**	135
	7.1. Summary of the results	137
	7.2. Scope for future work	140
References		143
Publications		159

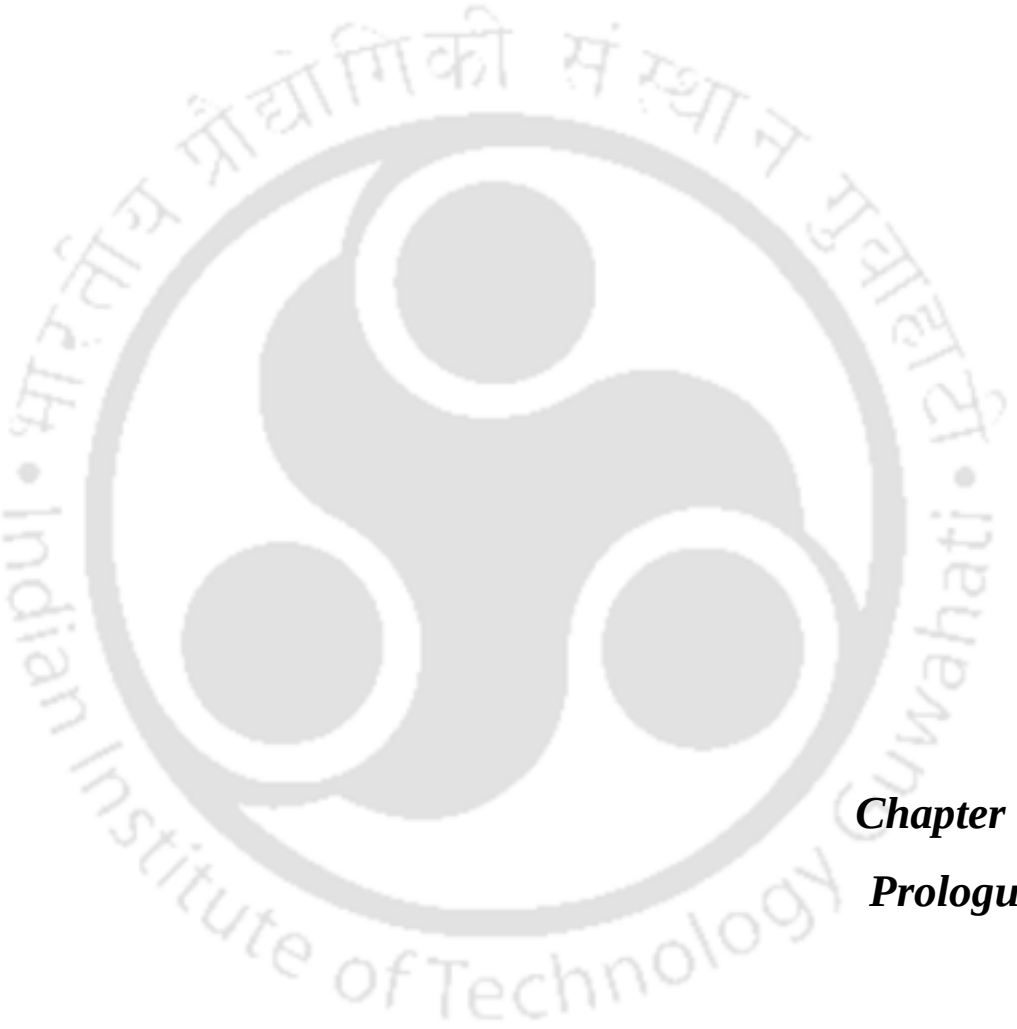

Chapter 1

Prologue

भारतीय प्रौद्योगिकी संस्थान गुवाहाटी
Indian Institute of Technology Guwahati

1.1. Introduction

More, faster, better, cheaper, *etc*. are the modern mantras and demands of our device-happy and data-centered world. With this connection, technologies required for processing and storing information have created two major industries of semiconductor and data storage, respectively. While ultra-high volume processing and communication devices are at present based on semiconductor devices, the information storage devices rely majorly on multilayers of magnetic materials [AKTA2013, CHEN20132, HART2013, HEDI2013, SHIN2014, SATO2015, SCHA2016]. Particularly, to achieve ultra-high storage density in the information storage devices, recently, the new field of research, termed as spin electronics or spintronics, is focused in multidisciplinary level and intensified by a strong synergy between breakthroughs in basic science and industrial applications in the fields of magnetic recording, non-volatile memories, semiconductor spintronics, magnetic field sensors, *etc* [SATO2015, XUY2015, BAND2016, SCHA2016]. Spintronics, in general, is the study of phenomena related to the spin of electrons and of devices that take advantage of the spin of the electron along with its charge. In contrast to conventional electronics, which is limited to transport and manipulation of electric charges in the form of electrons, spintronics makes use of both the spin and charge degree of freedom of the electron. As a result, two current channels for two types of spin orientations are considered. This postulation opens the door to novel effects and futuristic spintronics devices based on the manipulation and control of the spin degree of freedom by means of electric and magnetic fields. In addition, the time between discovering new spintronics-related materials or phenomena and the development and commercialization of devices using such materials or phenomena has been decreasing.

One of the most important milestones in the young field of spintronics is the discovery of giant magnetoresistance (GMR) in thin film structure consisting of two ferromagnetic layers separated by a metallic non-magnetic spacer [BAIB1988, BINA1989, REIG2013], which finds application in hard disks, where the magnetoresistive (MR) read heads convert information stored in recording media by a small magnetic stray field into electrical signal with a high spatial resolution [WOLF2001, PIRA2007, PIRA2011, MALL2012, HIRO2013]. Another recent development is the combination of tunnel magnetoresistance (TMR) elements in read heads with perpendicular recording which steeply increases the storage density [VILL2010, HIRO2015, SATO2015, TSYM2016, FREI2016, YOUC2017, ZHOU2017]. Magnetic random access memory, magnetic field sensors, lab-on-chip and reconfigurable magnetic logic are a few other examples of novel

spintronics devices [TANG2010, HEDI2013, IANN2014, LEON2014, DIEN2016, KURI2017, WANG2017]. Figure 1.01 displays the typical phenomena and devices based on spintronics [ANDO2015]. In the figure, three concepts such as magnetic engineering (spin), semiconductor engineering (electric charge) and light are overlapped to form a region, where typical spintronics phenomena may occur.

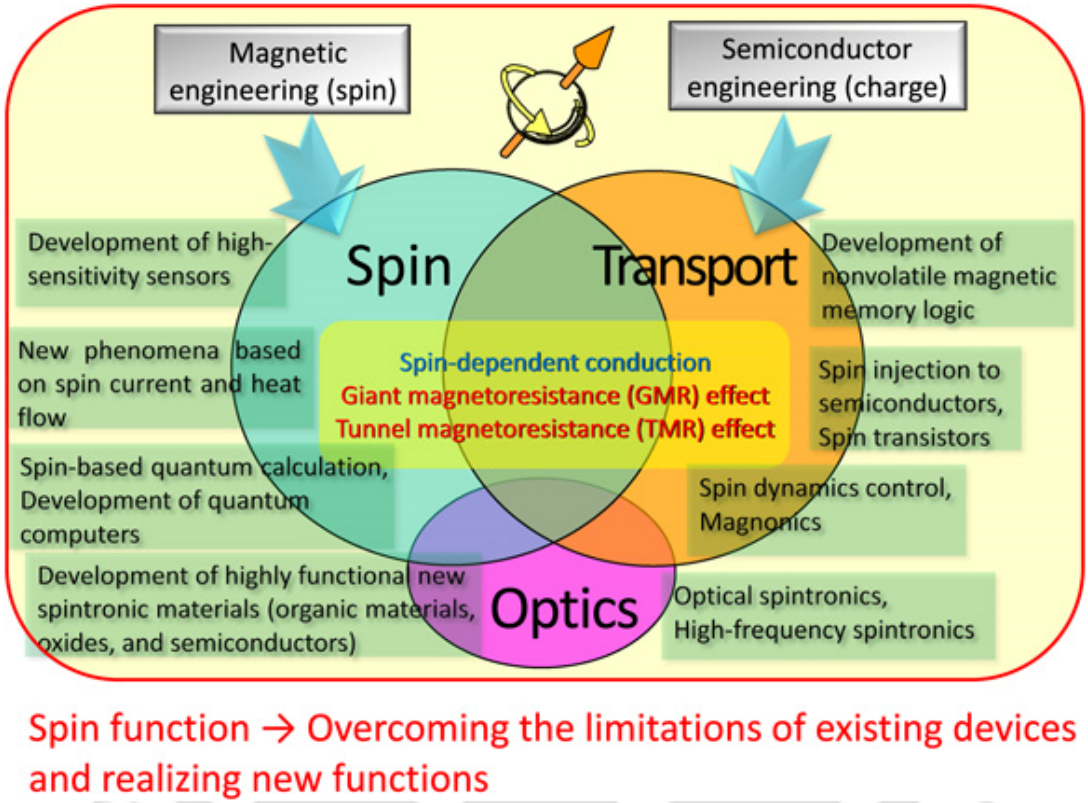

Figure 1.01: Conceptual diagram of spintronics [ANDO2015].

Recently, the scope of spintronics has been expanding progressively and now includes a phenomenon that relates the flow of spins with heat flow (called as spin-caloritronics) and high-frequency spintronics (called as magnonics) based on the extension of spin dynamics using lights. Recently, the technical committee of the IEEE magnetics society has selected seven research topics such as 1) hard disk drives; 2) magnetic random access memories; 3) domain-wall devices; 4) permanent magnets; 5) sensors and actuators; 6) magnetic materials; and 7) organic devices, to develop their roadmaps, where major developments should be listed alongside expected timelines. Among them, magnetic materials for spintronic devices have been surveyed by Hirohata et al. [HIRO2015] for targeting magnetic tunnel junction and spin-valve junction as spintronics devices. Figure 1.02 displays the roadmap for magnetic materials, where two key properties have been

identified to develop new spintronics devices. The first one is the achievement of half-metallicity at room temperature to realize large MR and resulting large spin polarization. The second one, based on the milestones including large perpendicular magnetic anisotropy and small damping constant, is the perpendicular anisotropy in nanoscale devices at room temperature. These developments are expected to be achieved not only by the development of these alloys but also by the fundamental understanding of the properties such that these materials can be implemented in the next-generation spintronics devices within next two decades.

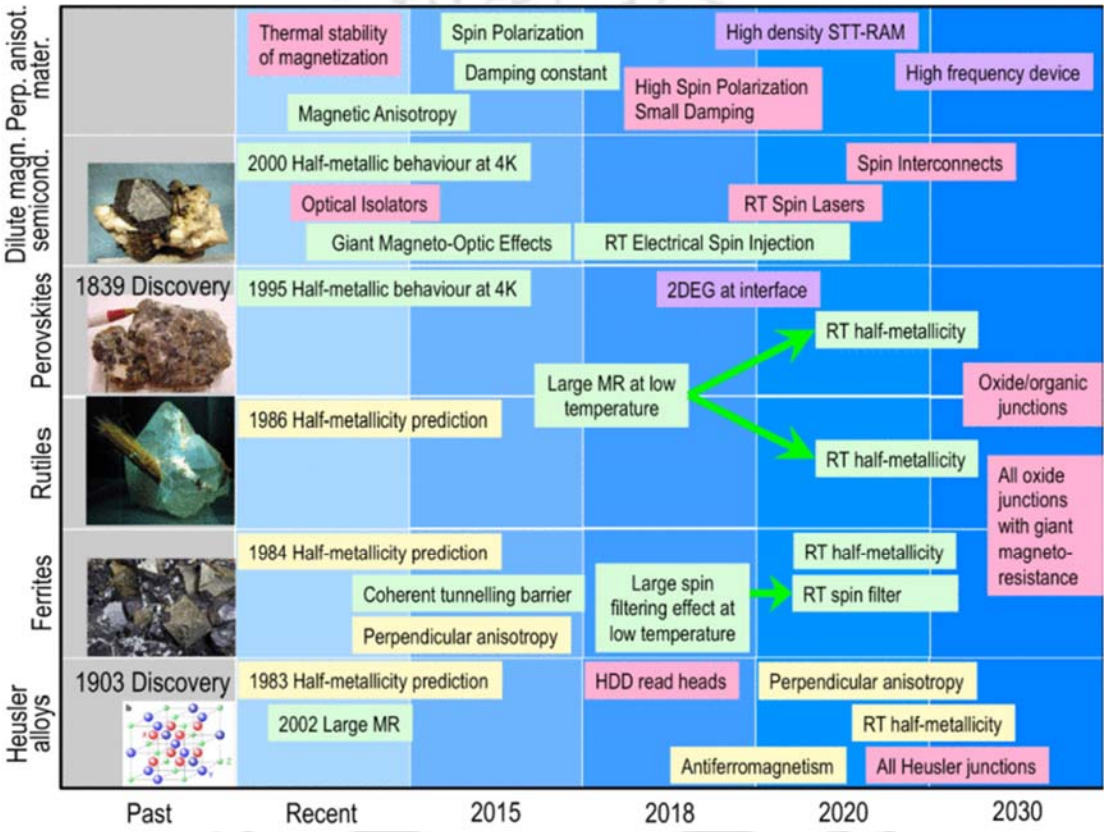

Figure 1.02: Roadmap for magnetic materials [HIRO2015].

1.2. Motivation behind the work

With the recent advances in the development of various spintronics devices, it is very much essential to study the magnetic properties of those films (alloys) that are commonly used in such applications. Among various magnetic thin films, CoFeB based thin films are found to be one of the promising materials suitable for various spintronics applications in modern magneto-electronic devices due to their tunable magnetic properties. A careful review of the literature on CoFeB based thin films suggests that the magnetic properties of the films are

strongly dependent on film thickness. For instance, ultra-thin CoFeB films with thickness less than 5 nm exhibit a strong perpendicular magnetic anisotropy of 0.5×10^6 J/m^3 - 2×10^6 J/m^3 due to interfacial effects [IKED2010, MANT2013, WANG2014]. Therefore, extensive studies have been carried out on CoFeB films to understand spin polarization [PALU2006], magnetic domain structure [YAMA2011], ferromagnetic resonance and damping properties [LIUX2011] and corrosion properties [PARK2011]. Interestingly, these films find applications in magnetic tunnel junctions [IKED2010, ISHI2014, ZHAN2015], magnetic random access memory [ZHUY2012, MANT2013, CUCH2016], spin logic based devices [SULI2015, WANC2017, ZHAN2017] and various other spintronics based applications [SONG2000, TEHR2000, UHRM2008, JIAN2009, SATO2014, THOM2014, ZHAO2015, LIUY2016, VEMU2016, LEES2017, MAEK2017]. The strong perpendicular magnetic anisotropy observed in ultra-thin films transforms into in-plane magnetic anisotropy with magnetization oriented along the film plane direction upon increasing CoFeB film thickness above 5 nm and up to 70 nm [HIND2011, KIPG2012, CUIB2013, TANG2014, QIAO2016]. The presence of simple magnetic domain structure in these films allows them to be mainly used as magnetic passives, energy transferring devices, magnetic flux amplifiers, magnetic recording heads, *etc* [MUNA2005, HASH2007, KAZI2013].

Considering the recent development of various flexible devices on plastic substrates for wearable electronics, smart cards, sensors, *etc.*, thick CoFeB based films are also grown on flexible substrates to investigate the influence of strain on the magnetic anisotropy of CoFeB films and to exploit them for the application in flexible electronics [YANG2013, TANG2014, QIAO2016]. Similarly, soft magnetic CoFeB thick films are quite indispensable for the magnetic tunnel junction based magnetic sensors [FREI2007, HUAN2017]. Furthermore, thick CoFeB based films have been used as soft magnetic underlayers in perpendicular magnetic recording media [ITOS2005, PIRA2007]. On further increasing film thickness, the effective magnetic anisotropy induced by the stress in the films overcomes the in-plane magnetic anisotropy and increases the degree of local disorder in the easy-axis of as-deposited films. As a result, the effective magnetic anisotropy increases and induces the formation of dense stripe domain in the as-deposited films [ITOS2005, TANG2014, GAYE2017]. Therefore, thicker CoFeB films become magnetically hard and display transcritical loop characterized by two magnetization reversal processes. Interestingly, these types of soft magnetic thin films also show spin-reorientation transition from in-plane magnetization to out-of-plane multi-domain state or vice-versa either with change in film thickness or with variation in substrate temperature during

deposition [SHAR2006]. However, most of the earlier reported works have been majorly focused on either tuning the magnetic properties of CoFeB films at ultra-thin level from application point of view or studying the magnetic properties of the CoFeB films at random thicknesses and compositions using different fabrication processes. Therefore, there are no systematic and detailed studies have been carried out to investigate the effects of composition, film thickness over a wide range of thicknesses and measurement temperature on the magnetic properties of CoFeB films prepared by a single fabrication technique.

Nevertheless, thicker CoFeB based films exhibiting high resistivity, high permeability, high saturation magnetization and appropriate anisotropy field were explored for the applications in magnetic flux amplifiers, magnetic recording heads, soft magnetic underlayers in perpendicular magnetic recording media, flexible electronics, *etc* [MUNA2005, ITOS2005, PIRA2007, KAZI2013, YANG2013, TANG2014, QIAO2016]. As revealed from the literature review that the magnetic properties of the amorphous CoFeB thin films degrade with increasing film thickness. However, only a few reports are available in the literature related to tuning of magnetic properties of thick CoFeB films [ITOS2005, GUPT2013, TANG2014] despite their vast applicability. In order to tune the magnetic properties of thick CoFeB films by controlling the development of effective magnetic anisotropy at larger thickness, the following methods are generally adopted: (i) fabricating multilayer structured thin films having ferromagnetic layers separated by non-magnetic (metallic and non-metallic) layer [NAKA1997, NAOE1998, HUAN2001, NAKA2001, TANA2003, SING2013] and (ii) executing controlled heat treatment of the amorphous precursor under different annealing environments [HERZ2013, DANI2014]. It may be noted that the fabrication of multilayer films with more number of layers (N) not only increases the number of interfaces, but also complicates interlayer coupling between the ferromagnetic layers [PARK2008, NAVA2014]. In addition, the magnetic coupling between ferromagnetic layers vary indiscriminately with spacer layer material and its thickness. However, there are no systematic studies available on magnetic interactions between (i) ferromagnetic layers through different spacer layer materials as a function of spacer layer thickness, (ii) different ferromagnetic layer thicknesses with different domain structures. The latter one, especially as a function of temperature, is expected to introduce different types of magnetic interactions and temperature dependent interface roughness induced interlayer coupling. This motivated us to plan this thesis work with the following objectives as given below:

1.3. Objective of the thesis work

- To prepare single-layer amorphous $Co_{80-y}Fe_yB_{20}$ (t nm) thin films with two different compositions [$Co_{40}Fe_{40}B_{20}$ (CoFeB442) and $Co_{20}Fe_{60}B_{20}$ (CoFeB262)] directly on thermally oxidized Si substrates using magnetron sputtering technique at ambient temperature.
- To understand the effect of thickness on the structural and magnetic properties of amorphous $Co_{80-y}Fe_yB_{20}$ (t nm) films over a wide range of thicknesses from 7 nm to 200 nm at room temperature.
- To investigate temperature dependent magnetic properties of amorphous CoFeB thin films in the temperature range between 30 and 700 K at different thicknesses.
- To prepare trilayer Substrate/CoFeB262 (y nm)/[Cr,Ta (x nm)]/CoFeB262 (20 nm) films with y = 20 and 100, and x = 0 – 6 directly on thermally oxidized Si substrates using magnetron sputtering technique at ambient temperature.
- To study the effect of spacer layer materials and its thickness on the magnetic interactions between two CoFeB262 layers having same domain structure [symmetric Substrate/CoFeB262 (20 nm)/[Cr,Ta (x nm)]/CoFeB262 (20 nm)] and different domain structures [asymmetric, Substrate/CoFeB262 (100 nm)/[Cr,Ta (x nm)]/CoFeB262 (20 nm)].
- To explore the effect of temperature on the magnetic interactions between CoFeB262 layers in symmetric and asymmetric films.
- To understand the effect of top CoFeB262 layer thickness on the magnetic properties of thick CoFeB262 bottom layer through different spacer layer materials (Cr and Ta) in trilayer Substrate/CoFeB262 (100 nm)/[Cr,Ta (x nm)]/CoFeB262 (y nm) films with y = 2, 5, 10, 30 and 50 nm.
- To optimize suitable trilayer film structure and obtain enhanced soft magnetic properties in thick amorphous CoFeB262 (100 nm) film.

This thesis is organized as follows: The second chapter covers the fundamental aspects and theoretical models including basics of magnetism, intrinsic properties of magnetic materials, anisotropy, magnetic domains and walls, interlayer coupling in multilayer thin films. In the third chapter, a short introduction of experimental methods and techniques used in this thesis are given. These include the fabrication of samples and characterization tools. Chapter 4 discusses thickness dependent structural and magnetic properties of amorphous $Co_{80-y}Fe_yB_{20}$ (t nm) thin films with two different compositions [$Co_{40}Fe_{40}B_{20}$ (CoFeB442) and $Co_{20}Fe_{60}B_{20}$

(CoFeB262)] at room temperature. The temperature dependent magnetic properties of CoFeB thin films in the temperature range between 30 and 700 K at different thicknesses are also examined in this chapter. The fifth chapter is meant for preparing trilayer Substrate/CoFeB262 (y nm)/[Cr,Ta (x nm)]/CoFeB262 (20 nm) films with y = 20 and 100, and x = 0 – 6 and studying the effect of spacer layer materials and its thickness, and temperature on the magnetic interactions between CoFeB262 layers having same domain structure (symmetric) and different domain structures (asymmetric). Chapter 6 focuses on understanding the effect of top CoFeB262 layer thickness on the magnetic properties of thick CoFeB262 bottom layer through different spacer layer materials (Cr and Ta) in trilayer Substrate/CoFeB262 (100 nm)/[Cr,Ta (x nm)]/CoFeB262 (y nm) films with y = 2, 5, 10, 30 and 50 nm. The summary of conclusions drawn from this thesis work and a brief write-up about the future scope of research in these types of materials is presented in Chapter 7. The list of publications arose out of the present thesis work and other research works is summarized at the end of the thesis.

भारतीय प्रौद्योगिकी संस्थान गुवाहाटी
Indian Institute of Technology Guwahati

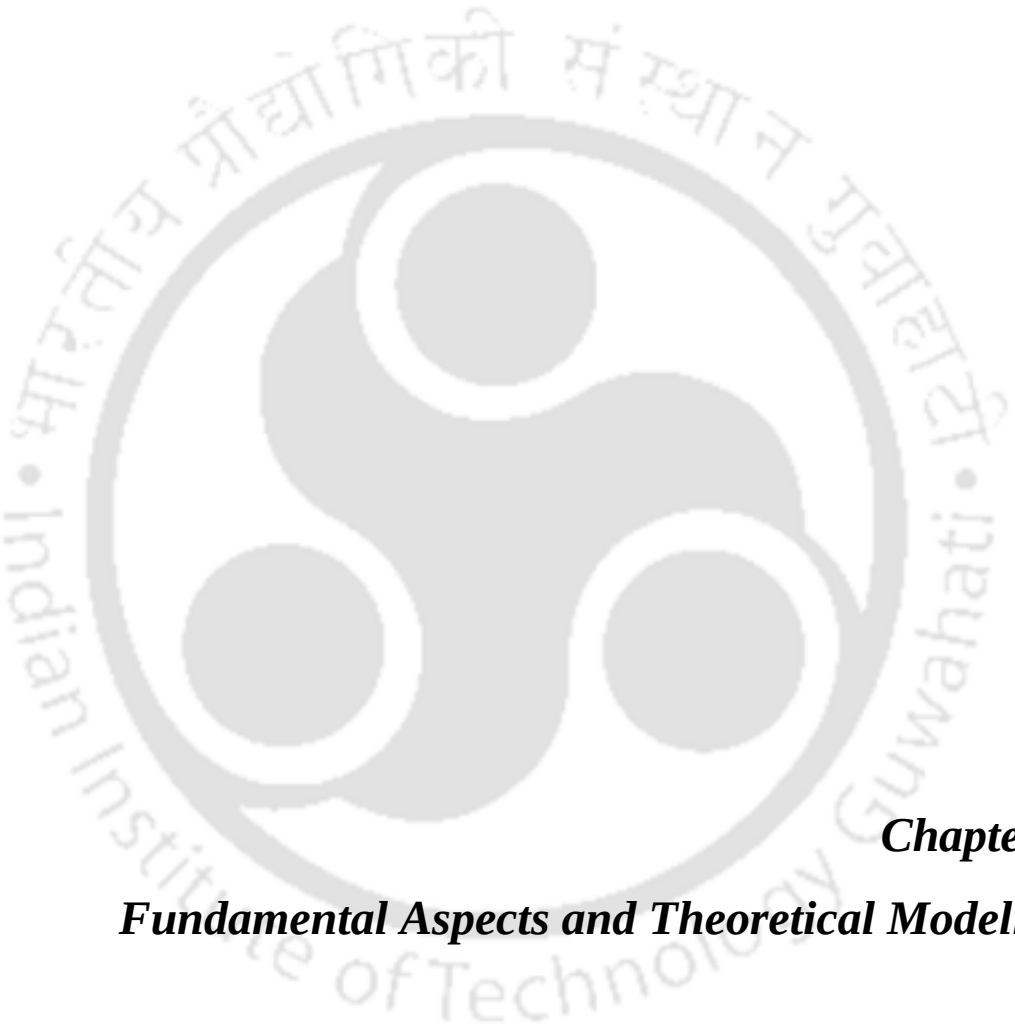

Chapter 2

Fundamental Aspects and Theoretical Modeling

भारतीय प्रौद्योगिकी संस्थान गुवाहाटी
Indian Institute of Technology Guwahati

2.1. Introduction

Magnetism is the kind of phenomenon by which materials affirm an attractive or repulsive force and known for thousands of years. Although the history of magnetism is coeval with the history of science, the underlying principles and mechanisms that explain the magnetic properties of the materials are however still complex and mysterious. It is well-known that most of the modern technological devices such as electrical power generators, transformers, electric motors, sensors, computers, and components of sound and video reproduction system rely on magnetism and magnetic materials. Recent endeavors to miniaturize magneto-electronic devices in order to reduce energy consumption and achieve higher speeds have generated a demand for new materials and new methods for their production. Therefore, (i) the understanding of development of magnetic properties in new materials in new forms, (ii) tuning its magnetic properties by thickness, composition and artificially layered structure and (iii) optimization of the magnetic properties for different applications are very much essential. This chapter provides a brief description of origin of magnetism in solids, the phenomenon of ferromagnetism and the various phenomena affecting ferromagnetic properties of the materials.

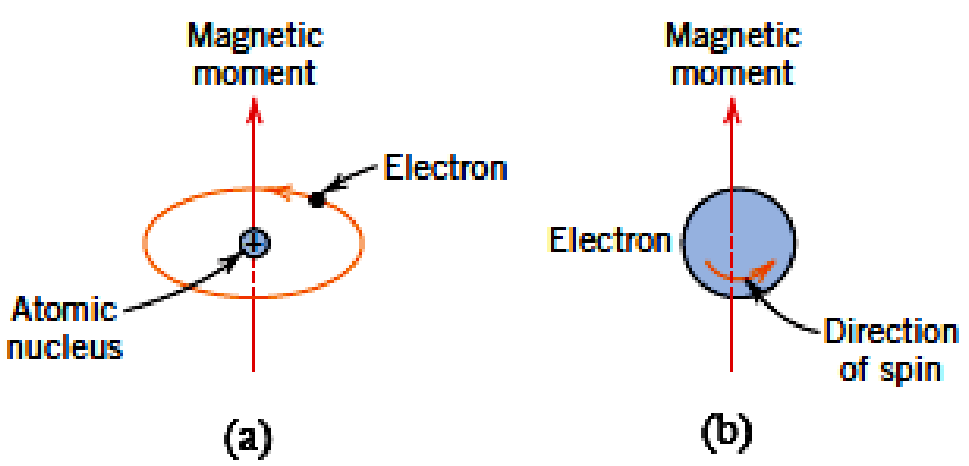

Figure 2.01: Demonstration of the magnetic moment associated with (a) an orbiting electron and (b) a spinning electron.

2.2. Origin of magnetism

The macroscopic magnetic properties of the materials are the consequences of magnetic moments associated with individual electrons [OHAN2000, KITT2004]. Each electron in an atom has magnetic moments originating from two different sources: (a) One is orbital motion of the electron around the nucleus, which generates a magnetic field and having

magnetic moment along the axis of rotation [see Figure 2.01(a)] and (b) Other magnetic moment originates from the electron spin, which is directed along the spin axis [see Figure 2.01(b)]. This suggests that the each electron in an atom may be thought of as being a small magnet having permanent orbital and spin magnetic moments. It may be noted that the electrons in an atom are occupied according to the Pauli's exclusion principle and Hund's rule. Therefore, the net magnetic moment for an atom is the sum of the magnetic moments of the each of constituting electrons, including both orbital and spin contributions and taking into the account of moment cancellation. For an atom having completely filled electron shells or subshells, when all electrons are considered, there is a total cancellation of both the moments. Hence, the materials composed of atoms having completely filled electron shells are not capable of being permanently magnetized. Based on number of unpaired electrons in atom, their orientation in the orbitals and the spin-orbit interaction between the electron orbital angular momentum and spin angular momentum and their response in the external applied field, the materials are classified into diamagnetism, paramagnetism, ferromagnetism, antiferromagnetism and ferrimagnetism [KRON2003].

2.2.1. Diamagnetism

Diamagnetism is a fundamental property of the materials and it is a manifestation of Lenz law, i.e., if one applies a field to a system of moving charges, then their motions change in such a way that they create a magnetization that opposes original applied field [OHAN2000]. Such effect is present in all the materials, but is often disguised by other types of magnetism. It generally occurs in materials having completely filled electronic configuration. The atoms and molecules of diamagnetic substances do not possess any net magnetic moments (i.e., all the orbital shells are filled and there is no unpaired electron). However, when exposed to a magnetic field, the electrons orient themselves such that they try to oppose the applied magnetic field and hence they register negative magnetization and negative susceptibility. Most of semiconductor material likes ZnO, SnO_2 *etc*. are diamagnetic in nature.

2.2.2. Paramagnetism

For some solid materials, each atom possesses a permanent dipole moment by virtue of incomplete cancellation of electron spin and/or orbital magnetic moments. The orientations of these atomic magnetic moments are random in the absence of an external magnetic field, resulting no net macroscopic magnetization. However, these atomic dipoles are free to rotate

and paramagnetism occurs when they preferentially align, by rotation, with an external field [KITT2004]. Some of the atoms or ions in this class of materials have a net magnetic moment due to unpaired electrons in partially filled orbital. However, the individual magnetic moments do not interact magnetically. In the presence of an applied magnetic field, there is a partial alignment of atomic magnetic moments in the direction of the applied field, resulting in a net positive magnetization and hence positive susceptibility. Both diamagnetic and paramagnetic materials are generally considered to be non-magnetic because they exhibit magnetization only under the application of an external field. The tendency of alignment of magnetic moments along the field direction is opposed by the thermal energy, which tries to randomize the spin orientation. So they exhibit a temperature (T) dependent susceptibility, χ known as the Curie Law,

$$\chi = \frac{C}{T} \tag{2.01}$$

with a Curie constant C [BLUN2003]. In classical theory, each atomic moment is considered as magnetic dipole alignment in a particular direction with an angle θ with respect to applied field and average magnetic moment along the field direction, z is written as

$$< \mu^z > = \mu L(y) \tag{2.02}$$

Here, μ is the magnetic moment of each dipole and $L(y)$ is the Langevin function, $L(y)=Cothy-1/y$ and $y = \mu_B/(k_B T)$. This function explains the magnetization of small particles made up of atomic clusters. For low applied field or at high temperature, such that y is small, $L(y)$ tends to $y/3$. So

$$< \mu^z > = \frac{\mu y}{3} = \frac{\mu^2 B}{3k_B T} \tag{2.03}$$

or the magnetization

$$M = N < \mu^z > = \frac{N\mu^2 B}{3k_B T} \tag{2.04}$$

So, the susceptibility

$$\chi = \frac{M}{H} = \frac{\mu^2 N \mu_0}{3k_B T} = \frac{C}{T} \tag{2.05}$$

and the Curie law is obtained by the classical theory. According to quantum mechanical treatment and by considering the quantization of total angular momentum of each atom, the average magnetic moment per atom aligned along the magnetic field direction (i.e., z

direction) of any paramagnetic sample can be written as [JILE1997, GUIM1998, BLUN2003].

$$< \mu_J{}^z > = g\mu_B J B_J(x) \tag{2.06}$$

Here g is Landgé g-factor and it depends on spin-orbit coupling of electrons in each atom. J is the total angular momentum quantum number. $\mu_B = 9.27\times10^{-24}$ J/T is Bohr magnetron. $B_J(x)$ is Brillouin function, which can be written as,

$$B_J(x) = \frac{1}{J}\left[\left(J+\frac{1}{2}\right)Coth\left(J+\frac{1}{2}\right)x - \frac{1}{2}Coth\frac{x}{2}\right] \tag{2.07}$$

Here, the variable $x = (g\mu_B B)/(k_B T)$, where k_B is the Boltzmann constant and T is the temperature. If N is the number of atoms per unit volume, the volume magnetization M can be written as,

$$M = N < \mu_J{}^z > = Ng\mu_B J B_J(x) \tag{2.08}$$

For the selection of magnetic field B and temperature T such that x is small, $B_J(x) \sim [J(J+1)/3]x$. Such assumption holds true for paramagnetic sample in a wide temperature region and for low applied field. So

$$< \mu^z > = Ng\mu_B J\frac{(J+1)}{3}x = \frac{Ng^2\mu_B^2 B}{3kT}J(J+1) \tag{2.09}$$

Or the susceptibility

$$\chi = \frac{\mu_0 N g^2 \mu_B^2}{3kT}J(J+1) \tag{2.10}$$

It is in the form of Curie law, C/T. Thus the magnetic susceptibility based on Brillouin function expression reduces to Curie-law. The examples of paramagnetic materials are W, Ce, Al, Li, Mg, *etc*. with typical χ value of 6.8×10^{-5}, 5.1×10^{-5}, 2.2×10^{-5},1.4×10^{-5},1.2×10^{-5} respectively in SI units [BLUN2003].

2.2.3. Ferromagnetism

Certain materials possess a permanent magnetic moment resulting in from strong interaction between the magnetic moments even in the absence of an external field. This dominates over the thermal energy and reveals an alignment of magnetization in a particular direction. Such behaviors are displayed by the transition metals and some of the rare earth metals. In ferromagnetic material, there are two distinct characteristics: (1) their spontaneous magnetization and (2) existence of magnetic ordering temperature. Spontaneous magnetization is the net magnetization that exists inside a uniformly magnetized

microscopic volume even in the absence of external magnetic field. The magnitude of this magnetization at absolute temperature depends on the spin magnetic moments of electrons. The atomic moments in ferromagnetic materials align either a parallel or an antiparallel arrangements showing very strong interactions, which are produced by electronic exchange forces. As a result, a large net magnetization even after removing the external applied magnetic field exists in ferromagnetic materials.

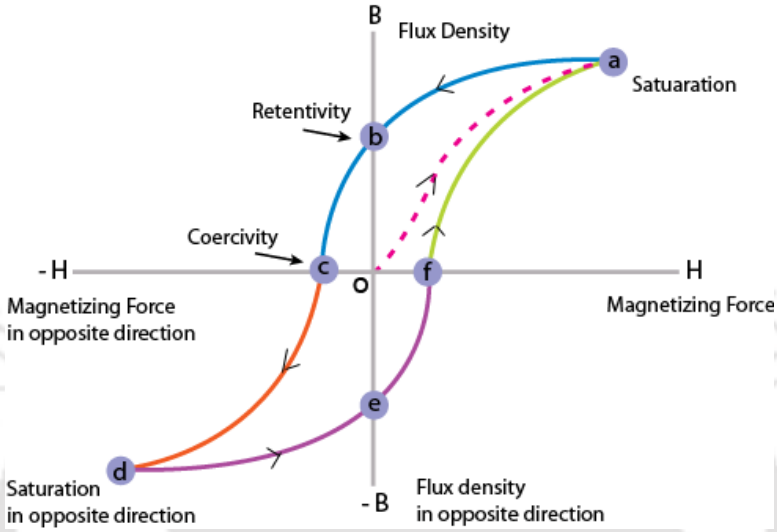

Figure 2.02: Magnetic hysteresis loop of a ferromagnetic material.

All ferromagnetic materials exhibit magnetic hysteresis loop (*M-H* loop) under the application of magnetic field as displayed in Figure 2.02. By studying its hysteresis loop we can get information about the magnetic properties of a ferromagnetic material. The loop is generated by measuring the magnetic flux of a ferromagnetic material while the magnetizing field is changed continuously. Ferromagnetic materials in virgin states follow the dashed line (starting from the origin '*o*') as applied field is increased and reach the point '*a*' where almost all of the magnetic domains are aligned to field direction and an additional increase in the magnetizing field produces a very little or no increase in magnetic flux. The magnetization obtained at this point is called saturation magnetization (M_S). When the field is reduced to zero, the curve moves from point '*a*' to '*b*'. At this point, some magnetic flux remains in the material even at zero magnetic field. This is called as retentivity and indicates the remanence or level of residual magnetism in the material. As the magnetic field is reversed, the curve moves to point '*c*', where the magnetization reaches to zero. This point is called as coercivity (H_C). On further increasing the field in the negative direction, materials become magnetically saturated but in the opposite direction (point '*d*'). Reducing the field to zero brings the curve to point '*e*'. At this point, the level of residual magnetism

is almost equal to that achieved in the other direction (point '*b*'). Increasing the field back in the positive direction returns the magnetization to zero. Subsequently, the curve takes a different path from point '*f*' back to the saturation point (point '*a*') and thereby completing the loop. From the *M-H* loop, the following magnetic parameters can be determined: (i) Retentivity: the material's ability to retain a certain amount of magnetization when the magnetizing field is removed after achieving saturation, (ii) Coercivity: The magnitude of reverse magnetic field is required to make the magnetization to zero; (iii) Permeability: A property of a material that describes the ease with which a magnetic flux is established in the component. These hysteresis parameters are not solely intrinsic properties but are dependent on various parameters such as grain size, domain state, internal stresses and temperature. Since the hysteresis parameters are dependent on grain size, they are useful for magnetic grain sizing of natural samples. The elements Fe, Ni, and Co and their alloys are typical examples of ferromagnetic materials. Ferromagnetic materials are mainly divided into two groups (see Figure 2.03): (a) hard ferromagnetic materials which exhibit very high H_C (> 1000 Oe). These materials are mainly used as permanent magnets and recording media for data storage and (b) soft ferromagnetic materials with low H_C (< 100 Oe) are used for transformer core, read head and magnetic sensor applications.

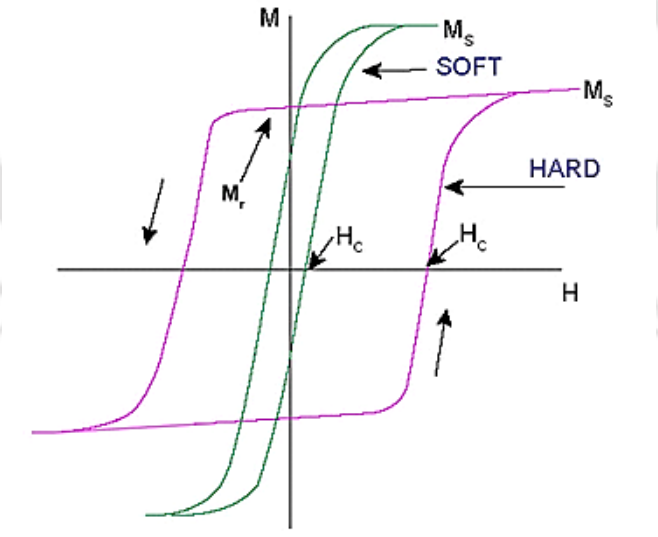

Figure 2.03: Typical magnetic hysteresis loops of soft and hard ferromagnetic materials.

Another important parameter is the magnetic induction [$B = \mu_0 (H + M)$], where μ_0 is the permeability of free space], which is the total flux of magnetic field lines through a unit cross sectional area of the material. From the initial magnetization curve, the initial magnetic permeability μ_I (= B/H), for very small applied magnetic field and maximum permeability

μ_{max} [=$(B/H)_{max}$] can be obtained. These parameters indicate the amount of induction generated by the material in a given magnetic field and are useful in characterizing magnetic materials. μ_I and H_C have a reciprocal relationship. So, materials exhibiting low H_C necessarily have a high μ_I. When increasing temperature, a transition from ferromagnetic state to paramagnetic state occurs at a temperature called Curie temperature (T_C) that is due to thermal energy eventually overcomes the exchange energy and produces a randomizing effect leading to paramagnetism. The phenomenon of ferromagnetic can often be described by mean field or molecular field model. The molecular field model simply assumes that all the interactions from the neighboring magnetic species can be described in terms of an effective internal or molecular field B_m, which is proportional to magnetization ($B_m = \lambda M$, where λ is Weiss molecular field constant). So total magnetic field experienced by each dipole is sum of applied field B and the molecular field B_m. The expression for magnetization can be re-written by following eqn.(2.08) as

$$M = \frac{Ng^2\mu_B^2 J(J+1)}{3kT}(B_a + \lambda M) \qquad (2.11)$$

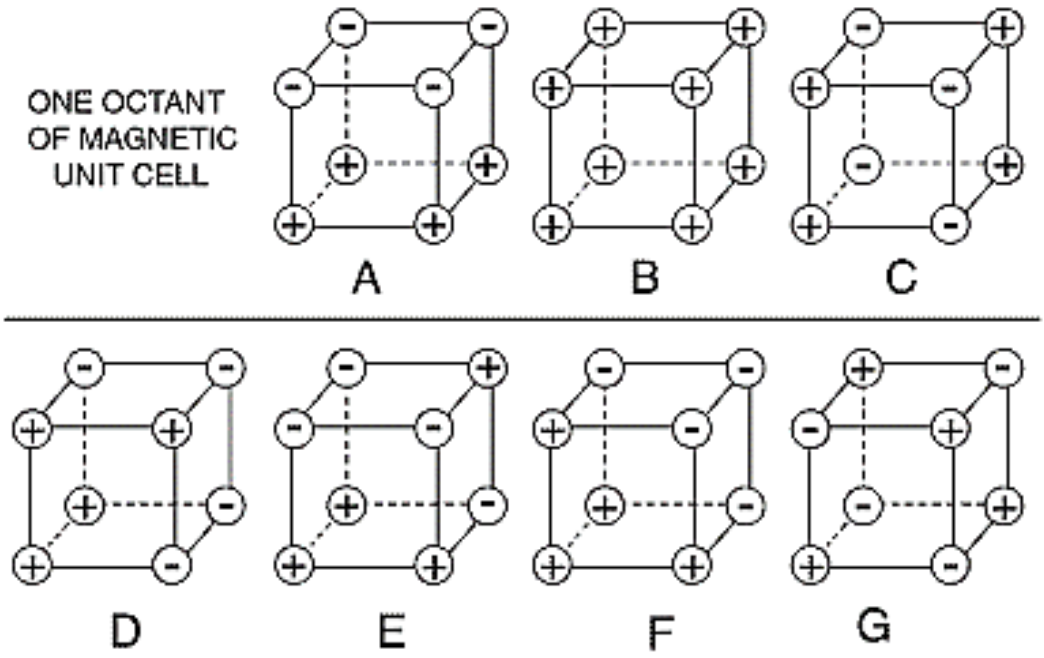

Figure 2.04: Different type of antiferromagnetic arrangement in a unit cell.

2.2.4. Antiferromagnetism

In antiferromagnetic materials, the spins of electrons align in a regular pattern with neighboring spins pointing in opposite directions, below a certain temperature called Néel temperature. Above the Néel temperature, the material is typically paramagnetic. The

magnetic susceptibility of antiferromagnetic material will appear to go through a maximum as the temperature is lowered. The antiferromagnetic ordering is possible based on different type of magnetic unit cell structure as shown in Figure 2.04 except for *B* type, which is a ferromagnetic one. In *A* type structure, the magnetic ions are coupled ferromagnetically in each (001) plane but with alternate planes aligned in opposite spin orientation such that it they exhibit net antiferromagnetic interaction. *B* type structure is a ferromagnetic one with all six nearest neighbor magnetic ions coupled ferromagnetically. In *C* type structure, the atoms in (101) and (110) planes are ferromagnetically aligned. Each atom has two ferro and four antiferromagnetic nearest neighbors such that there is net antiferromagnetic unit cell. In *G* type structure, each ion is coupled antiferromagnetically to all its six nearest neighbors. Hence the atoms of positive and negative number of ferromagnetic and antiferromagnetic bonds are shown in Figure 2.04. Some of the materials follow a structure which is a result of coupling of two types of magnetic structures. One such example is *CE* type, where there is coherent stacking of octants of *C* and *E* type structures. The examples of antiferromagnetic materials are MnF_2, MnO, CoO, FeO, Cr_2O_3, α-Fe_2O_3 with Néel temperature of 67 K, 116 K, 292 K, 116 K, 307 K, and 950 K with θ_C of -80 K, -510 K, -330 K, -610 K, -485 K, -2000 K respectively [BLUN2003].

2.3. Intrinsic properties of magnetic materials

Intrinsic properties of ferromagnetic materials are M_S, T_C and magnetocrystalline anisotropy (MCA). These properties describe the equilibrium properties of the material on the atomic scale.

2.3.1. Exchange Interaction

Weiss (1907) reported that in addition to any externally applied field *H*, there is an internal molecular field or exchange field in a ferromagnetic material proportional to its magnetization.

$$\overrightarrow{B_E} = \lambda \vec{M} \tag{2.12}$$

where λ is a temperature independent constant. According to eqn.(2.12), each spin sees the average magnetization of all the other spins. This molecular field is not really a magnetic field and therefore does not enter into the Maxwell equations. For example, there is no current density $\vec{j}$ related to $\overrightarrow{B_E}$ by $\vec{\nabla} \times \vec{H} = 4\pi\vec{j}/c$. The magnitude of the molecular field may be as high as 1000 Tesla. Now the question is what is the origin of such huge internal

molecular field? For instance, the magnetic field at distance r due to a magnetic dipole of dipole moment m is [KITT2004],

$$\overrightarrow{B_{dip}} = \left(\frac{\mu_0 m}{4\pi r^3}\right)[2cos\theta\overrightarrow{e_r} + sin\theta\overrightarrow{e_\theta}] \qquad (2.13)$$

The order of magnitude of B_{dip} (= $\mu_0 H_{dip}$) is $\mu_0 M/4\pi r^3$ and taking m = 1 μ_B and r = 0.1 nm provides $B_{dip} \approx$ 1 Tesla or 10 kG only. This reveals that the huge molecular field is not due to the magnetic dipole interaction. This lingered as a mystery until Heisenberg introduced the concept of exchange interaction in 1928 [HEIS1928]. The origin of the Heisenberg exchange interaction is electrostatic, but the explanation involves quantum mechanics. The charge distribution of a system of two spins depends on whether the spins are parallel or antiparallel. Pauli's exclusion principle dismisses that no two identical electrons occupy the same quantum state simultaneously. However, it does not exclude two electrons of opposite spin. Therefore, the electrostatic energy of a system depends on the relative orientation of the spins: the difference in energy defines the exchange energy. The energy of interaction between the atoms i and j bearing electron spins S_i and S_j is defined from the Heisenberg model as [OHAN2000],

$$E_{exch} = -2\sum_{i<j} J_{ij} S_i . S_j \qquad (2.14)$$

where J_{ij} is the exchange integral and related to the overlap of the charge distribution of the atoms i and j. Assuming that the exchange interaction is the same for each nearest-neighbor pair, eqn.(2.14) turns out to be

$$E_{exch} = -2J\sum_{i<j}^{nn} S_i . S_j \qquad (2.15)$$

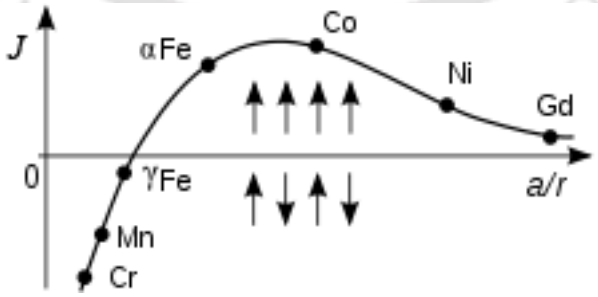

Figure 2.05: Bethe-Slater curve: Elements above (below) the horizontal axis are ferromagnetic (antiferromagnetic) [HTTP1].

For parallel orientation of the magnetization (ferromagnet), *J* should be positive and for antiparallel alignment of spins, *J* should be negative. The variation of *J* with respect to inter-atomic distance is shown in Figure 2.05. This curve is also known as the Bethe-Slater curve. It is clear from the Figure 2.05 that the value of *J* and hence the short-range exchange interaction depends strongly on the inter-atomic distance. The eqn.(2.15) can further be simplified by considering the energy of a particular atom *i* interacting with its *j* nearest neighbor:

$$E_{exch}^{i} = -2JS_i \sum_j S_j \tag{2.16}$$

while for the entire material,

$$E_{exch} = -\frac{1}{2}\sum_j E_{exch}^{i} \tag{2.17}$$

Thus, the discrete, pairwise interaction can be replaced by assuming that the magnetic moment $\mu_m^i = g\mu_B S_i$ at site *i* interact with a molecular field. H_{eff} given by the net effect of the *z* nearest neighbor spins:

$$E_{exch}^{i} = -\mu_0 \mu_m^i H_{eff} = -g\mu_0 \mu_B S_i H_{eff} \tag{2.18}$$

where g is the landé g-factor and μ_0 is the permeability of the free space (= $4\pi\times10^{-7}$ H/m or 1.256×10^{-6} H/m). Comparing eqn.(2.18) with eqn.(2.16) provides the effective field as,

$$H_{eff} = \frac{2J}{g\mu_0\mu_B}\sum_j S_j \cong \frac{2zJ}{g\mu_0\mu_B}\langle S_j\rangle \tag{2.19}$$

Here, the sum over *z* neighboring spins has been replaced by *z* times the average spin value $\langle Sj\rangle$. Using $M = N_v g\mu_B\langle S_j\rangle$, eqn.(2.19) gives,

$$H_{eff} \cong \frac{2zJ}{N_v g^2 {\mu_B}^2 \mu_0} M \tag{2.20}$$

From eqn.(2.20), it can be seen that H_{eff} is the Weiss molecular field defined as $H_{mol} = \lambda M$, provided

$$\lambda = \frac{2zJ}{N_v g^2 {\mu_B}^2 \mu_0} \tag{2.21}$$

Using the value of molecular field coefficient λ as 10^3, *J* is calculated to be 2×10^{-21} J or 0.01 eV/atom. Exchange interactions are weaker than the Coulomb interactions that distinguish levels of different principal and orbital quantum numbers, but stronger than spin-orbit

interaction. Following the treatment of Weiss molecular field that $T_C = \lambda C$ with $C = N_v {\mu_m}^2 \mu_0 / 3k_B$, the expression for T_C can be obtained from eqn.(2.21) as

$$T_C = \frac{2zJ{\mu_m}^2}{g^2{\mu_B}^2 3k_B} = \frac{2zJs(s+1)}{3k_B} \tag{2.22}$$

where $\mu_m = \sqrt{g\mu_B s(s+1)}$. Another important relation between exchange energy and the magnetization is defined as,

$$\frac{E_{exch}^{ij}}{V} = \frac{s^2 a^2 J N_v'}{2}\left(\frac{\nabla M}{M}\right)^2 = A\left(\frac{\nabla M}{M}\right)^2 \tag{2.23}$$

where *a* is the distance between the spins, *A* is called the exchange stiffness constant having 5×10^{-12} to 30×10^{-12} J/m for most ferromagnetic materials, and N_v' is number of nearest neighbor atoms per unit volume. Therefore, it is clear from the above equations that the exchange energy or the Heisenberg exchange interaction depends strongly on temperature due to the dependence of interatomic distance on temperature. In particular, the disorder ferromagnetic system is the subject of low T_C due to the low value of *J*.

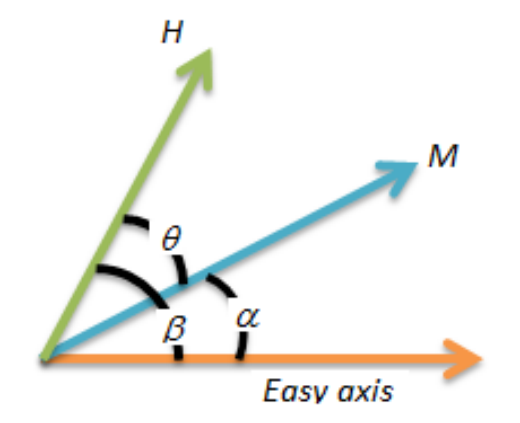

Figure 2.06: Schematic diagram of magnetization, applied field, and easy axis for a given material.

2.4. Anisotropy

When a physical property of any material depends on the direction of the materials that property is said to exhibit anisotropy. In magnetism, the preference of magnetization to lie in a particular direction of the sample is called as magnetic anisotropy. As anisotropy plays an important role in tuning the nature of *M–H* loop, it is much essential to understand the various possible sources of the magnetic anisotropy and its influence on the control of the magnetic properties. Figure 2.06 displays a typical situation where for zero applied field, the magnetization would point along the easy axis shown ($\alpha = 0$). When a field is applied,

the magnetization is pulled towards the field direction and approaches closer to the field direction with increasing the applied field. For any intermediate values of α, the magnetization is being attracted in opposite directions, i.e., up by the field and down by the anisotropy.

Let us assume that all the magnetization is pointing in the same direction in a magnetic material and the material exhibits an easy axis of magnetization. In such scenario, we can describe the energy per unit volume of the magnetization of this material by

$$E = K\ sin^2\alpha \tag{2.24}$$

where K is called anisotropy constant with a unit of energy per unit volume (J/m^3 or ergs/cc). Hence, the energy term, E, is also energy per unit volume. In general, the magnitude of uniaxial anisotropy is described in terms of the anisotropy field, which is defined as the field needed to saturate the magnetization of a uniaxial crystal in the hard axis direction, as given in eqn.(2.25)

$$H_k = \frac{2K_U}{\mu_0 M} \tag{2.25}$$

In general, the energy of the magnetization is given by,

$$E = K\ sin^2\alpha - \mu_0 MH\ cos(\beta - \alpha) \tag{2.26}$$

where the first term is anisotropy energy. The second term is due to the magnetic field and the difference in the angle (β - α) is the angle between $\boldsymbol{H}$ and $\boldsymbol{M}$. In order to get equilibrium, the first derivative is required to be zero.

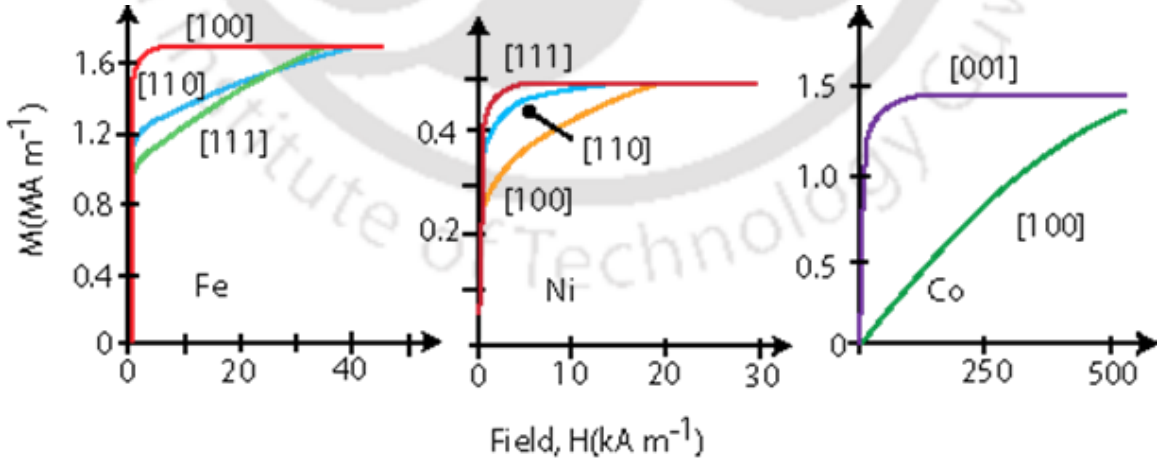

Figure 2.07: Magnetization of single crystals of iron, nickel and cobalt [HTTP2].

Therefore, taking derivative of eqn.(2.26) with respect to the angle provides,

$$\frac{dE}{d\alpha} = 2K \sin\alpha \cos\alpha - \mu_0 MH \sin(\beta - \alpha) = 0 \qquad (2.27)$$

Taking the value of β as 90° for the equilibrium angle for the magnetization relative to the easy axis and considering the eqn.(2.25) gives➔

$$\sin\alpha = \frac{H}{H_k} \qquad (2.28)$$

The above eqn. indicates that when field is zero, the magnetization points along the easy axis and when the field is equal to H_k, the magnetization points along the direction of field. For any intermediate value of the applied field, the magnetization points at a value of angle given by eqn.(2.28) rotating smoothly between the easy axis and the applied field.

Figure 2.08: Schematic drawing of broadside and head-to-tail configurations for a pair of ferromagnetically coupled magnetic moments.

2.4.1. Magnetocrystalline anisotropy

Figure 2.07 depicts initial magnetization curves of single crystals of different 3*d* ferromagnetic elements. It is seen that the materials approach to saturation in different ways when magnetized in different directions. For example, iron display a ⟨100⟩ as easy directions and ⟨111⟩ as hard directions, while nickel exhibits ⟨111⟩ as easy axis and ⟨100⟩ as hard directions. This behaviour can be understood by analyzing the development of anisotropy energy in different symmetries as given below:

For Hexagonal:

$$E_a = K_1 \sin^2\theta + K_2 \sin^4\theta + K_3 \sin^6\theta + K_3' \sin^6\theta \sin 6\phi \qquad (2.29)$$

For Tetragonal:

$$E_a = K_1 \sin^2\theta + K_2 \sin^4\theta + K_2' \sin^4\theta \cos 4\phi + K_3 \sin^6\theta + K_3' \sin^6\theta \sin 6\phi \qquad (2.30)$$

For Cubic:

$$E_a = K_{1c}(\alpha_1^2\alpha_2^2 + \alpha_2^2\alpha_3^2 + \alpha_3^2\alpha_1^2) + K_{2c}(\alpha_1^2\alpha_2^2\alpha_3^2) \qquad (2.31)$$

where α_i are the direction cosines of the magnetization. K_{1c} term is equivalent to $K_{1c}(\sin^2\theta\, cos^2\phi \sin^2\phi + \cos^2\theta \sin^2\theta)$. When, θ = 0, ϕ = 0, this term reduces to eqn.(2.24) [COEY2010].

Origin of magnetocrystalline anisotropy: There are two distinct sources of magnetocrystalline anisotropy: (i) single-ion contributions and (ii) two-ion contributions. The first one is essentially due to the electrostatic interaction of the orbitals containing the magnetic electrons with the potential created at the atomic site by the rest of the crystal. This crystal field interaction stabilizes a particular orbital and by spin-orbit interaction, the magnetic moment is aligned in a particular crystallographic direction. For example, a uniaxial crystal having 2×10^{28} ions/m^3 described by a spin Hamiltonian DS^2 with D/k_B = 1 K and S = 2 will have anisotropy constant $K_1 = nDS^2 = 1.1\times10^6$ J/m^3. On the other hand, the later contribution replicates the anisotropy of the dipole-dipole interaction. Considering the broadside and head-to-tail configurations of two dipoles each with moment m, as shown in Figure 2.08, the energy of the head-to-tail configuration is lower by $3\mu_0 m^2/(4\pi r^3)$ and hence the magnets tend to align head-to-tail. In non-cubic lattices, the dipole interaction is an appreciable source of ferromagnetic anisotropy.

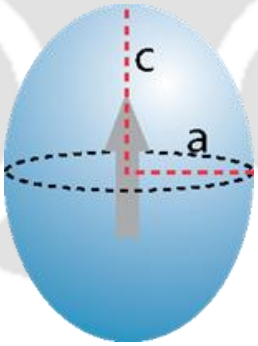

Figure 2.09: Magnetization of a prolate ellipsoid of revolution with $c > a$ and no magnetocrystalline anisotropy. c-axis is the easy direction of magnetization.

2.4.2. Shape anisotropy

Shape anisotropy arising due to the asymmetric shape of the material is important for thin films where one dimension is limited as compared to other two dimensions. The demagnetization field inside the material or the stray field outside the magnetic material depends on the magnetization and shape of the material [JILE1997, OHAN2000, BLUN2001]. The magnetostatic energy of a ferromagnetic ellipsoid (see Figure 2.09) with magnetization M_S is given as

$$E_m = \frac{1}{2}\mu_0 VNM_S^2 \tag{2.32}$$

The anisotropy energy is related to the difference in energy ΔE when the ellipsoid is magnetized along its hard and easy directions. N is the demagnetization factor tensor for the easy direction. N'=(1/2)(1-N) is the demagnetization factor tensor for the hard directions. Hence,

$$\Delta E_m = \frac{1}{2}\mu_0 VM_S^2\left[\frac{1}{2}(1-N) - N\right]$$

$$\Delta E_m = \frac{1}{4}\mu_0 VM_S^2[1-3N]$$

$$K_{sh} = \frac{1}{4}\mu_0 M_S^2[1-3N] \tag{2.33}$$

Table 2.01: Demagnetization factors (in Gaussian units) of selected shapes:

Shape	N_1	N_2	N_3
Sphere	4π/3	4π/3	4π/3
Long Cylinder along z-axis	2π	2π	0
Infinite plate normal to *z*-axis	0	0	4π
Strip film normal to *z*-axis	0	8*t*/*W*	4π
(with *t* – thickness, *W* – Width, *L* – Length; $t \le W \le L$)			

In addition, the demagnetization factor tensor that relates the demagnetization field with a specimen magnetization as a function of position is given by [NEAL1994]

$$N(r) = -\frac{1}{4\pi}\iiint d^3r'\nabla'\left(\nabla'\left(\frac{1}{r-r'}\right)\right) \tag{2.34}$$

This tensor is given by an integral over the object volume and can be evaluated either inside or exterior to the body. The value of tensor N significantly depends on the specimen shape, which is difficult to obtain in closed-form. It may be calculated exactly for an ellipsoidal shape only. In many symmetrical materials such as any ellipsoid of revolution, the demagnetization factor tensor only has three principal components, i.e.,

$$\begin{pmatrix} H_1 \\ H_2 \\ H_3 \end{pmatrix} = -\begin{pmatrix} N_1 & 0 & 0 \\ 0 & N_2 & 0 \\ 0 & 0 & N_3 \end{pmatrix}\begin{pmatrix} M_1 \\ M_2 \\ M_3 \end{pmatrix} \tag{2.35}$$

where $N_1 + N_2 + N_3 = 1$ (in SI) and $N_1 + N_2 + N_3 = 4\pi$ (Gaussian). The demagnetization factors for the selected shapes are summarized in Table 2.01. A detailed calculation of demagnetization factor for various objects can be found in [NEAL1994]. The shape anisotropy is zero for a sphere, as $N = 1/3$. Shape anisotropy is fully effective in samples which are so small that they do not break up into domains [COEY2010].

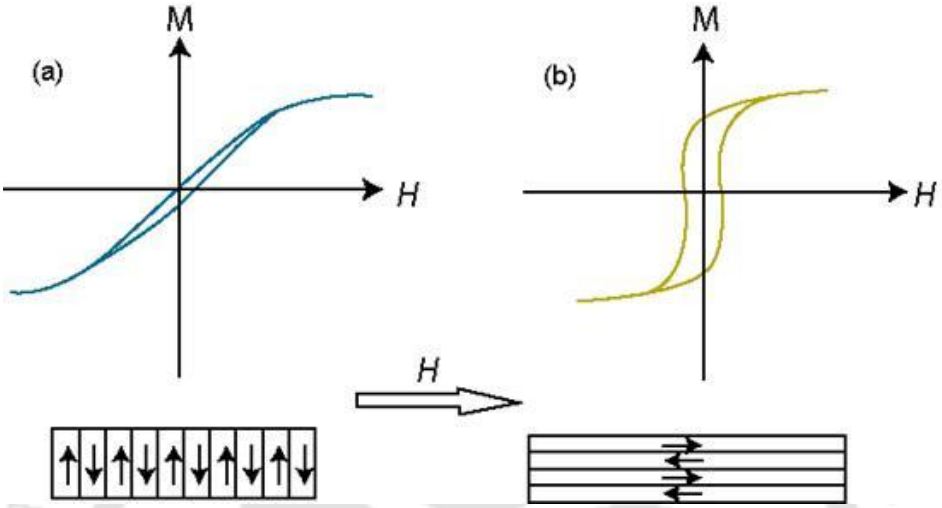

Figure 2.10: Magnetization of a thin film with induced anisotropy created by annealing in a magnetic field. The sheared (open) loop in a (b) is observed when the measuring field *H* is applied perpendicular (parallel) to the annealing field direction.

2.4.3. Induced anisotropy

In some materials, the magnetic anisotropy can be induced by many ways: (i) fabricate a film in the presence of a magnetic field, (ii) post annealing the materials in the presence of magnetic field and (iii) apply uniaxial stress. In the first two cases, after such treatment, the material may exhibit an easy axis of magnetization that points in the direction of the magnetic field. This induced anisotropy is certainly independent of any crystalline anisotropy or any other form of anisotropy that might be present. Figure 2.10 shows the typical example of inducing the anisotropy in ferromagnetic materials by field annealing.

In the last case, the uniaxial anisotropy is induced by applying uniaxial stress (σ) in a ferromagnetic solid [KRON2003]. The magnitude of the stress-induced anisotropy is

$$K_{u\sigma} = \frac{3}{2}\sigma\lambda_S \qquad (2.36)$$

where λ_S is the saturation magnetostriction. Both the single-ion and two-ion anisotropy contribute to the stress induced anisotropy. The highest values of uniaxial anisotropy are

found in hexagonal and other uniaxial crystals. Smallest values are found in cubic alloys and amorphous ferromagnets.

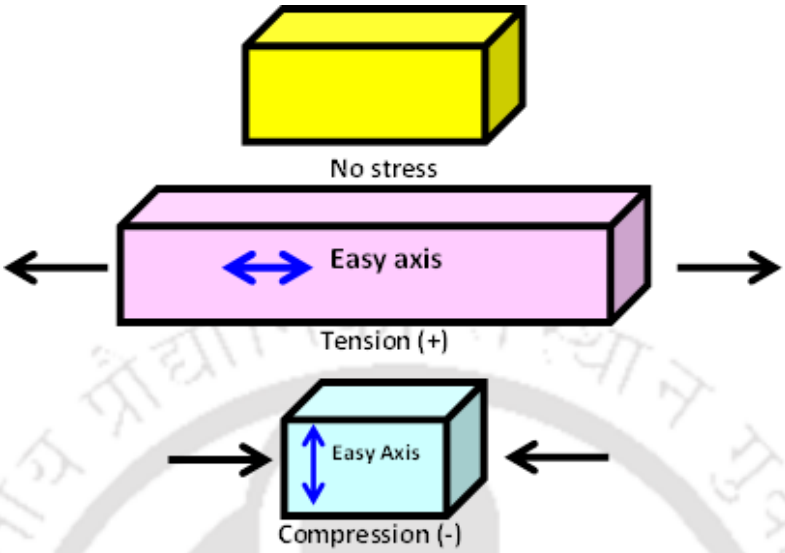

Figure 2.11: Schematic drawing of bars to demonstrate inducing an easy-axis in a material with the positive magnetostriction.

2.4.4. Magnetostrictive anisotropy

Another important form of anisotropy in magnetic materials is due to magnetostriction, a change of volume of an isotropic crystal due to magnetic order. Magnetostriction relates the stress in a magnetic material to an anisotropy created by that stress. Figure 2.11 shows the schematic views of bars with different applied stress conditions. If λ is positive, then application of a tensile stress to the bar creates an easy axis in the direction of the applied stress. If a compressive stress is applied, then the direction of the easy axis created will be perpendicular to the stress direction. On the other hand, if the magnetostriction constant for the material is negative, then the above phenomena would be reversed: a tensile stress will create an easy axis perpendicular to the stress direction and a compressive stress will create an easy axis in the direction of the applied stress.

2.4.5. Magnetic surface anisotropy

The orientation of magnetic moments in the ultra-thin film strongly affects the magnetic properties and hence attracts enormous interest in magnetic based random access memory and recording industry since past decades [PAND2016, IKHT2018]. It has been reported that in ultra-thin films, magnetic moments orient along perpendicular direction of the film

plane up to certain critical thickness due to the magnetic surface anisotropy, which has the following origins: a) the lack of the neighbors or reduced symmetry at the interface gives rise to magnetocrystalline surface anisotropy [NEEL1954], b) strain at the interface due to the lattice mismatch between the substrate and the film and c) the interface roughness. The direction of magnetization in the ultra-thin films is determined by the competition between shape (or dipolar anisotropy) and the magnetic surface anisotropy, i.e., when the thickness of the films is below the critical thickness, the surface anisotropy dominates over the shape anisotropy. On the other hand, the shape anisotropy dominates over the surface anisotropy above critical thickness, which leads to in-plane orientation of the magnetization [PESC1987, GARR2005, YILD20091, YILD20092, HIND2011]. Critical thickness and the easy direction of uniaxial surface anisotropy depend strongly on the deposition conditions, nature of substrate, temperature, materials and microstructure of the film [BRUN1989]. For example, the magnetization of Ni [111] ultrathin films deposited in Au/Ni/Au [111] multilayers always lies within the plane of films [BRUN1989]. On the other hand, the easy axis of magnetic surface anisotropy of body centered cubic (*bcc*) Fe [100] grown on Ag [100] is normal to the film plane [HEIN1987, KOON1987]. Hexagonal closed packed (HCP) Co deposited at room temperature on atomically flat polycrystalline Au[111] and covered by Au exhibits perpendicular magnetization for thickness less than 12 Å (6 ML) [CHAP1988]. Recently, CoFeB films show strong thickness dependent magnetic properties due to various anisotropy contribution including surface and interfacial anisotropy [NAIK2012, LIUT2012].

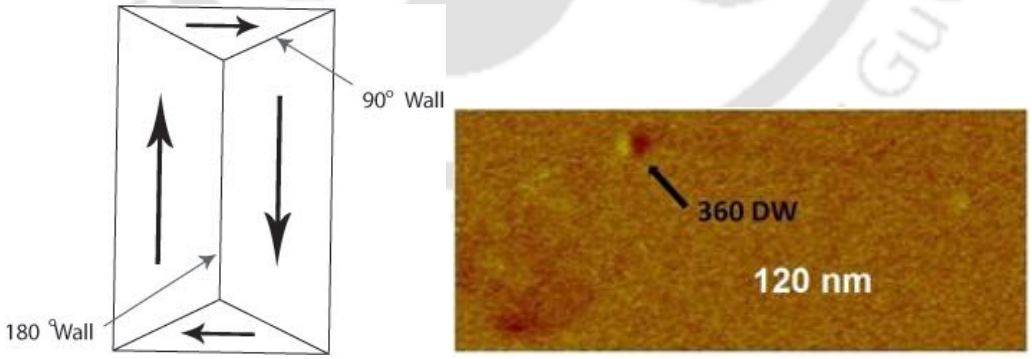

Figure 2.12: Schematic of 90°, 180° and domain image of 360° [ZHAN2016] domain walls in materials.

2.5. Magnetic domains and domain walls

Magnetic domains are the regions inside a ferromagnetic material that are magnetized in different directions so that the net magnetization is nearly zero. The walls separating one

domain from another are called as domain walls. There are different types of domain walls, i.e., 90°, 180°, and 360° domain walls [ZHAN2016] as shown in Figure 2.12. The main cause of formation of magnetic domains and domain walls is to reduce the magnetostatic energy of a finite and uniformly magnetized sample. The size of the domain and domain wall, and orientation of magnetization within the domain and domain walls are determined by the minimization of the total energy of the system. This energy includes exchange anisotropy, magnetocrystalline anisotropy, magnetostatic energy, magnetoelastic energy and domain wall energy [OHAN2000]. The width of a domain wall is dependent upon the exchange energy which prefers the magnetization to rotate slowly from one orientation to the other leading to wide walls, whereas the anisotropy and demagnetizing energies prefer the magnetization to switch immediately to the opposite direction and therefore leads to narrow walls. The thickness of the domain wall is determined by the equilibrium between these energies. There are three types of domain walls exist in thin films as shown in Figure 2.13: Bloch wall, Néel wall, and Cross tie wall.

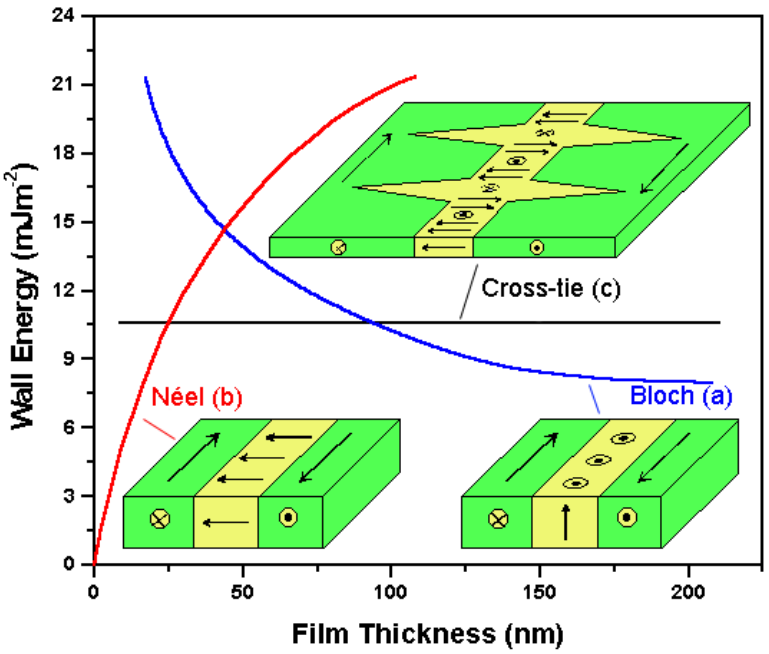

Figure 2.13: Comparison of domain wall energies for a (a) Bloch, (b) Néel and (c) Cross-tie wall for a permalloy film as function of film thickness [PRUT1964] and illustrative diagrams of the respective domain wall spin configuration.

As shown in Figure 2.13(a), magnetization rotates about an axis perpendicular to the wall is called as Bloch wall. Hence, for thin films, the magnetization rotation would be perpendicular to the film plane. This provides high stray field on the surface. Similarly, Néel

wall is defined by the magnetization rotating in the plane of the film which reduces the magnetostatic energy of the wall [see Figure 2.13(b)]. A cross-tie wall is defined by a mixture of spins pointing out and in the plane, and is identifiable by spike walls which form to ensure flux closure [see Figure 2.13(c)] [CRAI1965]. It is found that in thin films Néel walls have lower magnetostatic energy than Bloch walls and are therefore more energetically favorable. The variations of different types of wall energies in permalloy thin film are shown as a function of thickness in Figure 2.13. The cross-tie walls appear in between the transition region from Bloch wall to Néel wall. The widths of the domain walls also vary as a function of film thickness where Bloch walls become narrower and Néel walls become wider with decreasing film thickness [MIDD1963]. The typical length and energy scales related to different types of domain walls are defined as [OHAN2000],

Wall Type	Length scale	Energy Density
Bloch wall	$\delta_{Bw} = \pi\sqrt{\frac{A}{K}}$	$\sigma_{Bw} = 4\sqrt{AK}$
Néel wall	$\delta_{Nw} = \pi\sqrt{\frac{2A}{\mu_0 M_S^2}}$	$\sigma_{Nw} = 2\pi\sqrt{AK}$

where K is anisotropy constant, A is exchange stiffness constant ranging between 5×10^{-12} - 30×10^{-12} J/m for most ferromagnets and M_S is saturation magnetization. There are several types of domains observed both in bulk materials and in thin films: (a) star like domain patterns observed in $Fe_{40}Ni_{40}P_{14}B_6$ (metglass), (b) the laminar domain structure observed in the $Fe_{40}Ni_{40}B_{20}$ alloys and (c) the dense stripe domain structure observed in thin films above certain critical thickness [KRON2003]. The development of anisotropy perpendicular to the film plane arising due to the stress accumulated during the deposition of the film aligns the magnetization perpendicular to the film plane with dense stripe domain patterns [MURA1966, PRAD1997, CRAU2002]. The equation for the critical thickness above which the dense strip domain appears was derived from the micromagnetic equation with suitable approximations and the boundary conditions [HUBE2014] and given by,

$$t_{critical} = \frac{2\pi}{1 - \frac{\mu_0 M_S H_{Sat}}{2K}}\sqrt{\frac{A}{K}} = \frac{2\pi}{1 - S}\sqrt{\frac{A}{K}} \qquad (2.37)$$

where $t_{critical}$ is the critical thickness, S is the dimensionless quantity, and H_{Sat} is the critical field beyond which the stripe domains are unstable. These stripe domains are periodical

oscillations of the magnetization within a laminar conventional domain structure [CRAU2002, KRON2003, AMOS2008, HUBE2014], as shown in Figure 2.14. The advantage of such dense stripe domain structure along with the closer domains is the absence of stray field outside the specimen. The approximation for formation of the closer domains is given by [KRON2003],

$$Q = \frac{2K}{\mu_0 M_S^2} \ll 1 \qquad (2.38)$$

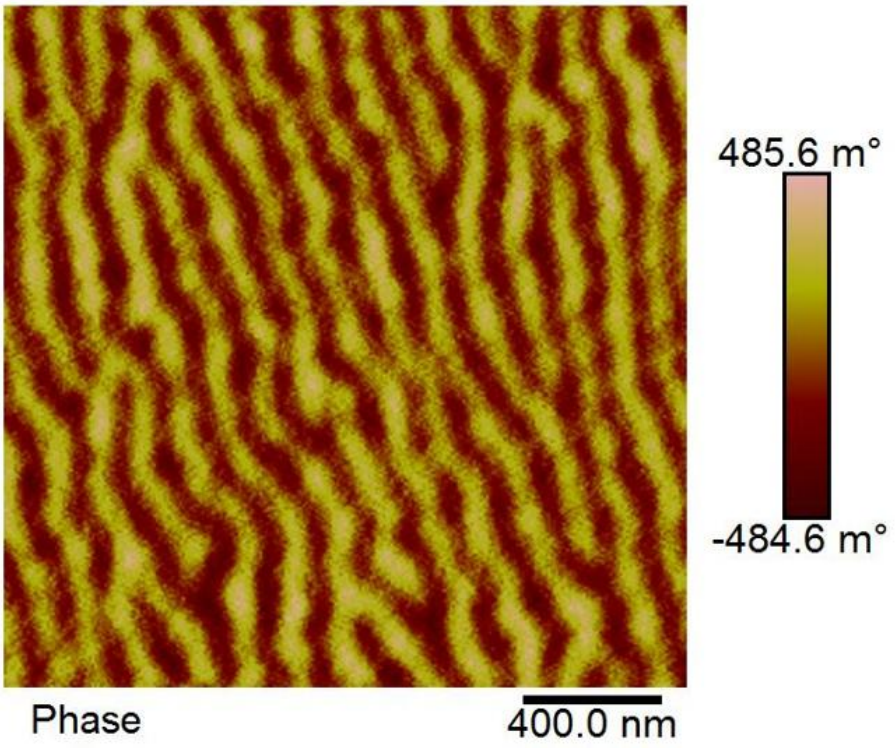

Figure 2.14: Stripe domain pattern observed in soft magnetic FeTaC thin films [DASC20182].

It is clear from eqn.(2.38) that the formation of closer domains depends strongly on the anisotropy and M_S values. Soft magnetic materials in general exhibit a low anisotropy and relatively high M_S. This favors the formation of closer domains for soft magnetic materials. For small Q (< 0.1), the critical thickness for the formation of stripe domains is approximately $t_{critical} = 2\pi\sqrt{A/K}$ in zero applied field. When Q approaches one, the critical thickness vanishes, i.e., stripe domains are expected even for ultra-thin films and reported experimentally in ultra-thin Co films [ALLE1990], where the surface anisotropy adds to the perpendicular anisotropy for ultra-thin films so that the effective value of Q becomes larger than unity.

2.6. Magnetic properties of amorphous and nanocrystalline materials

The reduction of structural correlation length of solids into nanoscale leads to a dramatic change in their physical properties, which are in general not predictable on the basis of their macroscopic properties. In particular, the enhancement of soft magnetic properties in Fe and Co based nanostructures is one of the examples of such size effects. After the development of $Fe_{74.5}Si_{13.5}B_9Nb_3Cu_1$ by Yoshizawa et al. [YOSH1988], the magnetic softening effect in nanostructures has opened the possibility of promising exploration for material developments in soft magnetic materials for magnetic cores for the purpose of magnetic flux multiplication. It has been reported that amorphous materials exhibit low H_C [KOBL1978, INOU1997] and high permeability. While the permeability of Co based amorphous materials is high as compared to Fe based amorphous alloys, M_S of Co based alloys is considerably lower than the Fe based amorphous alloys. In addition, the magnetostriction of Fe based amorphous alloys is quite high [ITOS1980, INOU1997] as compared to Co based alloys [OHAN1987, MCHE1999]. However, FeCo based amorphous alloys exhibit low values of permeability but relativity high M_S as compared to any other Fe based or Co based alloys.

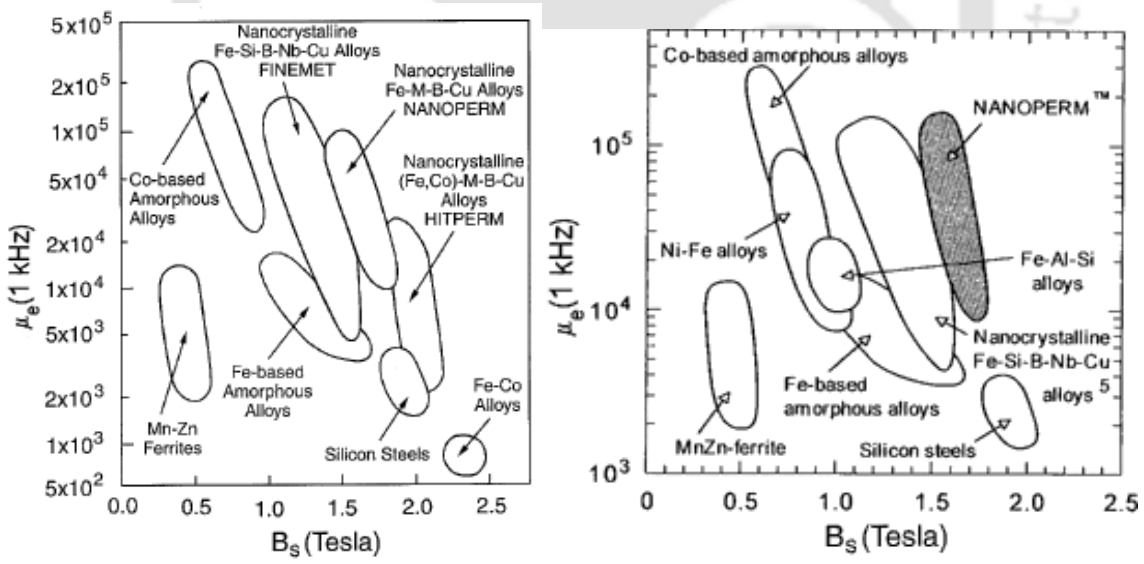

(a) (b)

Figure 2.15: Relation between permeability (at 1 kHz) and saturation induction for soft magnetic materials (a) [MAKI1995] and (b) [YOSH1988].

Figure 2.15 summarizes the relation between the permeability and saturation induction for various soft magnetic materials. The advantage of amorphous materials is high

electrical resistivity due to absence of long rang atomic ordering and makes them suitable for high frequency device applications. In case of thin films, they produce smooth surface for making devices without any pinning centers. However, they exhibit low T_C due to absence of long range ferromagnetic ordering and weak ferromagnetic exchange interaction.

2.7. Interlayer coupling in multilayer thin films

The study of magnetic properties of thin films composed of alternating magnetic and non-magnetic layers has recently attracted much attention, as the interplay between electron transport properties and magnetic behavior leads to variety of fascinating phenomena such as anisotropic magnetoresistance (AMR), giant magnetoresistance (GMR) and tunneling magnetoresistance (TMR) [IKHT2018, INOU2014]. These artificial structures are promising as potential memory elements, magnetic sensors and magnetic tunneling junctions, *etc*. One of the technological hurdles is to understand and control the interlayer magnetic coupling between the magnetic layers through non-magnetic films. It has been shown that two separate effects such as magnetostatic coupling due to uncompensated poles near the edges and the magnetostatic coupling between the stray fields of domain walls, and Néel coupling due to interface roughness tend to produce extraneous magnetic fields in the plane of the free layer. In addition, the interlayer coupling originates from two different types of interactions such as short-range exchange interaction and long-range exchange interaction.

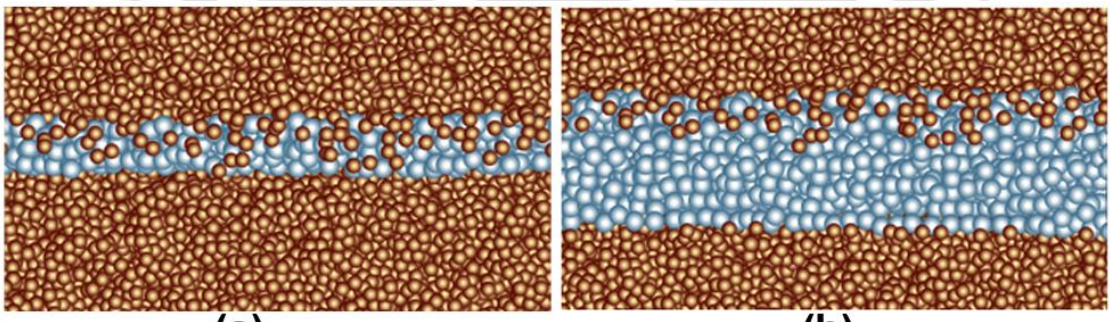

Figure 2.16: Schematic representation of multilayer films with thin and thick spacer layers.

2.7.1. Exchange coupling

2.7.1.1. Direct exchange coupling

Two magnetic layers separated by a thin non-magnetic insulating or metallic spacer layer are directly coupled through pinholes present in the thin spacer layer as shown in Figure 2.16(a). Since the pinhole appears mainly due to the formation of non-continuous spacer

layer at very low thickness films or high surface roughness of the initial ferromagnetic layer, number of pinholes, which control the strength of the coupling depends on the thickness of the spacer layer, growth conditions, atomic size of the elements present in the spacer and magnetic layers [SAIT2002, STIL2005, PONG2008, SING2015]. Multilayer films having the direct exchange coupling through the pinholes exhibit strong temperature dependent magnetic properties due to the temperature dependent magnetic properties of diffused magnetic atoms into the non-magnetic layers [OLIV1999, SING2013].

2.7.1.2. Indirect exchange coupling

The increase in the spacer layer thickness between the magnetic layers provides the interlayer coupling between ferromagnetic layers through conduction electrons of the non-magnetic metallic spacer layer [see Figure 2.16(b)]. This is called as indirect exchange interaction or Ruderman-Kittel-Kasuya-Yosida (RKKY) interaction. Theory of indirect exchange interaction was first predicted by Ruderman and Kittel [RUDE1954] and later extended by Tadao Kasuya [KASU1956] and Kei Yosida [YOSI1957]. RKKY interaction was implemented in the multilayer structured thin films to understand the magnetization orientation and the giant magnetoresistance of multilayer structured ultra-thin films. It was observed that RKKY coupling aligns the magnetization of adjacent ferromagnetic layers to be either ferromagnetic (parallel alignment) or antiferromagnetic (antiparallel alignment). Hence, the magnetoresistance of the multilayer films exhibits a strong dependence on the spacer layer thickness and shows an oscillating nature with spacer layer thickness. The amplitude of oscillation decreases with increasing spacer layer thickness [BAIB1988, PARK1990, BRUN1991, BRUN1992]. In addition, the coupling also depends on the roughness at the interfaces.

2.7.2. Magnetostatic coupling

2.7.2.1. Topological coupling

The topological coupling also known as Néel's orange peel coupling or the dipolar coupling is the magnetostatic interaction induced by the magnetic poles at the interface. These magnetic poles are generated by the interface roughness. Néel carried out the first calculation of topological coupling for semi-infinite magnetic layers with a correlated sinusoidal interface roughness [NEEL1962]. Later, the model was extended by other researchers for the roughness of arbitrary phase and finite magnetic film thickness [ZHAN19961, ZHAN19962, KOOL1999]. The coupling strength depends on the thickness

of magnetic layers and spacer layers, magnetization of magnetic layers, roughness amplitude at the interface and wavelength of the roughness profile. Néel coupling between two ferromagnetic layers is defined as [SCHR2000],

$$H_N = \frac{\pi^2}{\sqrt{2}}\left(\frac{h^2}{\lambda t_F}\right) M_S exp\left(-\frac{2\pi\sqrt{2}t_s}{\lambda}\right) \tag{2.39}$$

where t_F and t_s are the thickness of the magnetic layer and spacer layers respectively, h and λ are amplitude and wavelength of the roughness, respectively as demonstrated in the Figure 2.17(a). The coupling field strongly depends not only on the spacer layer thickness, but also depends on the ferromagnetic layer thickness [see Figure 2.17(b)].

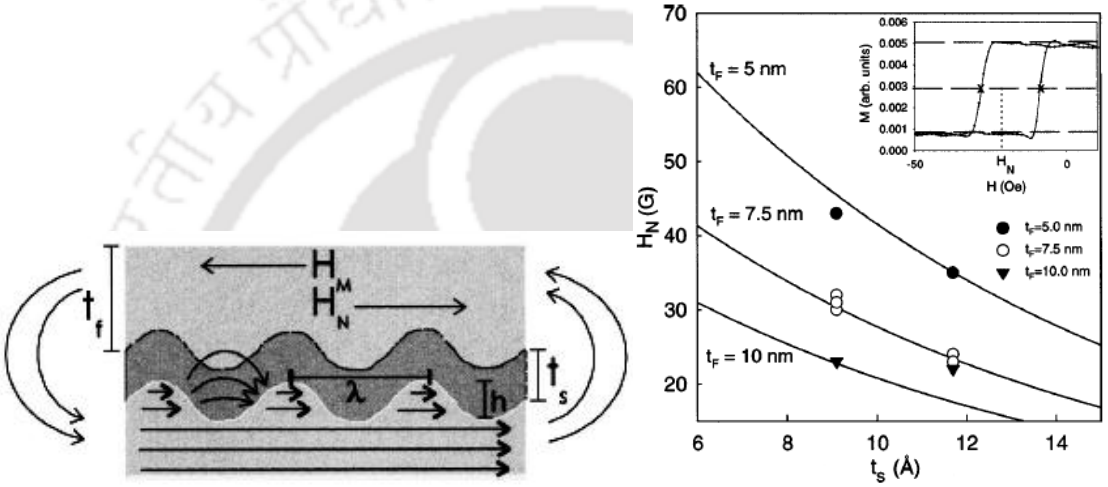

(a) (b)

Figure 2.17: (a) Schematic drawing of two dominant interlayer coupling mechanisms, and (b) variations of Néel coupling with spacer layer thickness for different multilayer films [SCHR2000].

2.7.2.2. Stray field coupling

Another magnetostatic coupling arises due to the magnetic poles at the edges of the film is stray field coupling. The stray field generated from the edges of the one magnetic layer magnetostatically couples the other layers as shown in the Figure 2.17(a). Since the coupling is magnetostatic in nature, it depends strongly on the films' dimension and provides a significant interlayer coupling for thicker films [ANGU2000]. The variation of stray field coupling on the films' dimension can be described as [ANGU2000],

$$H_M = A\frac{W^\alpha}{L} \tag{2.40}$$

where W and L are the width and length of the sample in micron, respectively, A and α (= 0.22) are constants. The value of α varies with the sample dimension, i.e., when the separation between the free layers and the relevant pinned layer is much larger than its width, α approaches to one, whereas in the opposite limit, the value of α should be nearly zero [ANGU2000].

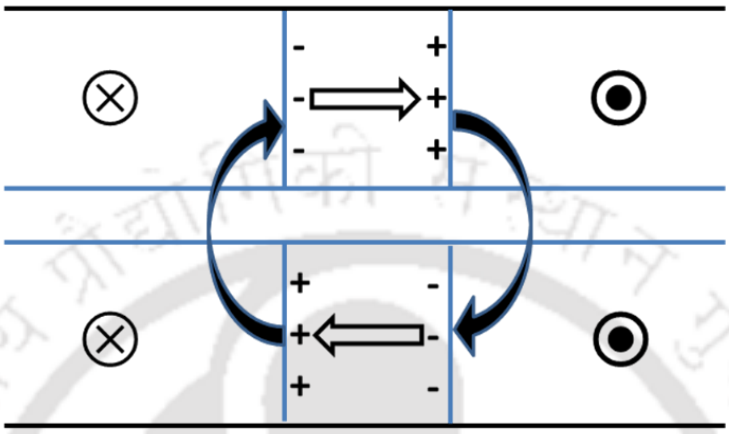

Figure 2.18: Schematic of Néel wall pair separating parallel domains. Superimposed Néel walls are energetically favorable entities due to a more complete flux closure associated with them [CHOP2000].

2.7.2.3. Domain wall stray field coupling

Stray fields emanating from domain walls of a given ferromagnetic layer magnetostatically lock in with the stray fields from walls in adjacent layers as shown in Figure 2.18 [CHOP2000, CHOP2005]. The rotation of magnetization within a Néel wall is denoted by the double arrows. The stray field emanating out of the Néel walls, denoted by curved arrows, causes a magnetization fluctuation in the adjacent layers above and below it, giving rise to quasi-Néel walls. This stray field emanating from each domain wall is able to close its flux by magnetostatic locking-in with the stray fields from domain wall in adjacent layers. This leads to an overall reduction in the wall energy and hence the coercivity. Magnetic thin films reveal strong thickness dependent magnetic properties. Particularly, ultrathin films having in-plane magnetic anisotropy exhibits in-plane magnetization with large sized domains and Néel wall [OHAN2000]. Similarly, the multilayer thin films with thin ferromagnetic layers also show in-plane magnetization with large sized domains and Néel wall, which gives a minimum or zero stray field coupling. On the other hand, the development of multidomain patterns above the critical thickness depends on the net magnetization of the ferromagnetic layers, anisotropy of the films, substrate nature,

microstructure of the film and the growth conditions of the thin films [FELD1971, OEPE1990, ALLE1994]. Therefore, at larger thicknesses, the multidomain pattern with Bloch wall is energetically more favorable. This reveals that the domain wall stray field provides a significant coupling among the ferromagnetic layers ensuing a strong variation in the magnetic properties of the multilayer structured films measured at different temperatures.

Indian Institute of Technology Guwahati

Chapter 3

Experimental Methods

भारतीय प्रौद्योगिकी संस्थान गुवाहाटी
Indian Institute of Technology Guwahati

3.1. Introduction

In the course of the present investigations, several experimental techniques were used for the preparation and characterization of single-layer and multilayer thin films. This chapter provides a brief description of those experimental techniques.

3.2. Techniques used for sample preparation

3.2.1. Sputtering technique

Sputtering is defined as the ejection of atoms from the cathode surface by impinging of energetic positive ions of noble gases such as helium, argon, neon and krypton, at a reduced gas pressure under high voltage [OHRI1992, WAGE1994, SESH2002]. In 1852, Sir W. R. Grove discovered surface coatings generated in the valve under a glow discharge. This phenomenon was called as spluttering by Sir W. Thomson and later it was adopted as sputtering. This sputtering process involves a momentum transfer between the impinging positive ions and the cathode surface atoms as displayed in Figure 3.01 and as a result of which a physical removal of atoms takes place.

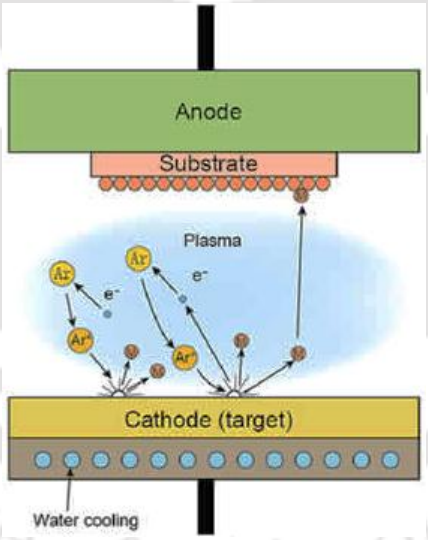

Figure 3.01: Schematic diagram of the sputtering process [HTTP3].

The yield of sputtering is defined as ratio between the average number of emitted atoms to number of incident ions on the target surface.

- The sputtering yield increases with a) energy, b) mass of the bombarding atoms and c) decrease of angle of incidence to the target.
- A minimum energy is required to initiate the sputtering process.

- The sputter atoms are ejected along the crystallographic directions of the cathode metal lattices.
- Sputtering yield decreases with larger increase of the ion-energy because of the deeper penetration of ions inside the lattice.
- Sputtering is also accompanied by the emission of secondary electrons from the cathode surface.
- The sputtering yield is insensitive to the cathode temperature.
- If the sputtering process does not involve any of the chemical reaction between bombarding gas ions and the cathode, it is known as physical sputtering.
- If some reactions are involved then it is named as reactive sputtering.

The physical deposition process consists of three steps

1. Emission of the atoms from the target source,
2. Their transport in the atmospheric condition to the substrate, and
3. Eventual condensation on the substrate.

There are four different types of sputtering process [direct current (DC), Radio-frequency (RF), Magnetron and Reactive sputtering] used for thin film deposition. We have used DC magnetron sputtering for depositing the films of present investigation.

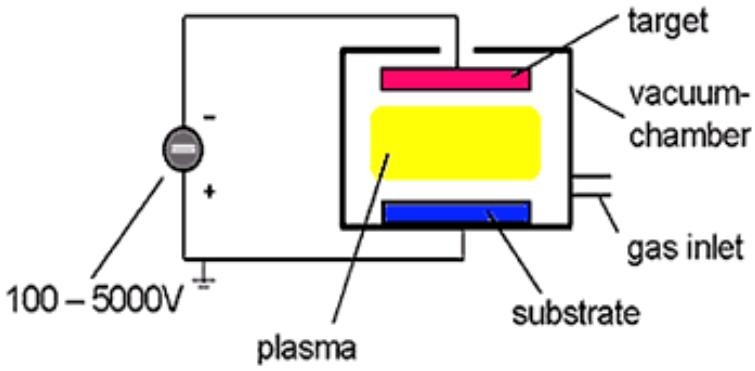

Figure 3.02: Schematic arrangement of DC sputtering technique [HTTP3].

3.2.1.1. DC sputtering technique

Figure 3.02 displays a typical arrangement used for DC sputtering. The target and substrate oppose each other in the vacuum chamber having a distance of few centimeters to few tens of centimeters. The target is connected to a negative output of a DC power supply and hence acting as the cathode. The substrate and chamber walls act as anode. After the creation of

required argon atmosphere with a pressure of about 1 - 100 mTorr, the gas discharge is ignited by applying a DC voltage. The created Ar^+ ions are now accelerated towards the target and eject atoms from the target. These atoms travel in the controlled atmospheric conditions and subsequently are deposited on the substrate. At low pressures, the mean free path between collisions is large, the ionization efficiency is low and self-sustained discharges cannot be maintained below few mTorr. As the pressure increases at a fixed voltage, the electron mean free path is decreased, more ions are generated and large current flow. If the pressure is too high, the sputtered atoms undergo increased collisional scattering resulting a low deposition process. The deposition rate is proportional to (a) power consumed, (b) square of current density and (c) 1/(electrode spacing). DC sputtering works with all types of target materials which are conductive in nature.

However, DC sputtering suffers from two major drawbacks as compared to conventional evaporation: (i) low deposition rates and (ii) high thermal load of the substrate due to bombardment of secondary electrons on the cathode surface. In order to increase the deposition rate and to control the thermal load, magnetron sputtering as described below in Figure 3.03 is utilized for the fabrication of the films.

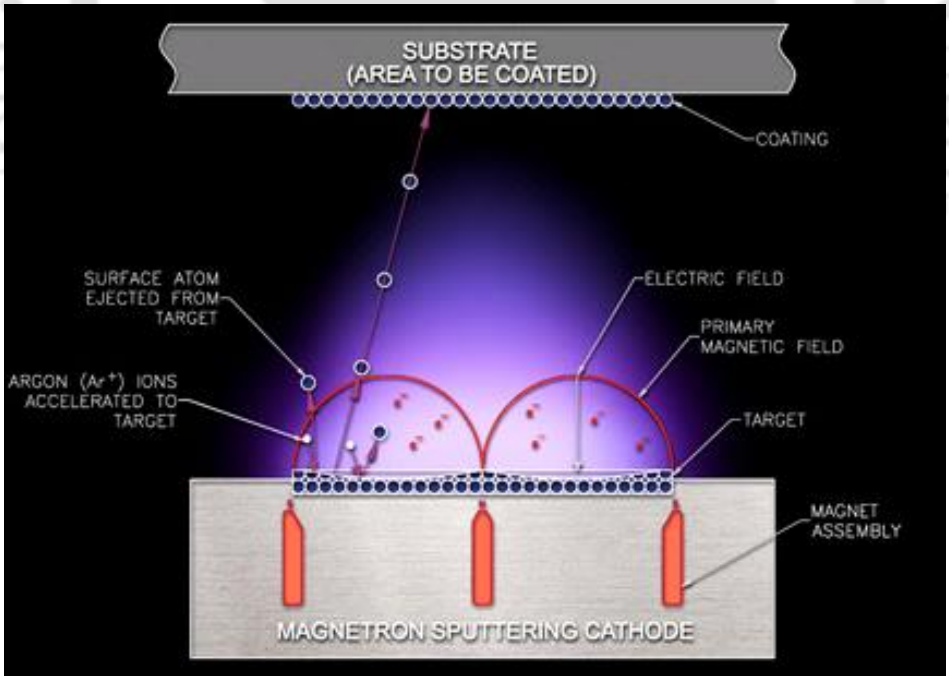

Figure 3.03: Schematic presentation of magnetron sputtering gun assembly [HTTP3].

3.2.1.2. Magnetron sputtering technique

In magnetron sputtering, electrons ideally don't reach the anode but are trapped near the target by the presence of magnetic field and thereby enhancing ionization efficiency. This

is accomplished by employing magnetic field oriented parallel to the target and perpendicular to the electric field. Practically, this is achieved by placing bar magnets behind the target as shown in Figure 3.03. The magnetic field lines emanate first normal to the target and then bend with a component parallel to the target surface and finally return to magnet completing the magnetic circuit. Electrons emitted from cathode are initially accelerated toward the anode, but undergoes a helical motion when they encounter the region of the parallel components of magnetic field. Therefore, they are bent in an orbit back to the target. The chief reasons of its success are (1) increased sputtering rates (~ 5 - 10 times) due to high plasma density around target, (2) low discharge voltages of 300 to 1000 V due to the reduced plasma impendence and (3) low thermal load of the substrate due to deflection of secondary electrons by the magnetic field.

Figure 3.04: Photographic view of the magnetron sputtering system used in the present work.

Figure 3.04 depicts the typical set up of magnetron sputtering used in the present thesis work for fabricating single and multilayer structured thin films. The chamber is equipped with four different guns for making multilayer films. The substrate was loaded on the rotating substrate holder. Subsequently, the chamber was pumped to high vacuum (< 10^{-}

^{4} Pa) using diffusion pump and rotary pump combination. The argon gas of fixed pressure was permitted into chamber continuously using mass flow controller (MFC) and the argon gas pressure in the chamber was maintained by adjusting the MFC and processing valve. The optimized sputtering Ar gas pressure for the deposition of CoFeB, Ta and Cr films was fixed at 10 mTorr, respectively. After stabilizing the set argon gas pressure in the chamber, a constant DC power was applied to commence the sputtering process. The deposition of the films was carried out after stabilizing the plasma and completing the pre-sputtering process. The nominal thickness of the films is controlled by sputtering time ranging from 0.2 nm to 6 nm for Ta/Cr spacer layer and from 7 nm to 200 nm for CoFeB film. The deposition rate for the films was calibrated by using an ex-situ surface profilometer (Vecco, Dektak-150) as described in the next section.

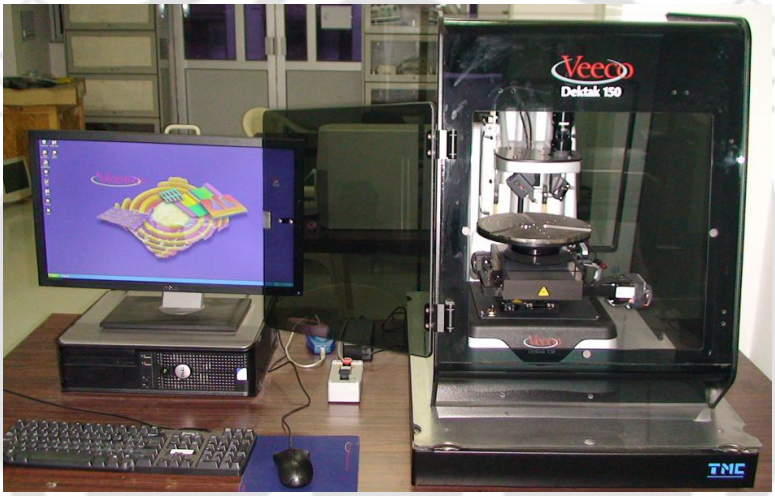

Figure 3.05: Photographic view of Vecco-Dektak 150 surface profilometer.

3.2.2. Calibration of deposition rate

To optimize the properties of the films at different thicknesses, it is very much essential to control the thickness of the film deposited under controlled sputtering conditions. Deposition rate of the films studied in the present investigations was calibrated with surface profilometer (Vecco, Dektak-150), as illustrated in Figure 3.05. Stylus profilers are versatile measurement tools for studying surface topography. Their primary function is to measure film thickness by scanning step heights and trench depths. The stylus profilers typically rely on a small-diameter stylus moving along a surface either by movement of the stylus or movement of the surface of interest. A true stylus profiler moves linearly to obtain the measurement. As the stylus encounters surface features, the stylus moves vertically to measure various surface features, such as deposited film and irregularities. The stylus

profiler used in the present work was sponsored by Defence Research & Development Organisation (DRDO), New Delhi [ERIP/ER/0900363/M/01/1185 Dated 16 November 2009]. To monitor the thickness of the deposited films, a proper marking using permanent marker was made on top of the cleaned substrate. Subsequently, the deposition was done under controlled sputtering environment (constant Ar gas pressure, DC power and target to substrate distance, *etc*.) for a given time at ambient temperature. After the completion of the deposition, the film was cleaned through sonication in acetone. As a result, the film deposited on the substrate reveals a clear step.

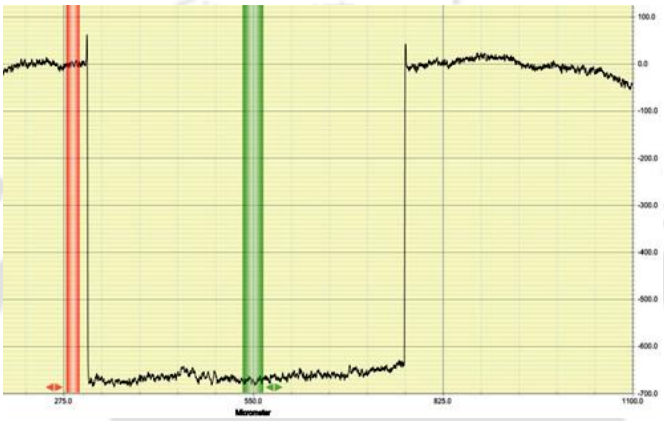

Figure 3.06: A typical scan profile of the Dektak surface profilometer.

The step size was evaluated using surface profiler as displayed in Figure 3.06 and the average deposition rate was eventually calculated by dividing the average thickness measured at various locations on the substrate with deposition time. In order to confirm the reproducibility, more films were subsequently made under the same sputtering conditions and analyzed using surface profilometer.

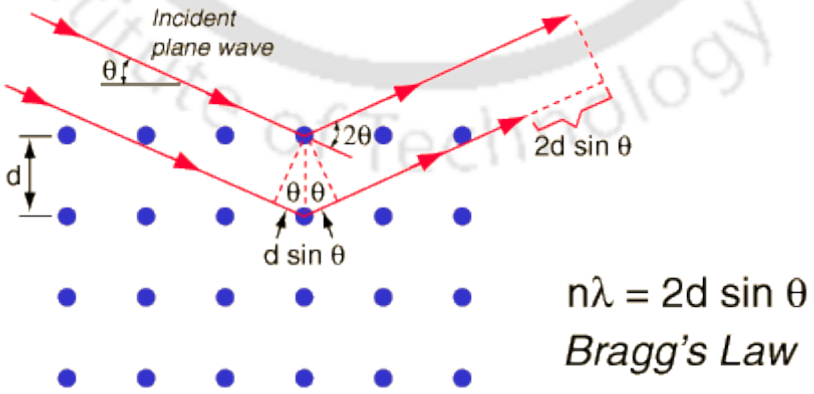

Figure 3.07: Schematic ray diagram of diffraction of X-rays by a crystal [THOR1993].

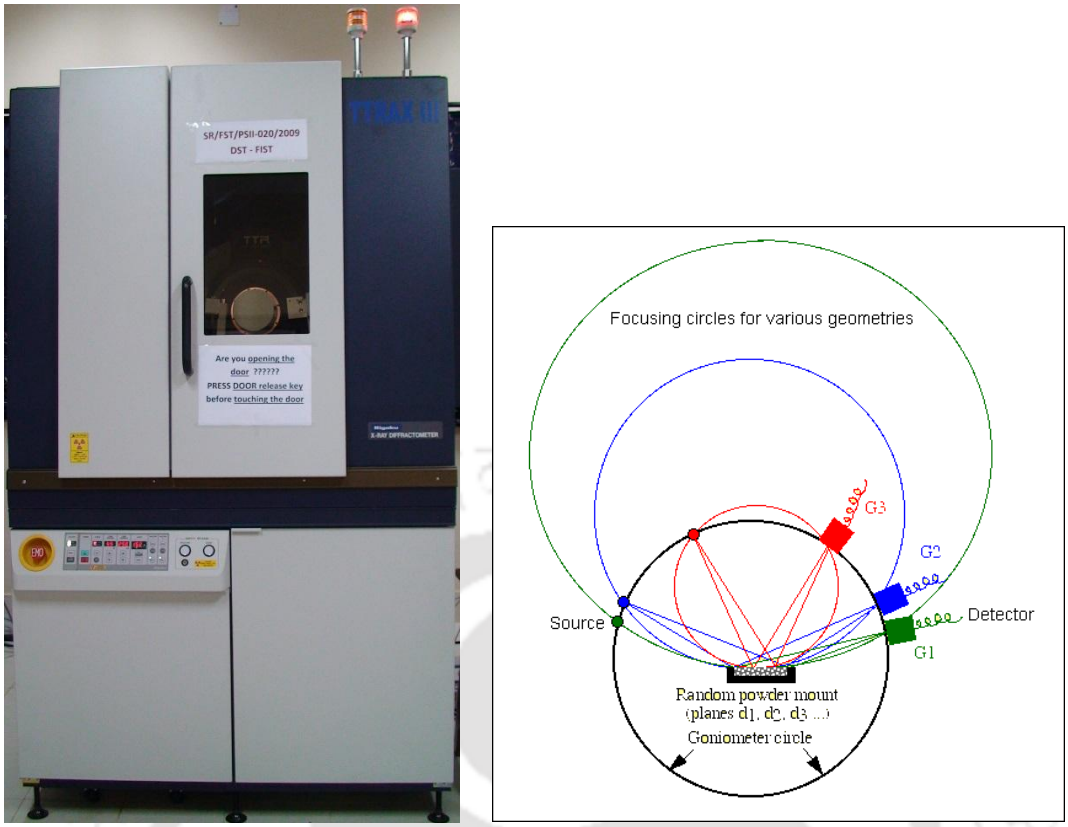

(a) (b)

Figure 3.08: (a) Photographic view of Rigaku TTRAX III 18 kW X-ray diffractometer and (b) Bragg-Brentano diffraction geometry of a powder X-ray diffractometer.

Similar procedures were followed for all the films prepared under different sputtering conditions. The thickness of the films for selected thickness range is also monitored using X-ray reflectivity technique discussed later in this chapter.

3.3. Structural property characterization

3.3.1. X-ray diffraction

X-ray diffraction (XRD) technique is useful to identify the existence of various phases, degree of crystalline order and quantitative analysis of secondary phases present in a two-phase system. An ideal crystal has a periodic arrangement of atoms. Diffraction of X-rays occurs through constructive interference of X-rays scattered from atoms of a set of parallel planes in crystal lattice at particular angular positions of the incident wave known as Bragg angles. This condition for obtaining constructive interference is known as Bragg's law and given by the relation

$$2d_{hkl} \sin\theta = n\lambda \qquad (3.01)$$

where, d_{hkl} is inter-planer spacing, θ is glancing angle, λ is wavelength of the X-ray and n is order of diffraction. A sequence of these angles can be used to determine the Miller indices (*hkl*) values and the crystal structure can be identified from the systematic behavior of these indices. Figure 3.07 shows the diffraction of X-rays from crystal lattice planes illustrating Bragg's law. The structural parameters such as the average size of the crystallites, *d*-spacing, lattice constant and strain present inside the crystallites, *etc* can be determined by a careful analysis of the XRD patterns using various models [CULL2001]. For the present work, Rigaku TTRAX III 18 kW as shown in Figure 3.08(a) was used in the thesis work. Cu-K_α X-ray radiation with wavelength 1.541 Å was used in all the cases. The theta-theta (θ–θ) goniometer was used in the reflection (Bragg-Brentano) geometry [see Figure 3.08(b)] [CULL2001].

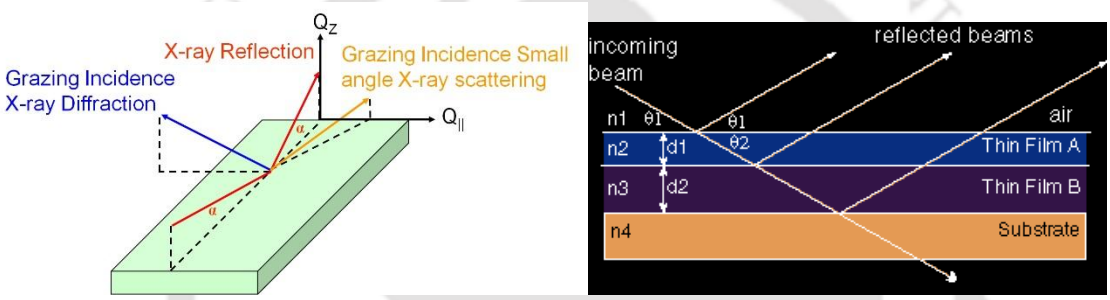

Figure 3.09: Schematic diagram of X-ray reflectivity arrangement [HTTP4].

3.3.2. X-ray reflectivity

Most of the recent technological applications require thin films of definite thickness and the literature review suggests that most properties of thin films are thickness dependent. Therefore, the determination of actual film thickness (*t*) is very crucial for these technologies. X-ray reflectivity (XRR) is a non-destructive and non-contact technique for studying the detailed surface properties and thickness determination of materials (between 2 nm and 100 nm with a precision of about 1-3 Å). In addition, this technique is also employed for the determination of density and roughness of films and also multilayers with a high precision.

The basic principle of the XRR method involves monitoring the intensity of the X-ray beam reflected by a sample at grazing angles. A monochromatic X-ray beam of wavelength (λ) irradiates a sample at a grazing angle ω and the reflected intensity at an angle 2θ is recorded by detector, as shown in Figure 3.09. The reflection at the surface and interfaces is due to the different electron densities in the different layers of films, which corresponds to different reflective indexes (in the classical optics). For incident angles θ

below a critical angle θ_C, total external reflection occurs. The critical angle for most materials is less than 0.3°. The density of the material is determined from the critical angle. Above θ_C the reflection from the different interfaces interfere and give rise to interference fringes. The period of the interference fringes and the fall in the intensity are related to the thickness and the roughness of the layer(s). The reflection obtained in the typical range between 0° and 5° can be analyzed using the classical theory (Fresnel equation).

For incident angles greater than θ_C, ($\theta > \theta_C$) the X-ray beam penetrates inside the film and therefore reflection occurs at the top and the bottom surfaces of the film. The interference between the rays reflected from the top and the bottom of the film surfaces produces interference fringes. Due to the low amplitude reflection coefficient of interface between adjacent layers, contributions of multiply reflected beams can be neglected. The m^{th} interference maximum for a path difference $\Delta = m\lambda$, is located at

$$m\lambda = \Delta = 2t\tilde{N}_{X,1}(\theta_m) \tag{3.02}$$

$$m\lambda = \Delta \approx 2t\sqrt{\theta_m^2 - 2\delta}$$

$$\theta_m^2 = m^2\frac{\lambda^2}{4t^2} + 2\delta$$

$$\theta_m^2 = m^2\frac{\lambda^2}{4t^2} + \theta_C^2 \tag{3.03}$$

The plot of θ_m^2 versus m^2 yields a straight line and fitting the experimental data to linear fit provides thickness of the films from the slope and critical angle from the intercept. The thickness is often determined with a precision better than 1 Å for measurements exhibiting interference fringes in a bigger angular range. Another important quantity determined from XRR measurements is the surface and interface roughness. Roughness gives rise to diffuse scattering, which reduces intensity in the specularly reflected beam. General scattering formalism have been developed that calculate the scattered fields for both specular and non-specular scattering. In one of the formalism, roughness is considered as non-homogeneous thickness. It is assumed that the thickness has a Gaussian distribution with a mean t and a standard deviation σ. With this assumption, the corrected Fresnel coefficients of reflection is given as $\rho exp(-x/(2\sigma^2))$. Alternatively, the XRR data can be analyzed using the analytical relation,

$$2tsin\theta = (2n+1)\lambda/2 \tag{3.04}$$

where t is thickness of the film, θ is Bragg angle, n is the number of XRR maxima and λ is the X-ray wavelength (=1.541 Å) [SERA2011, LALM2017]. The plot of $\sin\theta$ *vs* n provides almost linear behavior and the straight-line fit to the experimental data provides the value of $\lambda/(2t)$ from the slope. Subsequently, t is determined from the slope.

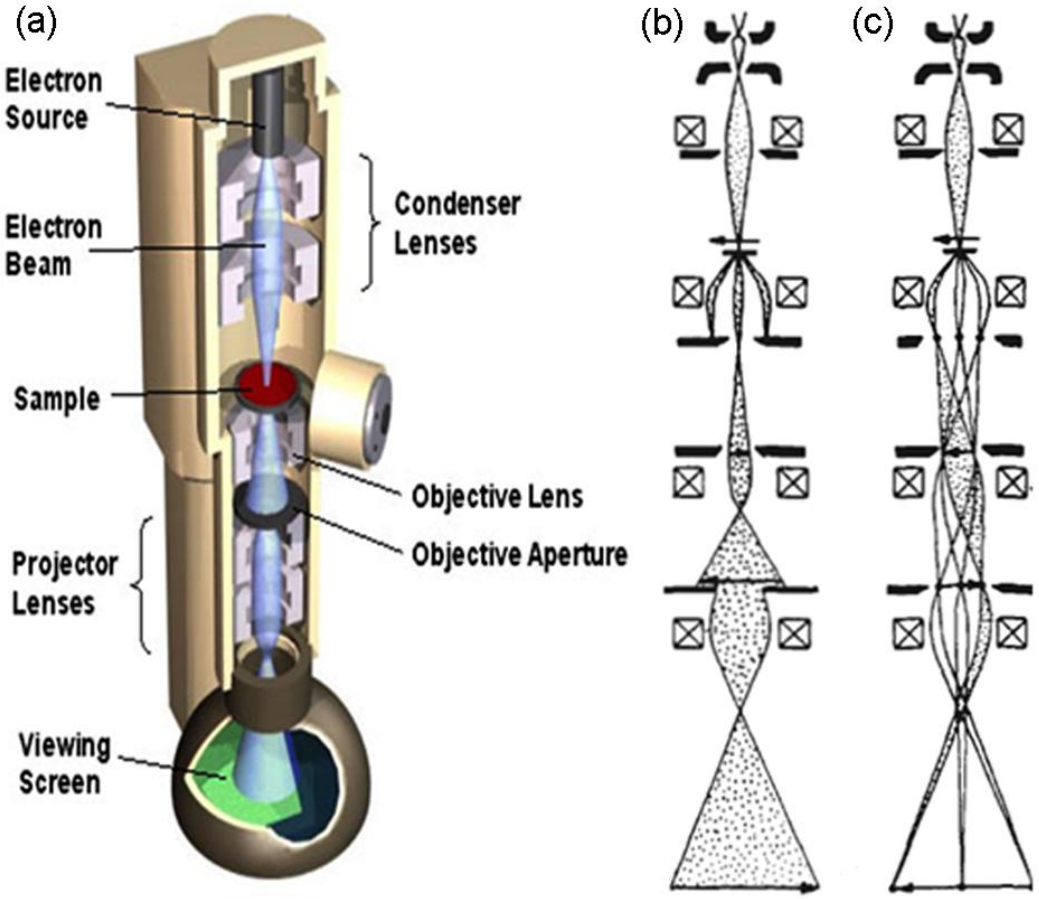

Figure 3.10: (a) Cut view of transmission electron microscope, (b) Schematic ray diagrams of image mode and (c) diffraction mode of TEM [HTTP5, HTTP6].

3.3.3. Transmission electron microscope

Transmission electron microscopy (TEM, TECNAI G^2 F30; JEOL 2100) was used to study the amorphous nature of the films depending on its availability. Figure 3.10 depicts the cut view of TEM [Figure 3.10(a)] and schematic ray diagrams for imaging [Figure 3.10(b)] and diffraction [Figure 3.10(c)] modes. Electrons emitted from the gun are accelerated to 200 keV or higher and first projected onto a thin specimen by means of the condenser lens system. The scattering processes experienced by electrons during their passage through the specimen determine the kind of information obtained. Elastic scattering, involving no energy loss when electrons interact with the potential field of the ion cores, gives rise to diffraction patterns. Inelastic interactions between beam and matrix electrons at

heterogeneities such as grain boundaries, dislocations, second-phase particles, defects, density variations, *etc*., cause complex absorption and scattering effects, leading to a spatial variation in the intensity of the transmitted beam. The transmitted beams are further magnified by a set of intermediate lens and projector lens and finally projected on a fluorescent screen.

Microstructural images are obtained in number of ways. The bright-field image is obtained by intentionally excluding all the diffracted beams and only allowing the central beam passing through the specimen. This is done by placing suitably sized apertures in the back focal plane of the objective lens. Dark-field images are also formed by magnifying a single beam of one of the diffracted beams by means of an aperture that blocks the central beam and the other diffracted beams. In a third method of imaging, the primary transmitted and one or more of the diffracted beams are made to recombine, thus preserving both their amplitudes and phases. This is the technique employed in high-resolution lattice imaging, enabling diffracting planes and arrays of individual atoms to be distinguished. From the high-resolution TEM (HR-TEM) micrograph, average grain size and dislocations can be evaluated. On the other hand, the selected area electron diffraction is done by intentionally excluding the central beam by beam blocker and collecting all the diffracted beams to form the diffraction patterns. The composition analysis of the samples can also be analyzed using X-ray energy dispersive analysis interfaced to TEM. Electrons emitted from the filament (cathode) are accelerated to high energies where they strike the specimen target (anode). In the process, X-rays characteristic of atoms in the irradiated area are emitted. The atoms can be identified by analyzing their energies and the concentration of atoms in the specimen can be determined by counting the number of X-rays emitted. In the present study, as-deposited films were polished mechanically from substrate side using Gatan Disc grinder to reduce the thickness down to 10 μm and subsequently thinned down using precision ion polishing system (PIPS) to suitable thickness for the TEM observation.

3.4. Magnetic property characterization

Magnetic properties of the magnetic materials can be characterized using various experimental techniques. One of the major techniques used for magnetic characterization is based on the induction methods and have sensitivity of at least 10^{-6} emu. Similarly, the magnetic domain structure of the materials can be imaged using magnetic Kerr microscope and magnetic force microscope (MFM). In this section, a brief description of the principle

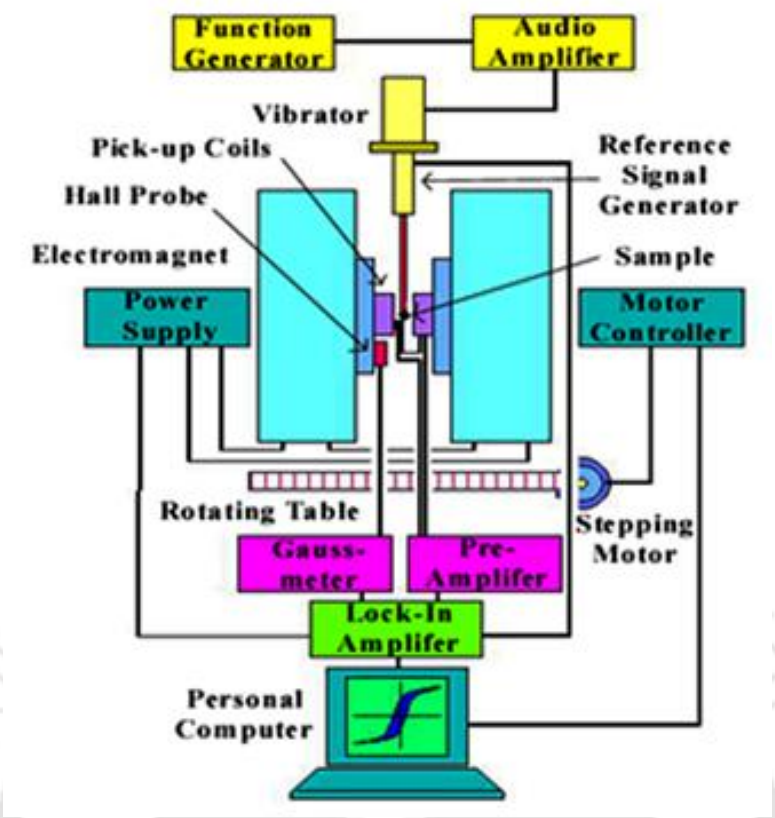

Figure 3.11: Schematic diagram of a vibrating sample magnetometer [HTTP6].

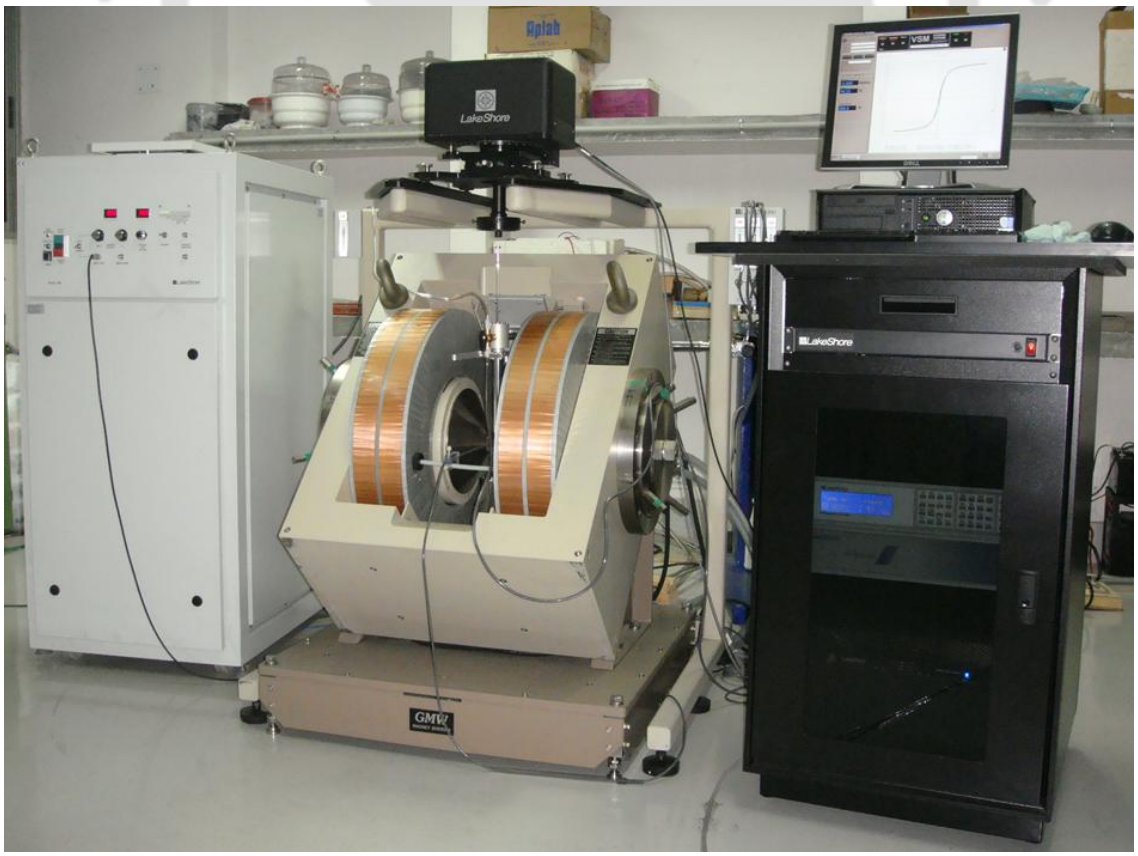

Figure 3.12: Photographic view of vibrating sample magnetometer (Model: Lakeshore 7410, USA) used in the present investigation.

involved in various magnetic measurement and domain imaging techniques employed in the present work is outlined.

3.4.1. Vibrating sample magnetometer

Vibrating sample magnetometer (VSM, Lakeshore 7410, USA) was used to characterize room temperature and temperature dependent magnetic properties in the temperature range of 30 K – 300 K and 300 K – 700 K. VSM measures net dipole moment when material is exposed to magnetic field [JANS2004, HORS2006]. The magnetic moment of the material can be obtained either as a function of field called magnetic hysteresis (*M-H*) loop to investigate the evolution of magnetic properties with field or as a function of temperature (*M-T*) to understand the magnetic phase transition of the material. Figures 3.11 and 3.12 display schematic diagram of VSM and a photographic view of VSM used in the present study, respectively.

When a sample is placed in a uniform magnetic field, a dipole moment proportional to the product of the sample susceptibility and the applied field is induced in the sample. If the sample is made to undergo sinusoidal motion, an electrical signal can be induced in suitably located stationary pickup coils (see Figure.3.11). This signal has amplitude proportional to the magnetic moment of the sample, the vibrating amplitude and the vibration frequency. Through the use of lock-in-amplifier and feedback techniques, only that portion of the signal arising from the magnetic moment is picked up and is converted into direct read-out in the unit of magnetization (e.g. emu) on a digital panel meter. As shown in Figure 3.12, VSM consists of the following major parts: a) Vibration exciter and sample holder, b) Water cooled electromagnet and power supply, c) Hall probe, d) pick-up coils, e) Amplifier, f) Control panel system, g) Lock-in amplifier and h) Computer interface.

The thin film sample was fixed at the lower end of the sample rod aligning either in-plane or out of plane direction with respect to applied field. Prior to the magnetic measurements, the calibration procedure was carried out using standard Ni sphere sample. The measurement sequence is programmed as per the users choice using the software (IDEASVSM) provided with the instrument such that the program starts either from the maximum field or from the zero applied field. The sequence is made to collect more number of data, which helps to extract the magnetic parameters (saturation magnetization, remenance magnetization, coercivity, *etc*.) more accurately. The exciter is vibrated at a frequency of 72 Hz (Lakeshore model 7410) and the signal received from the hall probe and the pick-up coils is converted into the magnetic moment of the sample. The magnetic field

is increased automatically in user-defined steps for measuring *M-H* loops. Similarly, for high temperature *M–T* measurements, a high temperature oven attachment capable of providing a controlled heating/cooling of the sample from room temperature to 1223 K was used. For *M–T* measurements, the film was loaded on a high temperature sustainable holder (ceramic holder or quartz rod) after the calibration using standard Ni sample. The oven was purged with nitrogen gas to avoid oxidization of the sample at high temperature. Magnetization was recorded at different temperatures at a constant in-plane applied magnetic field. The heating rate and *M–T* sequences were programmed using the IDEASVSM software.

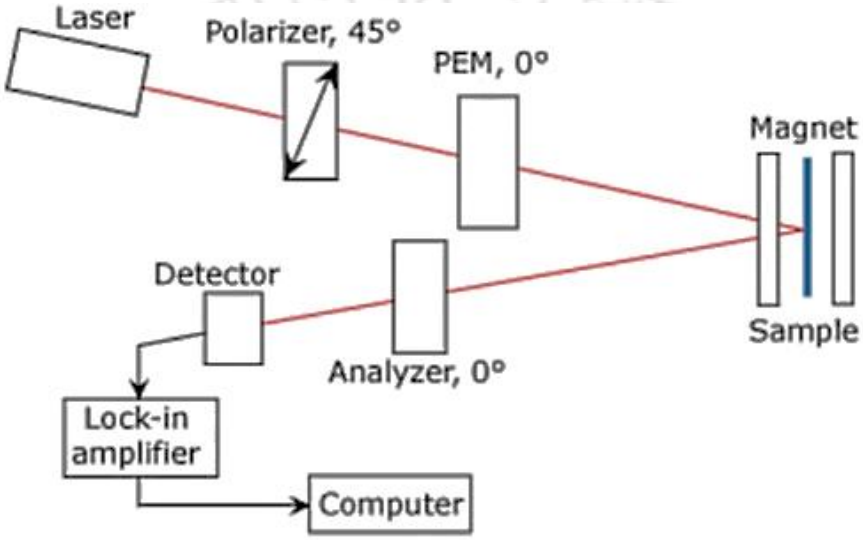

Figure 3.13: Schematic drawing of MOKE set up [HTTP6].

3.5. Magnetic domain structure analysis

3.5.1. MOKE microscope

The magneto-optical Kerr effect (MOKE) represents a change in the intensity or polarization state of the light reflected from a magnetic material. Figure 3.13 depicts a schematic view of conventional MOKE set up. The light beam from a laser is polarized using a linear polarizer, while a photo-elastic-modulator (PEM) superimposes periodic quarter-wave retardation ($\pm\lambda/4$) to this beam before it reaches the sample. After the beam is reflected from the sample, the light beam is again made to pass through a linear analyzer and then the signal is collected at the detector. In principle there are three different optical and magnetic geometries of the Kerr effect: (a) Longitudinal MOKE provides a signal proportional to the component of magnetization that is parallel to the film plane and the plane of incidence of the light. (b) In transverse MOKE, the signal is proportional to the component of

magnetization that is parallel to the film plane but perpendicular to the plane of incidence of the light. (c) Polar MOKE, in which a signal proportional to the component of magnetization that is perpendicular to the film plane is measured and often performed at normal incidence. There are three important properties to be noted that (i) the Kerr signal is a linear function of the Kerr amplitude *K* and therefore of the respective magnetization components, (ii) the Kerr signal can be enhanced by increasing the analyzer angle allowing to increase the signal-to-noise ratio and to adjust to the sensitivity of the detector and (iii) the visibility of domains is determined by the Kerr amplitude and not by the Kerr rotation.

To produce a Lorentz movement that leads to detectable Kerr rotation, an appropriate direction of light incidence and polarization has to be selected for a given magnetization direction. As a simple rule, the Kerr rotation is proportional to the magnetization component parallel to the reflected beam of light. This rule implies that domains that are magnetized parallel to the sample surface require oblique light incidence and that for maximum rotation the plane of incidence must be parallel to the axis of magnetization with the polarizer set either parallel or orthogonal to the incidence plane (longitudinal Kerr effect, $\vartheta \neq 0$). The Kerr amplitude is then proportional to the sine of the angle of incidence ϑ, and therefore disappears for perpendicular incidence. In this case, maximum rotation is exhibited by domains that are magnetized perpendicularly to the sample surface (polar Kerr effect, $\vartheta = 0$), while in-plane domains do not cause a Kerr amplitude. At oblique incidence, both in-plane and out-of-plane magnetization components generate a superimposed Kerr contrast. The separation of the two components is possible by proper difference images that are obtained at different microscope settings. Also, the transverse Kerr effect leads to in-plane magnetization sensitivity. Here, the in-plane *m* vector is normal to the plane of (oblique) incidence. Light with *E* parallel to this plane generates Kerr amplitude, but its polarization direction is the same as that of the normally reflected beam. The transverse Kerr effect thus causes an amplitude variation, which can be used for measuring purposes. A rotation that is detectable by an analyzer is obtained when the incident light is polarized at 45° to the plane of incidence. Here, the *E* component perpendicular to the incidence plane is not affected, while the parallel component is modulated in its amplitude on reflection, leading to polarization rotation by superposition [SCHA2007, HUBE2014].

Kerr microscopy allows the imaging of magnetic domain and magnetization processes in an optical polarization microscope. This is also based on the MOKE, but only with the difference that the domains are directly imaged. A schematic picture of the setup is

shown in Figure 3.14. In this set up, the light from a source passes through a polarizer which transmits only plane polarized light. This polarized light is then allowed to fall on the sample. The resulting light in the image plane strongly depends on the magnetization of the sample.

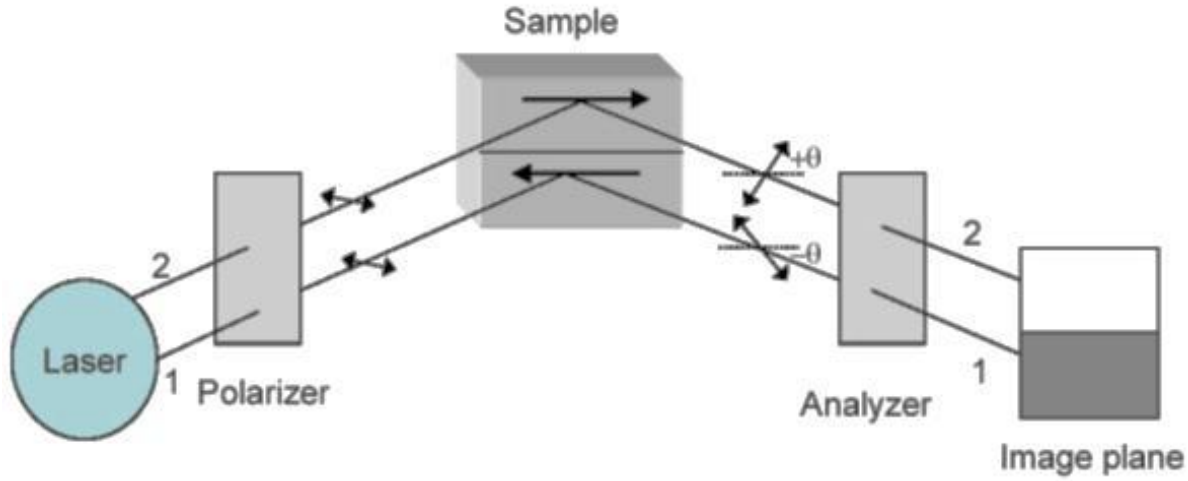

Figure 3.14: Schematic drawing of Kerr microscope [HTTP6].

Figure 3.15: Photographic view of the Kerr microscope (Evico Magnetics Ltd. Germany) used in the present study.

For example, let us consider a simplest case of two domain states which are antiparallel to each other as indicated by arrows in Figure 3.14. After reflection from the sample, the plane of polarization of beam 1 is rotated one way by certain angle $-\theta$ and that

of beam 2 is rotated by angle $+\theta$, as they encountered oppositely magnetized domains. The light then passes through an analyzer and into a camera to make images. Here, the analyzer is rotated until it is crossed with respect to the reflected beam 1 and the beam is therefore extinguished and the lower domain appears dark. At the same time, the analyzer is not crossed with respect to beam 2 and thus beam 2 is not extinguished resulting the upper domain as light one. This is the mechanism to find a contrast between two different domains.

In the present study, magnetic domain images and Kerr loops were obtained using a MOKE microscope (Evico Magnetics Ltd., Germany) as shown in Figure 3.15. Imaging was performed using linearly polarized light with white LED source. Magnetic domain images were observed in both branches of hysteresis loop in longitudinal MOKE mode. Hysteresis accompanied by simultaneous imaging has been performed for magnetic fields applied along various in-plane directions (easy and hard axes).

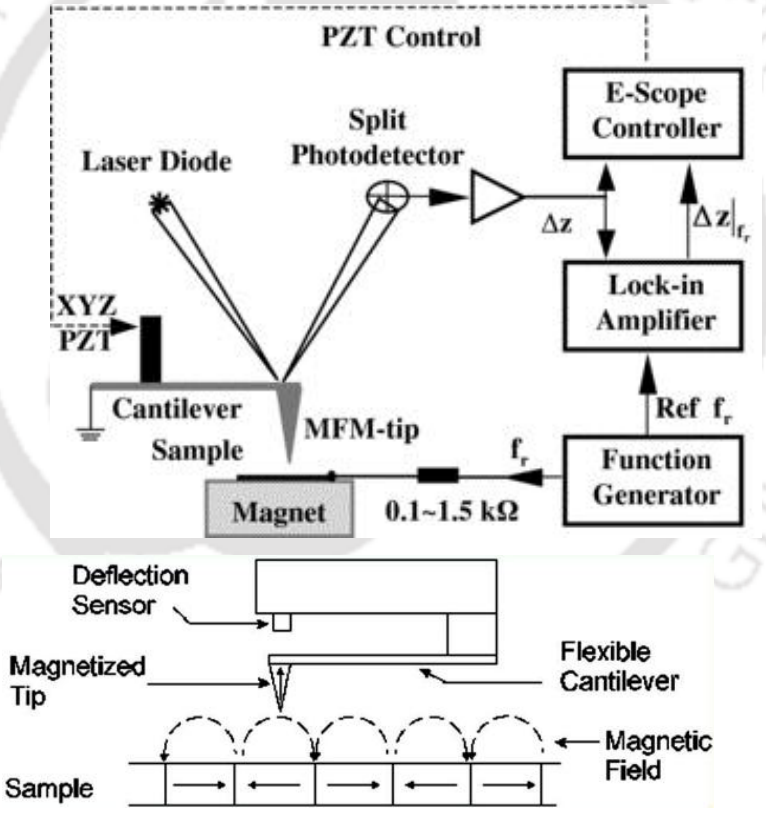

Figure 3.16: Schematic drawing of MFM set up and field lines realized by the tip from the sample surface [PUA2007].

3.5.2. Magnetic force microscope

The magnetic force microscope (MFM) is a special mode of operation of the atomic force microscope (AFM). In this technique, a sharp magnetized tip is brought close to a sample and interacts with the magnetic stray fields near the surface, as shown in Figure 3.16. The

tip-sample magnetic interactions are detected and used to reconstruct the magnetic structure of the sample surface. Many kinds of magnetic interactions are measured by MFM, including magnetic dipole–dipole interaction. MFM scanning often uses non-contact AFM mode. MFM was introduced shortly after the invention of the AFM [MART1987]. This technique became popular as a technique that offers high imaging resolution without a special need for sample preparation or environmental conditions. The operating principle of MFM is the same as in AFM. Both static and dynamic detection modes can be applied.

The cantilever is excited to vibrate close to its resonance frequency, with a certain amplitude and a phase shift with respect to the drive signal. The deflection sensor of the microscope monitors the motion of the tip. Under the influence of a probe-sample interaction, the cantilever behaves as if it had a modified spring constant, $c_F = c - \partial F/\partial z$. An attractive interaction with $\partial F/\partial z > 0$ makes the cantilever spring softer such that the resonance frequency decreases. This leads to a change of the oscillation amplitude of the probe and of its phase, which can be measured to map the lateral variation of $\partial F/\partial z$. The force derivative $\partial F/\partial z$ originates from a wide range of sources, including electrostatic probe-sample interactions, van der Waals forces, damping, or capillary forces [PORT1998]. However, MFM relies on those forces that arise from a long-range magnetostatic coupling between probe and sample. This coupling depends on the internal magnetic structure of the probe, which greatly complicates the mechanism of contrast formation.

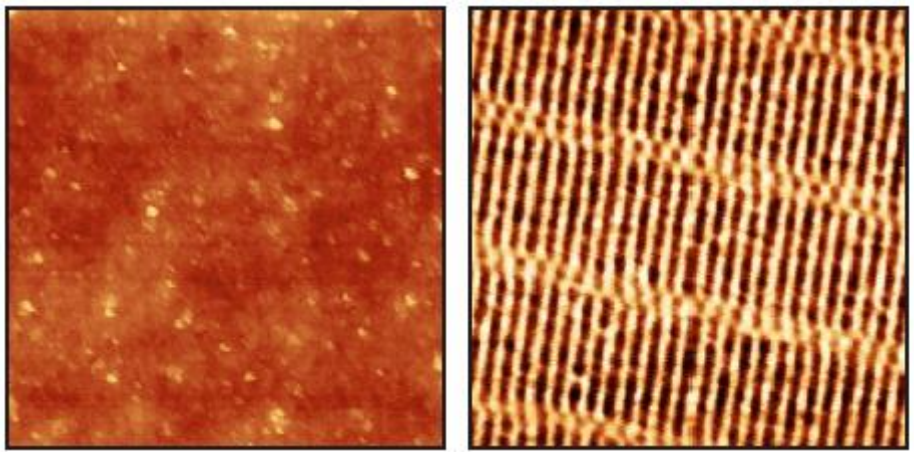

Figure 3.17: Typical AFM and MFM images (40×40 μm^2) of zip disk [HTTP7].

The cantilever/tip assembly is obviously the critical element of a magnetic force microscope [RUGA1998]. In addition, the tip shape is important due to the long-range nature of magnetic forces. Originally, electrochemically etched wires of cobalt or nickel were used as cantilevers [MART1987]. Recently, cantilevers with integrated sharp tips are

now fabricated in large numbers out of silicon-based materials. These tips can be coated with a thin layer of magnetic material for the purpose of MFM observations. A lot of effort has been spent on the optimization of magnetic tips in order to get quantitative information from MFM data [RUGA1998, HART1999]. However, the major problem with the coated conventional tips is that the magnetic domain pattern reduces the effective magnetic moment of the tip. As a result, the exact domain structure is unknown and can even change during MFM operation. The spatial resolution in MFM imaging is related to the tip-sample distance, but also to the magnetized part of the tip that is actually exposed to the sample stray field. To improve lateral resolution, it is beneficial to restrict the magnetically sensitive region to the smallest possible size. In ideal case, the effective volume of the probe would consist of a small single-domain ferromagnetic particle located at the probe apex. However, there is a physical lower limit for the dimensions because an ultra-small particle becomes superparamagnetic. The demand for a strong signal, produced by a small sensitive volume, indicates the need to maximize the magnetic moment in the tip. Hence, recently, the tips coated with 10-150 nm of CoCr alloy are used as standard probes for MFM. The typical AFM and MFM images of zip disk is shown in Figure 3.17.

In the present investigation, simultaneous atomic force microscopy (AFM) and magnetic force microscopy (MFM) studies were performed to study the topographic feature and local magnetic domains (Bruker Dimension Icon). MFM was performed in dual-pass lifting mode with commercially available CoCr-coated tips, which were magnetized along the tip axis and therefore sensitive to stray field gradients from out-of-plane oriented domains or the out-of-plane components of domains oblique to the surface. The domain images were acquired at the zero-field state.

भारतीय प्रौद्योगिकी संस्थान गुवाहाटी
Indian Institute of Technology Guwahati

Chapter 4

Thickness dependent properties of single-layer CoFeB magnetic thin films

भारतीय प्रौद्योगिकी संस्थान गुवाहाटी
Indian Institute of Technology Guwahati

4.1. Introduction

CoFeB based thin films are found to be one of the promising materials suitable for various applications in modern magneto-electronic devices due to their tunable magnetic properties. A careful review of the literature on CoFeB based thin films suggests that the magnetic properties of the films are strongly dependent on film thickness. For example, (i) films with thickness less than 5 nm exhibit a strong perpendicular magnetic anisotropy ranging between 0.5×10^6 J/m^3 and 2×10^6 J/m^3 due to interfacial effects [IKED2010, MANT2013, WANG2014]. Therefore, these ultra-thin films find applications in magnetic tunnel junctions [IKED2010, ISHI2014, ZHAN2015], magnetic random access memory [ZHUY2012, MANT2013, CUCH2016], spin logic based devices [SULI2015] and various other spintronics based applications [SONG2000, TEHR2000, UHRM2008, JIAN2009, SATO2014, THOM2014, ZHAO2015, LIUY2016, VEMU2016, LEES2017, MAEK2017]. (ii) Films with thickness larger than 5 nm exhibit in-plane magnetic anisotropy induced either by the formation of aligned ferromagnetic atom pairs during deposition or by bond-orientational anisotropy, especially for thicknesses up to 70 nm [HIND2011, KIPG2012, CUIB2013, TANG2014, QIAO2016]. As these films exhibit in-plane magnetic anisotropy with magnetization oriented in a particular direction, high resistivity, high permeability, high saturation magnetization and appropriate anisotropy field, they are mainly used as magnetic passives, energy transferring devices, magnetic flux amplifiers, magnetic recording heads, microwave integrated circuits, cores in high-frequency inductors, wireless inductors, microwave noise filters, electromagnetic wave absorbers, *etc* [MUNA2005, HASH2007, KAZI2013]. Thicker CoFeB based films are also grown on flexible substrates to investigate the influence of strain on the magnetic anisotropy of CoFeB films with applications in flexible electronics in mind [YANG2013, TANG2014, QIAO2016]. In addition, thick CoFeB based films with high in-plane magnetic anisotropy field as well as high saturation magnetization have been used as soft magnetic underlayers for obtaining high signal to noise ratio in perpendicular magnetic recording media [ITOS2005, PIRA2007]. (iii) On further increasing thickness, stress induced magnetic anisotropy overcomes in-plane magnetic anisotropy and increases the degree of local disorder in the easy-axis of as-deposited films. This leads to the formation of random magnetic anisotropy with an adverse influence on the soft magnetic properties and induces formation of dense stripe domain [ITOS2005, TANG2014, GAYE2017]. Therefore, thicker CoFeB films become magnetically hard and display transcritical loop. Furthermore, these types of soft magnetic thin films show spin-reorientation transition

from in-plane magnetization to out-of-plane multi-domain state or vice-versa either with change in film thickness or with variation in substrate temperature during preparation [SHAR2006]. However, most of the earlier reported works have been focused on either tuning the magnetic properties of CoFeB films at ultrathin level from application point of view or studying the magnetic properties of the films at random thicknesses using different fabrication processes. There are no systematic studies have been carried out to study the effects of composition, film thickness over a wide range of thicknesses and temperature on the magnetic properties of these films prepared by a single fabrication technique.

Hence, in this chapter, we focus on (i) the thickness dependent magnetic properties of CoFeB films over a wide range of thicknesses from 7 to 200 nm at room temperature and (ii) the temperature dependent magnetic properties of CoFeB thin films in the temperature range between 30 and 300 K at different thicknesses. The above studies are carried out for CoFeB films with two different compositions [$Co_{40}Fe_{40}B_{20}$ (CoFeB442) and $Co_{20}Fe_{60}B_{20}$ (CoFeB262)] to investigate the effect of composition as well on the magnetic properties.

4.2. Experimental details

Amorphous single-layer films of $Co_{80-y}Fe_yB_{20}$ (t nm) with two different compositions [$Co_{40}Fe_{40}B_{20}$ (CoFeB442) and $Co_{20}Fe_{60}B_{20}$ (CoFeB262)] were deposited at ambient temperature directly on thermally oxidized Si substrates using DC magnetron sputtering technique. The base pressure of the chamber was better than 2×10^{-4} Pa and the sputtering Ar gas pressure for the deposition of CoFeB films was optimized at 2 Pa. The optimization of sputtering Ar gas pressure was performed primarily by monitoring the changes in the thickness dependent structural and magnetic properties for both the compositions. The deposition rate was pre-calibrated using *ex-situ* surface profilometer (Vecco, Dektak-150) and found to be 1.5 Å/sec. The thickness of the CoFeB films was varied between 7 and 200 nm as 7, 10, 15, 20, 50, 75, 100 and 200 nm. The total thickness of each CoFeB film was controlled by monitoring the deposition time during the sample deposition.

Amorphous nature of the as-deposited films was confirmed by X-ray diffraction (XRD) using a Rigaku TTRAX diffractometer (18 kW, Rigaku TTRAX III) with *Cu-Kα* radiation (λ = 1.541 Å) and bright-field TEM images and selected area electron diffraction (SAED) using transmission electron microscopy (TEM, JEOL 2100 microscope). Thickness and surface roughness of the films were also measured by X-ray reflectivity

(XRR) technique using above mentioned Rigaku X-ray diffractometer. Room temperature and temperature dependent magnetic properties were carried out by measuring magnetic hysteresis (*M-H*) loops at different temperatures in the temperature range between 30 K and 300 K and thermomagnetization data at different temperature in the temperature range between 300 K and 700 K by using vibrating sample magnetometer (VSM, Lakeshore Model 7410). Magnetic domain images and Kerr loops were obtained using magneto-optic Kerr effect (MOKE) microscopy (Evico Magnetics Ltd, Germany) technique. Imaging was performed using linearly polarized light with white LED source. Magnetic domain images were observed in both branches of hysteresis cycle in longitudinal MOKE mode. Hysteresis accompanied by simultaneous imaging has been performed for magnetic fields applied along various in-plane directions (easy and hard axes). Magnetic force microscopy (MFM, Bruker Dimension Icon) was performed in dual-pass lifting mode with commercially available CoCr-coated tips, which were magnetized along the tip axis and therefore sensitive to stray field gradients from out-of-plane oriented domains or the out-of-plane components of domains oblique to the surface. The domain images were acquired at the zero-field state.

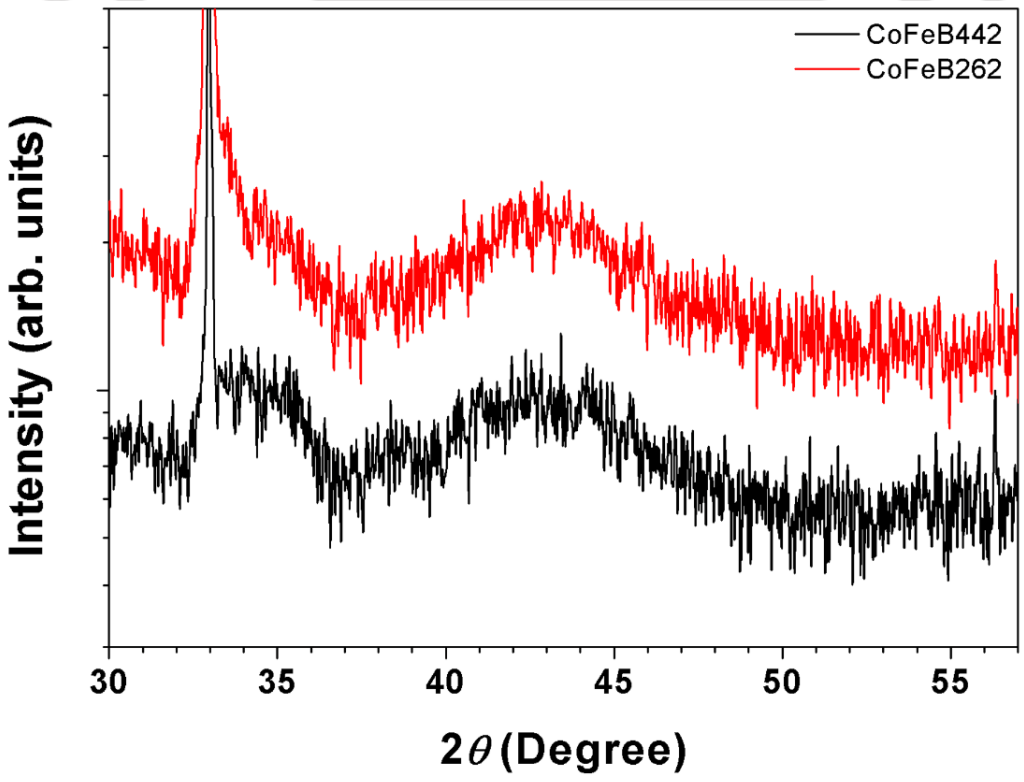

Figure 4.01: Room temperature XRD patterns of 200 nm thick CoFeB442 and CoFeB262 films.

4.3. Results and discussion

4.3.1. Structural properties

Figure 4.01 displays typical XRD patterns of CoFeB (200 nm) films with different compositions. It is clearly seen that as-deposited films exhibit only broad peaks at around $2\theta = 44°$ without any other sharp peaks corresponding to any crystalline phase. It may be noted that the XRD peak observed at $2\theta = 33.05°$ represents Si(200) peak emanating from the Si substrate [WUYM1998, CHOM2001]. In order to further confirm the amorphous local microstructure, bright-field and high-resolution TEM images were investigated by TEM technique.

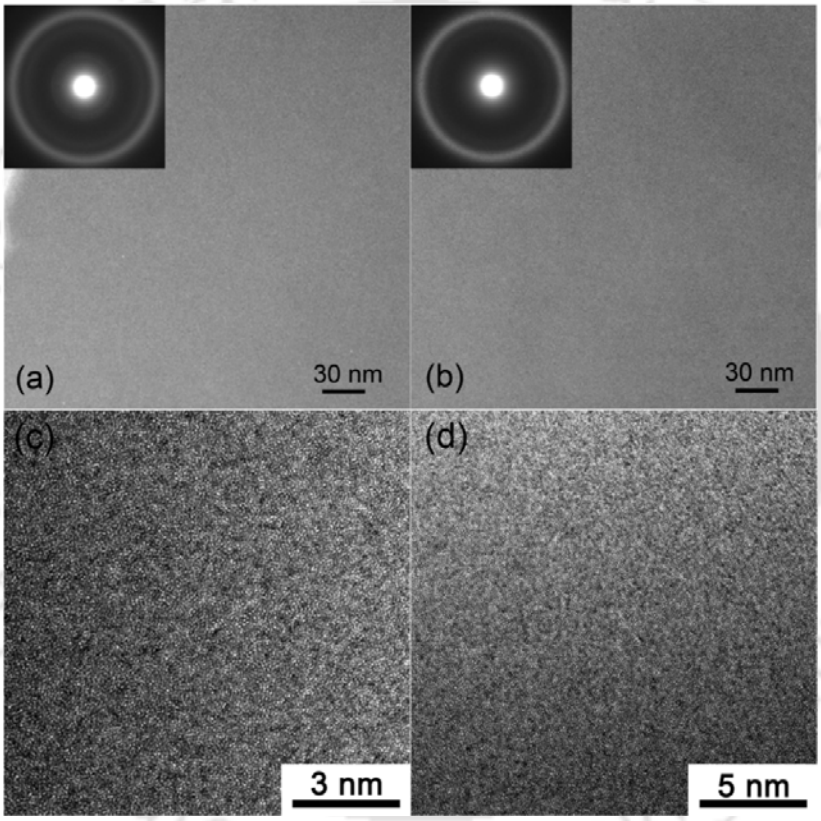

Figure 4.02: Bright-field TEM micrographs, selected area electron diffraction patterns and high-resolution TEM images of as-deposited 200 nm thick single-layer CoFeB442 (a,c) and CoFeB262 (b,d) films.

Figure 4.02 depicts the bright-field TEM images, SAED patterns and HRTEM images of 200 nm thick CoFeB442 and CoFeB262 films. While the bright-field TEM images and HRTEM images reveal the existence of plain and even contrast microstructure without any local lattice fringes, the SAED patterns display halo diffraction rings

corresponding to the amorphous structure. These results confirm the presence of amorphous structure in the as-deposited films. Since the magnetic properties of the thin films strongly depend on the film thickness, it is very much essential to study the actual film thickness and associated roughness as a function of thickness. XRR is one of the non-destructive techniques widely used to evaluate various film parameters such as film thickness, surface roughness, interface roughness, *etc*. Hence, the XRR curves are recorded for the as-deposited CoFeB films and the typical curves are presented in Figure 4.03.

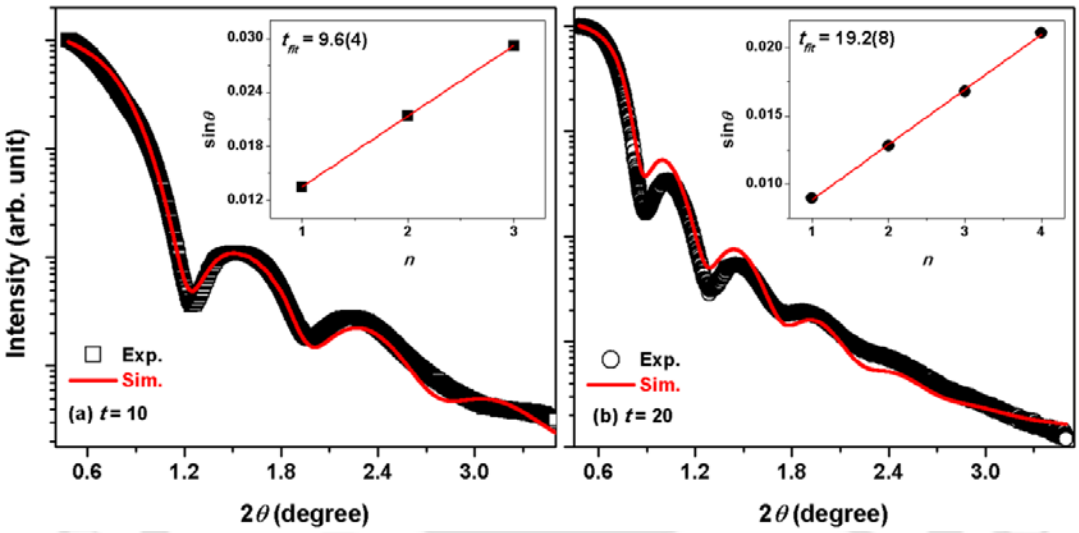

Figure 4.03: XRR curves for CoFeB442 (*t* nm) films with (a) *t* = 10 and (b) *t* = 20 nm. The solid lines passing through the data are the simulated data using Globalfit software for the layered sample model. Inset: The plots of sinθ *vs n* and linear fit to the data for the determination of *t*.

The interference patterns (open symbols) with clear oscillation peaks are observed for the as-deposited films. The oscillation intensity becomes smaller and attains the same level as the noise at higher angles. With increasing *t*, the number of oscillation peaks increases and peak width decreases. To understand the changes in the XRR curves with increasing *t*, fitting of the XRR curves is preceded by a pattern fitting procedure using the GlobalFit software offered by Rigaku, Japan. During the analysis, a layered sample model is constructed to generate a simulated reflectivity curve. The model consists of three simulated layers: (i) bulk Si(100), (ii) a thin film of SiO_2 and (iii) the CoFeB layer. The solid lines in Figure 4.03 represent simulated data using this model. For *t* = 10 film, the film thickness is predicted to be 9.5 nm with the interface and surface roughness values of 0.28 and 0.22 nm, respectively. Similarly, the thickness of the *t* = 20 film is determined to

be 19 nm with an interface roughness of 0.42 nm and surface roughness of 0.35 nm. For films with $t > 20$, the interface and surface roughness increase to a maximum value of 0.96 and 0.7 nm, respectively.

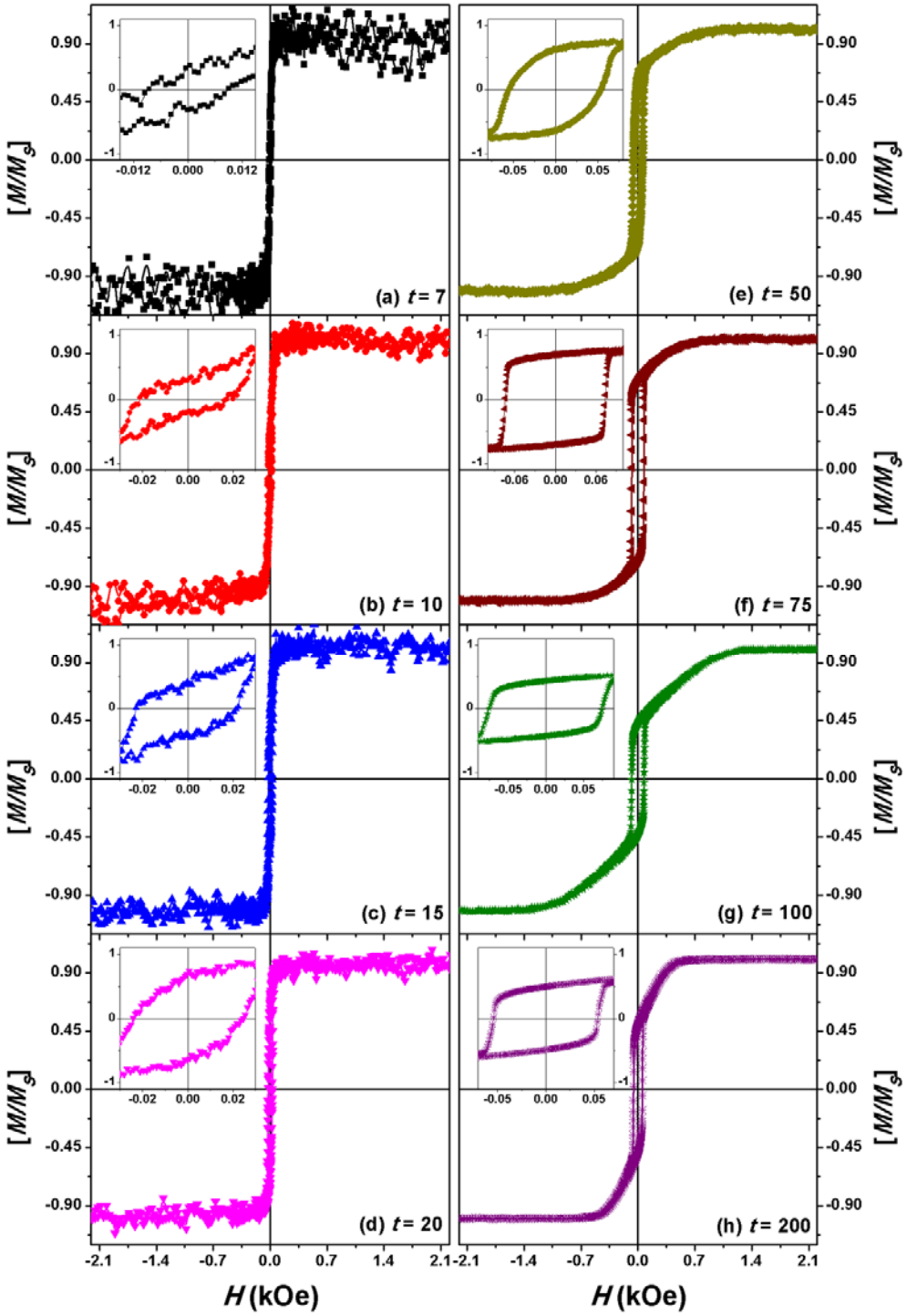

Figure 4.04: Room temperature *M-H* loops of CoFeB442 (*t* nm) films with different thicknesses measured along the film plane. Insets are having the expanded view.

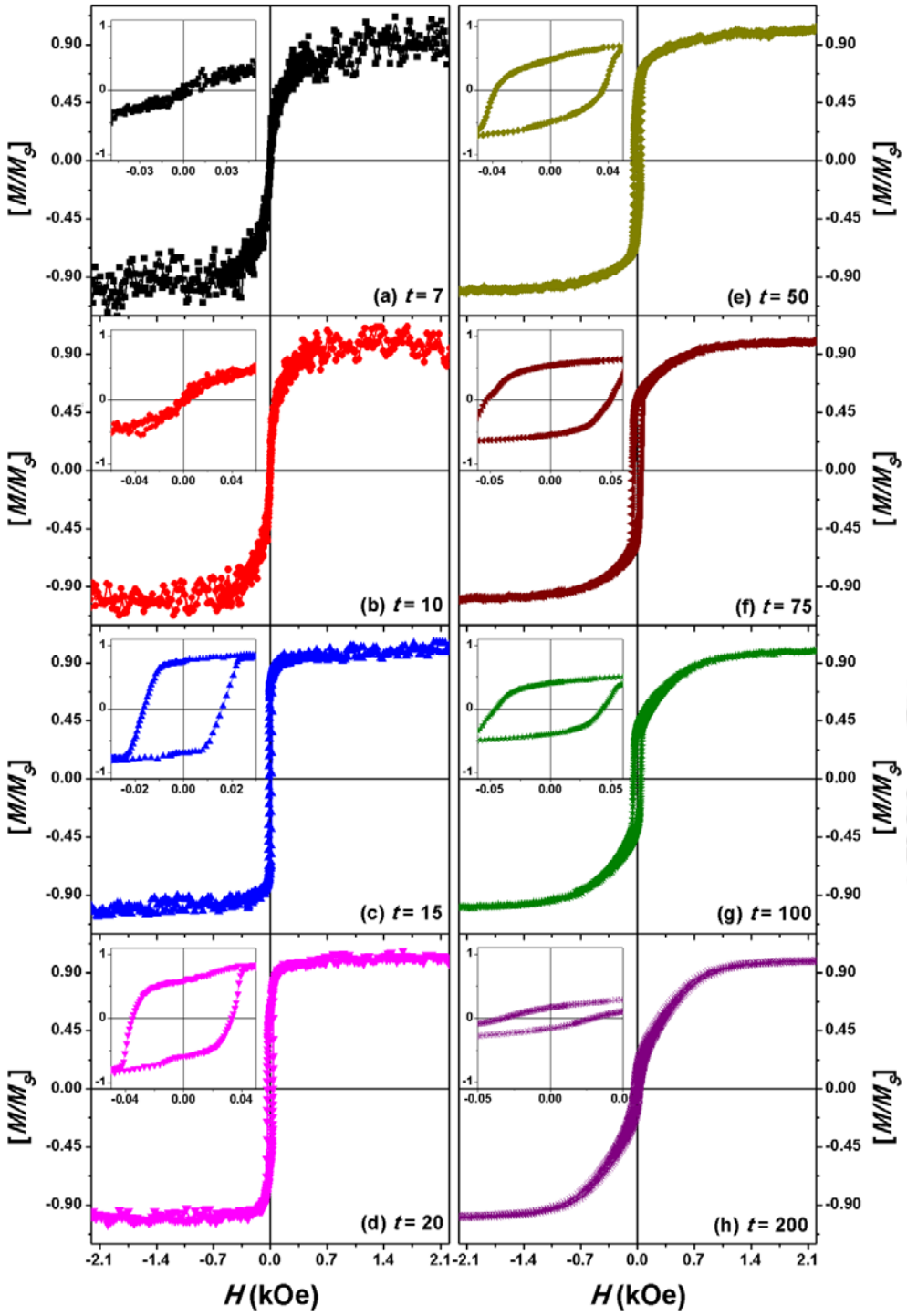

Figure 4.05: Room temperature *M-H* loops of CoFeB262 (*t* nm) films with different thicknesses measured along the film plane. Insets are having the expanded view.

In order to cross check the fitting procedure, the XRR data are also analyzed using the relation, $2tsin\theta = (2n+1)\lambda/2$, where *t* is thickness of the film, θ is Bragg angle, *n*

is the number of XRR maxima and λ is the X-ray wavelength (=1.541 Å) [SERA2011, LALM2017]. The plot of $\sin\theta$ *vs* n for each film as shown in insets of the figure shows almost linear behavior. Hence, the straight-line fit to the experimental data provides the value of $\lambda/(2t)$ from the slope. Subsequently, t is determined from the slope. The determined values of t are in close agreement with the values determined from fitting procedure using GlobalFit software.

4.3.2. Magnetic properties

4.3.2.1. Room temperature magnetic properties

Figures 4.04 and 4.05 show the room temperature normalized in-plane *M-H* loops of the CoFeB442 (t = 7 – 200 nm) and CoFeB262 (t = 7 – 200 nm) films measured along the film plane. The expanded view of the loops close to origin is shown in inset. It is observed that (i) CoFeB442 films with $t \leq 20$ nm exhibit nearly rectangular shaped loops with remanence ratio of more than 80 % and the loops saturate at lower applied magnetic fields. (ii) With increasing t to 50 nm, the shape of the loops changes from rectangular shape into different nature. (iii) On further increasing thickness, the *M-H* loops are constituted by two distinct magnetization reversal processes: (a) in-plane magnetic components, which reverse quickly at fields close to coercive field (H_C) and (b) perpendicular components, which rotate progressively under the application of magnetic field. The latter gives rise to a nearly linear variation of magnetization before saturation and also requires a large saturation field (H_{Sat}) of more than 1.5 kOe to saturate the film's magnetization. Such type of loop has been referred to as a transcritical loop [MURA1966, PRAD2004, SHAR2006], which in general is related to increase in effective magnetic anisotropy caused by the stress induced during the deposition of the films at a higher deposition rate to form amorphous nature and hence the stress accumulation in the samples during preparation increases progressively with increasing thickness [ITOS2005, SHAR2006, COIS2009, GAYE2017]. This leads to the formation of dense stripe domain pattern in the as-deposited films.

It may be noted that this type of magnetic anisotropy is different from the one reported for ultrathin CoFeB films originating primarily from the interfacial nature. (iv) With increasing t above 50 nm, the relative magnitude of in-plane components reversing close to H_C decreases gradually up to 100 nm and H_{Sat} increases considerably. Upon increasing t to 200 nm, the magnitude of in-plane component increases slightly and the value of H_{Sat} decreases marginally. This could be attributed to redistribution of

accumulated stress in the film with increasing *t*. On the other hand, (v) CoFeB262 films with *t* up to 10 nm show different loop shape as compared to CoFeB442 films, i.e., the loop shape is observed to be flat-type with a low remanence and requires significantly more applied magnetic field to saturate the magnetization. (vi) Upon increasing *t* from 15 nm to 100 nm, the loop shapes of CoFeB262 and CoFeB442 films are observed to be nearly the same. (vii) However, the relative magnitude of in-plane components reversing close to H_C decreases largely for CoFeB262 (200 nm) film, which is different from the behavior observed for CoFeB442 (200 nm) film. These results clearly reveal that CoFeB films with thickness between 7 and 20 nm exhibit in-plane magnetic anisotropy caused probably either by the formation of aligned ferromagnetic atom pairs due to their strong magnetic exchange coupling during deposition process or by bond-orientational anisotropy [HIND2011, KIPG2012, CUIB2013, TANG2014, QIAO2016]. Such anisotropy causes the magnetization to be parallel to the film plane.

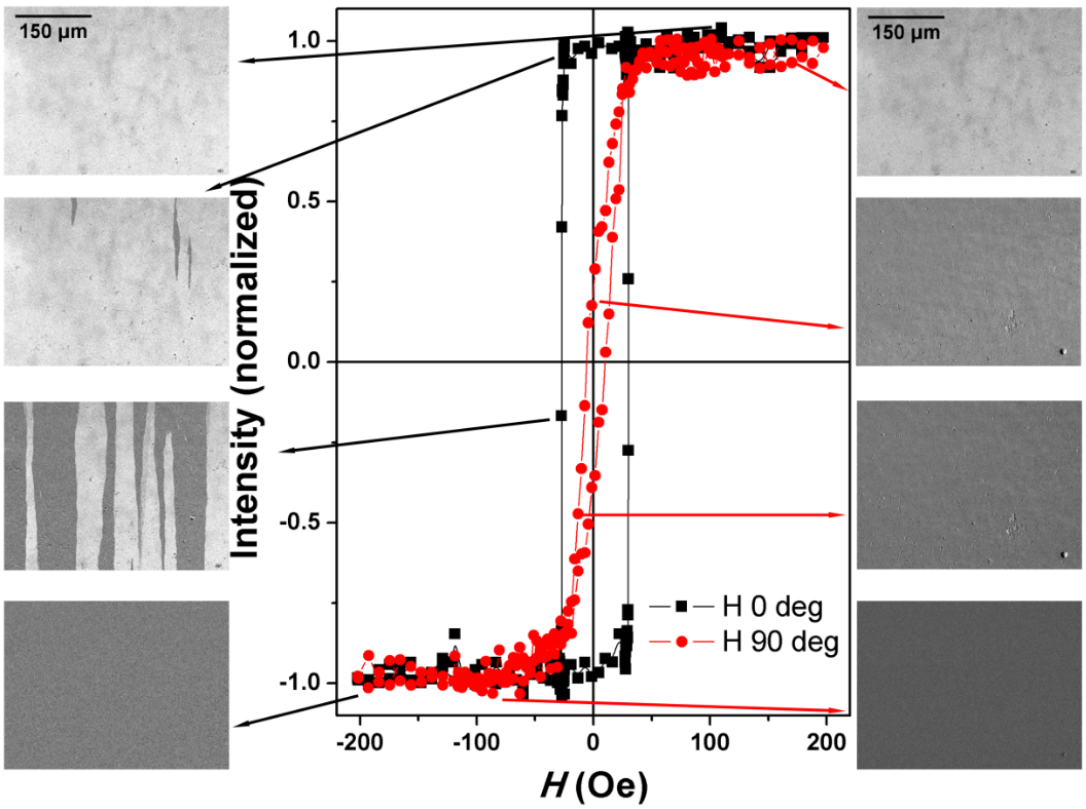

Figure 4.06: Room temperature Kerr loops and magnetic domain images for as-deposited CoFeB442 (20 nm) film measured along the film plane.

Therefore, this arrangement of in-plane orientation of magnetization provides the shape of the *M-H* loops either as rectangular shaped loop when the loop is recorded along the easy-axis or as flat-type loop when the loop is recorded along the hard-axis of magnetization in the plane. These results are in good agreement with those results reported earlier on similar systems [HIND2011, KIPG2012, CUIB2013, TANG2014, QIAO2016].

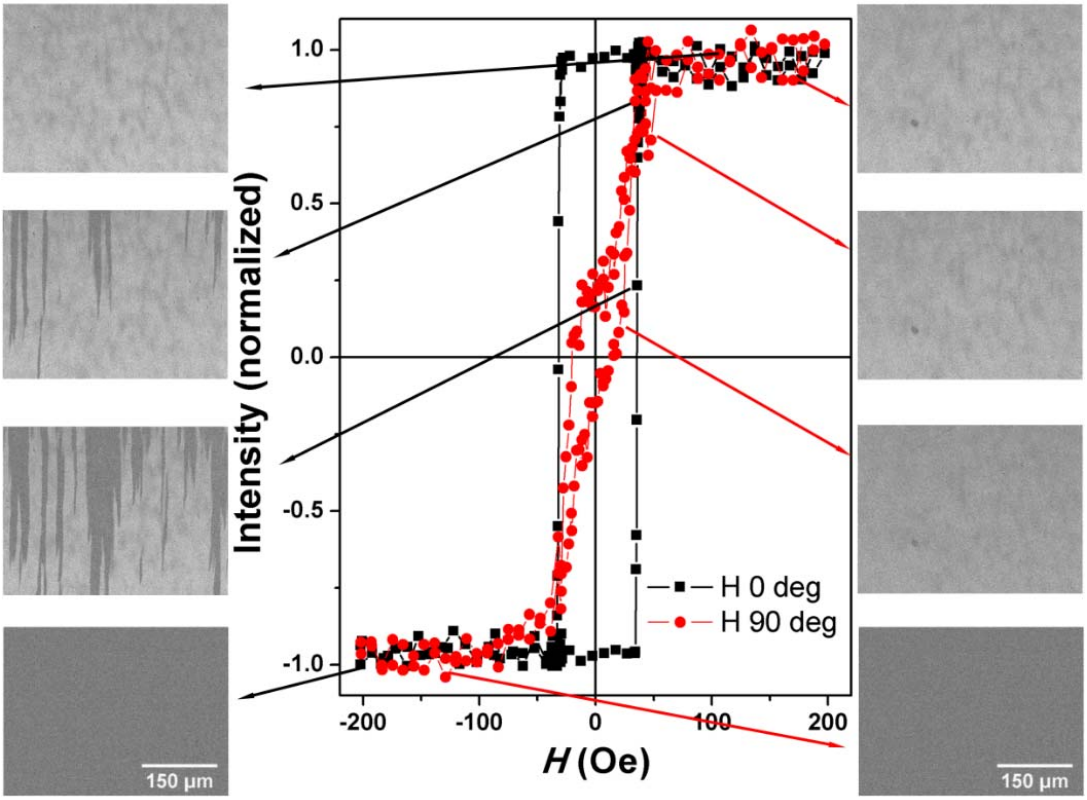

Figure 4.07: Room temperature Kerr loops and magnetic domain images for as-deposited CoFeB262 (20 nm) film measured along the film plane.

In order to further confirm the magnetic nature, the magnetic domain structure of the CoFeB films were studied by observing magnetic domain images and Kerr loops using the MOKE microscopy with the applied field along the film plane [easy (0°) and hard (90°) axes]. Figures 4.06 and 4.07 depict the magnetic domain images and Kerr loops obtained for CoFeB442 and CoFeB262 films along the film planes. It is clearly evident that both CoFeB442 (20 nm) and CoFeB262 (20 nm) films exhibit clear rectangular shaped loops in one direction [easy-axis (0°) direction] and flat-type loops characterized by central range of constant slope combined with low remanence and loop around the origin in another direction [hard-axis (90°) direction]. As a result, the magnetic domain images show a rapid

switching of large-sized domains with the applied field along easy-axis, while the domain images along the hard-axis reveal typical magnetization reversal through coherent rotational process. The average size of the magnetic domains decreases with increasing Fe content in CoFeB films. Nevertheless, the shape of the loops in an easy-axis direction is nearly the same for both the composition except for a slight change in the H_C values.

Table 4.01: The values of H_{Sat}, M_S, K_U, K_{eff}, w, M_R/M_S and θ_1 for CoFeB442 (t nm) and CoFeB262 (t nm) films with different thicknesses.

Composition (CoFeB)	***t*** **(nm)**	H_{Sat} **(Oe)**	M_S **(emu/cc)**	K_U **(10^4 erg/cc)**	K_{eff} **(10^6 erg/cc)**	***w*** **(nm)**	M_R/M_S	θ_1 **(°)**
442	12	77	382	1.471	–	–	0.39	–
442	15	86	392	1.685	–	–	0.41	–
442	20	96	464	2.227	–	–	0.71	–
442	75	1230	537	–	1.647	75.8	0.69	46.4
442	100	1360	546	–	1.743	86.1	0.43	64.5
442	200	1320	564	–	1.732	122.0	0.36	68.9
262	12	88	316	1.390	–	–	0.46	–
262	15	98	364	1.783	–	–	0.56	–
262	20	105	462	2.425	–	–	0.64	–
262	75	1440	475	–	1.174	71.2	0.54	57.3
262	100	1760	490	–	1.348	79.5	0.41	65.8
262	200	1880	510	–	1.420	110.9	0.17	80.2

However, the nature of the flat-type loops along the hard-axis changes significantly with the composition. These results clearly confirm the existence of in-plane magnetization with uniaxial anisotropy in CoFeB films with $t \leq 20$ nm. It may be noted that these films

are deposited at a high deposition rate to form amorphous structure and hence they are expected to have considerable stress quenched in during the deposition of the films in the as-prepared state. However, the magnitude of stress induced effective magnetic anisotropy in these thin CoFeB films is not sufficient to overcome the in- plane magnetic anisotropy. Therefore, the magnetization lies mainly within the plane of the films. Accordingly, the value of uniaxial anisotropy (K_U) is determined using eqn.(4.01)

$$K_U = \frac{M_S H_K}{2} \qquad (4.01)$$

where, H_K is the anisotropy field. The determined values of K_U for both the compositions, listed in Table 4.01, show a continuous increase up to t = 20 nm.

Upon increasing CoFeB film thickness continuously for $t \geq 50$ nm, the stress induced anisotropy overcomes in-plane anisotropy beyond the critical thickness and increases the degree of local disorder in the easy-axis of the as-deposited films. This leads to the formation of two different components of magnetization and giving rise to two distinct magnetization reversal processes for the CoFeB films beyond critical thickness causing higher saturation field (H_{Sat}). As discussed earlier this is correlated to increase in effective magnetic anisotropy caused by the stress induced during the deposition of the films at a higher deposition rate. This leads to the formation of stripe domain patterns in the as-deposited films and the loop shape to form transcritical nature.

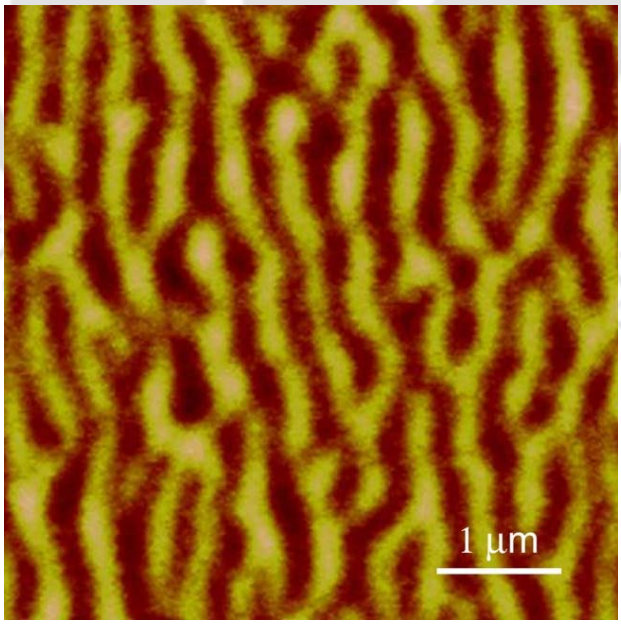

Figure 4.08: Domain image obtained using magnetic force microscopy for CoFeB262 (100 nm) film.

In order to confirm the existence of formation of stripe domain structure, MFM measurement is carried out for 100 nm thick films. Figure 4.08 depicts the MFM domain image for CoFeB262 (100 nm) film. The existence of dense stipe domain is clearly observed in thick CoFeB262 film. The width of the dense stripe domain determined by fast Fourier transformation analysis of the MFM image is found to be about 135 nm, which is in good agreement with the earlier reports on similar systems [CRAU2002, PORR2002, SUNZ2004, COIS2009, HUBE2014].

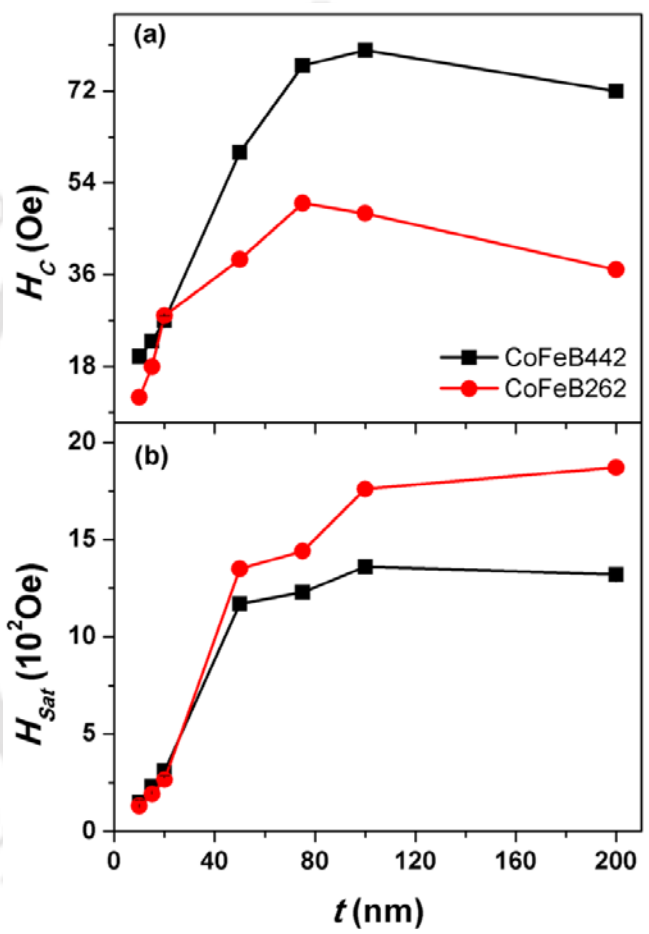

Figure 4.09: Variations of (a) coercivity (H_C) and (b) the field required for saturation (H_{Sat}) for as-deposited CoFeB442 (a) and CoFeB262 (b) films.

To understand the effect of different types of magnetic anisotropy on the resulting magnetic properties, we have extracted the values of H_C and H_{Sat} from the room temperature *M-H* loops and depicted as a function of CoFeB thickness for both the compositions in Figure 4.09. For CoFeB442 films, H_C increases gradually with increasing film thickness from 7 nm to 20 nm and then exhibits a large increase up to 75 nm. On

further increasing thickness, H_C attains saturation at around 100 nm and then decreases slightly for 200 nm thick films. A similar variation of H_C has been observed for CoFeB262 films as well. The low value of H_C for lower film thickness up to 20 nm is attributed to the existence of in-plane magnetization with uniaxial anisotropy, but the incessant increase in H_C with increasing film thickness up to 20 nm may be correlated to the gradual increase in the stress induced by the deposition. When the film thickness reaches a critical thickness, H_C increases largely due to large increase in effective magnetic anisotropy (K_{eff}) causing two magnetic components and forming dense stripe domain. On the other hand, the decrease in H_C at higher thicknesses above 100 nm could be correlated to the redistribution of the accumulated stress in the film without affecting the presence of dense stripe domain.

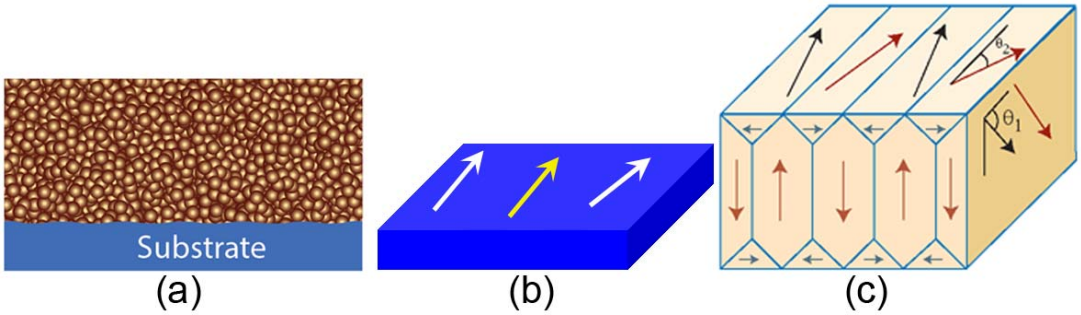

Figure 4.10: Schematic representation of (a) amorphous structure and magnetic structure corresponding to the films (b) with in-plane magnetization and (c) with stripe domains.

The development of dense stripe domain for higher thickness CoFeB films can be explained using the model proposed by Craus et al. [CRAU2002] following the original model developed by Murayama [MURA1966] and Alvarez-Prado et al. [PRAD2004]. According to their models, the bulk domains, forming in amorphous thin films as demonstrated in Figure 4.10, make an angle θ_1 with the surface domains and play a crucial role on the resulting magnetic properties of the thicker films. The angle θ_1 can be determined either from Mossbauer data [CRAU2002] or from the remanent magnetization (M_R) data measured using the VSM under the condition that the magnetization in the closure domains remains perpendicular to the direction of the applied magnetic field. The value of θ_1 can vary between 0 and 90° depending on the value of fractional change in the M_R with respect to M_S [CRAU2003]. By taking into account the continuous development of stress in the as-deposited films, there exists a critical thickness above which the presence of dense stripe domain in the as-deposited films strongly depends on the values of M_S and

K_{eff} of the films. This assumption provides a way to calculate the value of K_{eff} using the following relation

$$t_{critical} = \frac{2\pi}{\left(1 - \frac{\mu_0 M_S H_S}{2K_{eff}}\right)} \sqrt{\frac{A}{K_{eff}}} \qquad (4.02)$$

where $t_{critical}$ is the critical thickness above which the stripe domain appears depending on the values of M_S and K_{eff}, μ_0 is absolute permeability, A is exchange stiffness constant taken as 1.5×10^{-11} J/m [CONC2013] and 0.84×10^{-11} J/m [YAMA2011] for CoFeB442 and CoFeB262 films, respectively. Considering the existence of dense stripe domain in the presently investigated CoFeB films, K_{eff} was determined by substituting the values of H_{Sat}, M_S, A and $t_{critical}$ in eqn.(4.02). Similarly, the optimum domain wall width (w) is calculated by assuming a Landau domain structure [STIL2005, HUBE2014], which is compatible when the sample thickness is larger than $\sqrt{A/K_{eff}}$, as in the present case, using

$$w = 2\sqrt{2t\sqrt{\frac{A}{K_{eff}}}} \qquad (4.03)$$

The determined values of K_{eff}, w and θ_1 along with other extracted parameters such as H_{Sat}, M_S and squareness (M_R/M_S) are listed in Table 4.01 for both the compositions. Thickness dependence of magnetic parameters is clearly evident from Table 4.01 and the obtained values are in quite good agreement with the reported results for similar soft magnetic thin films [COIS2009]. The values of K_{eff} determined from the eqn.(4.02) are found to be of the order of 10^6 erg/cc, but increase slightly with increasing the thickness from 75 to 100 nm and then exhibit weak dependence on further increasing the film thickness to 200 nm. In general, the magnetic anisotropy in these films arises from magnetocrystalline anisotropy, shape anisotropy, and magnetoelastic anisotropy [WANG1999].

As reported in Figures 4.01 and 4.02, the as-deposited films are completely amorphous in nature. Hence, the contribution from magnetocrystalline anisotropy is not expected in these films. Considering thick amorphous CoFeB films, the magnetic anisotropy is expected to be majorly due to magnetoelastic effects caused by the stress induced during the deposition of the films. While the obtained value of K_{eff} in the presently investigated films is somewhat higher than the value reported in similar system [YUJU2002], a strong perpendicular magnetic anisotropy of 0.5×10^7 erg/cc to 2×10^7 erg/cc has been reported for ultrathin CoFeB films in a stack structure [MANT2013, TSAI2014,

ZHUT2015]. The first one could primarily be related to the stress induced in higher thickness films [PLAT2001] and the latter one is mainly originating from the interfaces between CoFeB and other stacking films, which was further supported through micromagnetic modelling [WANG2014].

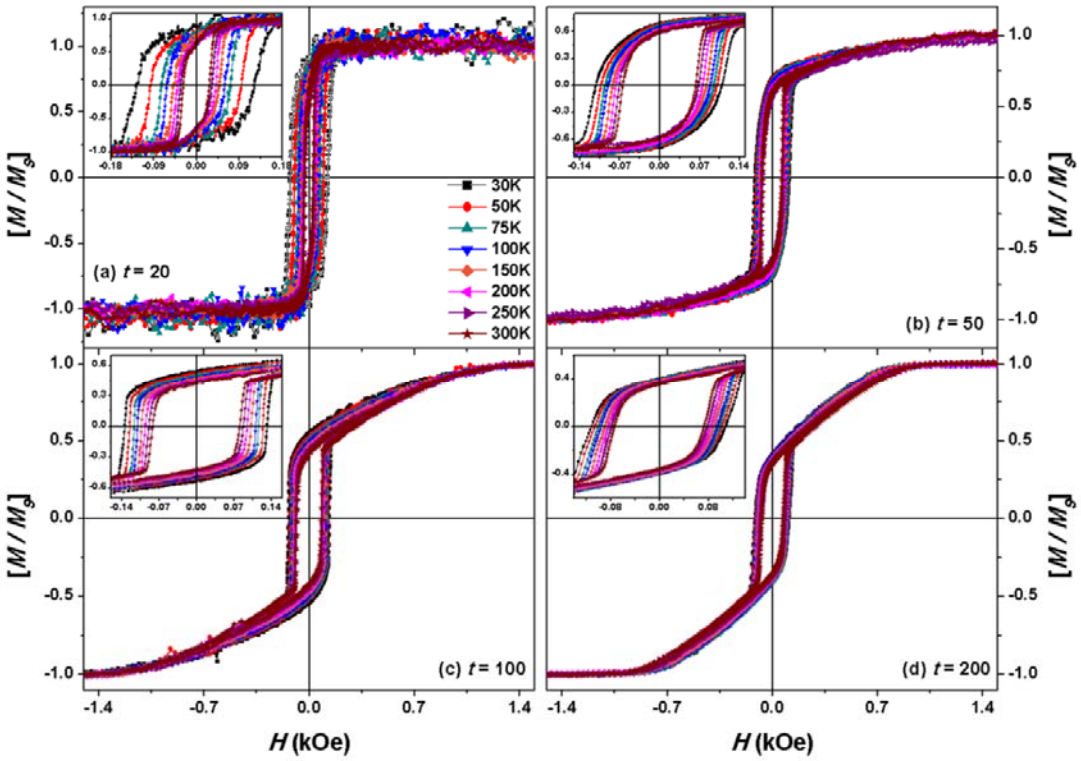

Figure 4.11: *M-H* loops measured at different temperatures (30–300 K) for CoFeB442 (*t* nm) films with four different thicknesses.

4.3.2.2. Temperature dependent magnetic properties

In order to understand the thickness and composition dependent magnetic nature of CoFeB films in more details, *M-H* loops were measured at different temperatures in the temperature range between 30 K and 300 K using VSM for selected films (20, 50, 100 and 200 nm). Figures 4.11 and 4.12 illustrate the temperature dependent *M-H* loops measured along the film plane for CoFeB (*t*) films. The expanded views of the *M-H* loops close to origin are depicted in insets. It is clear from the figures that the nature of the loops does not change significantly with the temperature for a particular film. However, the values of H_C and H_{Sat} increase with decreasing temperature. This is a typical temperature dependent magnetic behavior of a ferromagnetic material. In contrast, the values of H_{Sat} decrease significantly for the CoFeB262 (200 nm) film with decreasing temperature.

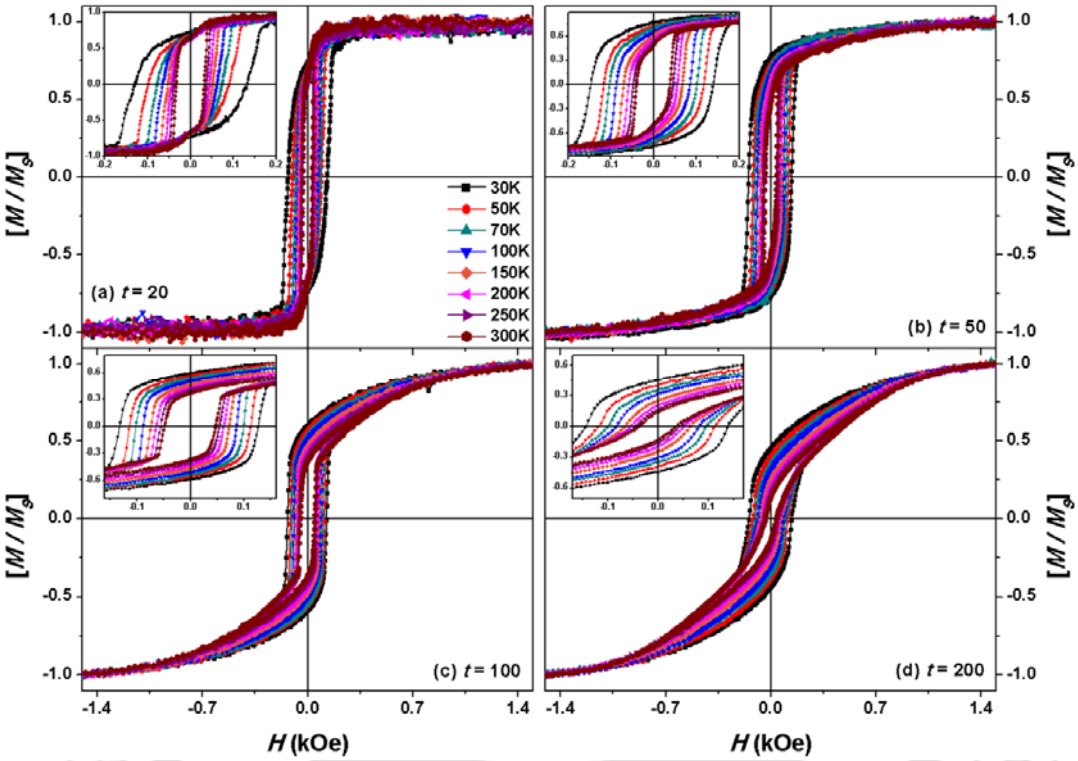

Figure 4.12: *M-H* loops measured at different temperatures (30–300 K) for CoFeB262 (*t* nm) films with four different thicknesses.

In order to quantify the variations in magnetic parameters with temperature, the values of H_C, H_{Sat} and M_S are extracted from the *M-H* loops measured at different temperatures and shown in Figure 4.13. H_C versus T exhibits two distinct regions of variation with temperature for lower thickness films (~20 nm), i.e., H_C increases at a slower rate of 137 (129) mOe/K down to 150 K followed by a larger rate of 1149 (1394) mOe/K at temperature below 100 K for CoFeB442 (CoFeB262) films, respectively. This, in total, provides a maximum relative change of H_C between 300 K and 30 K as 4.61 (3.98) for CoFeB442 (CoFeB262) films, respectively. Such behaviors can be attributed to the development of additional interfacial stress by the substrate on the lower thickness films with decreasing temperature.

With increasing CoFeB thickness, the maximum relative change in H_C decreases from 4.61 to 1.49 and from 3.98 to 2.72 for CoFeB442 and CoFeB262 films respectively. This indicates that the CoFeB442 films exhibit a large reduction in the maximum relative change in H_C with temperature as compared to CoFeB262 films. While the values of H_{Sat} increase with decreasing temperature for all the films as expected for typical ferromagnetic materials, H_{Sat} for CoFeB262 (200 nm) film decreases slightly with decreasing

temperature. This unusual behavior may be attributed to the change in the magnetic domain structure with decreasing temperature caused by the change in K_{eff} with temperature.

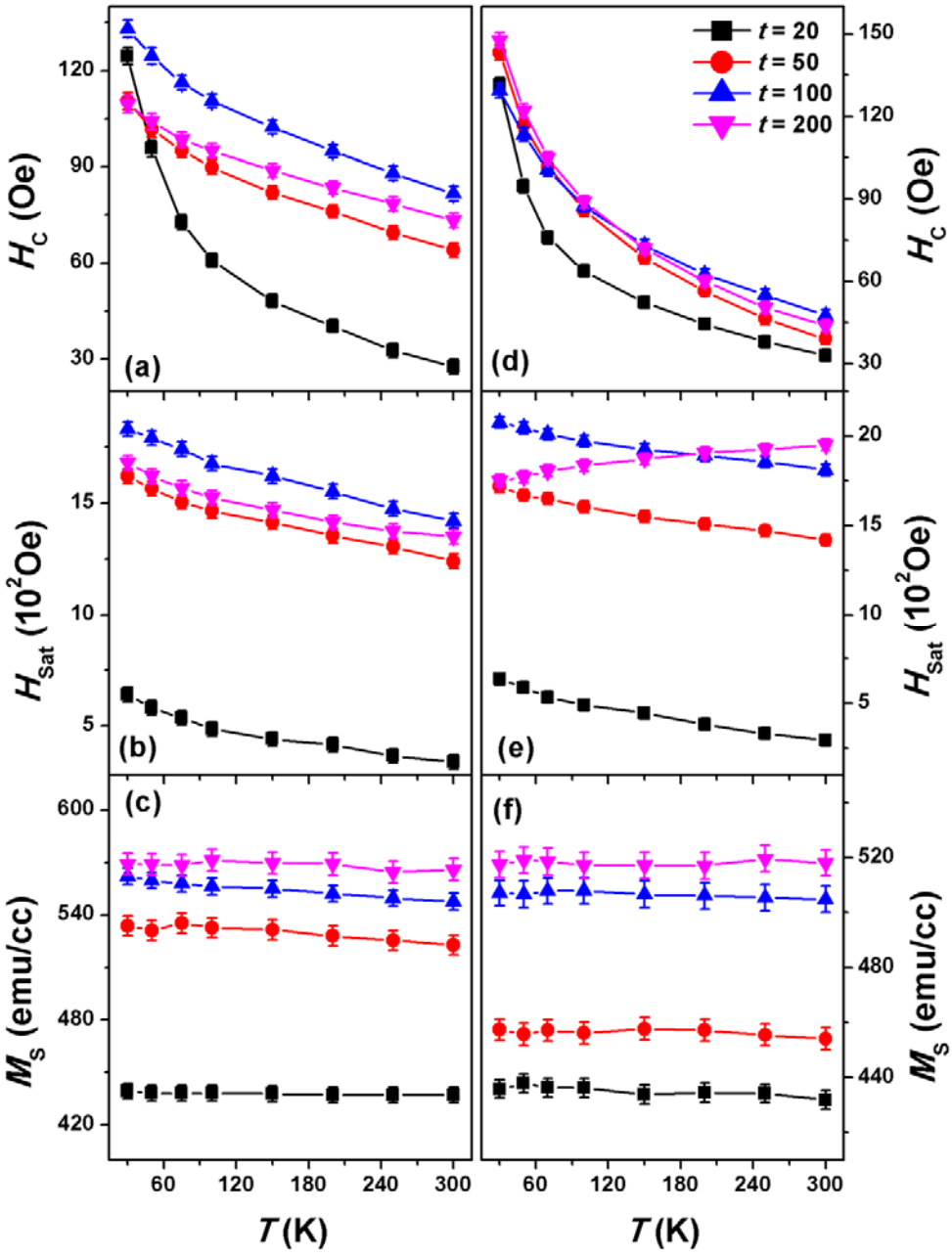

Figure 4.13: Temperature dependent variations of H_C, H_{Sat} and M_S for CoFeB442 (t nm) films [(a), (b) and (c)] and CoFeB262 (t nm) films [(d), (e) and (f)].

On the other hand, it is clear from Figures 4.13(c) and (f) that the values of M_S change weakly with temperature for all the films in both the compositions. This is possibly due to the high thermal stability of CoFeB films with temperature and high Curie

temperature (T_C) of the CoFeB films [YAMA2011]. Nagasaka et al. [NAGA2000] have reported similar behavior of M_S with temperature for CoFeB film and extracted Curie temperature for CoFeB film was reported as 1040 °C. To study the temperature dependence of K_{eff} in higher thickness CoFeB films, the calculation of K_{eff} was extended as a function of temperature using the eqn.(4.02) and by substituting the parameters obtained from temperature dependent *M-H* loops.

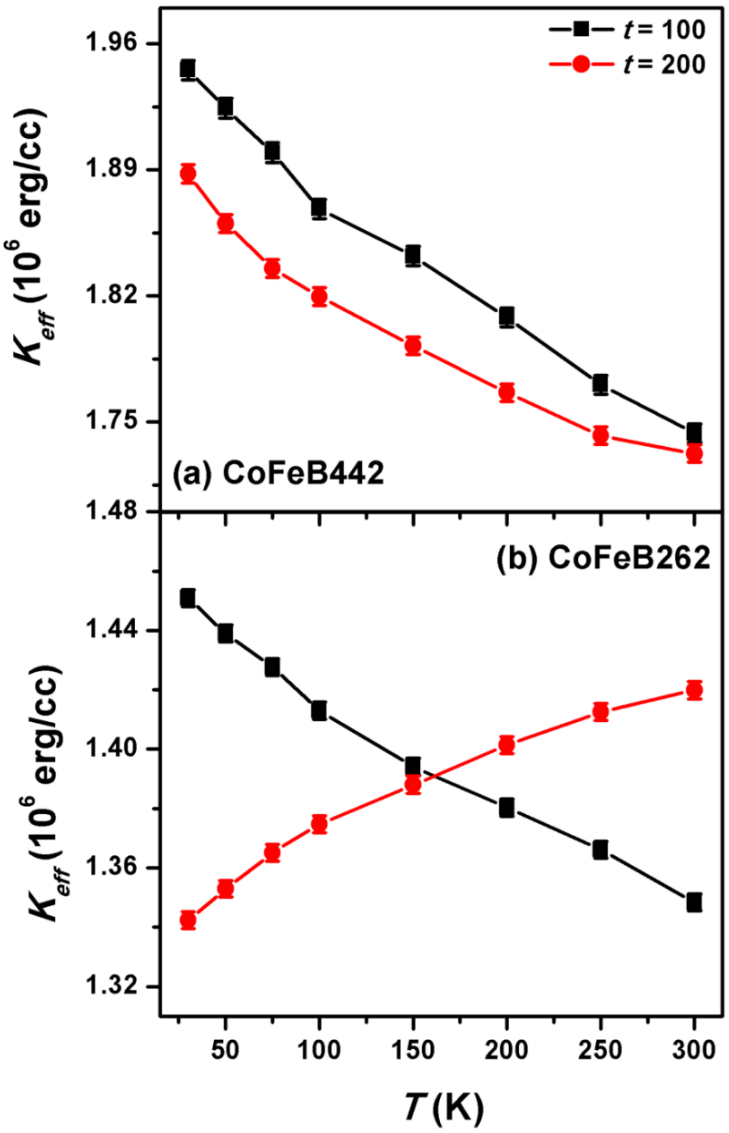

Figure 4.14: Temperature dependent effective magnetic anisotropy (K_{eff}) for 100 nm and 200 nm thick (a) CoFeB442 and (b) CoFeB262 films.

Figure 4.14 depicts the variations of K_{eff} as a function of temperature for 100 and 200 nm thick CoFeB442 and CoFeB262 films. It is revealed that even though the room

temperature values of K_{eff} are similar for 100 and 200 nm thick CoFeB442 films, their temperature dependence depends significantly on the thickness of the films. However, for the CoFeB262 films, the temperature dependent K_{eff} exhibits increasing and decreasing nature with decreasing temperature for 100 and 200 nm thick films, respectively. This is mainly due to the strong temperature dependent variation in the values of H_{Sat} with thickness (see Figure 4.13), resulting from the large variation in the angle between the bulk and surface domains with decreasing temperature. The temperature dependent analysis of magnetic domain structure would provide more insights for such unusual variation of K_{eff} in composition dependent CoFeB films.

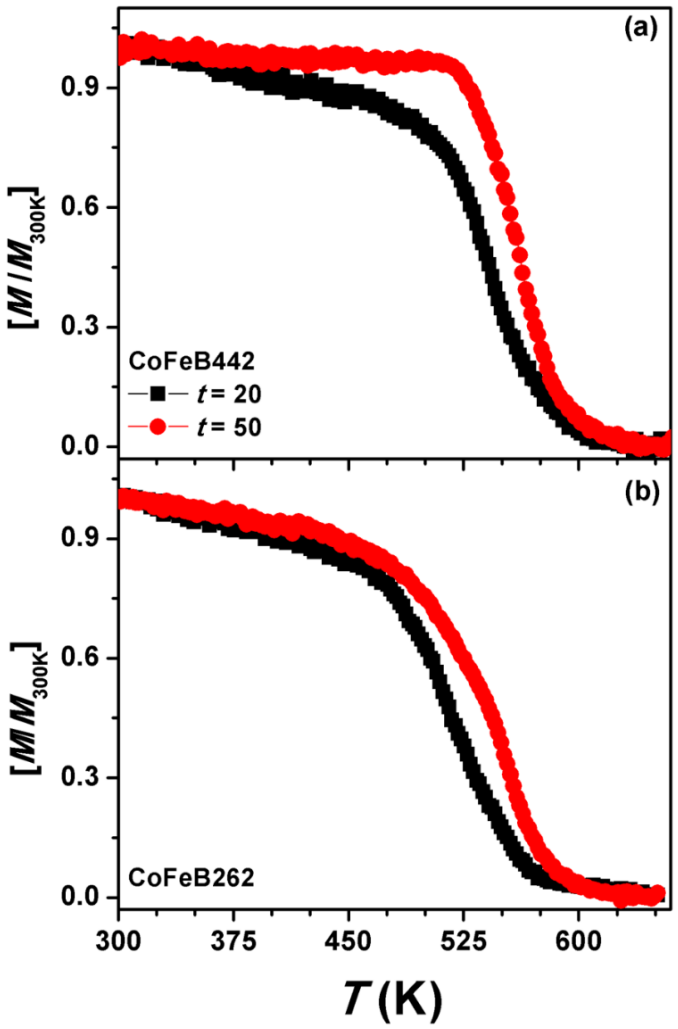

Figure 4.15: High temperature *M-T* data recorded under the applied field of 500 Oe for 20 nm and 50 nm thick (a) CoFeB442 and (b) CoFeB262 films.

To study the magnetic properties of the films up to Curie temperature, high temperature *M-T* data were measured at a constant applied field of 500 Oe for all the films using VSM magnetometer. Figure 4.15 illustrates *M-T* data above room temperature for 20 nm and 50 nm thick (a) CoFeB442 and (b) CoFeB262 films. In order to compare all the magnetization data in a single graph, *M-T* data are normalized with respect to the room temperature magnetization data of that particular sample. It could be clearly seen from the Figure 4.15 that (i) CoFeB442 (20 nm) film shows an incessant decrease in magnetization up to 590 K. The rate of decrease of magnetization decreases with further increase in temperature. (ii) A similar behavior is observed for CoFeB262 (20 nm) film but in this case the film shows faster decrease in magnetization up to 575 K. (iii) With increasing t to 50 nm, the temperature at which the magnetization starts decreasing shifts slightly towards high temperature. The above results clearly indicate that with increasing temperature above room temperature, CoFeB films exhibit a clear magnetic phase transition from ferromagnetic state to paramagnetic state. The values of T_C were obtained from the thermal derivative of the magnetization data and found to be 539 K and 562 K for CoFeB442 (t nm) films and 517 K and 553 K for CoFeB262 (t nm) films with t = 20 and 50 nm, respectively. The obtained values of T_C are found to be significantly lower than those reported in literature for similar alloys [YAMA2011, PELL2015]. For instance, Yamanouchi et al. [YAMA2011] have reported T_C value of 728 K and 1026 K for as-deposited and annealed $Co_{20}Fe_{60}B_{20}$ films, respectively. However, they determine T_C by extrapolating the temperature dependent domain wall surface energy. Pellegren et al. [PELL2015] have shown that T_C of CoFeB films can be decreased progressively by alloying CoFeB with Ta and Hf. The reported results were in good agreement with bulk materials as well [LUCA2011]. These results suggest that the low value of T_C in the presently investigated films could be correlated to the complete amorphous form of the films [LIUY2008, SAKU2013].

4.4. Summary

A systematic study of effects of composition, thickness and temperature on the structural and magnetic properties of amorphous CoFeB442 (t nm) and CoFeB262 (t nm) films, over a wide range of thicknesses, prepared directly on thermally oxidized Si substrates at ambient temperature using DC magnetron sputtering technique, has been carried out. The salient features of CoFeB films from the current investigations are as follows:

- Amorphous CoFeB442 (t) and CoFeB262 (t) films with different thicknesses (t = 7 – 200 nm) could be prepared directly on thermally oxidized Si substrate at ambient temperature using DC magnetron sputtering technique.
- Amorphous nature of all as-deposited films is confirmed through XRD and TEM studies.
- The average surface roughness obtained from the XRR studies increases significantly from 0.22 nm to 0.7 nm with increasing film thickness from 10 to 100 nm, respectively. The results of thickness determination from XRR analysis, analytical relation and surface profilometer are in close agreement with each other.
- CoFeB ($t \leq 20$) films exhibit soft magnetic nature with rectangular shaped or flat-type loops due to in-plane magnetization with uniaxial anisotropy.
- With increasing the film thickness above 50 nm, the soft magnetic properties are degraded due to the transition of in-plane magnetization to dense stripe domain due to enhancement of effective magnetic anisotropy caused by the stress quenched in during deposition at a faster deposition rate to form amorphous structure. However, the magnitude of coercivity and field required for saturation of CoFeB films strongly depends on the composition.
- The temperature dependent magnetic properties reveal that the maximum relative change in coercivity decreases from 4.61 to 1.49 and from 3.98 to 2.72 for CoFeB442 and CoFeB262 films, respectively with increasing film thickness.
- The effective magnetic anisotropy constant determined at different temperatures shows a compositional dependent properties mainly due to the change in saturation field values with film thickness and composition.
- The observed results are explained based on the development of compositional and thickness dependent effective magnetic anisotropy and change in the magnetic domain structure with increasing CoFeB film thickness.

Chapter 5

Magnetic interactions in trilayer structured CoFeB films with different domain structures: Effect of spacer layer

भारतीय प्रौद्योगिकी संस्थान गुवाहाटी
Indian Institute of Technology Guwahati

5.1. Introduction

The study of magnetism, magnetic interaction and the mechanism of interlayer exchange coupling between ferromagnetic (FM) thin films separated by non-magnetic (NM) and/or antiferromagnetic (AFM) interlayers has received considerable attention among the scientists from both theoretical and experimental points of view [RENY2009, DECH2012, ZHAN2015]. In particular, the interlayer interaction between FM layers in such artificially structured films seems to be critical for controlling the magnetic properties of the multilayer films. Among various magnetic thin films [CHEN20132, VAZQ2015, ZHUK2017], CoFeB based thin films are found to be one of the promising materials suitable for various applications in modern magneto-electronic devices due to their tunable magnetic properties [FELS2013, DIEN2016, TSYM2016]. The detailed investigation of CoFeB based thin films in Chapter 4 suggests that the magnetic properties of the films are strongly dependent on film thickness, i.e., with increasing CoFeB film thickness, the in-plane magnetization with uniaxial magnetic anisotropy observed for CoFeB films up to 20 nm transformed into dense stripe domain with increasing thickness above 50 nm. Therefore, thicker CoFeB films become magnetically hard and display transcritical loop. Nevertheless, thicker CoFeB based films exhibiting high resistivity, high permeability, high saturation magnetization and appropriate anisotropy field were explored for the applications in magnetic flux amplifiers, magnetic recording heads, soft magnetic underlayers in perpendicular magnetic recording media, flexible electronics, *etc* [ITOS2005, MUNA2005, PIRA2007, KAZI2013, YANG2013, TANG2014, QIAO2016]. However, only a few reports are available in the literature related to tuning of the magnetic properties of thick CoFeB films [ITOS2005, GUPT2013, TANG2014] despite their vast applicability.

In order to control the development of effective magnetic anisotropy at higher film thicknesses and to improve the magnetic properties of films with simple domain structure and tunable anisotropy (K_{eff}), low coercivity (H_C) and low saturation field (H_{sat}), various types of magnetic multilayer thin films with NM, AFM or semiconducting interlayers have been proposed. For instance, Huang et al. [HUAN2001] and Mishra et al. [MISH2011] reported that the magnetic properties of FM layers beyond critical thickness are enhanced by fabricating multilayer films with more number of layers and with different interlayer thicknesses. However, when the number of layers is increased, (i) the number of interfaces increases, (ii) the interlayer coupling between the FM layers becomes complex due to increased number of interfaces and (iii) the roughness associated with the number of interfaces increases and consequently the average magnetization of the films decreases. On

the other hand, Ren et al. [RENY2009] investigated the magnetic anisotropy and spin wave relaxation in FM/AFM/FM trilayer [CoFe (1-50 nm)/PtMn (12 nm)/CoFe (1-50 nm)] films. This type of structure produced lower H_C as compared to AFM/FM bilayers due to magnetic charge compensation at the magnetic film edges. In addition, the trilayer films exhibited higher effective magnetization and excellent soft magnetic properties [PETT2006]. Gong et al. [GONG2009] reported magnetic anisotropy, interlayer coupling and spin wave relaxation in CoFeB (5 nm)/ Cr (0.4-4 nm) /CoFeB (5 nm) symmetric trilayer films using ferromagnetic resonance technique and showed that effective interlayer coupling and out-of-plane anisotropy display oscillatory behavior, while the uniaxial in-plane anisotropy increased monotonically with increasing spacer layer thickness. However, there are no systematic studies available on magnetic interactions between (i) FM layers as a function of interlayer thickness, (ii) different FM layer thicknesses with different domain structures. The latter one, especially as a function of temperature, is expected to introduce different types of magnetic interactions and temperature dependent interface roughness induced interlayer coupling.

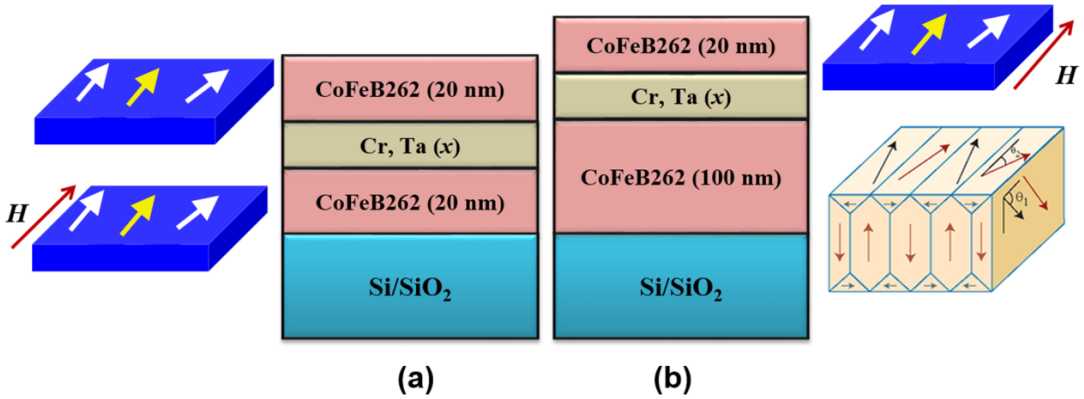

Figure 5.01: Schematic representation of trilayer [CoFeB262 (y nm) /Cr (x nm) /CoFeB262 (20 nm)] films with (a) y = 20 (symmetric) and (b) y = 100 (asymmetric) along with the magnetic domain structures.

Therefore, in this study, we have chosen two single-layer films of $Co_{20}Fe_{60}B_{20}$ (CoFeB262) with different thicknesses of 20 and 100 nm, exhibiting different magnetic domain structures respectively, and constructed trilayer Substrate/CoFeB262 (y nm)/[Cr, Ta (x nm)]/CoFeB262 (20 nm) films with y = 20 and 100 and x = 0 – 6. This is done mainly (i) to study the effect of spacer layer materials and its thickness on the magnetic interactions between two CoFeB262 layers having same domain structure (symmetric) and different

domain structure (asymmetric), as shown schematically in Figure 5.01, (ii) to understand the effect of temperature on the magnetic interactions between CoFeB262 layers in symmetric and asymmetric films, and also (iii) to explore the possibility of tuning the magnetic properties of thick CoFeB262 (100 nm) film using simple trilayer film structure.

5.2. Experimental details

Amorphous CoFeB262 single-layer films with different thicknesses (y = 20 and 100 nm) and trilayer films of substrate/CoFeB262 (y nm)/[Cr, Ta (x nm)]/CoFeB262 (20 nm) (where y = 20, 100 and x = 0 – 6) were prepared by DC magnetron sputtering technique. All the films were deposited directly on thermally oxidized Si substrates at ambient temperature. The base pressure of the chamber was better than 1×10^{-4} Pa. The working (Ar) gas pressure for the deposition of CoFeB262, Cr and Ta was fixed at 10 mTorr. Optimization of Ar gas pressure was done by analyzing the variations in structure, composition and magnetic properties of the single-layer and trilayer thin films. The deposition rate of the films was pre-calibrated *ex-situ* using a surface profilometer (Vecco, Dektak-150 model). The total thickness of each film in single-layer and trilayer films was controlled by monitoring the deposition time during the film deposition.

Amorphous nature of all as-deposited films was confirmed by X-ray diffraction (XRD) patterns obtained using a high-power X-ray diffractometer (Rigaku TTRAX III, 18 kW) with Cu-K_α radiation (λ = 1.541 Å) and transmission electron microscopy (TEM, JEOL 2100 and Technai G^2 F20). Magnetic properties of the films were measured using a vibrating sample magnetometer (VSM, LakeShore Model 7410) by performing magnetic hysteresis loops (M-H) between 30 K and 300 K. Magnetic domain images and Kerr loops were obtained using a magneto-optic Kerr effect (MOKE) microscope (Evico Magnetics Ltd, Germany). Imaging was performed using linearly polarized light with white LED source. Magnetic domain images were observed in both branches of hysteresis cycle in longitudinal MOKE mode. Both hysteresis loops and domain images were simultaneously recorded for magnetic fields applied along in-plane directions [easy (0°) and hard (90°) axes]. Simultaneous atomic force microscopy and magnetic force microscopy (MFM, Bruker Dimension Icon) studies were performed to study the topographic features and local magnetic domains. MFM was performed in dual-pass lifting mode with commercially available CoCr-coated tips, which were magnetized along the tip axis and therefore sensitive

to stray field gradients from out-of-plane oriented domains or the out-of-plane components of domains oblique to the surface. The domain images were acquired at the zero-field state.

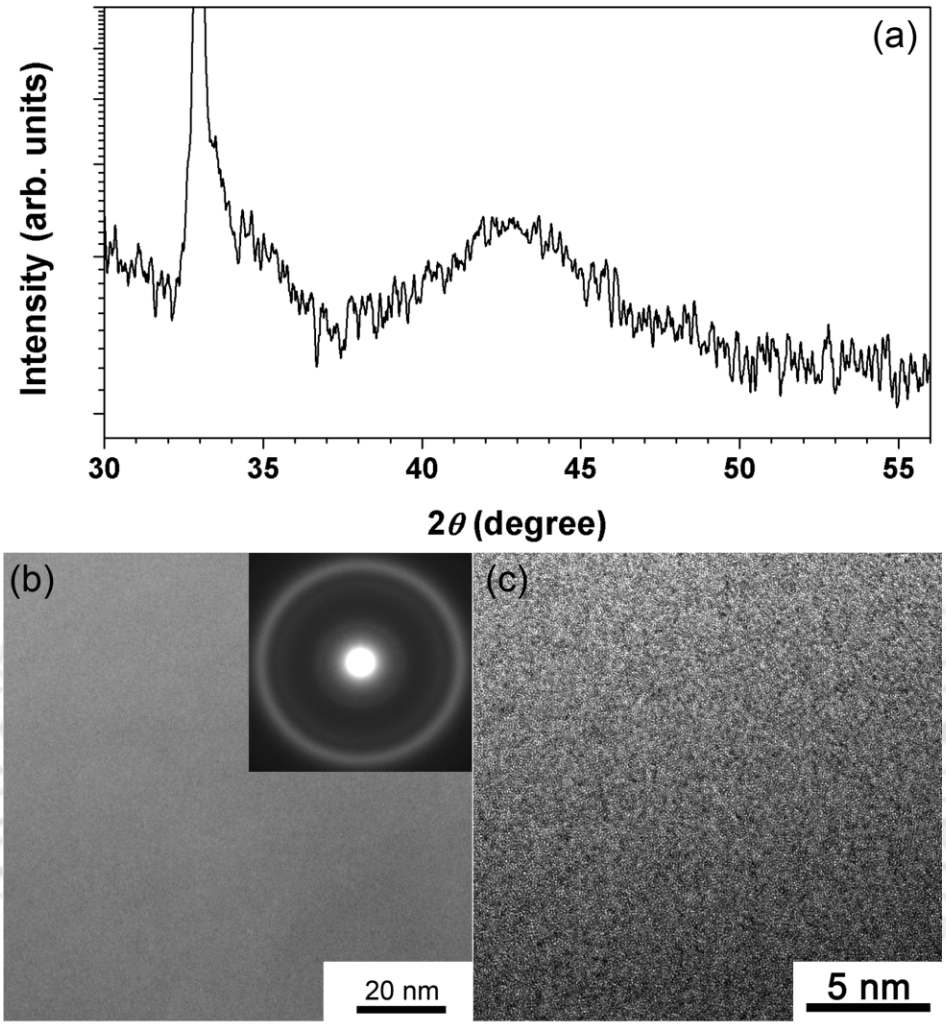

Figure 5.02: Room temperature (a) XRD pattern, (b) bright-field TEM image, selected area electron diffraction pattern and (c) high-resolution TEM image for as-deposited CoFeB262 (100 nm) film.

5.3. Results and Discussion

5.3.1. Structural properties

Figure 5.02 displays typical XRD pattern, bright-field TEM image, selected area electron diffraction (SAED) pattern and high-resolution TEM (HRTEM) image of as-deposited single-layer CoFeB262 (100 nm) film. It can be clearly seen that as-deposited film exhibits only a broad peak at around $2\theta = 44°$ without any other sharp peaks corresponding to any other crystalline phase. It may be noted that the XRD peak observed at $2\theta = 33.05°$

represents Si(200) peak emanating from the Si substrate [CHOM2001]. The bright-field TEM image, SAED pattern and HRTEM image reveal the plain and even contrast microstructure, devoid of any local lattice fringes or diffraction halos, respectively. These results confirm that as-deposited CoFeB262 films exhibit amorphous structure.

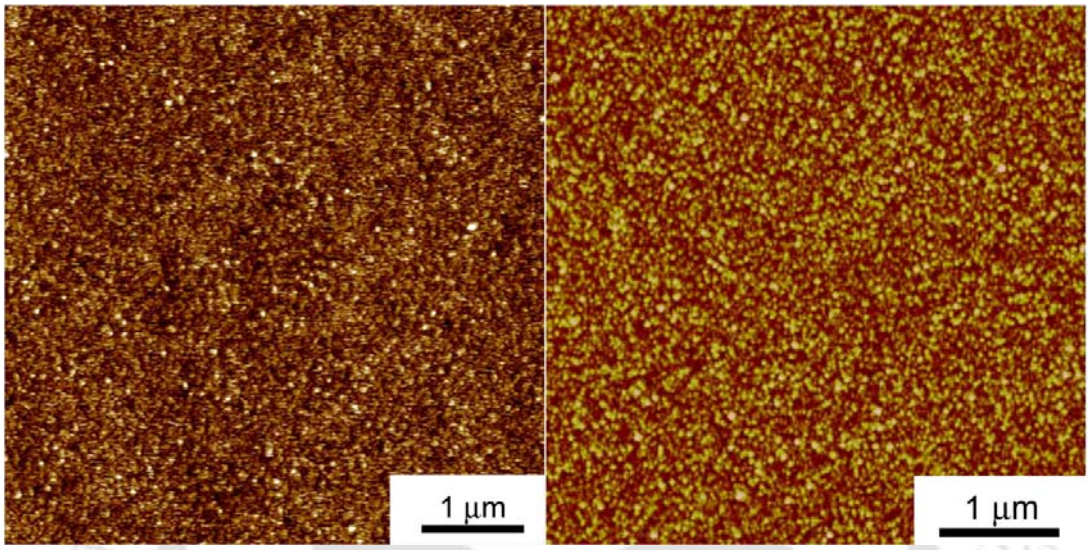

Figure 5.03: Atomic force microscopy images of single-layer CoFeB262 (*y* nm) films with (a) *y* = 20 and (b) *y* = 100.

To study the surface roughness of the single-layer CoFeB262 films, the surface topography is obtained for the CoFeB262 films deposited directly on the substrate using atomic force microscopy and displayed in Figure 5.03 for CoFeB262 (*y* nm) films with *y* = 20 and 100 nm. The topography images show the existence of very fine and sparsely dispersed nanosized grains of size ranging between 10 and 15 nm in the as-deposited films. In addition, the films exhibit a very clear uniform surface and the average roughness of the surface is found to be in the range of 0.3-0.6 nm and 0.4-0.7 nm for CoFeB262 films with *y* = 20 and 100, respectively. This shows that the average surface roughness of the CoFeB262 films increases marginally when *y* is increased from 20 to 100 nm.

5.3.2. Magnetic properties

5.3.2.1. Room temperature magnetic properties

In order to understand the magnetic properties and magnetic domain structure of single-layer CoFeB262 films, Kerr loops, *M-H* loops and magnetic domain images were obtained as depicted in Figure 5.04. It is clearly evident that CoFeB262 (20 nm) film exhibits a

rectangular hysteresis loop in one direction (easy-axis direction) and flat type loop characterized by central range of constant slope combined with low remanence in another direction (hard-axis direction) [Figure 5.04(a)]. In the easy-axis direction, the domain image illustrates a rapid switching of large sized domains due to domain wall motion [Figure 5.04(b)]. This indicates the existence of in-plane uniaxial magnetic anisotropy in CoFeB262 (20 nm) film with the magnetization oriented along the film plane. This observation is in close agreement with the earlier reports on similar systems [HIND2011, KIPG2012, CUIB2013, TANG2014, QIAO2016].

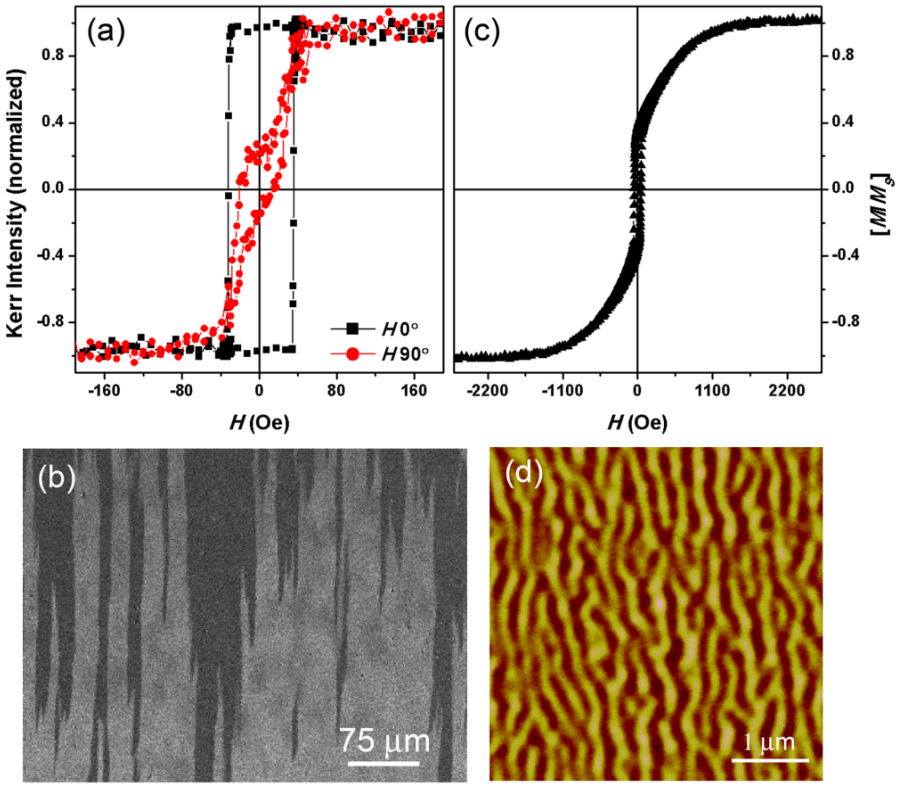

Figure 5.04: (a) Kerr loops measured along film plane at different applied field directions [easy (0°) and hard (90°) axes] and (b) magnetic domain image around H_C for CoFeB262 (20 nm) film, and (c) *M-H* loop measured along film plane and (d) MFM domain image for CoFeB262 (100 nm) film.

On the other hand, *M-H* loop of CoFeB262 (100 nm) film shows two distinct magnetization reversal processes, viz., (a) in-plane magnetic components, which reverse quickly at fields close to H_C, and (b) perpendicular components, which rotate progressively under the application of magnetic field [Figure 5.04(c)]. The latter gives rise to a nearly linear variation of magnetization before saturation and also require a large saturation field (H_{Sat})

of more than 1.5 kOe to saturate the film's magnetization. Such loop types with low remanence ratio ($M_R/M_S \sim 0.38$, where M_R is remnant magnetization and M_S is saturation magnetization) are called as transcritical loop [MURA1966, PRAD2004, ITOS2005, SHAR2006, TANG2014, GAYE2017], which in general is related to an increase in effective magnetic anisotropy caused by the stress induced during the deposition of the films.

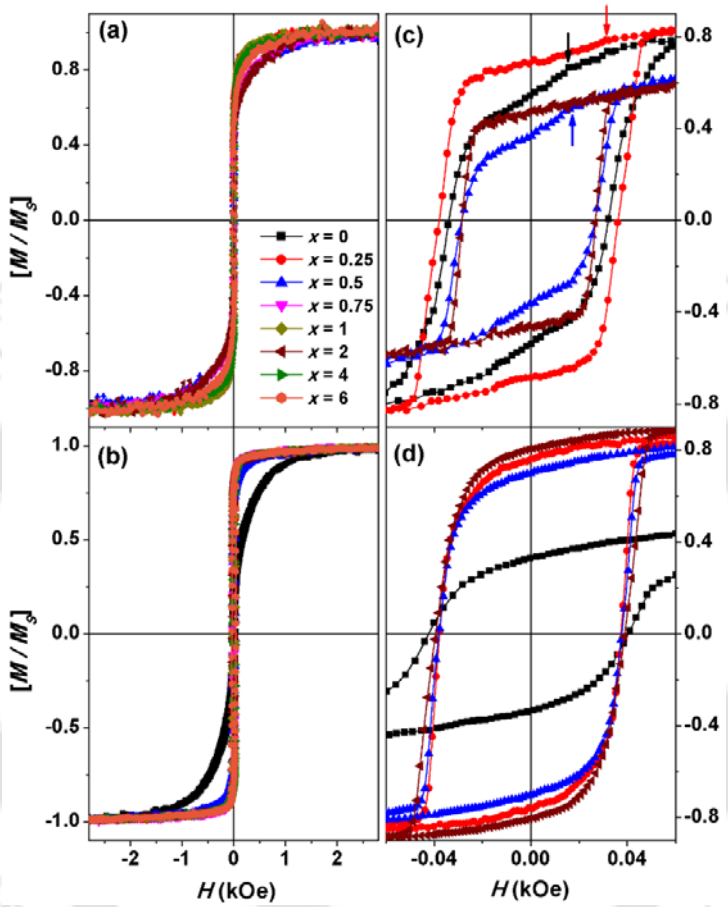

Figure 5.05: Room temperature *M-H* loops for Cr spacer layer measured along the film plane for (a) symmetric and (b) asymmetric trilayer films with different spacer layer thicknesses. The expanded view of the loops close to origin for selected *x* values is shown in (c) and (d) for symmetric and asymmetric films, respectively.

In order to form amorphous structure, the films were deposited at a slightly higher deposition rate and hence the stress accumulation in the samples during preparation increases progressively with increasing thickness. Therefore, the stress induced effective magnetic anisotropy dominates over in-plane magnetic anisotropy observed in low thickness films [ITOS2005, SHAR2006, COIS2009, TANG2014, GAYE2017] and increases the degree of local disorder in the easy-axis. This leads to the formation of

magnetic dense stripe domain in thick as-deposited films as shown in Figure 5.04(d). The width of the dense stripe domain determined by fast Fourier transform analysis of the MFM image is found to be about 135 nm, which is good agreement with the earlier reports on similar systems [CRAU2002, SUNZ2004, COIS2009, HUBE2014].

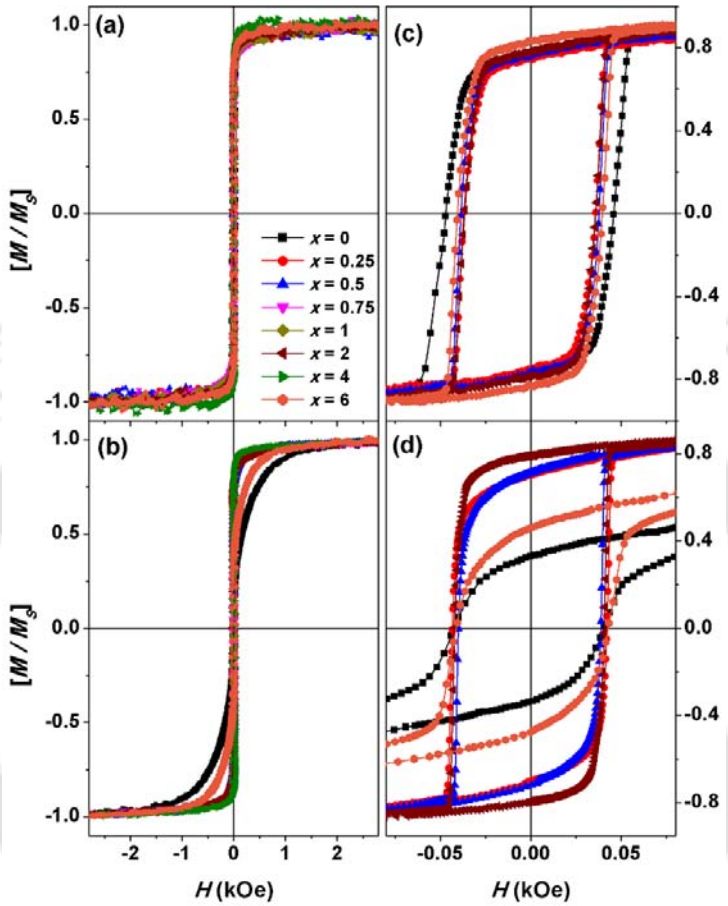

Figure 5.06: Room temperature *M-H* loops for Ta spacer layer measured along the film plane for (a) symmetric and (b) asymmetric trilayer films with different spacer layer thicknesses. The expanded view of the loops close to origin for selected *x* values is shown in (c) and (d) for symmetric and asymmetric films, respectively.

To study the effect of layer thickness on the room temperature magnetic properties of the trilayer films, *M-H* loops are measured along the film plane and presented in Figures 5.05 and 5.06 for Cr and Ta spacer layers, respectively. The loops reveal the following features for symmetric trilayer films: (i) All the films exhibit single magnetization reversal at H_C. (ii) The trilayer film with $x = 0$ shows a kink in the first quadrant [marked by arrow in Figure 5.05(c)] of the *M-H* loop along with reduced remanence ratio (M_R/M_S) (~ 0.54).

This behavior is certainly different from the single-layer film of CoFeB262 (20 nm), which showed rectangular loop as shown in Figure 5.04(a). (iii) The inclusion of 0.25 nm thick Cr interlayer shifts the kink to higher applied field and enhances M_R/M_S to 0.7. (iv) Upon increasing x_{Cr} to 0.5 nm, the kink shifts back to lower applied field and the M_R/M_S reduces sharply to 0.36. (v) On further increasing x_{Cr}, the kink disappears for films with $x_{Cr} > 1$, but M_R/M_S exhibits an oscillatory behavior. (vi) H_{sat} also shows an oscillatory nature with increasing x_{Cr}. (vii) The introduction of Ta spacer layer in symmetric trilayer films does not show any noticeable kink behavior [Figures 5.06(a) and 5.06(c)], but exhibits almost rectangular loops with high remanence ratio and single magnetization reversal at H_C for all values of x_{Ta}. On the other hand, the asymmetric trilayer films exhibit the following features: (i) The film without any spacer layer displays the transcritical loop with reduced M_R/M_S (~ 0.37) and a linear variation of magnetization before saturation. Hence, a higher H_{sat} (~ 1.5 kOe) is required for saturation. (ii) The introduction of even a small Cr interlayer (x_{Cr} = 0.25) changes the loop shape from transcritical into rectangular shape with enhanced M_R/M_S (~0.79) [Figures 5.05(b) and 5.05(d)]. As a result, H_{sat} reduces immensely. (iii) For films with $x_{Cr} > 0.25$, the loop shape does not change remarkably but the values of M_R/M_S, H_C and H_{sat} vary marginally. (iv) Almost similar behaviors are observed for asymmetric trilayer films with Ta spacer layer, i.e., the introduction of even a small Ta interlayer (x_{Ta} = 0.25) changes the loop shape drastically from transcritical into rectangular shape with enhanced M_R/M_S (~0.73) [Figures 5.06(b) and 5.06(d)]. (v) However, with increasing $x_{Ta} > 4$ nm, the loop shape changes towards transcritical one [Figure 5.06(d)] with reduced M_R/M_S (~0.47) value and increased H_C and H_{sat} values.

To understand changes in magnetic parameters of trilayer films, the extracted values of H_C, H_{sat} and M_R/M_S are plotted as a function of x in Figures 5.07 and 5.08 for symmetric and asymmetric trilayer films, respectively. For symmetric trilayer films, the variations of H_C, H_{sat} and M_R/M_S with x_{Cr} show oscillatory behaviors and the oscillation amplitude decreases with increasing x_{Cr} [Figures 5.07(a)-(c)]. In particular, the variations of H_{sat} and M_R/M_S display opposite behaviors, i.e., the increase in M_R/M_S reduces H_{sat} and vice versa. For Ta spacer layer films H_C, H_{sat} and M_R/M_S show completely different variations with x_{Ta} [Figures 5.07(d)-(f)]. H_{sat} displays a tiny oscillatory behavior for films with x_{Ta} up to 1 and then decreases largely with increasing x_{Ta} 4. On further increasing x_{Ta} = 6, H_{sat} again increases slightly. On the other hand, M_R/M_S increases progressively with increasing x_{Ta} up to 4 nm and then decreases slightly for x_{Ta} = 6 film. This leads to a maximum M_R/M_S value of 0.88 for film with x_{Ta} = 4.

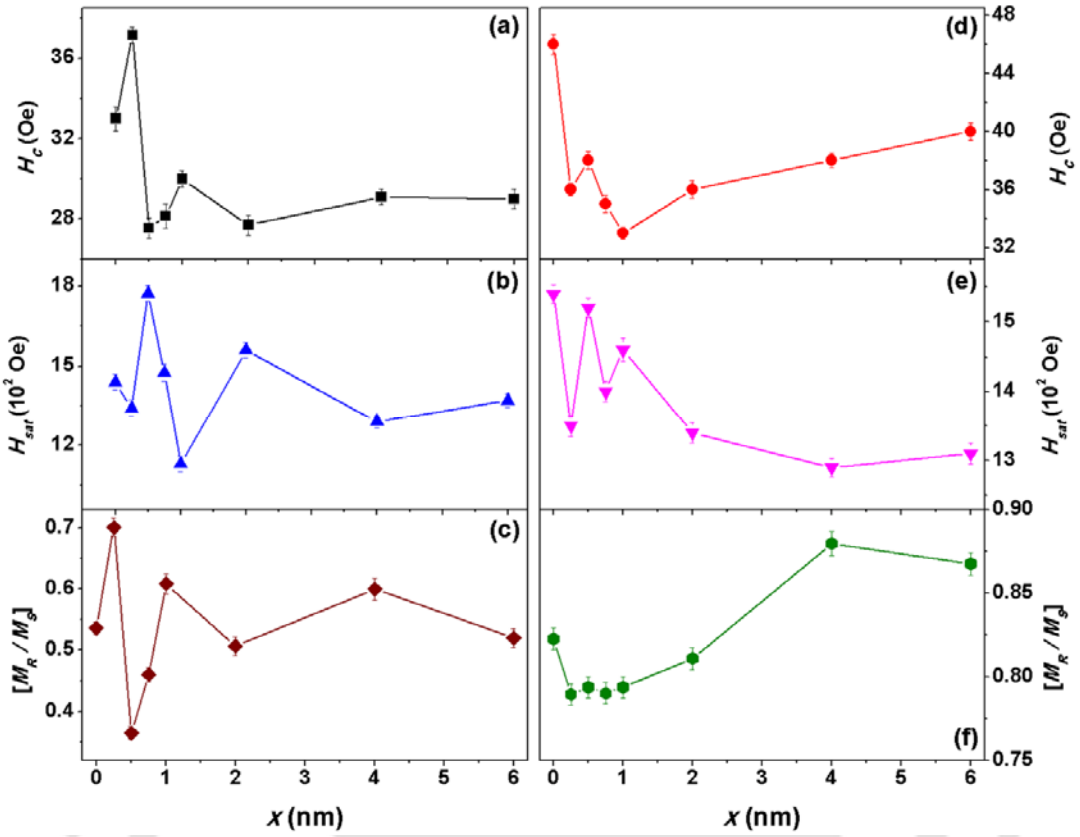

Figure 5.07: The variations of H_C, H_{sat} and M_R/M_S as a function of x for symmetric trilayer films with Cr spacer layer (a,b,c) and Ta spacer layer (d,e,f).

On the other hand, for asymmetric trilayer films with Cr spacer layer, (i) H_C reduces significantly with increasing x up to 0.75 and then increases slightly for x_{Cr} = 1 [Figure 5.08(a)]. However, H_C is found to be almost constant for the films with $x_{Cr} > 1$. (ii) H_{sat} decreases drastically from ~2100 Oe to 880 Oe when x_{Cr} is increased from 0 to 0.25 and then exhibits a weak oscillatory behavior for further increase in $x_{Cr} > 0.25$ [Figure 5.08(b)]. (iii) In contrast, M_R/M_S increases suddenly from 0.34 to 0.79 after introducing a thin Cr layer of 0.25 nm and then decreases slightly to 0.7 for x_{Cr} = 0.5 film [Figure 5.08(c)]. Upon increasing x_{Cr} above 0.5 nm, M_R/M_S increases up to 0.83 for x_{Cr} = 1 and then remains nearly constant for higher x_{Cr}. For Ta spacer layered asymmetric trilayer films [Figures 5.08(d)-(f)]: (i) H_C increases initially for x_{Ta} = 0.25 nm and then reduces significantly with increasing x_{Ta} up to 1. On further increasing x_{Ta}, H_C increases noticeably for x_{Ta} = 2 and the rate of increase in H_C decreases with increasing x_{Ta} up to 6 nm [Figure 5.08(d)]. (ii) H_{sat} decreases drastically from ~2100 Oe to 1080 Oe as the Ta layer (x_{Ta} = 0.25) is introduced and exhibits a weak oscillatory behavior for x_{Ta} up to 4 nm. Due to change in the loop shape towards

transcritical from rectangular for film with x_{Ta} = 6 nm, H_{sat} is found to be increased considerably to 1950 Oe [Figure 5.08(e)]. (iii) In contrast, M_R/M_S increases suddenly from 0.34 to 0.73 after the introduction of a thin Ta layer of 0.25 nm and then increases gradually to reach a maximum value of 0.88 for x_{Ta} = 4 [Figure 5.08(f)]. Upon increasing x_{Ta} further to 6 nm, M_R/M_S decreases drastically to 0.47 due to change in the loop nature.

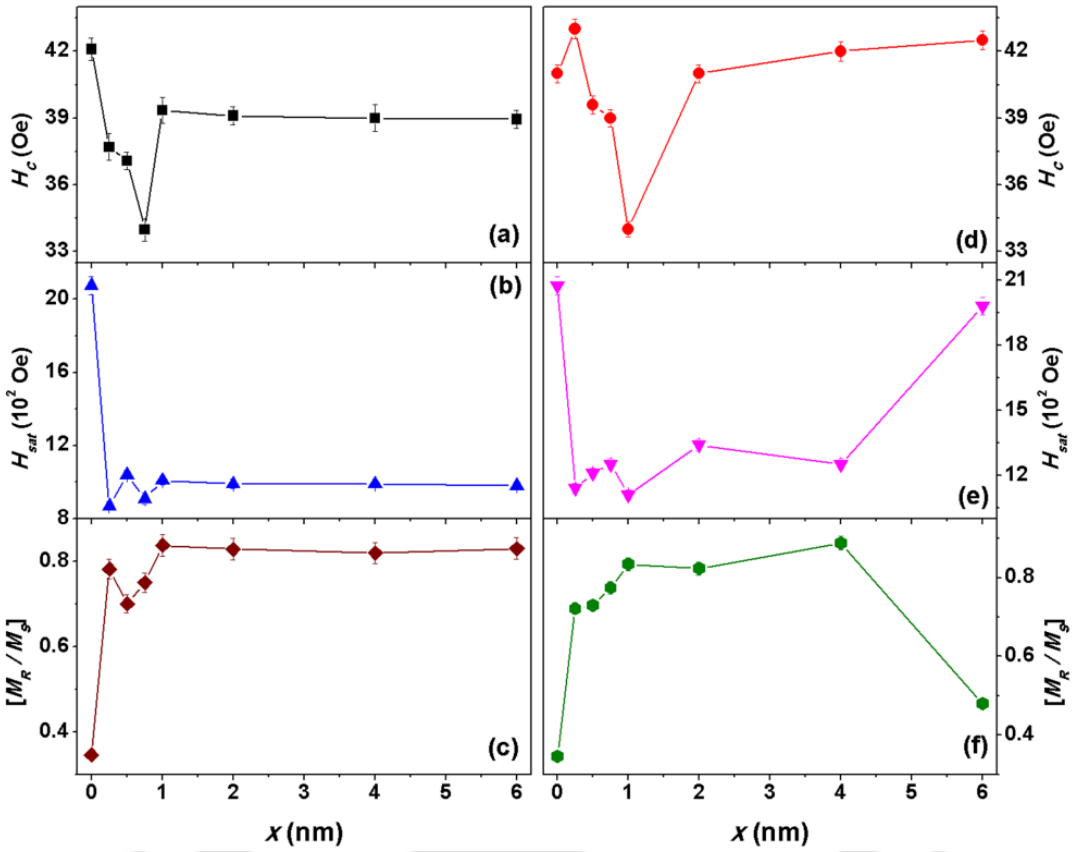

Figure 5.08: The variations of H_C, H_{sat} and M_R/M_S as a function of x for asymmetric trilayer films with Cr spacer layer (a,b,c) and Ta spacer layer (d,e,f).

The observed changes in the loop shape and magnetic properties of the trilayer films as compared to single-layer films can be explained on the basis of interlayer exchange coupling. It is well-known that the interlayer coupling between FM layers originates from the following sources: (i) direct exchange coupling between FM layers through pinholes in thin spacer layers [PONG2008, SING2013], (ii) indirect exchange coupling, i.e., Ruderman–Kittel–Kasuya–Yosida (RKKY) coupling through conduction electrons in the spacer material [KUDR1997, NIST2010], (iii) magnetostatic coupling induced by the correlated interfacial roughness, also known as Néel coupling or orange peel coupling [ZHAN19961, SCHR2000] and (iv) magnetostatic coupling either through stray fields of

domain walls [RIET1997, PRAD2004, KAZI2013] or (v) through the magnetic poles at the edges of the films [MURA1966, CRAU2003, COIS2009]. Single-layer film of CoFeB262 (20 nm) exhibits in-plane uniaxial anisotropy with the magnetization oriented in the film plane and hence the loop shape is observed to be perfectly rectangular along the easy-axis. However, the symmetric trilayer films with $x_{Cr} < 1$ nm show oscillatory behavior of M_R/M_S and kink in the first quadrant. This indicates the occurrence of possible AFM coupling between two the FM layers caused by the roughness of the interfaces due to very thin Cr interlayer [JIAN2006]. Kumar et al. showed that AFM coupling decreases with an increase in interface roughness [KUMA2005]. These results and the surface roughness of the bottom CoFeB262(20 nm) layer suggest that the interlayer coupling due to the direct FM coupling through pinholes and indirect exchange coupling through RKKY interaction depend on x. Since the average surface roughness of the bottom CoFeB262(20 nm) layer is found to be between 0.3 nm and 0.6 nm, the growth of the subsequent Cr interlayer with $x_{Cr} < 1$ nm on top of CoFeB262(20 nm) layer may not be continuous all the way. Therefore, the top CoFeB262(20 nm) layer may not be well separated from the bottom CoFeB262(20 nm) layer. As a result, there exists a direct exchange coupling between CoFeB262 layers at random locations depending upon the roughness profile. Such arrangement not only influences AFM coupling which incites the kink in the first quadrant [JIAN2006], but also helps to switch the CoFeB262 layers collectively leading to simple *M-H* loop. Upon increasing x above 1 nm, interaction between CoFeB262 layers is expected through magnetostatic coupling or indirect exchange coupling, which decreases with increasing x. The symmetric trilayer films with $x_{Ta} \leq 1$ nm show a tiny oscillatory behavior of H_{sat}, which may be correlated to the occurrence of possible AFM coupling between CoFeB262 layers caused by the roughness of the interfaces. For films with $x_{Ta} > 1$ nm, the decrease (increase) in H_{sat} (M_R/M_S) is related to the magnetostatic coupling between CoFeB262 layers [KOOL1999, SCHR2000, WIES2006]. The slight increase in H_{sat} (decrease in M_R/M_S) for film with $x_{Ta} = 6$ nm is attributed to the reduced coupling between CoFeB262 layers through thick Ta spacer layer [FENG1995, NAOE1998, HUAN2001, NAKA2001, SING2013].

On the other hand, the single-layer film of CoFeB262 (100 nm) shows the transcritical loop due to the existence of dense stripe domain. Addition of CoFeB262 (20 nm) directly on top of CoFeB262 (100 nm) film, i.e., trilayer film without any interlayer exhibits transcritical loop [Figures 5.05(d) and 5.06(d)]. This indicates that the dense stripe domain in thick CoFeB262 (100 nm) layer dominates over the in-plane magnetization of

thin CoFeB(20 nm) layer. But, the introduction of even 0.25 nm Cr (Ta) interlayer changes the transcritical loop into almost rectangular one with a large (suggestive) reduction in H_{sat} (H_C) and increase in M_R/M_S. This confirms the existence of interlayer coupling between CoFeB262 layers through direct or indirect ferromagnetic coupling, which helps in rotating them together and destabilizes the formation of dense stripe domain. The weak oscillatory behavior of H_{sat} up to $x_{Cr,Ta}$ = 1 indicates a weak AFM coupling at the interfaces due to roughness as discussed above for the earlier case.

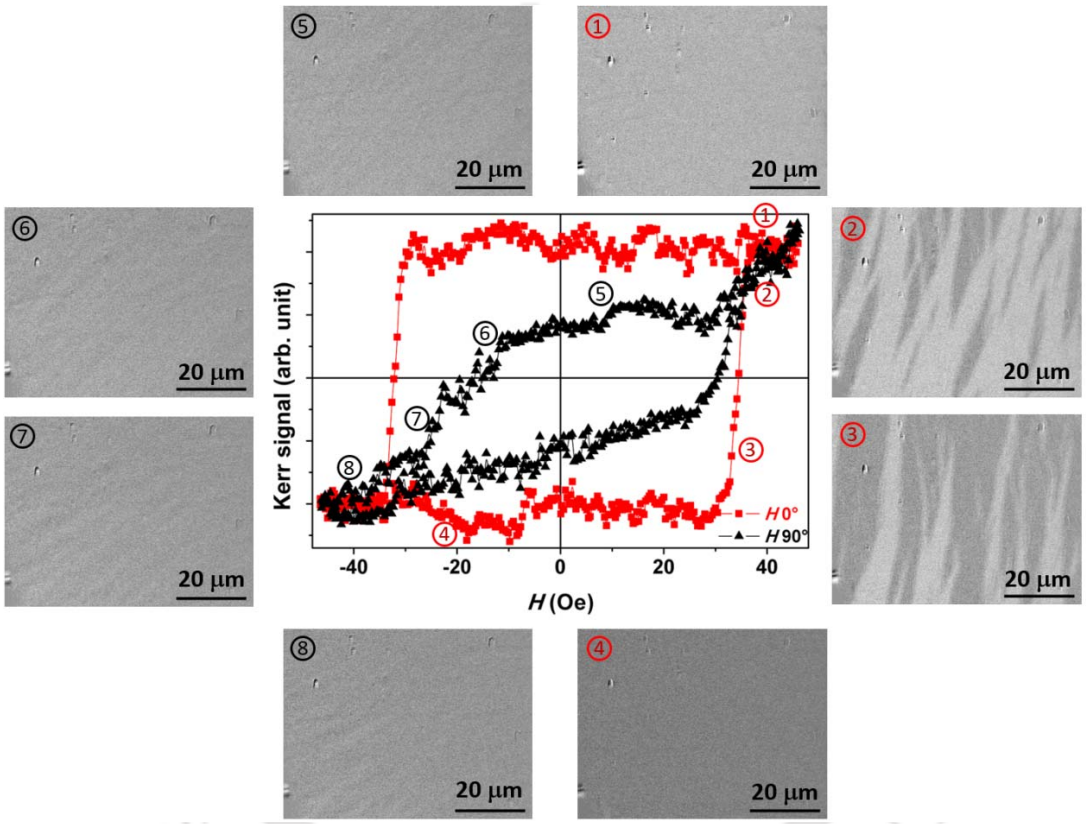

Figure 5.09: Room temperature Kerr loops and magnetic domain patterns for trilayer [CoFeB262 (100 nm)/ Cr (0.75 nm)/ CoFeB262 (20 nm)] film measured along film plane at different applied field directions [easy (0°) and hard (90°) axes].

On further increasing x_{Cr} above 1 nm, H_C, H_{sat} and M_R/M_S are found to be merely constant, revealing the existence of stable interlayer coupling between CoFeB262 layers. However, for films with x_{Ta} above 1 nm, the variations of H_C, H_{sat} and M_R/M_S depend strongly on the values of x_{Ta} due to spacer layer dependent interlayer coupling between CoFeB262 layers. The noticeable increase (decrease) in H_{sat} (M_R/M_S) for film with x_{Ta} = 6 nm is caused by the decrease in magnetostatic coupling strength with increased x_{Ta} [FENG1995, NAOE1998,

HUAN2001, NAKA2001, SING2013]. As a result, the dense stripe domain in thick CoFeB262 (100 nm) layer dominates over the in-plane magnetization of thin CoFeB262(20 nm) layer, causing the formation of transcritical loop [Figures 5.06(b) and 5.06(d)].

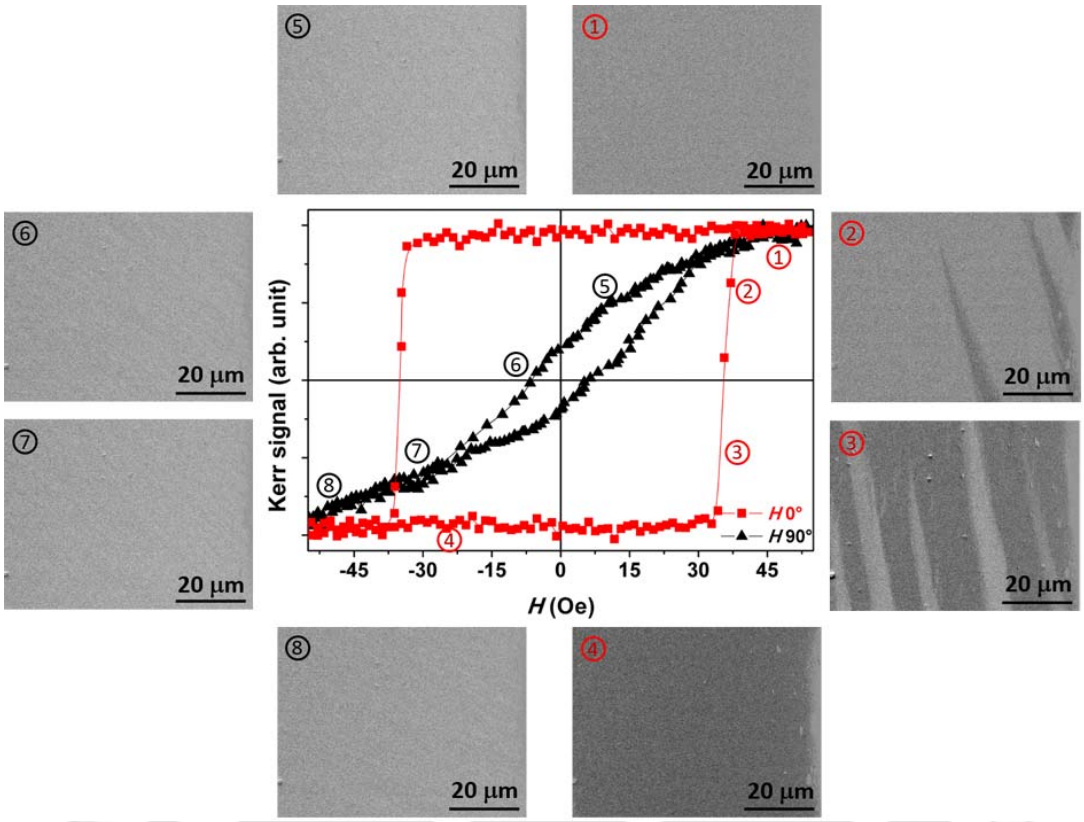

Figure 5.10: Room temperature Kerr loops and magnetic domain patterns for trilayer [CoFeB262 (100 nm)/ Ta (1 nm)/ CoFeB262 (20 nm)] film measured along film plane at different applied field directions [easy (0°) and hard (90°) axes].

To further confirm this interpretation, we have investigated the magnetization reversal behavior along the film plane using MOKE microscopy for the asymmetric trilayer film with x_{Cr} = 0.75 and x_{Ta} = 1 as depicted in Figures 5.09 and 5.10, respectively. It is clearly evident from Figure 5.09 that the film displays rectangular loop in one direction [easy-axis direction in the plane (0°)] and imprecise loop characterized by reduced remanence in another direction [hard-axis direction in the plane (90°)]. The magnetic domain images obtained along the easy-axis show a rapid switching of large-sized domains with the applied field due to domain wall motion, while the domain images along the hard-axis reveal faint ripple domains possibly due to an inhomogeneous local magnetic anisotropy distribution [NOWA1993] caused by the interaction between CoFeB262 layers.

The field required to switch the magnetization along the easy-axis from one direction to another is quite low (< 10 Oe). For the trilayer film with x_{Ta} = 1 nm, we have observed almost similar results along the easy-axis (Figure 5.10), i.e., a rapid switching of large-sized domains due to domain wall motion with slightly larger applied field (~ 12 Oe) required to switch the magnetization from one direction to another direction. However, the Kerr loop obtained along the hard-axis is found to be linear like behavior with a tiny loop close to origin. Interestingly, the magnetic domain images along the hard-axis illustrate a clear coherent like rotation process, but with very faint ripple domains. These results clearly confirm that the magnetic properties of the thick CoFeB262 layers with dense strip domain can easily be tuned in to in-plane magnetization by this simple trilayer structure concept. This is much easier approach than the earlier reported methods of fabricating multilayers with more layers [HUAN2001, MISH2011, DASC20181]. Nevertheless the detailed study of the room temperature magnetic properties of the trilayer films with different spacer layer clearly demonstrate that the resulting magnetic properties of the trilayer films depend strongly on spacer layer materials and its thickness.

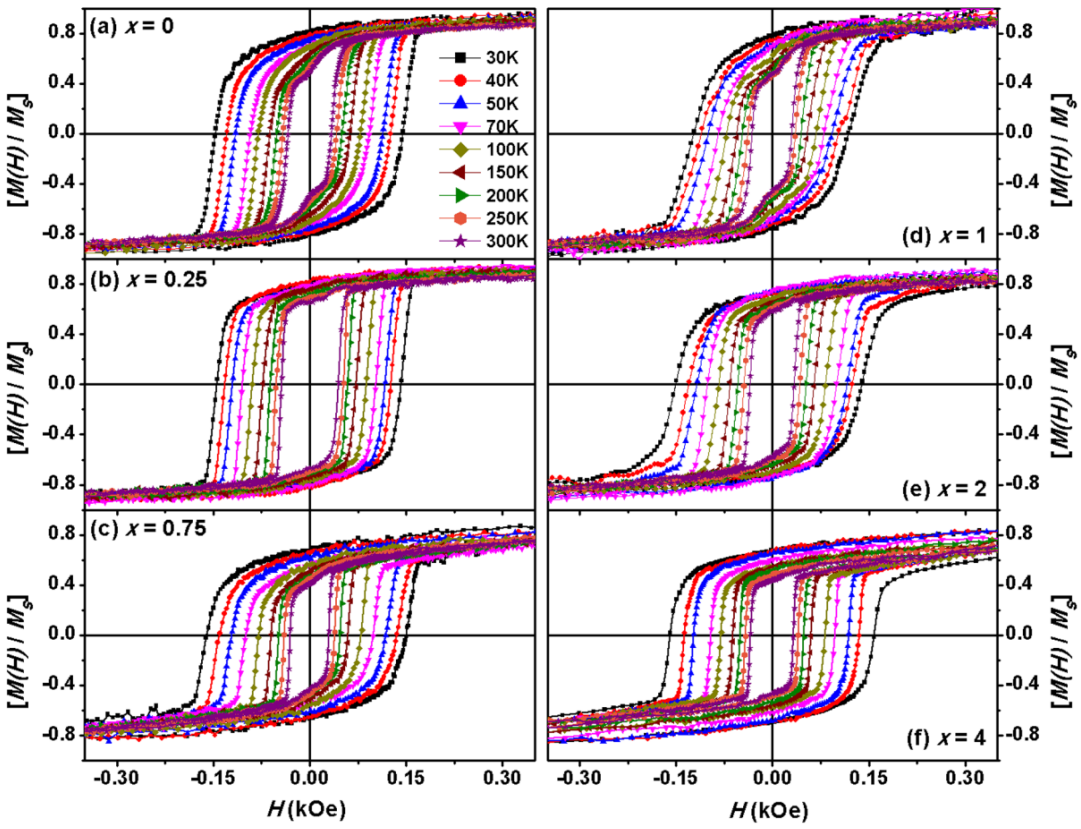

Figure 5.11: *M-H* loops measured at different temperatures for Cr symmetric trilayer films with x = 0 (a), 0.25 (b), 0.75 (c), 1 (d), 2 (e) and 4 nm (f).

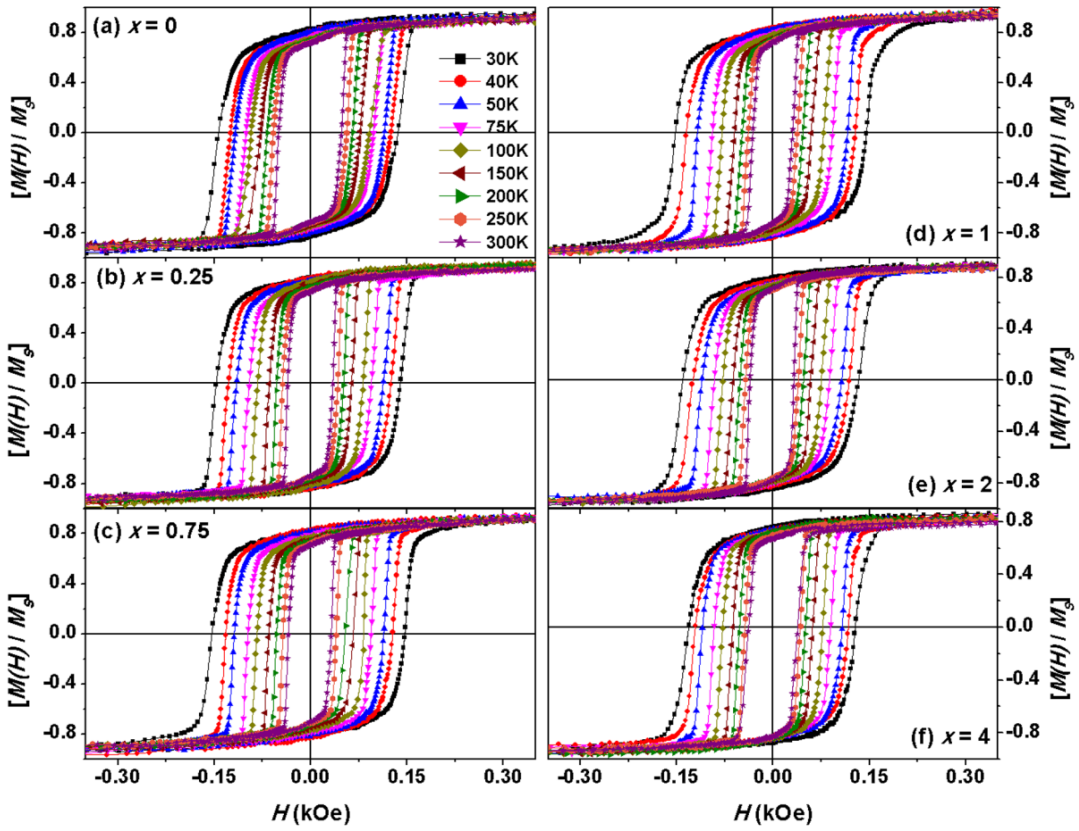

Figure 5.12: *M-H* loops measured at different temperatures for Ta symmetric trilayer films with x = 0 (a), 0.25 (b), 0.75 (c), 1 (d), 2 (e) and 4 nm (f).

5.3.2.2. Temperature dependent magnetic properties

It is known that the interlayer coupling between CoFeB262 layers gets modified by changing the measurement temperature due to the change in the interfacial strain caused by the materials at the interfaces. However, the literature related to interlayer coupling as a function of temperature is very limited. Therefore, temperature dependent *M-H* loops were recorded along the film plane over the temperature range of 30-300 K for all four series of films. Figures 5.11 and 5.12 display selective normalized *M-H* loops measured at different temperatures for symmetric trilayer films with Cr and Ta spacer layers, respectively, while the temperature dependent *M-H* loops for asymmetric trilayer films with Cr and Ta spacer layers are depicted in Figures 5.13 and 5.14, respectively. The temperature dependent *M-H* loops for symmetric trilayer films with Cr spacer layer (Figure 5.11) reveal that (i) the kink observed in the first quadrant disappears gradually with decreasing temperature, but the temperature at which the kink disappears varies with x_{Cr} for the films with $x_{Cr} \leq 1$, (ii) with increasing $x_{Cr} > 1$, the loop shape does not change with temperature, (iii) nevertheless, the

area under the loop, H_C and H_{sat} increase with decreasing temperature, as expected for a typical ferromagnetic material, and (iv) M_R/M_S increases in all the films with decreasing temperature, but the amount of increase varies with x_{Cr}.

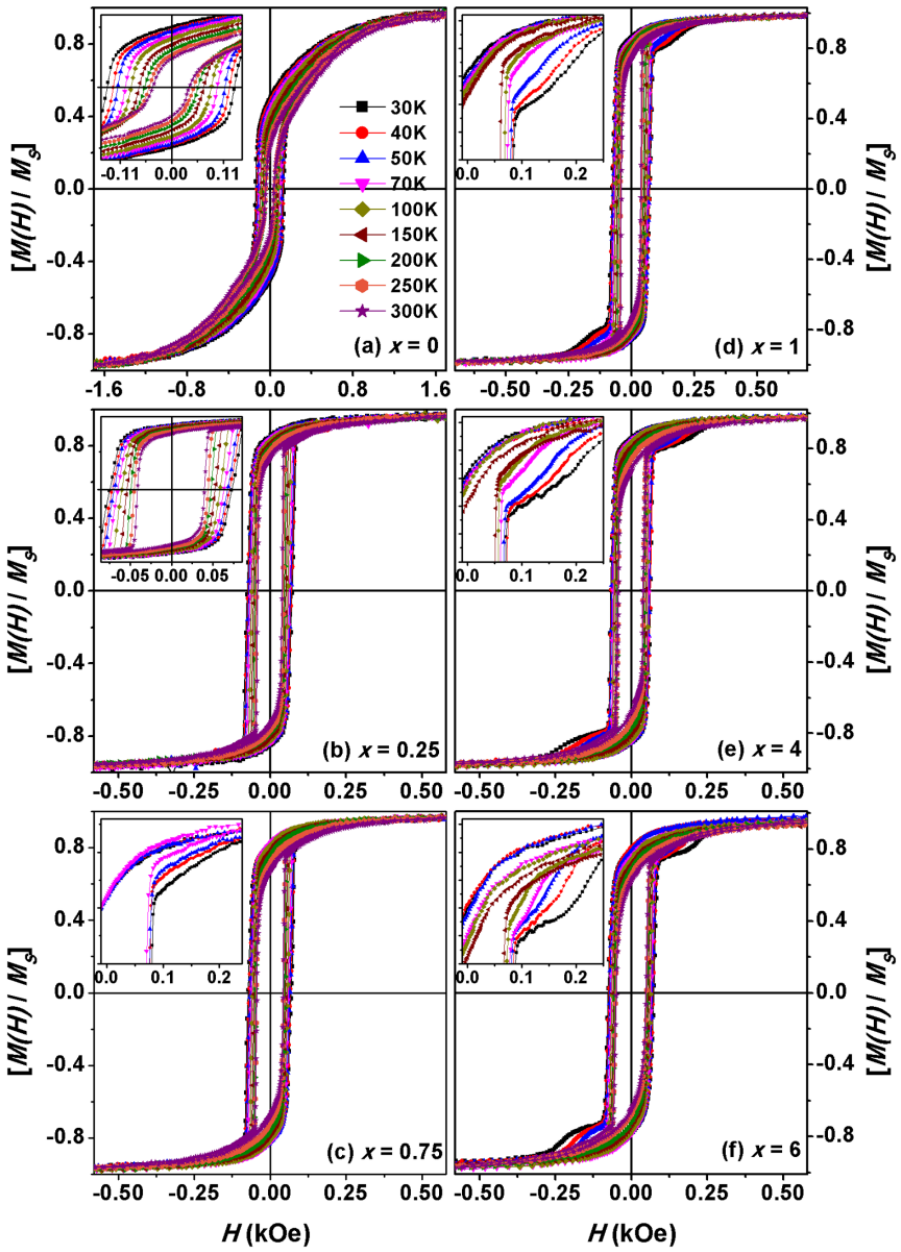

Figure 5.13: *M-H* loops measured at different temperatures for Cr asymmetric trilayer films with x = 0 (a), 0.25 (b), 0.75 (c), 1 (d), 4 (e) and 6 nm (f). The expanded view of corresponding *M-H* loops is shown as insets in the figure.

For example, M_R/M_S increases from 0.54 to 0.83 and 0.50 to 0.78 for the films with x = 0 and 2 nm, respectively. For symmetric trilayer films with Ta spacer layer (Figure 5.12), (i)

the shape of the loops does not change with decreasing temperature for all values of x_{Ta}. However, the area under the loops, H_C and H_{sat} increase progressively with decreasing temperature. In addition, all the loops exhibit single magnetization reversal behaviors suggesting that both top and bottom CoFeB262 layers reverse collectively at all temperatures. (ii) M_R/M_S increases in all the films with decreasing temperature.

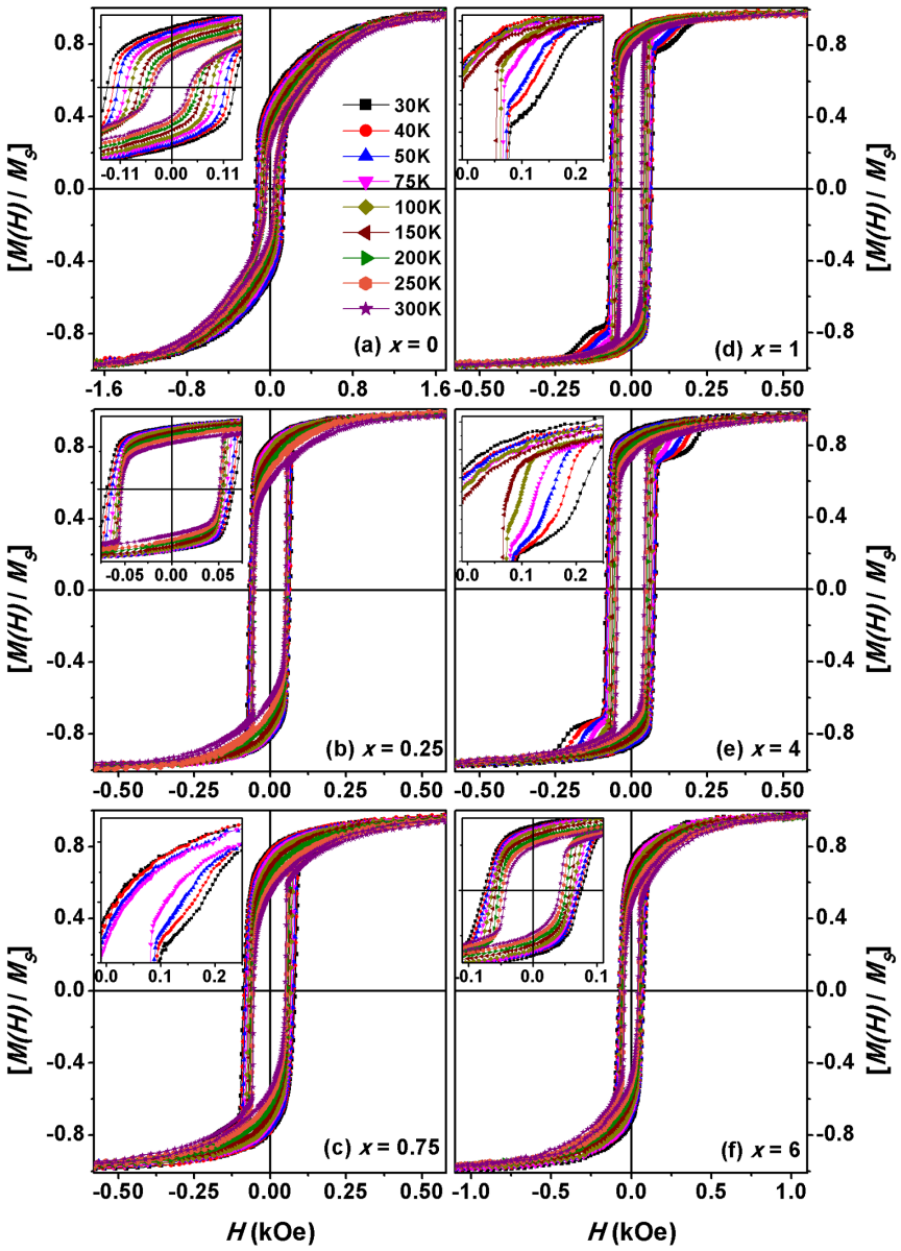

Figure 5.14: *M-H* loops measured at different temperatures for Ta asymmetric trilayer films with x = 0 (a), 0.25 (b), 0.75 (c), 1 (d), 4 (e) and 6 nm (f). The expanded view of corresponding *M-H* loops is shown as insets in the figure.

On the other hand, the *M-H* loops of asymmetric trilayer films with Cr spacer layer (Figure 5.13) show that (i) the loop shape does not change with decreasing temperature for the films with $x_{Cr} < 0.5$, (ii) however, the area under the loop, M_R/M_S, H_C, H_{sat} increases with decreasing temperature, (iii) *M-H* loops show additional features at low temperatures below 100 K for films with $x_{Cr} > 0.5$, viz., a step in the *M-H* loop before saturation. The step feature becomes more prominent as temperature is reduced for a particular film and also when x_{Cr} is increased [Figures 5.13(d-f)]. The relative magnitude of magnetization reversing as a separate step at 30 K increases from 17 % for $x_{Cr} = 0.75$ film to 26% for $x_{Cr} = 6$ film. The asymmetric trilayer films with Ta spacer layer also show almost similar temperature dependent behaviors for x_{Ta} up to 4 nm (Figure 5.14). The relative magnitude of magnetization reversing as a separate step at 30 K increases from 19 % for $x_{Ta} = 0.75$ film to 27 % for $x_{Ta} = 4$ film [Figures 5.15(c-e)].

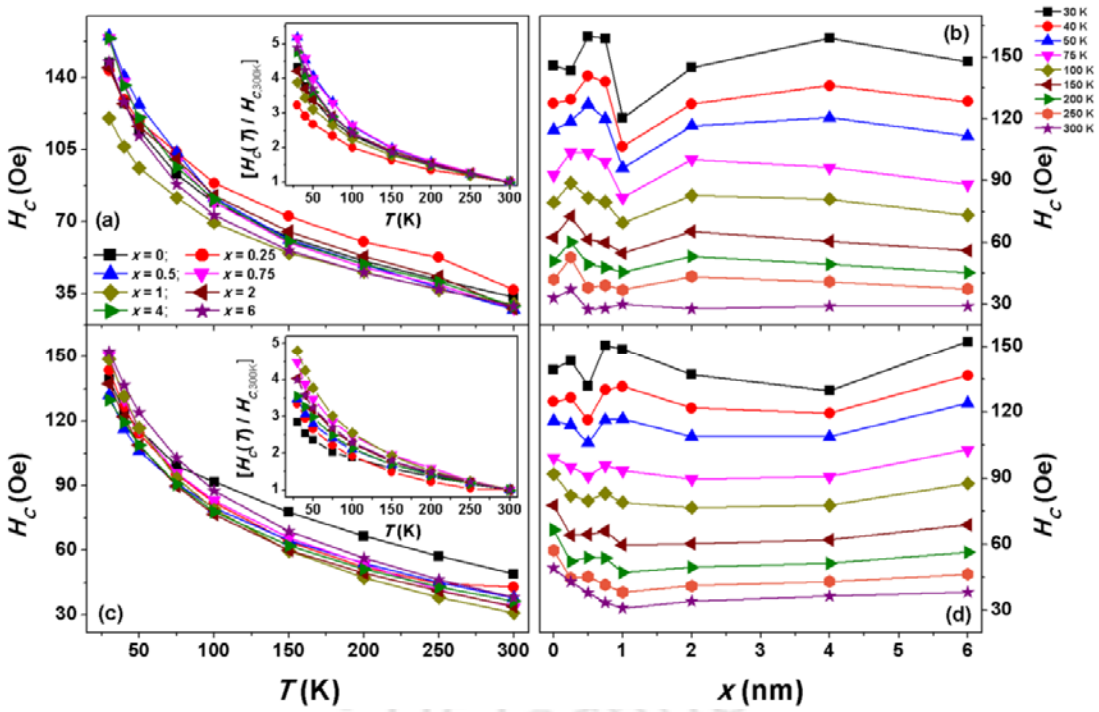

Figure 5.13: H_C variations as a function of temperature and x for symmetric trilayer films with Cr spacer layer (a,b) and Ta spacer layer (c,d). Insets show the normalized H_C $[H_C(T)/H_{C,300K}]$ as a function of temperature.

Figure 5.15 and Figure 5.16 depict the extracted values of H_C plotted as a function of temperature for different x_{Cr} (x_{Ta}) and as a function of x_{Cr} (x_{Ta}) at different measurement temperatures for both symmetric and asymmetric series, respectively. The relative variation

of H_C, i.e., $H_C(T)/H_{C,300K}$, is also plotted as a function of temperature for both the series as insets in the figures. H_C increases with decreasing temperature for all the films. However, the amount of increase in H_C not only depends on x (for both Cr and Ta) but also depends on the type of domain structure in the CoFeB262 films.

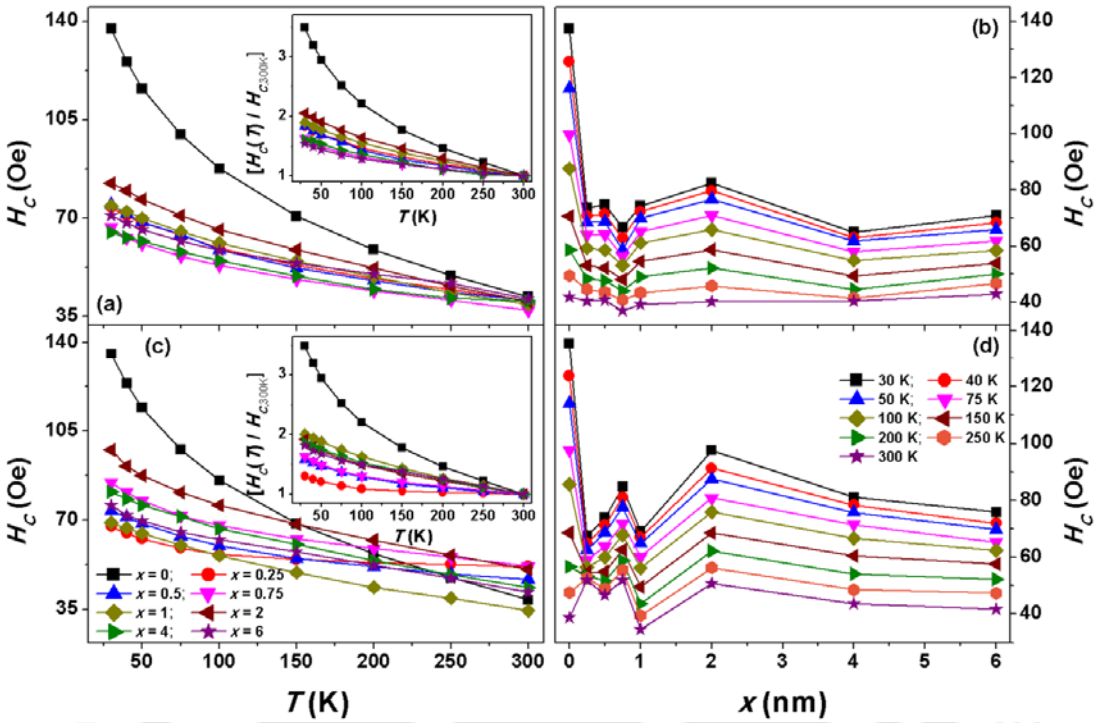

Figure 5.16: H_C variations as a function of temperature and x for asymmetric trilayer films with Cr spacer layer (a,b) and Ta spacer layer (c,d). Insets show the normalized H_C $[H_C(T)/H_{C,300K}]$ as a function of temperature.

For instance, room temperature H_C increases slightly for the asymmetric films as compared to symmetric one for both the spacer materials. However, with decreasing temperature, H_C varies largely from 29-33 Oe at 300 K to 120-160 Oe at 30 K for symmetric films with x_{Cr} [Figure 5.15(a)]. Similarly, H_C varies from 30-43 Oe at 300 K to 129-152 Oe at 30 K for symmetric films with x_{Ta} [Figure 5.15(c)]. On the other hand, for asymmetric films with x_{Cr}, H_C varies from 37-42 Oe at 300 K to 64-82 Oe at 30 K, while H_C varies from 36-50 Oe at 300 K to 67-84 Oe at 30 K for asymmetric films with x_{Ta}. Similarly, $H_C(T)/H_{C,300K}$ increases from 1 to 5.2 and from 1 to 4.8 [insets of Figures 5.15(a) and 5.15(c)] for symmetric films with Cr and Ta, respectively. For asymmetric trilayer films, $H_C(T)/H_{C,300K}$ increases from 1 to 2 and from 1 to 2.1 [insets of Figures 5.16(a) and 5.16(c)] for Cr and Ta spacer layers, respectively. On the other hand, the plot of H_C versus x for symmetric films with x_{Cr} shows

that with decreasing temperature, (i) the maximum H_C observed at a particular x shifts sluggishly from x_{Cr} = 0.25 at 300 K to x_{Cr} = 0.5 at 50 K and x_{Cr} = 0.75 at 30 K [Figure 5.15(b)], and (ii) the difference between minimum and maximum H_C also increases. Similarly, the plot of H_C versus x for symmetric films with x_{Ta} shows that (i) at 300 K, H_C decreases considerably with increasing x_{Ta} up to 1 nm and then increases slightly for higher x_{Ta}. (ii) With decreasing temperature, the variation of H_C versus x changes and shows a non-linear behavior. For asymmetric films (Figure 5.16): (i) H_C increases largely with decreasing temperature for x = 0 films. (ii) However, the amount of increase in H_C with decreasing temperature decreases for trilayer films with different x. On the other hand, the plot of H_C versus x [Figures 5.16(b) and 5.16(d)] displays that H_C exhibits a large drop between the films with x = 0 and x = 0.25 films. In addition, the magnitude of oscillatory behavior of H_C for x up to 1 nm increases with decreasing temperature. Furthermore, the variation in H_C with temperature for films with higher x values decreases. This signifies firm coupling between two CoFeB262 layers in asymmetric trilayer films persist throughout the temperature regime.

Temperature dependent magnetic properties of trilayer films can be explained as follows: For symmetric trilayer films with Cr spacer layer, the disappearance of kink in the first quadrant with decreasing temperature can be correlated with the enhanced magnetic interaction between the CoFeB262 layers due to the increase in the magnetization of CoFeB262 layer and vanishing of AFM coupling between two CoFeB262 layers caused by the roughness. For asymmetric films with Cr and Ta spacer layers, the formation of additional step with increased magnitude of relative magnetization reversing as a separate step at lower temperature could be attributed to (i) reduction in interlayer coupling between CoFeB262 layers with increasing x [SCHR2000, HUAN2001, SING2013] and (ii) strong temperature dependent interfacial strain realized from the substrate on thick CoFeB262 (100 nm) bottom layer due to the different thermal expansion coefficients of the film and substrate [HUAN2001, COIS2009, SING2014, SING20161, SING20162], which does not allow CoFeB262 (100 nm) layer to switch collectively with the top CoFeB262 (20 nm) layer. As a result, the magnitude of separate switching increases with decreasing temperature and also with increasing x. Interestingly, the temperature dependent H_C data reveals that the amount of increase in H_C with decreasing temperature decreases for the asymmetric trilayer films as compared to the symmetric trilayers. This is due to the firm interlayer coupling between dense stripe domain and in-plane magnetization in asymmetric films, which changes the nature of effective domain structures. Temperature dependent

study also reveals that magnetic properties of the trilayer films depend strongly on spacer layer materials and its thickness. The obtained results suggest that the asymmetric trilayer film with suitable interlayers (Cr or Ta) is promising and a novel approach to tune the magnetic properties and domain structure of the thick CoFeB262 films.

5.4. Summary

A systematic investigation of effect of spacer layer materials and its thickness (x), CoFeB262 layer thickness (y), and temperature on the magnetic properties of trilayer CoFeB262 (y nm)/[Cr, Ta (x nm)]/CoFeB262 (20 nm) films with y = 20 and 100 and x = 0 – 6, has been carried out. The salient features of the trilayer films from the current investigations are as follows:

- Amorphous trilayer CoFeB262 (y nm)/[Cr, Ta (x nm)]/CoFeB262 (20 nm) thin films with symmetric (y = 20) and asymmetric (y = 100) domain structures and x = 0 – 6 are successfully prepared directly on the thermally oxidized Si substrate at ambient temperature using DC magnetron sputtering technique.
- Amorphous nature of the as-deposited CoFeB films is confirmed through XRD and TEM studies.
- Atomic force microscopy study of CoFeB262 films with y = 20 and 100 nm shows the existence of very fine and sparsely dispersed nanosized grains of size ranging between 10 nm and 15 nm in the as-deposited films. The topography pattern of the films exhibits a very clear uniform surface and the average roughness of the surface is found to be in the range of 0.3-0.6 nm and 0.4-0.7 nm for CoFeB262 films with y = 20 and 100, respectively.
- The single-layer as-deposited amorphous CoFeB262 (20 nm) film exhibits in-plane uniaxial magnetic anisotropy with the magnetization oriented along the film plane, while CoFeB262 (100 nm) film displays magnetic dense stripe domain and transcritical hysteresis loop due to large effective magnetic anisotropy caused by the stress induced during deposition of the films.
- The shape of the *M-H* loops in trilayer films strongly depends on x, y and temperature.
- All symmetric trilayer films (y = 20) show single magnetization reversal process at room temperature (i) with a kink in the first quadrant for films with x_{Cr}<1 and (ii)

without any kink for higher x_{Cr}. No such kink behavior was observed in trilayer films with Ta spacer layer.

- For asymmetric films, the transcritical loop changes into rectangular one with the introduction of spacer layer. This reduces H_{sat} and enhances M_R/M_S largely. However, for trilayer films with x_{Ta} = 6 nm, the rectangular loop again changes towards transcritical.
- H_C, H_{sat} and M_R/M_S show strong dependence on spacer layer materials and its thickness for both symmetric and asymmetric trilayer films.
- Magnetic domain images obtained using Kerr microscopy in trilayer films show rapid switching of large-sized domains along the easy-axis and weak ripple domains along the hard-axis. In addition, the nature of magnetic domains along the hard-axis strongly depends on spacer layer material.
- Temperature dependent *M-H* loops for symmetric trilayer films at low temperatures reveal (i) the disappearance of the kink in Cr symmetric trilayer films and (ii) single magnetization reversal at H_C for all value of x_{Ta} throughout the temperature range.
- Temperature dependent *M-H* loops for asymmetric trilayer films show the formation of additional steps with $x > 0.5$ for both spacer layer materials.
- The relative increase in H_C with decreasing temperature is found to be larger for symmetric films as compared to asymmetric ones for both spacer layer materials.
- The observed results are explained on the basis of change in the interlayer coupling between CoFeB262 layers with change in x, y and temperature dependent interfacial strain, which modifies the nature of interlayer coupling.
- The obtained results also demonstrate that dense stripe domain of thicker CoFeB262 layers can be easily converted into simple in-plane magnetization by resorting to asymmetric trilayer thin film structure.

Indian Institute of Technology Guwahati

Chapter 6

Tuning magnetic properties of thick CoFeB films by simple trilayer structure: Effect of top CoFeB layer thickness

Indian Institute of Technology Guwahati

6.1. Introduction

Magnetic thin films with enhanced soft magnetic properties, simple magnetic domain structure and reduced media noise are enormously required in areas like magnetic recording, communication devices, automotive industry, and other modern magneto-electronic devices. In these applications, the ferromagnetic thin films are used as either magnetic flux guide or magnetic flux amplifier in high-frequency applications, provided these magnetic films exhibit a simple magnetic domain structure with the magnetization oriented in a particular direction [PIRA2007, CHTC2013, CHEN20131, KAZI2013, VARV2016]. Hence, over last two decades extensive studies have been carried out on various types of magnetic thin films [HITPERM, CoFeB, CoNbFe, Co(Ta,Nb,Fe)Zr, FeAlSi, FeBSi, FeCuNbSiB, Fe(Co)TaN, FeTaC, *etc*.] in both single-layer and multilayer forms to improve the soft magnetic properties [MAPP1991, NAKA1997, NAOE1998, HUAN2001, NAKA2001, TANA2003, LIXW2007, COIS2008, SING2012]. Among these films, amorphous CoFeB thin film is found to be one of the promising materials suitable for various applications due to its tunable magnetic properties [HASH2007, PIRA2007, UHRM2008, IKED2010, FELS2013, KAZI2013, TANG2014, CUCH2016, DIEN2016, TSYM2016]. However, the magnetic properties of the CoFeB films, as discussed in Chapter 4, are strongly dependent on its thickness.

In order to control the development of effective magnetic anisotropy (K_{eff}), complex magnetic domain structure at larger thickness and to improve soft magnetic properties with simple domain structure, the most commonly adopted approaches are (i) to fabricate the multilayer structured thin films having ferromagnetic layers separated by non-magnetic (metallic and non-metallic) layers [NAKA1997, NAOE1998, NAKA2001, HUAN2001, TANA2003, SING2013] and (ii) to execute controlled heat treatment of the amorphous precursor under different annealing environments [HERZ2013, DANI2014]. For instance, Feng et al. [FENG1994, FENG1995] reported spacer layer materials and its thickness dependence of soft magnetic properties, where H_C decreases with increasing spacer layer thickness (x). Similarly, Mishra et al. [MISH2011] and Camelia et al. [DASC20181] reported that the soft magnetic properties of ferromagnetic layers beyond critical thickness are enhanced by fabricating multilayer thin films with more number of multilayers (N) and different x. Nevertheless, with increasing N, (i) the number of interfaces increases, (ii) the interlayer coupling between the ferromagnetic layers becomes complex due to increased number of interfaces [PARK2008, NAVA2014], (iii) the nature and strength of magnetic coupling between ferromagnetic layers vary indiscriminately with spacer layer material and

its thickness and (iv) the roughness associated with the number of interfaces increases and the average magnetization of the films decreases. Although the post heat treatment of amorphous precursor provides excellent soft magnetic properties with high Curie temperature [TANA2003, SING2014], H_C increases progressively with increasing heat treatment temperature in the multilayer films [GUSE2011, SING20161]. As a result, the magnetic properties and magnetization reversal behaviors are highly modified [CHOP2000, SCHR2000, CHOP2005, BALT2007, NIST2010, HUBE2014]. While most of the earlier works on CoFeB films have been focused mainly on controlling the perpendicular magnetic anisotropy [IKED2010, GAJE2012, NAIK2012, MANT2013, LIUY2016] from applications point of view, there are only limited reports available on tuning the magnetic properties of thick amorphous $Co_{20}Fe_{60}B_{20}$ (CoFeB262) based films for other possible applications such as flux guide, flux amplifiers, flexible electronics, *etc*. [SHAR2006, KIPG2012, CHEN20131, DASC20181] and from fundamental point of view.

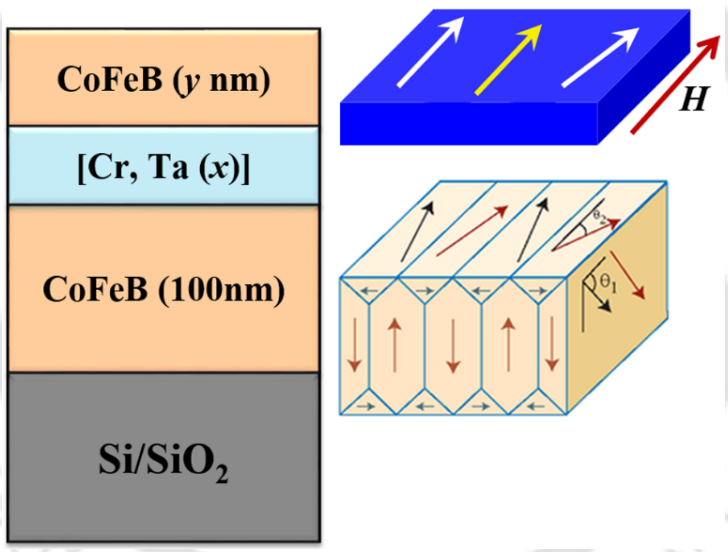

Figure 6.01: Schematic representation of trilayer structured thin films of Substrate/ [CoFeB262 (100 nm) /[Cr,Ta (*x* nm)] /CoFeB262 (*y* nm)].

The detailed investigation of asymmetric trilayer structured [CoFeB262 (100 nm)/ [Cr, Ta (*x* nm)]/ CoFeB262 (20 nm)] thin films in Chapter 5 revealed that the magnetic properties of the thick CoFeB262 (100 nm) layers with dense stripe domain structure can easily be converted into simple in-plane magnetization by resorting to asymmetric trilayer thin film structure. This approach seems to be one of promising and novel approaches to tune the magnetic properties and domain structure of thick CoFeB films. In order to further explore the possibility of tuning the magnetic properties of the thick CoFeB films with dense

stripe domain using the asymmetric trilayer structure, we report in this chapter an alternative approach of fabricating trilayer structured films of [CoFeB262 (100 nm)/ [Cr, Ta (*x* nm)]/ CoFeB262 (*y* nm)], as schematically shown in Figure 6.01. These trilayer films are fabricated and characterized mainly (i) to study the effect of top CoFeB262 layer thickness on the magnetic properties of thick CoFeB262 bottom layer through different spacer layer materials (Cr and Ta), (ii) to investigate the variation in magnetic interactions between two CoFeB262 layers for various *x*, (iii) to understand the effect of temperature (*T*) on the magnetic interactions between CoFeB262 layers and (iv) to optimize the suitable trilayer film structure and obtain enhanced soft magnetic properties in thick amorphous CoFeB262 (100 nm) film.

6.2. Experimental details

Amorphous CoFeB262 (100 nm) single-layer film and trilayer films of [CoFeB262 (100 nm)/ [Cr, Ta (*x* nm)]/ CoFeB262 (*y* nm)] with *y* = 2, 5, 10, 30 and 50 nm, x_{Cr} = 0.75, 2 nm and x_{Ta} = 1, 4 nm were prepared using magnetron sputtering technique. All the films were deposited directly on the thermally oxidized Si substrate at ambient temperature. The base pressure of the chamber was maintained to be better than 1×10^{-4} Pa. The working gas pressure for the deposition of CoFeB262, Cr and Ta was fixed at 10 mTorr. The deposition rate of the films was pre-calibrated using *ex-situ* surface profilometer (Vecco, Dektak-150 model). The total thickness of each film in single-layer and trilayer films was controlled by monitoring the deposition time during the film deposition.

Amorphous nature of all the as-deposited CoFeB262 films was confirmed by X-ray diffraction (XRD) obtained using a high-power X-ray diffractometer (Rigaku TTRAX III, 18 kW) with Cu-Kα radiation (λ = 1.54056 Å) and transmission electron microscopy (TEM, JEOL 2100 and Technai G^2 F20) techniques. Room temperature and temperature dependent magnetic properties of the films were analyzed using vibrating sample magnetometer (VSM, LakeShore Model 7410) by performing magnetic hysteresis loops (*M-H*) at room temperature and at low temperatures in the temperature range between 30 K and 300 K. Magnetic domain images and Kerr loops were obtained using magneto-optic Kerr effect (MOKE) microscopy (Evico Magnetics Ltd, Germany) technique. Imaging was performed using linearly polarized light with white LED source. Magnetic domain images were observed in both branches of hysteresis cycle in longitudinal MOKE mode. Hysteresis accompanied by simultaneous imaging has been performed for magnetic fields applied

along various in-plane directions [easy (0°) and hard (90°) axes]. Simultaneous atomic force microscopy (AFM) and magnetic force microscopy (MFM) studies were performed to study the topographic feature and local magnetic domains (Bruker Dimension Icon). MFM was performed in dual-pass lifting mode with commercially available CoCr-coated tips, which were magnetized along the tip axis and therefore sensitive to stray field gradients from out-of-plane oriented domains or the out-of-plane components of domains oblique to the surface. The domain images were acquired at the zero-field state.

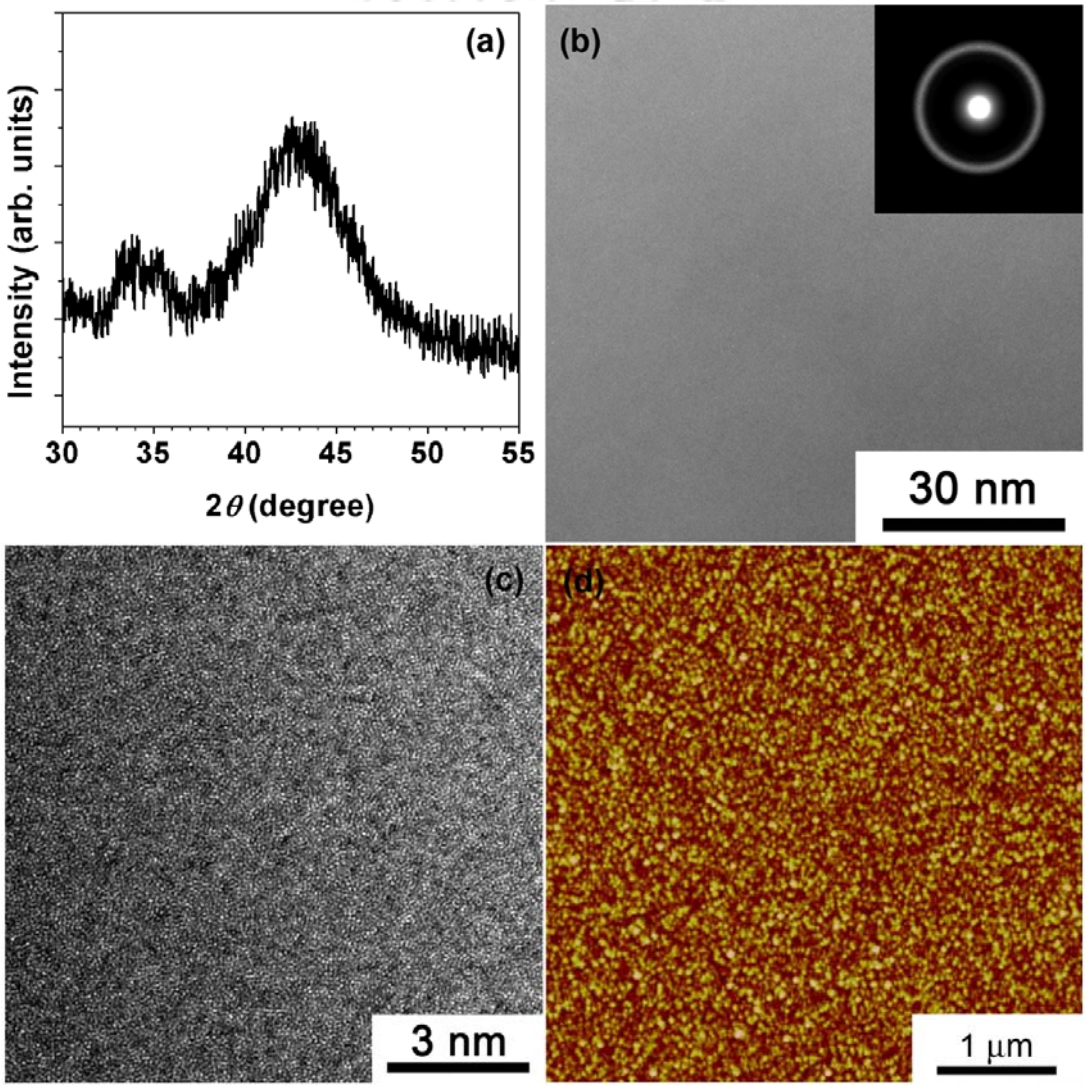

Figure 6.02: Room temperature (a) XRD pattern and (b) bright-field TEM image and selected area electron diffraction pattern, (c) high-resolution TEM image and (d) topography image obtained using AFM for the as-deposited amorphous CoFeB262 (100 nm) film.

6.3. Results and discussion

6.3.1. Structural properties

Figure 6.02 shows typical XRD pattern, bright-field TEM image, selected area electron diffraction (SAED) pattern, high-resolution TEM (HRTEM) image and AFM topography of the as-deposited single-layer CoFeB262 (100 nm) thick film. It is clearly seen that as-deposited film exhibits only a broad peak at around $2\theta = 44°$ without any sharp peaks corresponding to any other crystalline phases. The XRD peak observed at $2\theta = 33.05°$ represents Si(200) peak due to thermally oxidized Si substrate [CHOM2001]. The amorphous nature is also confirmed from bright-field TEM image, SAED pattern and HRTEM image, which revealed the existence of plain and even contrast microstructure without any local lattice fringes and halo diffraction ring, respectively. AFM topography displays the existence of very fine and sparsely dispersed nanosized grains of size ranging between 11 and 15 nm in the as-deposited films. In addition, the film exhibits a very clear uniform surface and the average roughness of the surface is found to be between 0.4 nm and 0.7 nm.

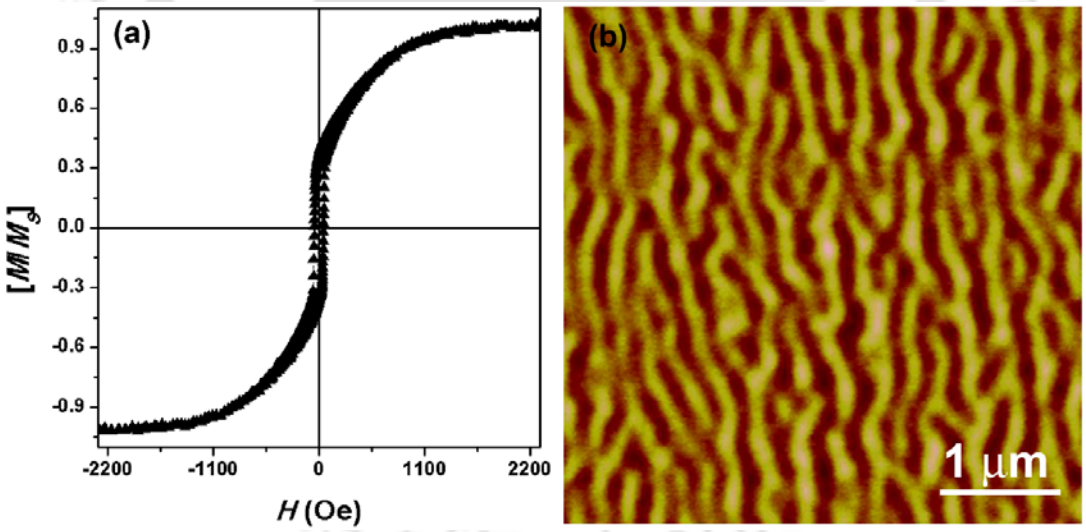

Figure 6.03: Room temperature (a) *M-H* loop measured along the film plane and (b) MFM domain image for CoFeB262 (100 nm) film.

6.3.2. Magnetic properties

6.3.2.1. Room temperature magnetic properties

Figure 6.03 depicts room temperature *M-H* loop measured along the film plane and magnetic domain structure of the as-deposited CoFeB262 (100 nm) single-layer film. It is clearly evident that the *M-H* loop is constituted by two different magnetization reversal processes

before saturation: (a) in-plane magnetic component, which reverses quickly at fields close to H_C and (b) perpendicular component, which rotates progressively under the application of magnetic field. The latter one gives rise to almost a linear-like variation of magnetization before saturation and also requires a large applied magnetic field (H_{Sat}) of more than 1400 Oe to stature film's magnetization. This type of hysteresis behavior with low remanence ratio ($M_R/M_S \sim 0.38$, where M_R is remnant magnetization and M_S is saturation magnetization) is called as transcritical loop [CRAU2002, PORR2002, SUNZ2004, SHAR2006, COIS2009, MISH2011, CHEN20131, SING2013, DASC20181], which is generally correlated to increase in effective magnetic anisotropy caused by the stress induced during the deposition of the films at a higher deposition rate to form amorphous structure.

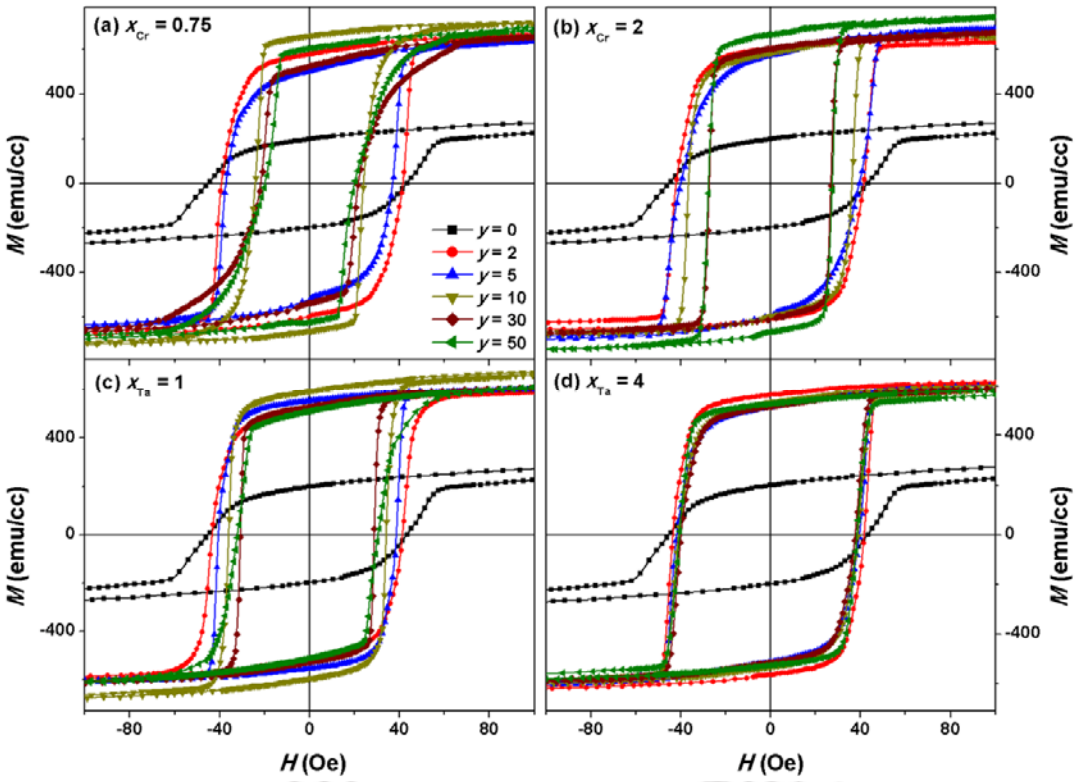

Figure 6.04: Room temperature *M-H* loops measured along the film plane for trilayer CoFeB262 (100 nm)/ [Cr, Ta (*x* nm)]/ CoFeB262 (*y* nm) films with (a) $x_{Cr} = 0.75$, (b) $x_{Cr} = 2$, (c) $x_{Ta} = 1$ and (d) $x_{Ta} = 4$ and different values of *y*.

In addition, this leads to the formation of magnetic dense stripe domain pattern in thick amorphous CoFeB262 films, as obtained and demonstrated in Figure 6.03(b). The width of the stripe domains determined by a fast Fourier transform analysis of the MFM image is

found to be about 135 nm, which is in good agreement with the earlier reports on similar amorphous systems [CRAU2002, PORR2002, SUNZ2004, SHAR2006, COIS2009].

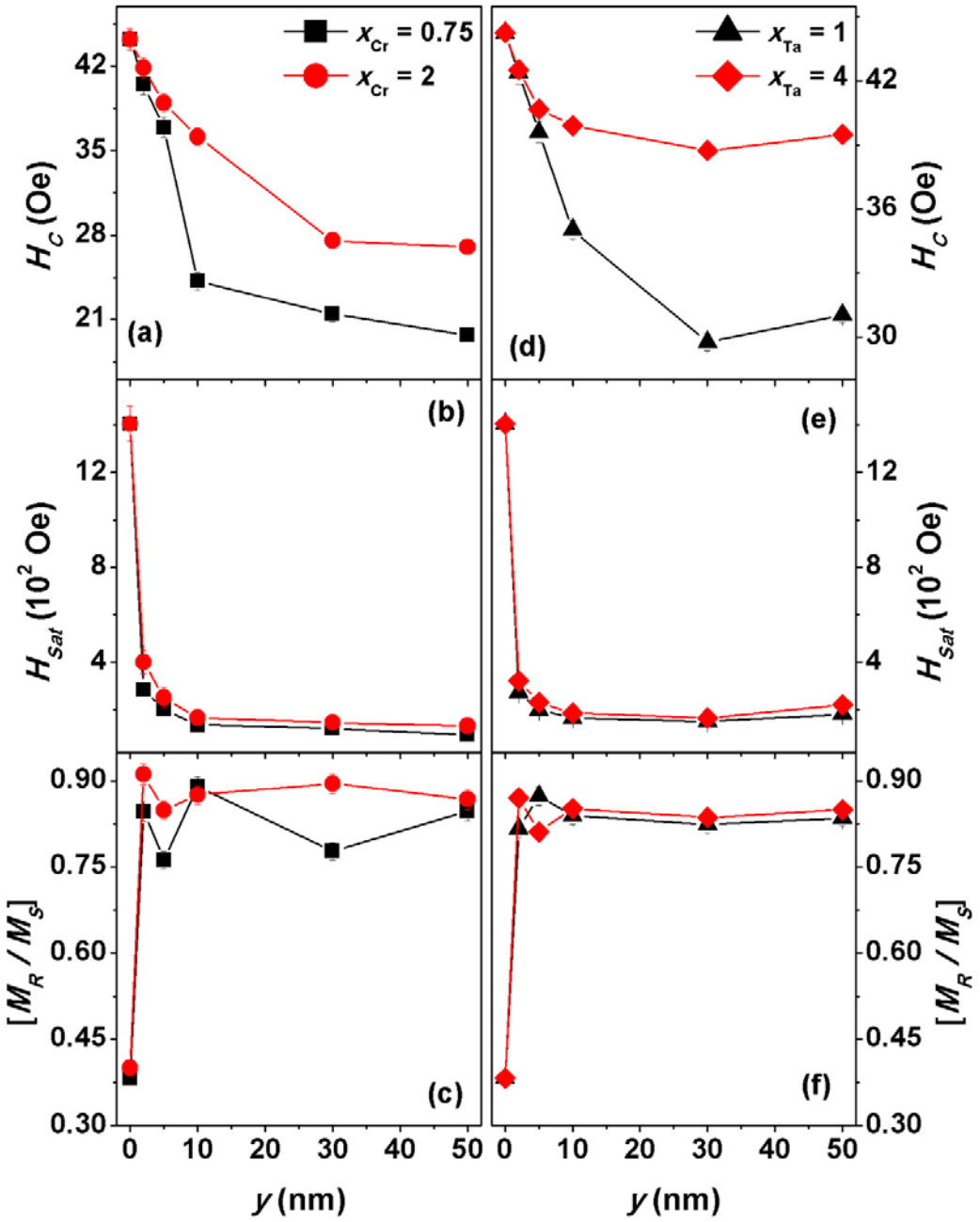

Figure 6.05: The variations of H_C, H_{Sat} and M_R/M_S as a function of y for trilayer CoFeB262 (100 nm)/ [Cr, Ta (x nm)]/ CoFeB262 (y nm) films with different spacer layer materials.

To study the effects of trilayer structures, spacer layer materials with different thicknesses (x) and thickness of the top CoFeB262 layers (y) on the room temperature magnetic properties of the thick CoFeB262 (100 nm) film, the room temperature *M-H* loops

are measured along the film plane for the trilayer films and shown in Figure 6.04. Figure 6.05 depicts the extracted parameters, such as H_C, H_{Sat} and M_R/M_S, plotted as a function of y for different x. For [CoFeB262 (100 nm)/ Cr (x nm)/ CoFeB262 (y nm)] films; (i) the shape of the *M-H* loop is observed to be transcritical for the film with $y = 0$. (ii) On the other hand, the introduction of top CoFeB262 film changes the nature of *M-H* loops drastically and all the trilayer films exhibit simple *M-H* loops with enhanced M_R/M_S and single magnetization reversal at H_C [see Figure 6.04(a)]. (iii) For instance, the introduction of even a thin top CoFeB262 layer (y = 2 nm, x_{Cr} = 0.75 nm) changes the loop shape drastically from transcritical into rectangular shaped loop and fades away the linear variation of magnetization before the saturation of magnetization. This certainly reduces H_{Sat} drastically from 1405 Oe to 285 Oe and enhances M_R/M_S from 0.38 to 0.85 [see Figure 6.05(b,c)]. (iv) With increasing y up to 10 nm, the rectangular shaped loops hold along with progressive reduction in H_C. (v) On further increasing $y > 10$ nm, the nature of magnetization reversal varies gradually with unfavorable shearing of the loop, i.e., a rapid fall in magnetization followed by a long-tailed loop before saturation. In addition, M_R/M_S varies sluggishly and H_{Sat} decreases slowly. (vi) H_C decreases almost linearly at a rate of 1.98 Oe/nm with increasing y up to 10 and then the rate of decrease in H_C decreases to 0.12 Oe/nm with the further increase in y from 10 to 50 nm [see Figure 6.05(a)]. (vii) With increasing x_{Cr} to 2 nm, the change in the loop shape is found to be different. In contrast to x_{Cr} = 0.75 films, no sheared loops are observed for films with x_{Cr} = 2 and $y > 10$. (viii) But, the magnitude of reduction in H_C decreases considerably. Similarly, for [CoFeB262 (100 nm)/ Ta (x nm)/ CoFeB262 (y nm)] films; (i) the shape of the *M-H* loops changes drastically with the introduction of top CoFeB262 layer and all the trilayer films exhibit simple *M-H* loops with enhanced M_R/M_S and single magnetization reversal at H_C. (ii) With increasing x_{Ta} from 1 to 4 nm, the shape of the loops is observed to be merely the same with a small reduction in H_C for films with different y. This provides almost similar *M-H* loops for films with x_{Ta} = 4 nm and y = 2 – 50 nm. In addition, these films with different x_{Ta} do not show any sheared loops for any values of y.

The observed changes in the magnetic properties of the trilayer films as compared to single-layer film can be explained based on the nature of coupling between the CoFeB262 films through spacer layers. Generally, the interlayer coupling between two ferromagnetic layers originates from (i) the direct exchange coupling between ferromagnetic layers through pinholes in thin spacer layer [PONG2008], (ii) indirect exchange coupling through the conduction electrons of the spacer layer [Ruderman–Kittel–Kasuya–Yosida (RKKY)]

[KUDR1997], (iii) the magnetostatic coupling induced by the correlated interfacial roughness, also known as orange peel coupling or Néel coupling as shown in Figure 6.06(a) [ZHAN19961, SCHR2000] and (iv) the magnetostatic coupling through stray fields of domain walls [see Figure 6.06(b)] [RIET1997, PRAD2004, HUBE2014], and (v) the magnetostatic coupling through the magnetic poles at the edges of the films [MURA1966, CRAU2003].

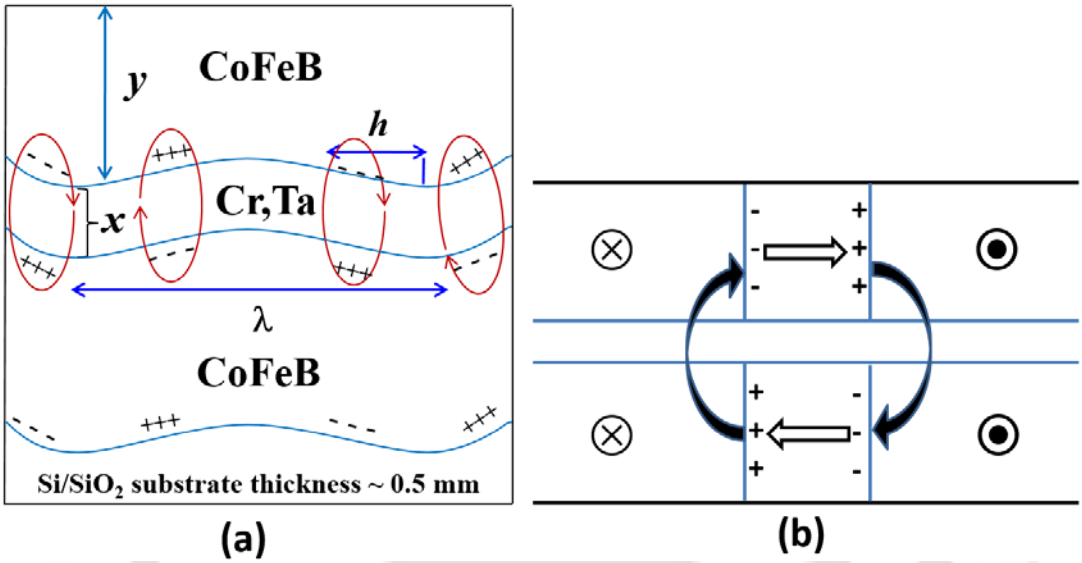

Figure 6.06: Schematic drawing of (a) Néel's orange peel coupling and (b) magnetostatic coupling between the stray fields of domain walls in trilayer thin films.

The single-layer film of CoFeB262 (100 nm) showed the transcritical loop due to the existence of in-plane and perpendicular magnetic components, which formed dense stripe domain structure. The introduction of even a thin top CoFeB262 layer with x_{Cr} = 0.75 nm changed the nature of *M-H* loop from transcritical into rectangular shaped loop. These results and the surface roughness of the bottom CoFeB262 layer suggest that the interlayer coupling due to the direct ferromagnetic coupling through pinholes and the indirect exchange coupling through RKKY interaction depends strongly on *x*. Since the average surface roughness of the bottom CoFeB262 (100 nm) layer is observed to be between 0.4 nm and 0.7 nm, the growth of the subsequent Cr space layer with x_{Cr} = 0.75 nm on top of thick CoFeB262 layer may not be continuous all the way and therefore the top CoFeB262 layer may not be well separated from the bottom CoFeB262 layer perfectly. As a result, there exists a direct exchange coupling between CoFeB262 layers at random locations depending on the roughness. This arrangement helps to switch the CoFeB262 layers

collectively and displays simple loop. However, with increasing $y > 10$, the rectangular shaped loop changed into sheared loop with long tailing. Navas et al. [NAVA2014] reported thickness dependent slow approach to saturation in CoCrPt films and attributed to the existence of small bubble domains that are magnetostatically stabilized by the surrounding regions [DAVI2004]. Similarly, Park et al. [PARK2008] reported that with increasing N in $(Co/Pt)_N$ films, the shape of the *M-H* loops deviated away from perfect rectangular shape to sheared loop with long-tailing. This was correlated to the inherited increase in interface roughness accompanied with increasing the film thickness since a large interface roughness with increasing N is likely to cause local variation of the perpendicular anisotropy and broadening the pinning field distribution. Therefore, the observed sheared loop for trilayer films with $x_{Cr} = 0.75$ nm could be attributed to the increase in local variation of in-plane anisotropy in top CoFeB262 layer with increasing y [PRAD2004, GAYE2017], which changes the nature of magnetic interaction between CoFeB262 layers. With increasing $x_{Cr} = 0.75$ to 2 nm in trilayer films, no shearing of the loops was observed with increasing y. This could be attributed to the fact that with increasing x_{Cr}, the direct interaction between CoFeB262 layers is preferably discontinued and hence the interaction between CoFeB262 layers is majorly of magnetostatic in nature. In addition, the stray field coupling is always present in magnetic multilayers, because each ferromagnetic layer is placed in the demagnetization field of the others, which tends to align the magnetization of adjacent layers. But, the interlayer magnetostatic interaction through the stray fields at the edges of the continuous film of larger dimensions may be assumed to be weak [ANGU2000, THOM2000] and hence any contribution to the net coupling from stray fields is almost negligible [BALT2007, LIUX2012].

On the other hand, the Néel coupling is magnetostatic in nature, which strongly depends on the interfacial phenomena. If the surface of ferromagnetic layers has correlated roughness, then dipoles are set up at homologous protrusions and bumps at the interfaces as shown in Figure 6.06(a). Such arrangements favor ferromagnetic alignment between the nearest magnetic layers. Therefore, the Néel coupling caused by the correlated interface roughness [Figure 6.06(a)] and magnetostatic coupling between the stray fields of domain walls [Figure 6.06(b)] play a key role on the magnetization reversal process of the trilayer films. The magnitude of the Néel coupling field is given as [SCHR2000],

$$H_C = \frac{\pi^2}{\sqrt{2}}\left(\frac{h^2}{\lambda y}\right) M_S exp\left(-\frac{2\pi\sqrt{2}x}{\lambda}\right) \qquad (6.01)$$

where, h and λ are the amplitude and wavelength of the interface roughness, x and y are the thicknesses of the spacer layer and top CoFeB262 layer and M_S is the saturation magnetization of the free layer respectively. The magnetostatic coupling between CoFeB262 layers disrupts the magnetic dense stripe domain in bottom layer and enhances the magnetic softness. Nevertheless, the magnitude of reduction in H_C decreases with increasing x_{Cr}. This could be attributed to the spacer layer thickness dependent coupling between CoFeB262 layers [KOOL1999, SCHR2000, WIES2006], which decreases with increasing x as given in eqn.(6.01). This argument also supports the results observed for trilayer films with Ta spacer layer materials, i.e., the change in the loop shape for trilayer films with x_{Cr} = 2 nm and x_{Ta} = 1 nm is found to be nearly the same. With increasing x_{Ta} = 4 nm, we observed almost same type of loops for all films, which could be related to the reduced coupling between CoFeB262 layers through thick Ta spacer layer [FENG1995, NAOE1998, HUAN2001, NAKA2001, SING2013]. As a result, H_C reduces sluggishly as compared to all other films.

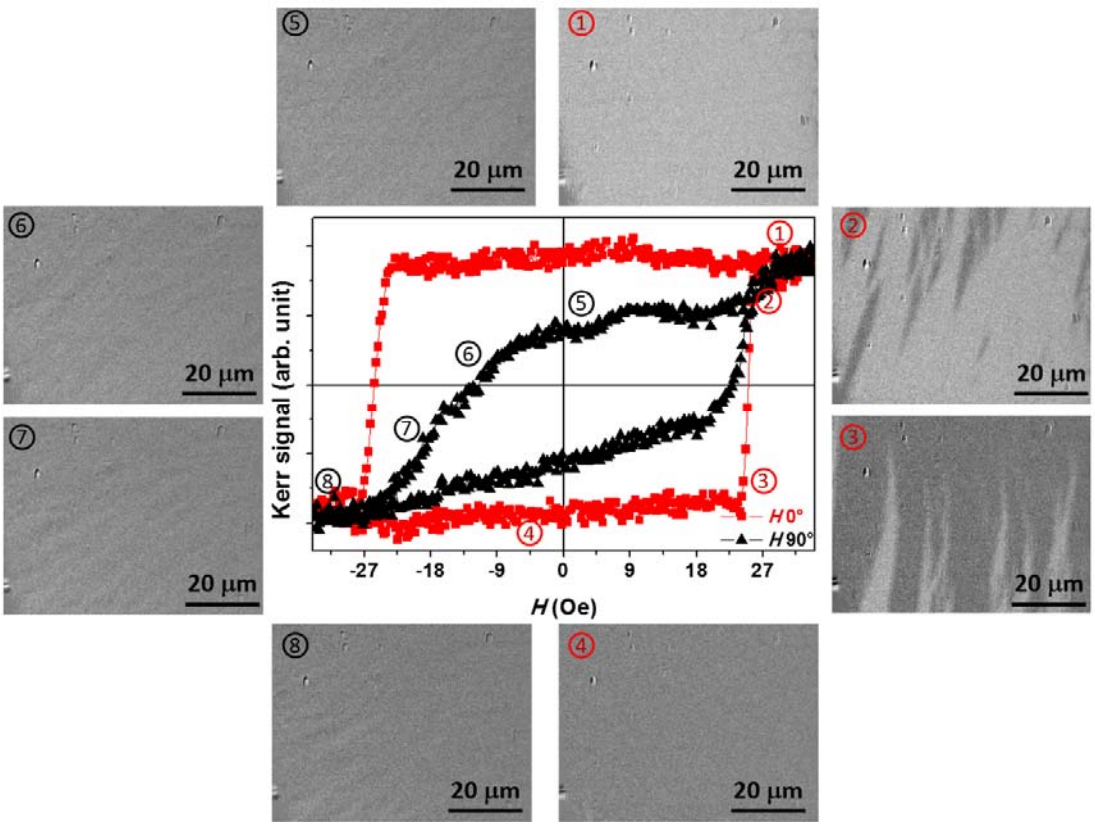

Figure 6.07: Room temperature Kerr loops measured along the film planes and magnetic domain images for trilayer film of [CoFeB262 (100 nm)/ Cr (0.75 nm)/ CoFeB262 (10 nm)].

To further understand the magnetic coupling and magnetic interaction in trilayer structured films, we have investigated the magnetization reversal behavior along the film plane using MOKE microscopy. Figures 6.07 and 6.08 display the typical Kerr loops and magnetic domain images for the trilayer films with $x_{Cr} = 0.75$ and $y = 10$ nm and $x_{Ta} = 1$ and $y = 10$ nm. It is clearly evident that trilayer film with $x_{Cr} = 0.75$ displays rectangular shaped loop in one direction [easy-axis direction in the plane (0°)] and nearly imprecise loop characterized by reduced remanence in another direction [hard-axis direction in the plane (90°)]. The magnetic domain images obtained along the easy-axis show a rapid switching of large-sized domains due to domain wall motion. The magnetic field required to switch the magnetization along the easy-axis from one direction to another direction is observed to be quite low (< 5 Oe).

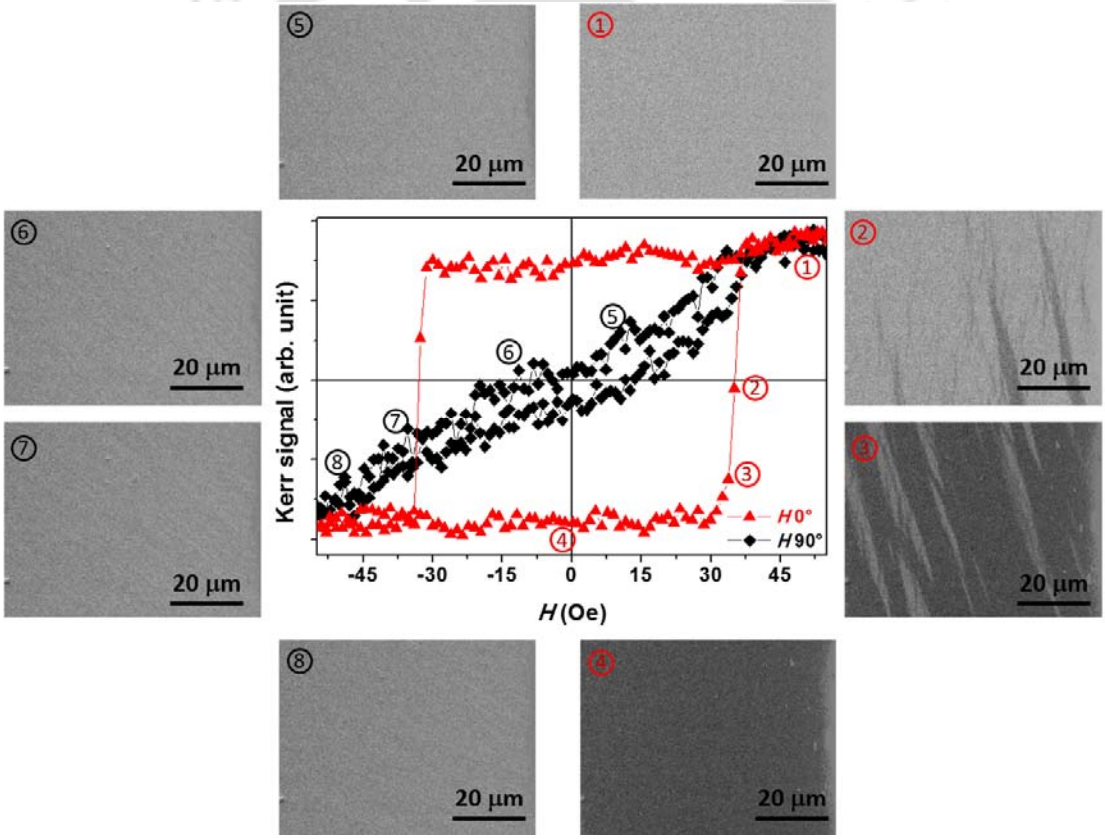

Figure 6.08: Room temperature Kerr loops measured along the film planes and magnetic domain images for trilayer film of [CoFeB262 (100 nm)/ Ta (1 nm)/ CoFeB262 (10 nm)].

From the VSM results [see Figure 6.04(a)], the applied field required to switch the magnetization from one direction to another direction is found to be nearly 30 Oe, which is much larger than the one obtained from MOKE microscopy. This could be attributed to the

contribution from the finite edge effect of the sample used in VSM measurement. On the other hand, the magnetic domain images obtained along the hard-axis reveal a weak ripple domains possibly due to an inhomogeneous local magnetic anisotropy distribution [NOWA1993] caused by the interaction between CoFeB262 layers from the direct ferromagnetic coupling at random locations. For the trilayer film with x_{Ta} = 1 nm, we have observed almost similar results along the easy-axis, i.e., a rapid switching of large-sized domains due to domain wall motion with slightly larger applied field (~ 6.2 Oe) required to switch the magnetization from one direction to another direction. However, the Kerr loop obtained along the hard-axis is found to be nearly straight line without any significant loop close to origin. Interestingly, the magnetic domain images along the hard-axis illustrate a clear coherent like rotation process, but with very faint ripple domains. These results clearly confirm that the magnetic properties of the thick CoFeB262 layers with dense stripe domain structure can easily be tuned in to in-plane magnetization by this simple trilayer structure concept. This is found to be much easier approach than the earlier reported methods of fabricating more number of multilayers [HUAN2001, MISH2011, DASC20181].

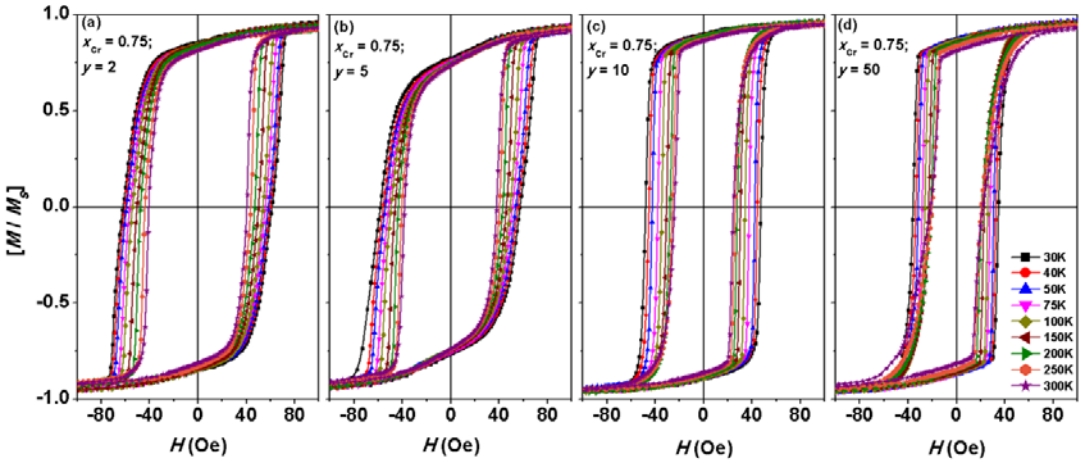

Figure 6.09: *M-H* loops measured along the film plane at different temperatures for trilayer [CoFeB262 (100 nm)/ Cr (0.75 nm)/ CoFeB262 (*y* nm)] films with different values of *y*.

6.3.2.2. Temperature dependent magnetic properties

As the magnetic properties of the films are affected by the measurement temperature, it is very much essential to understand the change in the magnetic interaction and interlayer coupling between CoFeB262 layers in trilayer films as a function of *T*. Therefore, *M-H* loops are measured along the film plane at different *T* ranging between 30 K and 300 K for all the series of films.

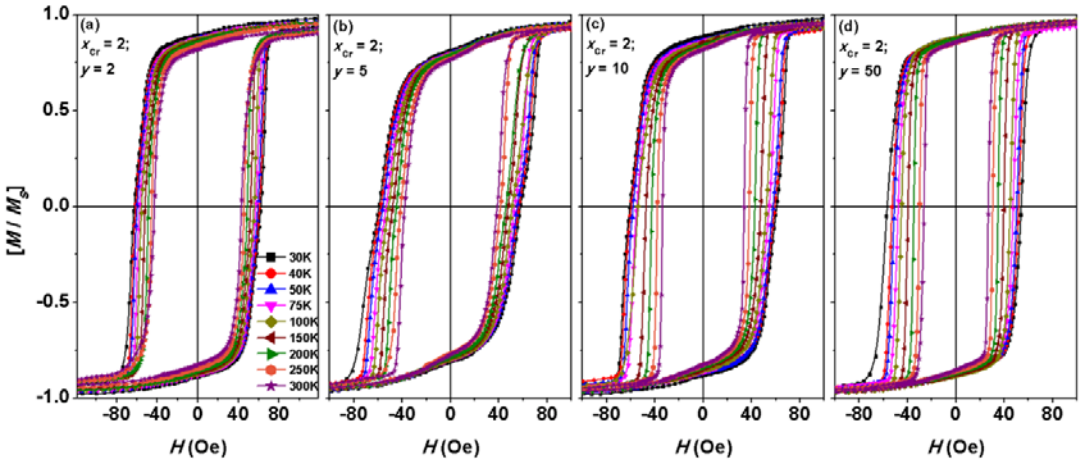

Figure 6.10: *M-H* loops measured along the film plane at different temperatures for trilayer [CoFeB262 (100 nm)/ Cr (2 nm)/ CoFeB262 (*y* nm)] films with different values of *y*.

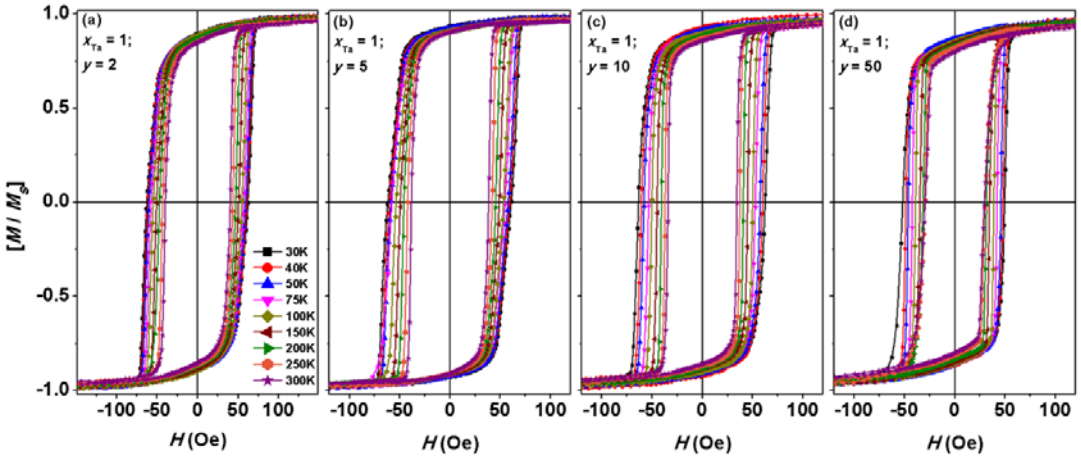

Figure 6.11: *M-H* loops measured along the film plane at different temperatures for trilayer [CoFeB262 (100 nm)/ Ta (1 nm)/ CoFeB262 (*y* nm)] films with different values of *y*.

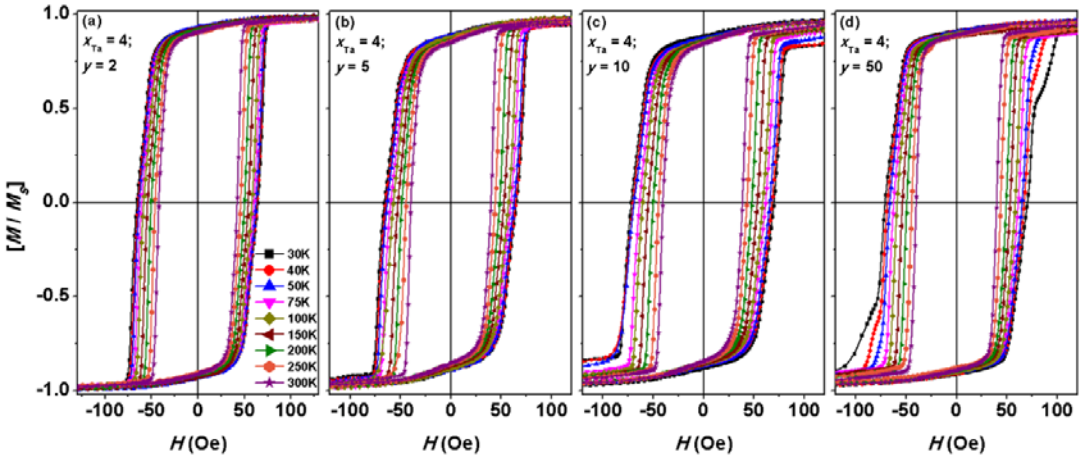

Figure 6.12: *M-H* loops measured along the film plane at different temperatures for trilayer [CoFeB262 (100 nm)/ Ta (4 nm)/ CoFeB262 (*y* nm)] films with different values of *y*.

Figures 6.09 and 6.10 display *M-H* loops obtained at different temperatures for films with x_{Cr} = 0.75 and 2, respectively. Similarly, Figures 6.11 and 6.12 depict *M-H* loops obtained at different temperatures for films with x_{Ta} = 1 and 4, respectively. *M-H* loops obtained at different *T* reveal the following features: For trilayer films with x_{Cr} = 0.75 [see Figure 6.09], (i) with decreasing *T*, the shape of the loops does not change for *y* up to 5 nm. However, the area under the loops increases progressively with decreasing temperature. This behavior is similar to the one observed for a typical ferromagnetic material. In addition, all the loops exhibit single magnetization reversal behavior suggesting that both top and bottom CoFeB262 layers reverse collectively at all *T*. (ii) With increasing $y \geq 10$, the shearing of the loop observed at room temperature diminishes with decreasing *T* and the loop shape turns out to be rectangular shape at *T* below 200 K, (iii) interestingly the temperature at which the shearing of the loop diminishes shifts to lower *T* with increasing *y*, i.e., for the film with *y* = 50, the sheared loop transforms into rectangular shaped one at *T* below 75 K. This could be attributed to the enhanced coupling between CoFeB262 layers as the average magnetization increases, and possibly because of reduction in local variation of in-plane anisotropy in top CoFeB262 layer with decreasing *T*. In contrast, we have not observed any major change in the loop shape with decreasing *T* for films with x_{Cr} = 2 nm and different *y* (see Figure 6.10) Similarly, no change in the loop shapes is observed for trilayer films with x_{Ta} = 1 nm and *y* = 2 − 50 nm (Figure 6.11) and x_{Ta} = 4 nm and *y* = 2 – 5 (Figure 6.12). However, with increasing $y \geq 10$ nm for films with x_{Ta} = 4 nm, we observed not only sheared loops at lower *T* below 50 K [see Figure 6.12(c)], but also additional step like behavior before saturation, which is more pronounced with decreasing *T* [see Figure 6.12(d)]. This could be correlated to (i) reduction in interlayer coupling between CoFeB262 layers with increasing *x* [SCHR2000, HUAN2001, SING2013] and (ii) strong temperature dependent interfacial strain realized from the substrate on thick CoFeB262 (100 nm) bottom layer due to the different thermal expansion coefficients of the film and substrate [HUAN2001, COIS2009, SING2014, SING20161, SING20162], which does not allow CoFeB262 (100 nm) layer to switch collectively with the top CoFeB262 (20 nm) layer.

To quantitatively understand the effect of *T* on the magnetic parameters, the extracted values of H_C are plotted as a function of *T* and *y* in Figures 6.13 and 6.14 for films with x_{Cr} and x_{Ta}, respectively. The relative variation of H_C, i.e., $H_C(T)/H_{C@300K}$ is also plotted as a function of *T* for both the series as insets. H_C increases with decreasing *T* for all the films. However, the amount of increase in H_C depends on the values of *x*, *y* and *T*. For

instance, the single-layer thick CoFeB262 film exhibits a non-linear variation of $H_C(T)$ and H_C varies from 47 Oe to 130 Oe with decreasing T from 300 K to 30 K. As a result, $H_C(T)/H_{C@300K}$ increases by 2.7 times. On the other hand, the variation in $H_C(T)$ decreases largely for the trilayer films, i.e., H_C increases from 40.5, 25.4 and 20.3 Oe to 61.6, 47.6 and 35.4 Oe, respectively for the films with x_{Cr} = 0.75 nm and y = 2, 10 and 50 nm. Accordingly, the maximum variation of $H_C(T)/H_{C@300K}$ is found to be 1.53, 1.88, and 1.75 for the films with x_{Cr} = 0.75 nm and y = 2, 10 and 50 nm.

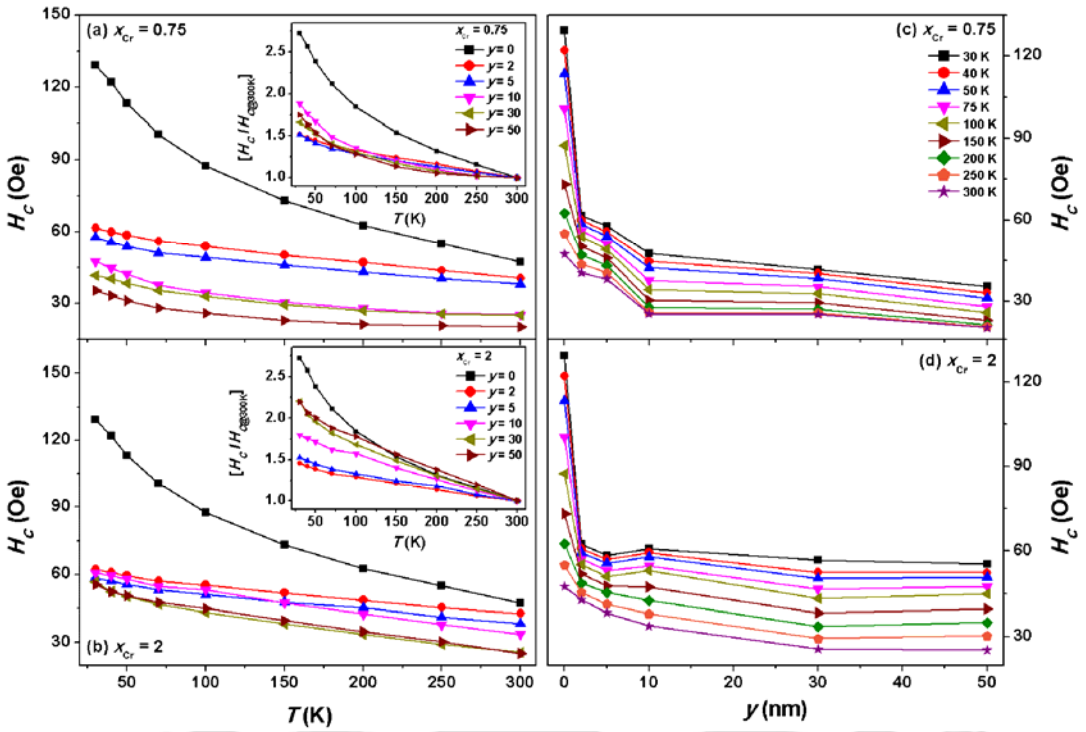

Figure 6.13: The variations of H_C as a function of temperature and y for trilayer CoFeB262 (100 nm)/ [Cr (x nm)]/ CoFeB262 (y nm) films with different values of x_{Cr} and y. Inset shows the normalized coercivity, $H_C(T)/H_{C@300K}$, plotted as a function of temperature.

On the other hand, with increasing spacer layer thickness from 0.75 to 2 nm, the variation of $H_C(T)$ for different y values diminishes, i.e., H_C increases from 42.8, 33.7, 25.2 Oe to 62.3, 60.7, 55.5 Oe, respectively for the films with x_{Cr} = 2 nm and y = 2, 10 and 50 nm. Similarly, the plot of H_C as a function of y at different T [see Figure 6.13 (c) and (d)] shows that (i) H_C decreases not only with increasing y, but also with increasing T at a particular y and (ii) the amount of reduction in H_C strongly dependent on the values of x. These results suggest that with increasing T, the coupling between top and bottom

CoFeB262 layers is modified due to temperature dependent magnetization and interfacial strain, which helps them to reverse faster and leads to a reduction in H_C.

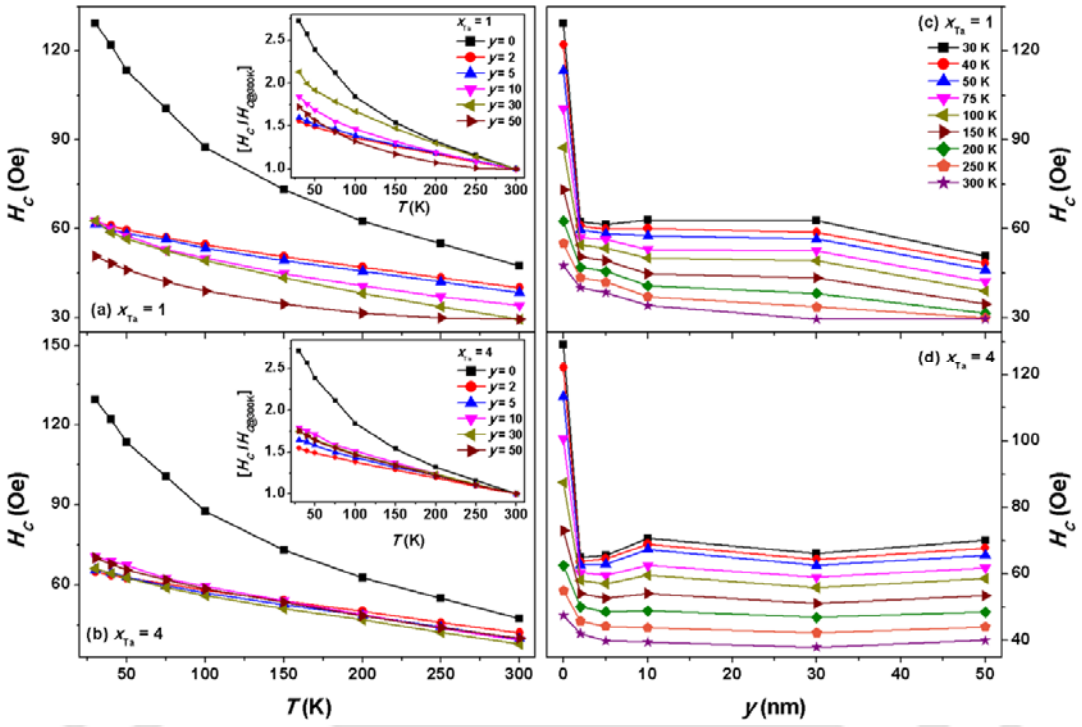

Figure 6.14: The variations of H_C as a function of temperature and y for trilayer CoFeB262 (100 nm)/ [Ta (x nm)]/ CoFeB262 (y nm) films with different values of x_{Ta} and y. Inset shows the normalized coercivity, $H_C(T)/H_{C@300K}$, plotted as a function of temperature.

A similar nature of $H_C(T)$ is also observed for trilayer films with Ta spacer layer, but the relative variation in H_C is found to be nearly insensitive to y for the trilayer films with large spacer layer thickness of x_{Ta} = 4 nm (see Figure 6.14). For instance, H_C increases from 40.1, 34.1 and 29.5 Oe to 62.4, 62.9 and 50.8 Oe and from 42.1, 39.4 and 39.9 Oe to 64.9, 70.7, 70.2 Oe, respectively for the films with x_{Ta} = 1 nm and x_{Ta} = 4 nm with y = 2, 10 and 50 nm. This could be attributed to the effective reduction in the interlayer coupling with increasing x.

To study $H_C(T)$ behavior in more details, $H_C(T)$ versus T curves for all the series of the films are analyzed using thermal activation effect and fitted using eqn.(6.02).

$$H_C(T) = H_0\left[1 - \left(\frac{k_B T ln(t/t_0)}{E_0}\right)^{1/\alpha}\right] \qquad (6.02)$$

where H_0 is coercivity at zero temperature, k_B is Boltzmann constant, E_0 is energy barrier, t is the time necessary to jump over the energy barrier at temperature T and t_0 is treated as a

constant typically of the order of 10^{-9} to 10^{-11} sec. Almost all series of the data could be fitted using eqn.(6.02) and by taking $\alpha = 2$ for T between 50 K and 300 K. However, the extension of T below 50 K shows obvious deviation of $H_C(T)$ from eqn.(6.02) due to larger increase in H_C at low temperatures. Considering the magnetization reversal process in these trilayer films as domain wall motion (see Figures 6.07 and 6.08) [THOM1997], the behavior of $H_C(T)$ is further analyzed using eqn.(6.03)

$$H_C^{1/2}(T) = H_0^{1/2} + AT^{2/3} \qquad (6.03)$$

where H_0 is coercivity at zero temperature and A is a constant. Interestingly, H_C versus T could be fitted using eqn.(6.03) over the complete temperature range of $30 - 300$ K and the extracted parameters are listed in Table 6.01.

Table 6.01: The variation of H_0 and A for trilayer films with different spacer layer materials (x) and top CoFeB262 layer thickness (y). The number given within the parenthesis represents the error with respect to last decimal value.

y	$x_{Cr} = 0.75$		$x_{Cr} = 2$		$x_{Ta} = 1$		$x_{Ta} = 4$	
	$H_0^{1/2}$ ($Oe^{1/2}$)	A ($Oe^{1/2}$ $K^{3/2}$)	$H_0^{1/2}$ ($Oe^{1/2}$)	A ($Oe^{1/2}$ $K^{3/2}$)	$H_0^{1/2}$ ($Oe^{1/2}$)	A ($Oe^{1/2}$ $K^{3/2}$)	$H_0^{1/2}$ ($Oe^{1/2}$)	A ($Oe^{1/2}$ $K^{3/2}$)
0	12.35 (4)	-0.127 (2)	12.35 (4)	-0.127 (2)	12.35 (4)	-0.127 (2)	12.35 (4)	-0.127 (2)
2	8.22 (3)	-0.041 (5)	8.24 (3)	-0.038 (2)	8.33 (3)	-0.044 (3)	8.53(3)	-0.044 (2)
5	7.89 (2)	-0.039 (3)	8.02 (3)	-0.040 (1)	8.29 (2)	-0.046 (2)	8.62 (2)	-0.050 (4)
10	7.21 (4)	-0.054 (4)	8.39 (2)	-0.056 (2)	8.40 (2)	-0.059 (3)	9.01 (4)	-0.060 (3)
30	6.76 (3)	-0.043 (4)	8.05 (4)	-0.066 (3)	8.49 (1)	-0.068 (2)	8.67 (3)	-0.055 (3)
50	6.14 (5)	-0.041 (2)	8.04 (3)	-0.065 (2)	7.45 (3)	-0.050 (2)	8.90 (2)	-0.057 (2)

While the values of $H_0^{1/2}$ and A exhibit oscillatory nature with increasing y for all the films with Ta spacer layer, the variation of $H_0^{1/2}$ and A strongly depends on x_{Cr} due to different types of interaction between CoFeB262 layers in trilayer films depending on the values of x_{Cr}. These observed results suggest that temperature together with the thickness of the top CoFeB262 layer and type of spacer material has an intense effect in tuning the magnetization reversal process of thick CoFeB262 layer in trilayer films. To the best of our knowledge, this is the first detailed report on tuning magnetic properties of a thick CoFeB262 film, having dense stripe domain structure, by fabricating simple trilayer structure and also on examining the effect of thickness of top CoFeB262 layer, different spacer material, and temperature on the resulting magnetic properties of trilayer films.

6.4. Summary

A systematic investigation of effect of trilayer structure, the spacer layer materials and its thickness (x), the thickness of top CoFeB262 layers (y) and temperature on the magnetic properties of the thick CoFeB262 (100 nm) films by using interlayer magnetic coupling in trilayer films of CoFeB262 (100 nm)/ [Cr,Ta (x nm)] / CoFeB262 (y nm) has been carried out. The salient features of the trilayer films from the current investigations are as follows:

- Amorphous trilayer films of [CoFeB262 (100 nm)/ [Cr, Ta (x nm)]/ CoFeB262 (y nm)] with different top layer thicknesses (y = 2, 5, 10, 30 and 50 nm), and different spacer layer (Cr and Ta) thicknesses (x_{Cr} = 0.75, 2 nm and x_{Ta} = 1, 4 nm) are successfully prepared directly on the thermally oxidized Si substrate at ambient temperature using DC magnetron sputtering technique.
- Amorphous nature of the as-deposited CoFeB films is confirmed through XRD and TEM studies.
- Atomic force microscopy study shows the existence of very fine and sparsely dispersed nanosized grains of size ranging between 11 nm and 15 nm. The topography pattern of 100 nm film exhibits a very clear uniform surface and the average roughness of the surface is found between 0.4 nm and 0.7 nm.
- The single-layer as-deposited amorphous CoFeB262 (100 nm) film exhibits magnetic dense stripe domain and transcritical hysteresis loop due to large effective magnetic anisotropy caused by the stress induced during deposition of the films.
- The shape of magnetic hysteresis loops in trilayer films transforms from transcritical loop to rectangular loop with enhanced remanence ratio (M_R/M_S) of

more than 75 % and single magnetization reversal behavior at coercivity. This is attributed to the magnetic coupling between top and bottom CoFeB262 layers through the spacer layers (Cr and Ta). The changes in the loop shape and reductions in H_C and H_{Sat} depend strongly on the values of x and y.

- Magnetic domain images obtained using Kerr microscopy in trilayer films show rapid switching of large-sized domains along the easy-axis and weak ripple domains along the hard-axis. In addition, the nature of magnetic domains along the hard-axis strongly depend on $x_{(Cr,Ta)}$.
- *M-H* loops obtained at different low temperatures reveal almost no change in the loop shape for trilayer films with small values of x and y. However, the disappearance of shearing in the loop shape and formation of additional steps at low temperatures are observed for trilayer films with large values of x and y.
- The temperature dependent H_C could be well fitted over the entire temperature range by considering the magnetization reversal process in these trilayer films as domain wall motion.
- The observed results are explained on the basis of change in interlayer coupling between CoFeB262 layers with x, y and T. Furthermore, the obtained results clearly confirm that the magnetic properties of thick CoFeB262 films with dense stripe domain could easily be tuned in to in-plane magnetization by this simple trilayer films.

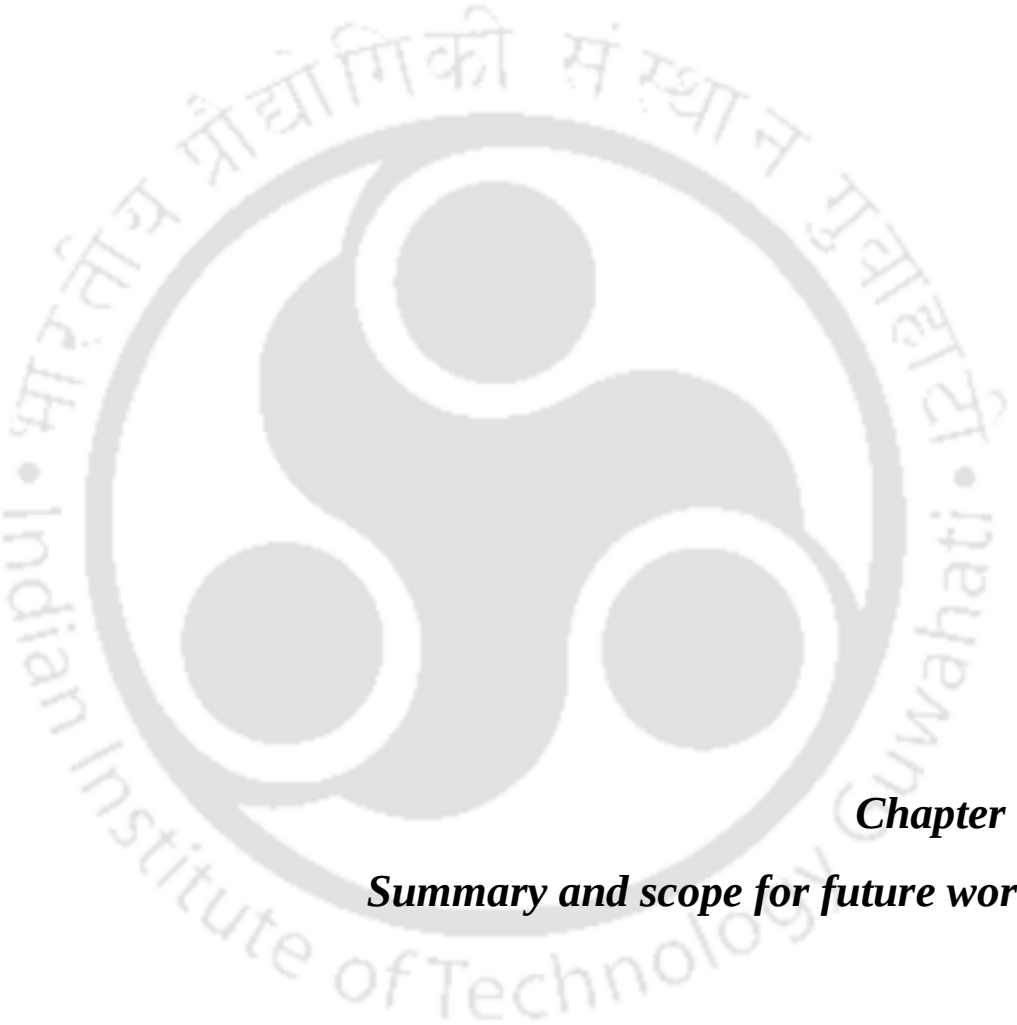

Chapter 7

Summary and scope for future work

The overall summary of the significant results obtained on the structural and magnetic properties of CoFeB (*t* nm) single-layer films of different thicknesses and compositions and trilayer [CoFeB (*y* nm)/Cr, Ta (*x* nm)/CoFeB (*y* nm)] films is described in this chapter. Highlights of the current investigations and the possibilities for future work are also summarized below:

7.1. Summary of the results

Amorphous single-layer films of $Co_{80-y}Fe_yB_{20}$ (*t* nm) with two different compositions [$Co_{40}Fe_{40}B_{20}$ (CoFeB442) and $Co_{20}Fe_{60}B_{20}$ (CoFeB262)] and different thicknesses (*t* = 7, 10, 15, 20, 50, 75, 100 and 200 nm), (ii) trilayer [CoFeB262 (*y* nm)/ Cr, Ta (*x* nm)/ CoFeB262 (20 nm)] films with symmetric (*y* = 20) and asymmetric (*y* = 100) domain structures and *x* = 0 – 6 nm (0, 0.25, 0.5, 0.75, 1, 2, 4, 6 nm), and (iii) trilayer [CoFeB262 (100 nm)/ [Cr, Ta (*x* nm)]/ CoFeB262 (*y* nm)] films with *y* = 2, 5, 10, 30, 50 nm, x_{Cr} = 0.75, 2 nm and x_{Ta} = 1, 4 nm were prepared using DC magnetron sputtering technique at ambient temperature directly on the thermally oxidized Si substrates.

Structural investigations using X-ray diffraction and transmission electron microscopy techniques confirmed the existence of amorphous structure in all the as-deposited CoFeB films. The results of thickness determination from X-ray reflectivity (XRR) analysis, analytical relation and surface profilometer were in close agreement with each other. The average surface roughness obtained from the XRR studies increased significantly from 0.22 nm to 0.7 nm with increasing film thickness from 10 to 100 nm, respectively. Surface morphology study using atomic force microscope revealed that the existence of very fine and sparsely dispersed nanosized grains of size ranging between 10 nm and 15 nm in the as-deposited films. The topography pattern of the films exhibited a very clear uniform surface and the average roughness of the surface was found to be in the range of 0.3-0.6 nm and 0.4-0.7 nm for CoFeB262 films with *y* = 20 and 100, respectively.

The magnetic properties of CoFeB (*t* nm) single-layer films revealed a strong thickness dependence in the thickness range between 7 nm and 200 nm. CoFeB ($t \leq 20$ nm) films exhibited soft magnetic nature with rectangular or flat-type loops due to in-plane magnetization with uniaxial anisotropy. With increasing $t > 50$ nm, the soft magnetic properties were degraded due to the transition of in-plane magnetization to dense stripe domain caused by the enhancement of effective magnetic anisotropy (K_{eff}) induced by the stress quenched in during deposition at a faster deposition rate to form amorphous structure.

Room temperature coercivity (H_C) and saturation field (H_{Sat}) increased almost linearly with increasing t between 7 and 20 nm, but exhibited a rapid increase for the films with t up to 100 nm and then decreased slightly for t = 200 nm film. The temperature dependent magnetic properties revealed that while the nature of the loops did not change significantly with the temperature for a particular film, the maximum relative change in H_C decreased from 4.61 to 1.49 and from 3.98 to 2.72 with increasing t for CoFeB442 and CoFeB262 films, respectively. K_{eff} determined at different temperatures showed a compositional dependent properties mainly due to the change in H_{Sat} values with film thickness and composition. High-temperature thermomagnetization data depicted a clear magnetic phase transition from ferromagnetic state to paramagnetic state with Curie temperature of above 520 K. The observed results were explained based on the development of compositional and thickness dependent effective magnetic anisotropy and change in the magnetic domain structure with increasing CoFeB film thickness.

In order to study the magnetic interactions between CoFeB262 layers having same domain structure (symmetric) and different domain structures (asymmetric) and also to study the effects of different spacer layer materials and its thickness and temperature, trilayer [Substrate/CoFeB262 (y nm)/[Cr,Ta (x nm)]/CoFeB262 (20 nm)] films with y = 20 (symmetric) and 100 (asymmetric), and x = 0 – 6 were prepared by using DC magnetron technique at ambient temperature directly on thermally oxidized Si substrate. The shape of magnetic hysteresis (M-H) loops of single-layer CoFeB262 (y nm) films transformed from rectangular shape for CoFeB262 (20 nm) film to transcritical one for CoFeB262 (100 nm) film. This was attributed to change in magnetic domain structure from in-plane magnetization to dense stripe domain with increase in y. On the other hand, the shape of the M-H loops in trilayer films strongly dependent on x, y and temperature. All symmetric trilayer films at room temperature showed single magnetization reversal at room temperature, (i) with a kink in the first quadrant for films with x_{Cr}<1, but (ii) without any kink for all values of x_{Ta}. For asymmetric trilayer films, the transcritical loop shape changed into rectangular one with the introduction of spacer layer (for both Cr and Ta). This led to a large reduction in H_{sat} and sharp enhancement in squareness (M_R/M_S). However for x_{Ta} = 6, the rectangular loop again changed towards transcritical. H_C, H_{sat} and M_R/M_S showed strong dependence on spacer layer materials and its thickness for both symmetric and asymmetric trilayer films. Magnetic domain images obtained using Kerr microscopy in trilayer films displayed rapid switching of large-sized domains along the easy-axis and weak ripple domains along the hard-axis. In addition, the nature of magnetic domains along the hard-

axis strongly dependent on spacer layer materials. Temperature dependent *M-H* loops revealed (i) the disappearance of the kink in Cr symmetric trilayer films and (ii) single magnetization reversal at H_C for all value of x_{Ta} throughout the temperature range. Temperature dependent *M-H* loops for asymmetric trilayer films showed the formation of additional steps with $x > 0.5$ for both spacer layer materials. The relative increase in H_C with decreasing temperature was found to be larger for symmetric films as compared to asymmetric ones for both spacer layer materials. The observed results were explained on the basis of change in the interlayer coupling between CoFeB262 layers with change in *x*, *y* and temperature dependent interfacial strain, which modified the nature of interlayer coupling. The obtained results also demonstrated that dense stripe domain of thicker CoFeB262 layers could be easily converted into simple in-plane magnetization by resorting to asymmetric trilayer thin film structure.

In order to control the development of random magnetic anisotropy, complex magnetic domain structure at larger *t* (> 50 nm) and to improve soft magnetic properties of thick CoFeB262 films, trilayer [Substrate/CoFeB262 (100 nm)/[Cr,Ta (*x* nm)]/CoFeB262 (*y* nm)] films with *y* = 2, 5, 10, 30 and 50 nm, x_{Cr} = 0.75, 2 nm and x_{Ta} = 1, 4 nm were fabricated by using DC magnetron technique at ambient temperature directly on thermally oxidized Si substrate. The single-layer as-deposited amorphous CoFeB262 (100 nm) film displayed magnetic dense stripe domain and transcritical hysteresis loop. Interestingly, the shape of magnetic hysteresis loops in trilayer films transformed from transcritical loop to rectangular loop with enhanced remanence ratio (M_R/M_S) of more than 75 % and single magnetization reversal behavior at coercivity. This was attributed to the magnetic coupling between top and bottom CoFeB262 layers through the spacer layers (Cr and Ta). The changes in the loop shape and reductions in H_C and H_{Sat} depend strongly on the values of *x* and *y*. Magnetic domain images obtained using Kerr microscopy in trilayer films showed rapid switching of large-sized domains along the easy-axis and weak ripple domains along the hard-axis. In addition, the nature of magnetic domains along the hard-axis strongly dependent on $x_{(Cr,Ta)}$. *M-H* loops obtained at different low temperatures revealed almost no change in the loop shape for trilayer films with small values of *x* and *y*. However, the disappearance of shearing in the loop shape and formation of additional steps at low temperatures were observed for trilayer films with large values of *x* and *y*. The temperature dependent H_C could be well fitted over the entire temperature range by considering the magnetization reversal process in these trilayer films as domain wall motion. The obtained

results clearly confirmed that the magnetic properties of thick CoFeB262 films with dense stripe domain could easily be tuned in to in-plane magnetization by this simple trilayer films. This approach has been found to be much easier approach than the earlier reported methods of fabricating more number of multilayers.

7.2. Scope for future work

The current investigations have brought out some new and interesting aspects and characteristics of CoFeB single-layer and trilayer thin films. These observations have not only exposed the potential of this material and trilayer films for specific applications in modern magneto-electronic devices, but have also shown paths for future scope of work in CoFeB single-layer and trilayer films. Some of the possibilities are briefly discussed below to serve as appropriate conclusion to the current thesis work.

Since the trilayer thin films exhibit single and multistep magnetization reversal behaviors depending on the spacer layer materials and its thickness, and the changeover in the magnetic domains from dense stripe domain to in-plane magnetization in trilayer films, it would be interesting to measure the electrical transport properties in these trilayer films as a function of applied magnetic field (magnetoresistance), spacer layer thickness and at different temperatures. This would hopefully reveal a correlation between the magnetic and transport properties, provided the transport properties are affected by the change in the domain structure, spacer layer materials and its thickness. Furthermore, the nature of the interlayer coupling between the ferromagnetic layers in the trilayer films depends on the thickness of spacer and ferromagnetic layers. In the current investigation, we have analyzed the switching of magnetic domains in trilayer films at two different angles [easy-axis (0°) and hard-axis (90°)] along the film plane to understand the effect of trilayer film structure on the magnetization reversal behavior of symmetric and asymmetric domain structures. Hence, a careful analysis of switching of magnetic domains as a function of different applied field angles along the film plane would reveal the nature of magnetic interaction between two CoFeB262 layers as a function of thickness of spacer and ferromagnetic layers.

Recently, nanocrystalline metallic materials produced by systematic crystallization of amorphous precursors attract much attention from a view point of industrial applications because of their promising characteristics as high magnetization soft magnets and from a view of fundamental studies because of their unconventional magnetic properties. The nanocrystalline soft magnetic materials consist of fine nanocrystallites randomly nucleated

in a soft amorphous matrix. Hence, it will be interesting to anneal the as-deposited amorphous single-layer films at different constant temperatures to investigate how the static and dynamic magnetic properties are altered with resulting crystallinity. In case of trilayer films, the crystallinity will modify the interlayer coupling and hence the resulting magnetic properties and domain structure.

References

भारतीय प्रौद्योगिकी संस्थान गुवाहाटी
Indian Institute of Technology Guwahati

[AKTA2013] Aktas B, Tagirov L, Mikailov F, Nanostructured Magnetic Materials and their Applications, Springer Science & Business Media, Dordrecht (2013).

[ALLE1990] Allenspach R, Stampanoni M, Bischof A, Phys. Rev. Lett. 65 (1990) 3344.

[ALLE1994] Allenspach R, J. Magn. Magn. Mater. 129 (1994) 160.

[AMOS2008] Amos N, Fernandez R, Ikkawi R, Lee B, Lavrenov A, Krichevsky A, Litvinov D, Khizroev S, J. Appl. Phys. 103 (2008) 07E732.

[ANDO2015] Ando Y, Jpn. J. Appl. Phys. 54 (2015) 070101.

[ANGU2000] Anguelouch A, Schrag B.D, Xiao G, Trouilloud Y.L.P.L, Wanner R.A, Gallagher W.J, Parkin S.S.P, Appl. Phys. Lett. 76 (2000) 622.

[BAIB1988] Baibich M.N, Broto J.M, Fert A, Van Dau F.N, Petroff F, Eitenne P, Creuzet G, Friederich A, Chazelas J, Phys. Rev. Lett. 61 (1988) 2472.

[BALT2007] Baltz V, Marty A, Rodmacq B, Dieny B, Phys. Rev. B 75 (2007) 014406.

[BAND2016] Bandyopadhyay S, Cahay M, Introduction to Spintronics, 2nd Edition, CRC Press, Taylor & Francis Group, London (2016).

[BINA1989] Binasch G, Grunberg P, Saurenbach F, Zinn W, Phys. Rev. B 39 (1989) 4828.

[BLUN2001] Blundell S, Magnetism in Condensed Matter, Oxford University Press Inc., New York (2001).

[BLUN2003] Blundell S, Magnetism in Condensed Matter, Oxford University Press, Chapter 3 (2003).

[BRUN1989] Bruno P, Renard J.P, Appl. Phys. A 49 (1989) 499.

[BRUN1991] Bruno P, Chappert C, Phys. Rev. Lett. 67 (1991) 1602.

[BRUN1992] Bruno P, Chappert C, Phys. Rev. B 46 (1992) 261.

[CHAP1988] Chappert C, Bruno P, J. Appl. Phys. 64 (1988) 5736.

[CHEN20131] Chen Y-T, Hsieh W.H, J. Alloys Compd. 552 (2013) 283.

[CHEN20132] Chen C-W, Magnetism and Metallurgy of Soft Magnetic Materials. (1st edn), Dover Publications, USA (2013).

[CHOM2001] Cho M.-H, Ko D.-H, Choi Y.G, Jeong K, Lyo I.W, Noh D.Y, Kim H.J, Whang C.N, J. Vac. Sci. Technol. A 19 (2001) 192.

[CHOP2000] Chopra H.D, Yang D.X, Chen P.J, Parks D.C, Egelhoff W.F, Phys. Rev. B 61 (2000) 9642.

[CHOP2005] Chopra H.D, Sullivan M.R, Ludwig A, Quandt E, Phys. Rev. B 72 (2005) 054415.

[CHTC2013] Chtchelkanova A, Wolf S A, Idzerda Y, Magnetic Interactions and Spin Transport. Springer Science & Business Media, New York (2013).

[COEY2010] Coey J.M.D, Magnetism and Magnetic Materials, Cambridge university press, Cambridge (2010).

[COIS2008] Coisson M, Celegato F, Olivetti E, Tiberto P, Vinai F, Baricoo M, J. Appl. Phys. 104 (2008) 033902.

[COIS2009] Coisson M, Vinai F, Tiberto P, Celegato F, J. Magn. Magn. Mater. 321 (2009) 806.

[CONC2013] Conca A, Greser J, Sebastian T, Klingler S, Obry B, Leven B, Hillebrands B, J. Appl. Phys. 113 (2013) 213909.

[CRAI1965] Craik D.J, Tebble R.S, Ferromagnetism and Ferromagnetic Domains, North-Holland Publishing Company, New York (1965).

[CRAU2002] Craus C.B, Chezan A.R, Siekman M.H, Lodder J.C, Boerma D.O, Niesen L, J. Magn. Magn. Mater. 240 (2002) 423.

[CRAU2003] Craus C.B, Magnetic Properties of Nanocrystalline Materials for High Frequency Applications, Thesis (PhD), University of Groningen (2003).

[CUCH2016] Cuchet L, Rodmacq B, Auffret S, Sousa R C, Prejbeanu I.L, Dieny B, Sci. Rep. 6 (2016) 21246.

[CUIB2013] Cui B, Song C, Wang Y Y, Yan W S, Zeng F, Pan F, J. Phys. Condens. Matter 25 (2013) 106003.

[CULL2001] Cullity B.D, Stock S.R, Elements of X-ray diffraction, 3rd edn, Pearson Eduaction, Boston (2001).

[DANI2014] Daniil M, Knipling K.E, Fonda H.M, Willard M.A, New J. Phys. 16 (2014) 55016.

[DASC20181] Das C, Alagarsamy P, J. Magn. Magn. Mater. 448 (2018) 23.

[DASC20182] Das C, PhD Thesis, Indian Institute of Technology Guwahati, Guwahati, India (2018).

[DAVI2004] Davies J.E, Hellwig O, Fullerton E.E, Denbeaux G, Kortright J.B, Liu K, Phys. Rev. B 70 (2004) 224434.

[DECH2012] Decher G, Schlenoff J.B, Multilayer Thin Films : Sequential Assembly of Nanocomposite Materials, Wiley-VCH, Weinheim (2012).

[DIEN2016] Dieny B, Goldfarb R.B, Lee K-J, Introduction to Magnetic Random-Access Memory, John Wiley & Sons, New Jersy (2016).

[FELD1971] Feldtkeller E, J. De Physique 32 (1971) 452.

[FELS2013] Felser C, Fecher G.H, Spintronics: From Materials to Devices, Springer Science & Business Media, Dordrecht (2013).

[FENG1994] Feng Y.C, Laughlin D.E, Lambeth D.N, IEEE. Trans. Magn. 30 (1994) 3960.

[FENG1995] Feng Y.C, Laughlin D.E, Lambeth D.N, IEEE. Trans. Magn. 31(1995) 2845.

[FREI2007] Freitas P.P, Ferreira R, Cardoso S, Cardoso F, Magnetoresistive sensors, J. Phys. Condens. Matter. 19 (2007) 165221.

[FREI2016] Freitas P.P, Ferreira R, Cardoso S, Proc. of IEEE 104 (2016) 1894.

[GAJE2012] Gajek M, Nowak J.J, Sun J.Z, Trouilloud, P.L, O'Sullivan E.J, Abraham D.W, Gaidis M.C, Hu G, Brown S, Zhu Y, Robertazzi R.P, Gallagher W.J, Worledge D.C, Appl. Phys. Lett. 100, (2012) 132408.

[GARR2005] Garreau G, Hajjar S, Bubendorff J.L, Pirri C, Berling D, Mehdaoui A, Stephan R, Wetzel P, Zabrocki S, Gewinner G, Boukari S, Beaurepaire E, Phys. Rev. B 71 (2005) 094430.

[GAYE2017] Gayen A, Prasad G.K, Mallik S, Bedanta S, Perumal A, J. Alloys Compd. 694 (2017) 823.

[GONG2009] Gong Y, Cevher Z, Ebrahim M, Lou J, Pettiford C, Sun N.X, Ren Y.H, J. Appl. Phys. 106 (2009) 63916.

[GUIM1998] Guimaraes A.P, Magnetism and Magnetic Resonance in Solids, Oliveira I.S, John Wiley and Sons, New York (1998).

[GUPT2013] Gupta R, Gupta A, Gupta M, Rajput P, Wildes A, J. Appl. Phys. 114 (2013) 63903.

[GUSE2011] Gusenbauer C, Ashraf T, Stangl J, Hesser G, Plach T, Meingast A, Kothleitner G, Koch R, Phys. Rev. B 83 (2011) 035319.

[HART1999] Hartmann U, Annual Review of Materials Research, 29 (1999) 53.

[HART2013] Hartmann U, Magnetic Multilayers and Giant Magnetoresistance: Fundamentals and Industrial Applications, Springer Science & Business Media, Germany (2013).

[HASH2007] Hashimoto A, Nakagawa S, Yamaguchi M, IEEE Trans. Magn. 43 (2007) 2627.

[HEDI2013] Hedin E.R, Joe Y.S, Spintronics in Nanoscale Devices, CRC Press, USA (2013).

[HEIN1987] Heinrich B, Urquhart K.B, Arott A.S, Cochran J.F, Myrtle K, Purcell S.T, Phys. Rev. Lett. 59 (1987) 1756.

[HEIS1928] Heisenberg V.W, für. Z, Phys. 49 (1928) 619.

[HERZ2013] Herzer G, Acta Mater. 61 (2013) 718.

[HIND2011] Hindmarch A T, Rushforth A W, Campion R P, Marrows C H, Gallagher B L, Phys. Rev. B 83 (2011) 212404.

[HIRO2013] Hirota E, Sakakima H, Inomata K, Giant Magneto-Resistance Devices, Springer Science & Business Media, UK (2013).

[HIRO2015] Hirohata A, Sukegawa H, Yanagihara H, Žutic I, Seki T, Mizukami S, Swaminathan R, IEEE Trans. Magn. 51 (2015) 0800511.

[HORS2006] Czichos H, Saito T, Smith L, Handbook of Materials Measurements methods, Springer, Berlin (2006).

[HTTP1] https://en.wikipedia.org/wiki/Bethe%E2%80%93Slater_curve#/media/File: Bethe-Slater_curve_by_Zureks.svg

[HTTP2] https://nptel.ac.in/courses/115103038/3

[HTTP3] https://nptel.ac.in/courses/115103039/

[HTTP4] https://www.diamond.ac.uk/Instruments/Structures-and-Surfaces/I07.html

[HTTP5] http://barrett-group.mcgill.ca/tutorials/nanotechnology/nano02.htm

[HTTP6] https://nptel.ac.in/courses/115103030/

[HTTP7] https://www.afmworkshop.com/atomic-force-microscope-magnetic-mode.html

[HUAN2001] Huang M-Q, Hsu Y.N, McHenry E, Laughlin D.E, IEEE Trans. Magn. 37 (2001) 2239.

[HUAN2017] Huang L, Yuan Z.H, Tao B.S, Wan C.H, Guo P, Zhang Q.T, Yin L, Feng J.F, Nakano T, Naganuma H, Liu H.F, Yan Y, Han X.F, J. Appl. Phys. 122 (2017) 113903.

[HUBE2014] Hubert A, Schäfer R, Magnetic Domains: the Analysis of Magnetic Microstructures, Springer, New York (2014).

[IANN2014] Iannone E, Labs on Chip: Principles, Design and Technology, CRC Press, Florida (2014).

[IKED2010] Ikeda S, Miura K, Yamamoto H, Mizunuma K, Gan H.D, Endo M, Kanai S, Hayakawa J, Matsukura F, Ohno H, Nat. Mater. 9 (2010) 721.

[IKHT2018] Ikhtiar, Sukegawa H, Xu X, Belmoubarik M, Lee H, Kasai S, Hono K, Appl. Phys. Lett. 112 (2018) 022408.

[INOU1997] Inoue A, Zhang T, Takeuchi A, Appl. Phys. Lett. 71 (1997) 464.

[INOU2014] Inoue J-I, Nanomagnetism and Spintronics: 2. GMR, TMR, BMR, and Related Phenomena, Elsevier Inc. USA (2014).

[ISHI2014] Ishikawa S, Sato H, Yamanouchi M, Ikeda S, Fukami S, Matsukura F, Ohno H, J. Appl. Phys. 115 (2014) 17C719.

[ITOS1980] Ito S, Aso K, Makino Y, Uedaira S, Appl. Phys. Lett. 37 (1980) 665.

[ITOS2005] Ito S, Okamoto T, Kong S-H, Nakagawa S, J. Magn. Magn. Mater. 287 (2005) 281.

[JANS2004] Svoboda J, Magnetic Technique for the Treatment of Materials, Kluwer Academic Publishers, Dordrecht (2004).

[JIAN2006] Jiang J, Tezuka N, Inomata K, J. Magn. Magn. Mater. 302 (2006) 40.

[JIAN2009] Jiang L, Naganuma H, Oogane M, Ando Y, Appl. Phys. Express. 2 (2009) 83002.

[JILE1997] Jiles. D, Introduction to Magnetism and Magnetic Materials, Chapman and Hall, Boca Raton (1997).

[KASU1956] Kasuya T, Progress of Theoretical Physics 16 (1956) 45.

[KAZI2013] Kazimierczuk M.K, High-frequency magnetic components, Second ed., Wiley-VCH, UK (2013).

[KIPG2012] Kipgen L, Fulara H, Raju M, Chaudhary S, J. Magn. Magn. Mater. 324 (2012) 3118.

[KITT2004] Kittel C, Introduction to Solid state Physics, 7th edn Wiley, Singapore (2004).

[KLEM2000] Klemmer T J, Ellis K.A, Chen L.H, van Dover B, Jin S, J. Appl. Phys. 87 (2000) 830.

[KOBL1978] Kobliska R.J, Aboaf J.A, Gangulee A, Cuomo J.J, Klokholm E Appl. Phys. Lett. 33 (1978) 473.

[KOOL1999] Kools J.C.S, Kula W, Mauri D, Lin T, J. Appl. Phys. 85 (1999) 4466.

[KOON1987] Koon N.C, Jonker B.T, Volkening F.A, Krebs J.J, Prinz G.A, Phys. Rev. Lett. 59 (1987) 2463.

[KRON2003] Kronmuller H, Fahnle M, Micromagnetism and the Microstructure of Ferromagnetic Solids, Cambridge University Press, New York (2003).

[KUDR1997] Kudrnovský J, Drchal V, Bruno P, Turek I, Weinberger P, Phys. Rev. B 56 (1997) 8919.

[KUMA2005] Kumar D, Gupta A, Hyperfine Interact. 160 (2005) 165.

[KURI2017] Kurinec S.K, Iniewski K, Nanoscale Semiconductor Memories: Technology and Applications, CRC Press, Florida (2017).

[LALM2017] Lal M, Ph.D. Thesis, Indian Institute of Science, Bangalore (2017).

[LEES2017] Lee S-E, Baek J-U, Park J-G, Sci. Rep. 7 (2017) 11907.

[LEON2014] León J.C.-, Svendsen W.E, Lab-on-a-Chip Devices and Micro-Total Analysis Systems: A Practical Guide, Springer, UK (2014).

[LIUT2012] Liu T, Cai J.W, Sun L, AIP Adv 2 (2012) 032151.

[LIUX2011] Liu X, Zhang W, Carter M J, Xiao G, J. Appl. Phys. 110 (2011) 33910.

[LIUX2012] Liu X.M, Ho P, Chen J.S, Adeyeye A.O, J. Appl. Phys. 112 (2012) 073902.

[LIUY2008] Liu Y, Sellmyer D.J, Shindo D, Handbook of Advanced Magnetic Materials: Vol 1. Nanostructural Effects. Vol 2. Characterization and Simulation. Vol 3. Fabrication and Processing. Vol 4. Properties and Applications, Tsinghua University Press, Springer (2008).

[LIUY2016] Liu Y, Hao L, Cao J, AIP Adv. 6, (2016) 45008.

[LIXW2007] Li X.W, Song C, Yang J, Zeng F, Geng K.W, Pan F, J. Magn. Magn. Mater. 315 (2007) 120.

[LUCA2011] Lucas M.S, Bourne W.C, Sheets A.O, Brunke L, Alexander M.D, Shank J.M, Michel E, Semiatin S.L, Horwath J, Turgut Z, Mater. Sci. Eng. B 176 (2011) 1079.

[MAEK2017] Maekawa S, Valenzuela S.O, Saitoh E, Kimura T, Spin Current, OUP Oxford (2017).

[MAKI1995] Makino A, Inoue A, Masumoto T, Mat. Trans. JIM 36 (1995) 924.

[MALL2012] Mallinson J.C, The Foundations of Magnetic Recording, Elsevier, Academic Press, UK (2012).

[MANT2013] Mantovan R, Lamperti A, Tallarida G, Baldi L, Mariani M, Ocker B, Ahn S.-M, Barisic I, Ravelosona D, Thin Solid Films. 533 (2013) 75.

[MAPP1991] Mapps D.J, Akhter M.A, Pan G, J. Appl. Phys. 69 (1991) 5178.

[MART1987] Martin Y, Wickramasinghe H.K, Appl. Phys. Lett. 50 (1987) 1455.

[MCHE1999] McHenry M.E, Willard M.A, Laughlin D.E, Prog. Mater. Sci. 44 (1999) 291.

[MIDD1963] Middelhoek S, J. Appl. Phys. 34 (1963) 1054.

[MISH2011] Mishra D, Singh A.K, Shyni P.C, Sharma D, Perumal A, J. Appl. Phys. 109 (2011) 07A304.

[MUNA2005] Munakata M, Shin-Ichi Aoqui, Yagi M, IEEE Trans. Magn. 41 (2005) 3262.

[MURA1966] Murayama Y, J. Phys. Soc. Jpn. 21 (1966) 2253.

[NAGA2000] Nagasaka K, Varga L, Shimizu Y, Eguchi S, Tanaka A, J. Appl. Phys. 87 (2000) 6433.

[NAIK2012] Naik V.B, Meng H, Sbiaa R, AIP Adv. 2, (2012) 42182.

[NAKA1997] Nakagawa S, Suemitsu K, Naoe M, J. Appl. Phys. 81 (1997) 3782.

[NAKA2001] Nakamura F, Hikosaka T, Tanaka Y, J. Magn. Magn. Mater. 235 (2001) 64.

[NAOE1998] Naoe M, Matsumiya H, Ichihara T, Nakagawa S, J. Appl. Phys. 83 (1998) 6673.

[NAVA2014] Navas D, Redondo C, Badini Confalonieri G.A, Batallan F, Devishvili A, Iglesias-Freire Ó, Asenjo A, Ross C.A, Toperverg B.P, Phys. Rev. B 90 (2014) 54425.

[NEAL1994] Neal H.B, Theory of Magnetic Recording, Cambridge University Press, New York (1994).

[NEEL1954] Neel L, J. Phys. Rad. 15 (1954) 376.

[NEEL1962] Néel L, Comptes. Rendus Acad. Sci. 255 (1962) 1676.

[NIST2010] Nistor L.E, Rodmacq B, Auffret S, Schuhl A, Chshiev M, Dieny B, Phys.Rev. B 81 (2010) 220407.

[NOWA1993] Nowak J, Wenda J, J. Magn. Magn. Mater. 124 (1993) 119.

[OEPE1990] Oepen H.P, Benning M, Ibach H, Schneider C.M, Kirschner J, J. Magn. Magn. Matt. 86 (1990) L137.

[OHAN1987] O'Handley R.C, J. Appl. Phys. 62 (1987) R15.

[OHAN2000] O'Handley R.C, Modern Magnetic Materials Principles and Applications, Wiley, New York (2000).

[OHRI1992] Ohring M, Materials Science of Thin Films, Academic Press, London (1992).

[OLIV1999] Oliveira A.J.A.de, Ortiz W.A, Mosca D.H, Mattoso N, Mazzaro I, Schreiner W.H, J. Phys.: Condens. Matter. 11 (1999) 47.

[PALU2006] Paluskar P.V., Kohlhepp J.T, Swagten H.J.M, Koopmans B, J. Appl. Phys. 99 (2006) 08E503.

[PAND2016] Pandey H, Perumal A, Wang J, Takahashi Y.K, Hono K, IEEE Trans Magn 52 (2016) 3201004.

[PARK1990] Parkin S.S.P, More N, Roche K.P, Phys. Rev. Lett. 64 (1990) 2305.

[PARK2008] Park J-H, Park C, Jeong T, Moneck M.T, Nufer N.T, Zhu J-G, J. Appl. Phys. 103 (2008) 07A917.

[PARK2011] Park J-Y, Kang S-K, Jeon M-H, Jhon M.S, Yeom G-Y, J. Electrochem. Soc. 158 (2011) H1.

[PELL2015] Pellegren J.P, Sokalski V.M, IEEE Trans. Magn. 51 (2015) 3400903.

[PESC1987] Pescia D, Stampanoni M, Bona G.L, Vaterlaus A, Willis R.F, Meier F, Phys. Rev. Lett. 58 (1987) 2126.

[PETT2006] Pettiford C.I, Zeltser A, Yoon S.D, Harri V.G, Vittoria C, Sun N.X, J. Appl. Phys. 99 (2006) 08C901.

[PIRA2007] Piramanayagam S.N, J. Appl. Phys. 102 (2007) 11301.

[PIRA2011] Piramanayagam S.N, Chong T.C, Developments in Data Storage: Materials Perspective, John Wiley & Sons, New Jersy (2011).

[PLAT2000] Platt C.L, Berkowitz A.E, Smith D.J, McCartney M.R, J. Appl. Phys. 88 (2000) 2058.

[PLAT2001] Platt C.L, Minor N.K, Klemmer T.J, IEEE Trans. Magn. 37 (2001) 2302.

[PONG2008] Pong P.W.T, Dennis C.L, Castillo A, J. Appl. Phys. 103 (2008) 07A902.

[PORR2002] Porrati F, Spatially Varying Magnetic Anisotropies in Ultrathin Films, Thesis (PhD) Martin-Luther-University (2002).

[PORT1998] Porthun S., Abelmann L., Lodder C, J. Magn. Magn. Magn. 182 (1998) 238.

[PRAD1997] Prado L.M.A, Pérez G.T, Morales R, Salas F.H, Alameda J.M, Phys. Rev. B 56 (1997) 3306.

[PRAD2004] Prado L.M.A, Alamedo J.M, Physica B 343 (2004) 241.

[PRUT1964] Prutton M, Thin Ferromagnetic Films, Butterworth Inc, University of California (1964).

[PUA2007] Pu A and Thomson D.J, Meas. Sci. Technol. 18 (2007) L19–L22.

[QIAO2016] Qiao X, Wang B, Tang Z, Shen Y, Yang H, Wang J, Zhan Q, Mao S, Xu X, Li R.-W, AIP Adv. 6 (2016) 56106.

[REIG2013] Reig C, Cardoso S, Mukhopadhyay S.C, Giant Magnetoresistance (GMR) Sensors: From Basis to State-of-the-Art Applications, Springer Science & Business Media, Berlin (2013).

[RENY2009] Ren Y.H, Wu C, Gong Y, Pettiford C, Sun N.X, J. Appl. Phys. 105 (2009) 73910.

[RIET1997] Riet V.D.E, Klaassens W, Roozeboom F, J. Appl. Phys. 81 (1997) 806.

[RUDE1954] Ruderman M.A, Kittel C, Phys. Rev. 96 (1954) 99.

[RUGA1998] Rugar D, Mamin H.J, Guethner P, Lambert S.E, Stern J.E, McFadyen I, Yogi T, J. App. Phys. 68 (1998) 11694.

[SAIT2002] Saitoh E, Matumoto H, Nakamura T, Miyajima H, J. Appl. Phys. 91 (2002) 7215.

[SAKU2013] Sakurai Y, Hamakawa Y, Shirae K, Masumoto T, Suzuki K, Current Topics in Amorphous Materials: Physics & Technology, North-Holland, Elsevier (2013).

[SATO2014] Sato H, Enobio E.C.I, Yamanouchi M, Ikeda S, Fukami S, Kanai S, Matsukura F, Ohno H, Appl. Phys. Lett. 105 (2014) 62403.

[SATO2015] Sato K, Saitoh E, Spintronics for next generation innovative devices, Wiley Series in materials for electronic & optoelectronic applications, Willoughby A, Capper P, Kasap S (Edts). Wiley, UK (2015).

[SCHA2007] Schäfer R, Novel Techniques for Characterizing and Preparing Samples in Handbook of Magnetism and Advanced Magnetic Materials, ed. H. Kronmüller, Parkin S, Vol. 3, Wiley, Chichester (2007).

[SCHA2016] Schapers T, Semiconductor spintronics, Walter de Gruyter GmbH & Co KG, Germany (2016).

[SCHR2000] Schrag B.D, Anguelouch A, Ingvarsson S, Xiao G, Trouilloud Y.L.P.L, Gupta A, Wanner R.A, Gallagher W.J, Rice P.M, Parkin S.S.P, Appl. Phys. Lett. 77 (2000) 2373.

[SERA2011] Serafinczuk J, Pietrucha J, Schroeder G, Gotszalk T.P, Optica Applicata XLI(2) (2011) 315.

[SESH2002] Seshan K, Handbook of Thin-film Deposition Processes and Techniques: Principles, Methods, Equipment, and Applications, Noyes publication, New York (2002).

[SHAR2006] Sharma P, Kimura H, Inoue A, Arenholz E, Guo J.H, Phys. Rev. B 73 (2006) 052401.

[SHIN2014] Shinko T, Nanomagnetism and spintronics, 2nd Ed. Elsevier, USA (2014).

[SING2012] Singh A.K, Kisan B, Mishra D, Perumal A, J. Appl. Phys. 111 (2012) 93915.

[SING2013] Singh A.K, Mallik S, Bedanta S, Perumal A, J. Phys. D. Appl. Phys. 46 (2013) 445005.

[SING2014] Singh A.K, Mallik S, Bedanta S, Perumal A, IEEE Trans. Magn. 50 (2014) 2000804.

[SING2015] Singh A.K, PhD Thesis, Indian Institute of Technology Guwahati, Guwahati (2015).

[SING20161] Singh A.K, Perumal A, J. Phys. D. Appl. Phys. 49 (2016) 85001.

[SING20162] Singh A.K, Perumal A, J. Magn. Magn. Mater. 401 (2016) 1015.

[SONG2000] Song D, Nowak J, Larson R, Kolbo P, Chellew R, IEEE Trans. Magn. 36 (2000) 2545.

[STIL2005] Stiles M.D, Interlayer Exchange Coupling in Ultrathin Magnetic Structures III: Fundamentals of Nanomagnetism ed. Bland J.A.C, Heinrich B, Springer, New York (2005).

[SULI2015] Su L, Zhang Y, Klein J-O, Zhang Y, Bournel A, Fert A, Zhao W, Sci. Rep. 5 (2015) 14905.

[SUNZ2004] Sun Z.G.G, Kuramochi H, Mizuguchi M, Takano F, Semba Y, Akinaga H, Surf. Sci. 556 (2004) 33.

[TANA2003] Tanahashi K, Kikukawa A, Takahashi Y, Hosoe Y, J. Appl. Phys. 93 (2003) 6766.

[TANG2010] Tang D.D, Lee Y.-J, Magnetic Memory: Fundamentals and Technology, Cambridge University Press, UK (2010).

[TANG2014] Tang Z, Wang B, Yang H, Xu X, Liu Y, Sun D, Xia L, Zhan Q, Chen B, Tang M, Zhou Y, Wang J, Li R-W, Appl. Phys. Lett. 105 (2014) 103504.

[TANG2017] Tang Z, Ni H, Lu B, Zheng M, Huang Y-A, Lu S-G, Tang M, Gao J, J. Magn. Magn. Mater. 426 (2017) 444.

[TEHR2000] Tehrani S, Engel B, Slaughter J.M, Chen E, DeHerrera M, Durlam M, Naji P, Whig R, Janesky J, Calder J, IEEE Trans. Magn. 36 (2000) 2752.

[TEIX2006] Teixeira J.M, Silva R.F.A, Ventura J, Pereira A.M, Carpinteiro F, Araújo J.P, Sousa J.B, Cardoso S, Ferreira R, Freitas P.P, Mater. Sci. Eng. B 126 (2006) 180.

[THOM1997] Thomson T, O'Grady K, IEEE Trans. Magn. 33 (1997) 795.

[THOM2000] Thomas L, Samant M.G, Stuart S.P.P, Phys. Rev. Lett. 84 (2000) 3462.

[THOM2014] Thomas L, Jan G, Zhu J, Liu H, Lee Y-J, Le S, Tong R-Y, Pi K, Wang Y-J, Shen D, He R, Haq J, Teng J, Lam V, Huang K, Zhong T, Torng T, Wang P-K, J. Appl. Phys. 115 (2014) 172615.

[THOR1993] Thornton S.T and Rex A, Modern Physics for Scientists and Engineers, Saunders College Publishing (1993).

[TSAI2014] Tsai C.C, Cheng C.-W, Tsai M.-C, Chern G, IEEE Trans. Magn. 50 (2014) 1.

[TSYM2016] Tsymbal E.Y, Zutic I, Handbook of Spin Transport and Magnetism, CRC Press, Florida (2016).

[UHRM2008] Uhrmann T, Dimopoulos T, Brückl H, Lazarov V.K, Kohn A, Paschen U, Weyers S, Bär L, Rührig M, J. Appl. Phys. 103 (2008) 63709.

[VARV2016] Varvaro G, Casoli F, Ultra-High-Density Magnetic Recording: Storage Materials and Media Designs. Pan Stanford Publishing, CRC Press, Taylor & Francis Group, Florida (2016).

[VAZQ2015] Vázquez M, Magnetic Nano- and Microwires: Design, Synthesis, Properties and Applications, Woodhead Publishing, Elsevier, UK (2015).

[VEMU2016] Vemulkar T, Mansell R, Fernández-Pacheco A, Cowburn R P, Adv. Funct. Mater. 26 (2016) 4704.

[VILL2010] Villard P, Ebels U, Houssameddine D, Katine J, Mauri D, Delaet B, Vincent P, Cyrille M.-C, Viala B, Michel J.-P, Prouvee J, Badets F, IEEE J. Solid-State Circuits 45 (2010) 214.

[WAGE1994] Wagendristel A, Wang Y, An Introduction to Physics and Technology of Thin Films, World Scientific, Singapore, 1994.

[WANC2017] Wan C.H, Zhang X, Yuan Z.H, Fang C, Kong W.J, Zhang Q.T, Wu H, Khan U, Han X.F, Adv. Electron. Mater. 3 (2017) 1600282.

[WANG1999] Wang S.X, Hong J, IEEE Trans. Magn. 35 (1999) 782.

[WANG2014] Wang Y, Wei D, Gao K, Cao J, Wei F, J. Appl. Phys. 115 (2014) 053901.

[WANG2017] Wang X, Metallic Spintronic Devices, CRC Press, Florida (2017).

[WIES2006] Wiese N, Coupling phenomena and scalability of CoFeB/Ru/CoFeB sandwiches. Dissertation (PhD), Bielefeld University, Germany (2006).

[WOLF2001] Wolf S.A, Awschalom D.D, Buhrman R.A, Daughton J.M, Von Molnar S, Roukes M.L, Chtchelkanova A.Y, Treger D.M, Spintronics: A spin-based electronics vision for the future, Science 294 (2001) 1488.

[WUYM1998] Wu Y.M, Lo J.-T, Jpn. J. Appl. Phys. 37 (1998) 4943.

[XUY2015] Xu Y, Awschalom D.D, Nitta J, Handbook of Spintronics, Springer, Netherlands (2015).

[YAMA2011] Yamanouchi M, Jander A, Dhagat P, Ikeda S, Matsukura F, Ohno H, IEEE Magn. Lett. 2 (2011) 3000304.

[YANG2013] Yang F.F, Yan S.S, Yu M.X, Kang S.S, Dai Y.Y, Chen Y.X, Pan S.B, Zhang J.L, Bai H.L, Zhu D.P, Qiao S.Z, Pan W.W, Liu G.L, Mei L.M, J. Alloys Compd. 558 (2013) 91.

[YILD20091] Yildiz F, Przybylski M, Kirschner J, J. Appl. Phys. 105 (2009) 07E129.

[YILD20092] Yildiz F, Przybylski M, Ma X.D, Kirschner J, Phys. Rev. B 80 (2009) 064415.

[YOSH1988] Yoshizawa Y, Oguma S, Yamauchi K, J. Appl. Phys. 64 (1988) 6044.

[YOSI1957] Yosida K, Phys. Rev. 106 (1957) 893.

[YOUC2017] You C.-Y, Kim H, IEEE Trans. Magn. 53 (2017) 1400504.

[YUJU2002] Yu J, Chang C, Karns D, Ju G , Kubota Y, Eppler W, Brucker C, Weller D, J. Appl. Phys. 91 (2002) 8357.

[ZHAN19961] Zhang J, White R.M, J. Appl. Phys. 79 (1996) 5113.

[ZHAN19962] Zhang J, White R.M, IEEE Trans. Magn. 32 (1996) 4630.

[ZHAN2015] Zhang X, Zhang Y, Cai J.W, J. Appl. Phys. 118 (2015) 143903.

[ZHAN2016] Zhang J, Siddiqui S.A, Ho P, Incorvia J.A.C-, Tryputen L, Lage E, Bono D.C, Baldo M.A, Ross C.A, New Journal of Physics 18 (2016) 053028.

[ZHAN2017] Zhang X, Wan C.H, Yuan Z.H, Fang C, Kong W.J, Wu H, Zhang Q.T, Tao B.S, Han X.F, J. Magn. Magn. Mater. 428 (2017) 401–405.

[ZHAO2015] Zhao W, Prenat G, Spintronics-based computing, Springer International Publishing, Switzerland (2015).

[ZHOU2017] Zhou J, Zhao W, Peng S, Qiao J, Klein J.-O, Lin X, Zhang Y, Bournel A, IEEE Trans. Magn. 53 (2017) 1300504.

[ZHUK2017] Zhukov A, High Performance Soft Magnetic Materials, Springer, Switzerland (2017).

[ZHUT2015] Zhu T, Zhang Q, Yu R, in: 2015 IEEE Magn. Conf., IEEE, (2015): pp. 1.

[ZHUY2012] Zhu Y, Zhang Z, Ma B, Jin Q.Y, J. Appl. Phys. 111 (2012) 07C106.

Indian Institute of Technology Guwahati

Publications

भारतीय प्रौद्योगिकी संस्थान गुवाहाटी
Indian Institute of Technology Guwahati

LIST OF PUBLICATIONS

IN JOURNALS

Sl.	Published / Under Review & Submission
[1].	Interlayer coupling in symmetric and asymmetric CoFeB based trilayer films with different domain structures: Role of spacer layer and temperature **Anabil Gayen**, G. Kr. Prasad, K. Umadevi, J. Arout Chelvane, Perumal Alagarsamy *Journal of Magnetism and Magnetic Materials 462 (2018) 29-40.
[2].	Effects of composition, thickness and temperature on the magnetic properties of amorphous CoFeB thin films **Anabil Gayen**, G. Kr. Prasad, S. Mallik, S. Bedanta and Perumal Alagarsamy *Journal of Alloys and Compounds 694 (2017) 823-832.
[3].	Tuning magnetic properties of thick CoFeB film by interlayer coupling in trilayer structured thin films **Anabil Gayen**, Kosuri Umadevi, J. Arout Chelvane and Perumal Alagarsamy *Journal of Material Sciences & Engineering 7 (2) (2018) 1000437.
[4].	Static and dynamic magnetic properties of CoFeB based thin films **Anabil Gayen**, R. Modak, A. Srinivasan, V.V. Srinivasau, Perumal Alagarsamy **Manuscript under submission*
[5].	Magnetic properties of annealed CoFeB thin films **Anabil Gayen**, Perumal Alagarsamy **Manuscript under submission*
[6].	Structural and magnetic properties of Ni-Mn-Sn thin films R. Modak, B. Deka, A. K. Singh, **Anabil Gayen**, A. Perumal, M. Manivel Raja, and A. Srinivasan AIP Conference Proceedings 1665 (2015) 080072.
[7].	Magnetic Properties of FePt based Nanocomposite Thin Films Grown on Low Cost Substrates **Anabil Gayen**, B. Biswas, A.K. Singh, P. Saravanan, A. Perumal Physics Procedia 54 (2014) 23-29.

[8].	Study on the depth profile analysis of Fe/Co intermixing in $[SmCo_5/Fe]_{11}$ magnetic multilayers P. Saravanana, Jen-Hwa Hsu, A. Perumal, **Anabil Gayen**, G.L.N. Reddy, Sanjiv Kumar, and S.V. Kamat, Physica B 448 (2014) 1.
[9].	Effect of Fe layer thickness and Fe/Co intermixing on magnetic properties of Sm-Co/Fe bilayer exchange spring magnets P Saravanan, Jen-Hwa Hsu, **Anabil Gayen**, Akhilesh Kr. Singh, A Perumal, G L N Reddy, Sanjiv Kumar and S V Kamat Journal of Physics D: Applied Physics 46 (2013) 155002.
[10].	Magnetic Properties of Ultra-Thin FePt Films Grown on Oxidized Si Substrates **Anabil Gayen**, P. Saravanan and A. Perumal Springer Proceedings in Physics 143 (2013) 457-464.
[11].	High temperature magnetic properties of indirect exchange spring FePt/M(Cu,C)/ Fe trilayer thin films **Anabil Gayen**, B. Biswas, A. K. Singh, P. Saravanan, and A. Perumal J. Nanomaterials 2013 (2013) 718365.

*Publications from thesis work

In Conferences

[1].	Tuning magnetic properties of thick CoFeB films by interlayer coupling through simple trilayer structure **Anabil Gayen** and Perumal Alagarsamy, Presented in National Conference on Condensed Matter (CMDAYS-2017), 29-31 August, 2017, Tezpur University, Assam.
[2].	Role of nanostructure on the magnetic properties of novel materials and its applications in future magnetoelectronics devices A. Perumal, K. Bhagaban, Patta Ravikumar, D. Camelia, **Anabil Gayen**, Anneta Padhan Manjari Invited Talk given in School of Physics, Madurai Kamaraj University, July 06, 2017.

[3].	Study on the magnetic interactions of CoFeB based trilayer films using vibrating sample magnetometer **Anabil Gayen** and Perumal Alagarsamy, Presented in International Conference on Sophisticated Instruments in Modern Research (ICSIMR-2017), 30th June and 1st July 2017, CIF, IIT Guwahati, Assam.
[4].	Understanding spacer layer thickness and temperature dependent magnetic interactions in CoFeB based trilayer films with different domain structures **Anabil Gayen,** Gobinda Kr. Prasad and Perumal Alagarsamy, Presented in The International Conference on Magnetic Materials and Applications (ICMAGMA - 2017), Leonia Holistic Resorts, Hyderabad, 1 - 3 February 2017.
[5].	Spacer and ferromagnetic layers driven temperature dependent magnetic properties of amorphous CoFeB based bilayer films **Anabil Gayen**, Gobinda Kr. Prasad, Perumal Alagarsamy, Presented in The International Conference on Magnetic Materials and Applications (ICMAGMA - 2015), VIT University, December 2-4, 2015, Vellore, Tamil Nadu.
[6].	Thickness Dependent Magnetic Properties of Amorphous CoFeB Thin Films **Anabil Gayen** and Perumal Alagarsamy, Presented in The International Conference on Magnetic Materials and Applications (ICMAGMA - 2014), 15-17 September 2014, Pondicherry University, Pondicherry.

* * * * * * * * *